THREE-DIMENSIONAL CARBON NANOTUBE BASED PHOTOVOLTAICS

A Thesis
Presented to
The Academic Faculty

by

Jack Flicker

In Partial Fulfillment
of the Requirements for the Degree
Doctor of Philosophy in the
School of Materials Science and Engineering

Georgia Institute of Technology
August 2011

THREE-DIMENSIONAL CARBON NANOTUBE BASED PHOTOVOLTAICS

Approved by:

Dr. W. B. Carter, Committee Chair
School of Materials Science and Engineering
Georgia Institute of Technology

Dr. W. Jud Ready, Advisor
School of Materials Science and Engineering
Georgia Institute of Technology

Dr. Z. L. Wang
School of Materials Science and Engineering
Georgia Institute of Technology

Dr. Samuel Graham
Department of Mechanical Engineering
Georgia Institute of Technology

Dr. Alex Howard
Advanced Solar Power Group
Air Force Research Laboratory

Date Approved: 15 June 2011

To Jackie...

and Dunkin' and Grumbles.

ACKNOWLEDGEMENTS

This work would not be possible without the monetary support of the Air Force Research Lab, National Aeronautics and Space Administration, Defense Advanced Research Projects Agency, Robert G. Shackelford Graduate Fellowship, and Boeing Graduate Fellowship.

I would like to thank my advisor, Dr. Ready, for his support and guidance of my research. I would also like to thank the members of my committee for their hard work and guidance.

This research could not be completed without the help of fellow students and researchers. I would like to thank Rodolfo Camacho and Chris Haverly for their help in the lab, Stephan Turano for his advice, Dr. Bong Jae Lee for his help with transfer matrix formulation, and Xiaojia Wang for her guidance on the optical properties of carbon nanotubes. I would also like to acknowledge GTRI EOSL members Virginia Meyers, Jason Nadler, Zhitao Kang, Brent Wagner, Matt King, Stan Halpern, David Stollberg, and Mike Harris.

Finally, no acknowledgment section would be complete without a thank you to my friends and family, without whom balancing research and life would be much more difficult.

TABLE OF CONTENTS

DEDICATION . . . . . **iii**

ACKNOWLEDGEMENTS . . . . . **iv**

LIST OF TABLES . . . . . **viii**

LIST OF FIGURES . . . . . **x**

LIST OF SYMBOLS OR ABBREVIATIONS . . . . . **xvi**

SUMMARY . . . . . **xxiii**

I MOTIVATION **1**

II BACKGROUND **6**

2.1 Introduction to Photovoltaics 6

2.1.1 History of Photovoltaics 6

2.1.2 Basic Operating Principles 9

2.1.3 CdTe Cells 23

2.1.4 $CdCl_2$ Post Treatment 41

2.1.5 Solar cell texturing 44

2.1.6 Third Generation Solar Cells 47

2.2 Introduction to CNTs 53

2.2.1 History 53

2.2.2 Structure and Bonding 55

2.2.3 Types of CNTs 56

2.2.4 Electronic Conduction in CNTs 63

2.2.5 CNT Synthesis 72

2.2.6 CNT Growth Mechanism 74

2.2.7 Vertical Alignment of CNT 76

2.3 Introduction to 3DCNTPV cells 79

III EXPERIMENTAL PROCEDURE 82
3.1 Photolithography 83
3.2 Catalyst Deposition 85
3.2.1 Results of catalyst deposition 87
3.3 CNT Growth 87
3.3.1 Results of CNT growth 89
3.4 Molecular Beam Epitaxy 92
3.4.1 Results from CdTe deposition 95
3.4.2 Results from CdS deposition 99
3.5 Ion Assisted Deposition 106
3.5.1 Results from ITO deposition 106
3.6 IV characterization 115
IV THEORY OF OPERATION 120
4.1 Derivation of η_{3D} 121
4.2 Derivation of Γ 128
4.3 Simulations 142
4.3.1 Azimuthal Angle 143
4.3.2 Tower Separation 143
4.3.3 Tower height 144
4.3.4 Absorption Efficiency 146
4.3.5 Tower Shape 151
4.4 Nonspecular Reflection 153
4.5 Reflection at different angles 157
V RESULTS AND DISCUSSION 163
5.1 MBE Cells 163
5.2 Chemical Bath Deposition Cells 166
5.3 Planar Cells 171
5.4 MBEOx Cells 177

5.5 Area Fraction Cells . . . 182
5.6 Metallized Cells . . . 186
5.7 Increased Growth Time . . . 201
5.7.1 Altered ITO Deposition . . . 210
5.7.2 Electron beam Depostion . . . 213
5.7.3 RF sputter Deposition . . . 223
5.8 High Resistance and Transparent Layer . . . 228
5.9 $CdCl_2$ Processing . . . 238
5.9.1 Post-CdTe Deposition . . . 238
5.9.2 Pre-MBE Deposition . . . 243
5.10 Summary of Device Production . . . 247
5.11 Power versus solar incident angle . . . 249
5.11.1 Testing Setup . . . 249
5.11.2 Error Source Discussion . . . 251
5.11.3 Testing Procedure . . . 266
5.11.4 Results . . . 266
5.11.5 Experimental Comparison to Theory . . . 268
5.11.6 Geometry of MBEOxAu 80 . . . 270
VI SUMMARY AND FUTURE WORK . . . 280
6.1 Summary of Contributions . . . 280
6.2 Future Work . . . 282
REFERENCES . . . 284
VITA . . . 305

LIST OF TABLES

Table

1 Peak List for XRD of CdTe 100

2 Peak List for XRD of CdS 104

3 Peak List for XRD of ITO 113

4 Photon in an infinite trench 135

5 Figures of merit for 3DCNTPV cells 164

6 Materials used in CBD of CdS 166

7 Figures of merit for CBD cells 167

8 Figures of merit for planar cells 172

9 Figures of merit for MBEOx cells 179

10 Figures of merit for Area Fraction cells 184

11 Figures of merit cells metallized with Cu 197

12 Figures of merit cells metallized with Ag 197

13 Figures of merit cells metallized with Au 198

14 Cells with increased MBE deposition time 201

15 Figures of merit for cells with increased deposition time 202

16 Figures of merit for cells with Ni barrier layer 211

17 Figures of merit for cells with 2-stage ITO deposition 212

18 Figures of merit for cells with electron beam deposited ITO 215

19 R_{sheet} of ebeam ITO after anneal in various environments 220

20 Figures of merit for sputtered ITO cells 227

21 Figures of merit for cells with HRT layer 232

22 Figures of merit for cells with 100% O_2 during ZnO deposition 234

23 Figures of merit for cells with wet $CdCl_2$ anneal 239

24 Figures of merit for cells with dry $CdCl_2$ anneal 241

25 Figures of merit for cells with CdTe only $CdCl_2$ anneal 242

26 Figures of merit for cells with two-stage CdS and $CdCl_2$ anneal . . . 243

27 Figures of merit for cells with pre-MBE $CdCl_2$ 245
28 Calculation of Γ for non point source light 253
29 Heating and cooling of ELH lamp 259
30 P_{mp} vs. ψ measurements for MBEOxAg 80 267
31 P_{mp} vs. ψ measurements for Planar Cell 07 268
32 Parameters used to calculate theoretical P_{mp} vs. ψ 273
33 Theoretical Γ and P_{mp} for 3DCNTPV cell 274

LIST OF FIGURES

Figure

1 3D CNT PV 4

2 Three generations of phovoltaics devices 7

3 Generation of a space charge region and built-in field in a p-n junction 10

4 Absorption and loss mechanisms in a solar cell 11

5 Heterojunction band diagram 13

6 IV curves and circuit diagram for an ideal solar cell in the dark and light 15

7 Recombination mechanisms in a solar cell 17

8 Effect of R_s and R_{sh} on solar cell IV curve 19

9 Circuit diagram of a non-ideal solar cell 20

10 Dark IV curve analysis 22

11 AM1.5 solar spectrum 24

12 IV curve of a CdTe cell at η_{SQ} 27

13 Maximum efficiency vs. bandgap 27

14 CdTe solar cell makeup 30

15 Superstrate vs. substrate configuration 31

16 Electron affinity of CdTe compared to the work function of common materials 38

17 Roll-over effect on IV curve of CdTe cell 40

18 Three types of nanostructured solar cells 48

19 Orthogonalization of light absorption and carrier collection in 1D nanostructures 49

20 CNT/CdS band structure 52

21 Fullerene structures 54

22 CNT chiral vector 57

23 CNT chiral indices 58

24 Spiral of chiral CNTs 59

25 Fermi points of CNT 60
26 Allowed chiral angles in MWCNTs 62
27 Classic and1D conductors 64
28 Bandstructure of zigzag s-CNT and m-CNT 66
29 Conductance vs. applied voltage for CNT 68
30 Conducting through multiple MWCNT shells 69
31 Conduction of CNTs compared to Cu 71
32 Chemical Vapor Deposition of CNTs 73
33 Mechanisms of CNT growth 75
34 Vertical alignment of CNTs 78
35 3DCNTPV 80
36 3DCNTPV process flow 82
37 Block Photolithography Pattern 84
38 Waffle Photolithography Pattern 84
39 Denton thermal evaporator system 86
40 Catalyst thickness results 87
41 First Nano CVD system 88
42 CVD temperature and gas flow vs. time profiles 89
43 Scanning electron micrographs of as grown CNTs 90
44 Transmission electron micrographs of as grown CNTs 91
45 Molecular Beam Epitaxy System 94
46 CdTe on CNTs 96
47 EDS on MBE CdTe and CdS 97
48 Absorption of CdTe 99
49 Xray diffraction spectrum of CdTe sample 100
50 PL spectra of CdS 102
51 CdS bandgap vs. temperature 103
52 Xray diffraction spectrum of CdS sample 105
53 IAD system 107

54 Transmission of IAD deposited ITO 109
55 ITO on VACNTs 111
56 ITO TEM and EDS spectrum 112
57 ITO X-ray diffractogram 114
58 Dark IV curve of CdTe cell from NREL 117
59 GaAs light IV curve as measured by NREL and Keithley SCS 119
60 Idealized 2D slice of VACNT tower 122
61 Power output of a 3DCNT cell vs. ψ 127
62 Definition of photon coordinate system 129
63 Dwell time for photon in system 132
64 Simple 3D cell composed of a single trench 134
65 Photon in a box 137
66 2D array of towers 139
67 Γ vs. ψ for various θ 143
68 Γ vs. ψ for various tower separation 144
69 Γ vs. ψ for various height 145
70 Error between theory and simulation 147
71 P_{mp} vs. ψ for η_{2D} 148
72 P_{mp} vs. time 150
73 Maximum output energy ratio between 3D and planar cells 151
74 Difference simulation tower geometries 152
75 Energy output for various geometries 153
76 Lambertian reflection 155
77 Lambertian reflection model of an infinite x-trench 156
78 P_{mp} vs ψ for x-trench with varying percent nonspecular reflection . . 157
79 Reflection and transmission at a boundary 159
80 P_{mp} vs. ψ with Fresnel's equations 162
81 Typical dark IV curve for 3DCNTPV cell 165
82 Typical light IV curve for 3DCNTPV cell 165

83 SEM of CBD cells 168
84 I_{sc} and V_{oc} comparisons for MBE and CBD cells 169
85 Typical dark IV curve for CBD cell 170
86 Typical light IV curve for CBD cell 171
87 I_{sc} and V_{oc} comparisons for MBE and planar cells 173
88 Typical dark IV curve for planar cell 175
89 Typical light IV curve for planar cell 176
90 Schematic of MBEOx cells 177
91 I_{sc} and V_{oc} comparisons for MBE and MBEOx cells 180
92 Typical dark IV curve for MBEOx cell 181
93 Typical light IV curve for MBEOx cell 181
94 Sample with VACNTs of different shapes 183
95 I_{sc} and V_{oc} comparisons for MBE and Area Fraction cells 184
96 Dark and Light IV curve for an Area Fraction cell 185
97 Dark and Light IV curves of Area Fraction cell in the fourth quadrant 186
98 Schematic for metallized 3DCNTPV cells 187
99 Aixtron Black Magic System 189
100 PECVD destruction of metal underlayer 190
101 PECVD of VACNTs with metal underlayer 192
102 PECVD destruction of metal underlayer 193
103 Schematic for metallized 3DCNTPV cells 195
104 Double top contact solar cell plan view 196
105 Typical dark IV curve for a metallized cell 199
106 Typical light IV curve for a metallized cell 200
107 I_{sc} and V_{oc} comparisons for MBE and metallized cells 202
108 Dark IV curve for 3DCNTPV cell showing curvature 204
109 R_s vs R_{sh} for cells with IAD deposited ITO 205
110 IV curves of cell on ITO and MBE layers 206
111 R_s vs R_{sh} for IV curves on ITO and MBE layers 207

112 Planar cell exposed to plasma during IAD 209
113 Dark IV curves of cells with 2-stage ITO deposition 212
114 Transmission of ebeam ITO 214
115 I_{sc} and V_{oc} comparisons for metallized cells and ebeam ITO 216
116 R_s vs R_{sh} for cells with electron beam deposited ITO 217
117 Dark IV curve for cell created with ebeam deposited ITO 219
118 Transmission of electron beam deposited ITO after anneal 221
119 IV curve before and after anneal 222
120 R_{sh} and V_{oc} of cells during anneal 224
121 ITO deposition thickness vs. time 225
122 Transmission of sputtered ITO 226
123 IV curve of sputter ITO 227
124 ZnO thickness vs time 229
125 ITO change vs O_2 concentration 231
126 Light IV curve from MBEOxAu 68 233
127 ZnO transmission at different O_2 concentrations 235
128 R_{sh} vs. R_s of HRT samples 236
129 I_{sc} vs. V_{oc} of HRT samples 237
130 CdTe delamination from $CdCl_2$ 240
131 I_{sc} and V_{oc} of cells treated with $CdCl_2$ 246
132 P_{mp} vs ψ testing setup 250
133 Graph of Γ vs. ψ for point and non-point source light 254
134 P_{mp} vs. ψ for non-point source light 255
135 Blackbody emission of ELH lamp 257
136 Substrate heating by ELH lamp 260
137 Necessary cooling times for ELH lamp 261
138 Discretization error 264
139 Normalized P_{mp} vs ψ for MBEOxAu 80 and Planar Cell 07 269
140 SEM micrograph of MBEOxAu 80 271

141 Reflectivity vs. wavelength for PlanarAu 105 272
142 Comparison of theoretical and experimental P_{mp} vs. ψ 275
143 P_{mp} vs. ψ for 3DCNTPV cell with altered η_{2D} and ω 278

LIST OF SYMBOLS OR ABBREVIATIONS

(n, m)	Chirality indices.
1D	One Dimensional.
2D	Two Dimensional.
3DCNTPV	Three dimensional carbon nanotube photovoltaics.
AFM	Atomic force microscopy.
ALD	Atomic layer deposition.
AR	Anti-Reflective.
A	Area.
BEP	Beam equivalent pressure.
BZ	Brillouin zone.
CBD	Chemical bath deposition.
CNT	Carbon Nanotube.
CSS	Close Spaced Sublimation.
CVD	Chemical vapor deposition.
C_{60}	Buckminster fullerene molecule.
DI	De-ionized.
D_o	Original diameter.
D	Diameter.
EDS	Electron dispersive spectroscopy.
E_F	Fermi Energy.
E_g	Badgap.
$E_{\frac{3D}{Planar}}$	Ratio of energy produced by a 3D cell compared to a planar cell.
FF	Fill Factor.
F_o	Open area fraction.
GBs	Grain Boundaries.

G_0	Conductance quantum.
G	Conductance.
HRT	High resistance transparent.
IAD	Ion-assisted deposition.
IBAD	Ion Beam Assisted Deposition.
ICDD	International center for diffraction data.
ITO	Indium Tin Oxide.
IV	Current-Voltage.
I_D	Dark current.
I_L	Light current.
I_d	Direct insolation per unit area.
I_{01}	Leakage current in quasi-neutral region.
I_{02}	Leakage current in depletion region.
I_{diff}	Intensity of diffusely reflected light.
I_{mp}	Current at max power point.
I_{sc}	Short circuit current.
I	Current.
K	Number of photons which interact with tower tops.
L_A	Absorption Length.
L_C	Carrier collection length.
L_o	Mean free path of electron in CNT.
L	Length.
MBE	Molecular beam epitaxy.
MIS	Metal-insulator-semiconductor.
MWCNT	Multi-wall Carbon Nanotubes.
NREL	National Renewable Energy Laboratory.
NW	Nanowire.

N_D	Donor density.
N_{Tph}	Total number of photons with $E \geq E_g$.
N_{ph}	Number of incident photons.
N	Number of unit cells.
PDF	Powder diffraction file.
PECVD	Plasma enhanced chemical vapor deposition.
PL	Photoluminescence.
PV	Photovoltaics.
P_{in}	Incident power.
P_{mp}	Power at max point.
P	Power.
QD	Quantum dot.
RF	Radio-frequency.
RIE	Reactive Ion Etch.
RO	Roll-over.
RR_o	Equilibrium recombination rate.
RR	Recombination rate under applied voltage.
RT	Room temperature.
R_s	Series resistance.
$R_{p-polarized}$	Reflection coefficient for p-polarized light.
$R_{s-polarized}$	Reflection coefficient for s-polarized light.
R_{sheet}	Sheet resistance.
R_{sh}	Shunt resistance.
R	Reflectance.
SCR	Space-charge region.
SCS	Semiconductor characterization station.
SEM	Scanning electron microscopy.

SRH	Shockley-Reed-Hall.
SWCNT	Single-wall Carbon Nanotubes.
S	Number of photons entering area between towers.
T(n, m)	Translation vector of a Carbon Nanotube.
TCO	Transparent conductive oxide.
TEM	Transmission Electron Microscopy.
T	Temperature.
UHV	Ultra high vacuum.
UV	Ultraviolet.
VACNT	Vertically Aligned Carbon Nanotube Array.
V_b	Schottky rectifying barrier.
V_o	Oxygen vacancies.
V_{bi}	Built-in voltage.
V_{mp}	Voltage at max power point.
V_{oc}	Open circuit voltage.
V	Voltage.
W	Width.
XRD	X-ray diffraction.
ΔE_c	Conduction band discontinuity.
ΔE_v	Valence band discontinuity.
$\Delta x, \Delta y, \Delta z$	Velocity vectors in cartesian coordinates.
Γ_x	Average number of photon interactions with just sidewalls for a trench infinite in the x-direction.
Γ_y	Average number of photon interactions with just sidewalls for a trench infinite in the y-direction.
Γ_{box}	Average number of photon interactions for a box.
Γ_{tower}	Average number of photon interactions for an infinite array of towers.

$\Gamma_{\mathrm{x-trench}}$	Average number of photon interactions for a trench infinite in the x-direction with floor reflection.
$\Gamma_{\mathrm{y-trench}}$	Average number of photon interactions for a trench infinite in the y-direction with floor reflection.
Γ	Average number of interactions per photon.
Φ_{m}	Work function of material m.
α_{i}	Incident light angle with respect to normal.
α_{t}	Transmitted light angle with respect to normal.
α	Angle between incident light and surface normal.
χ	Electron affinity of material.
$\dot{\delta}, \dot{\omega}, \dot{\psi}$	Velocity vectors in spherical coordinates.
η_{u}	Ultimate efficiency.
η_{2D}	Efficiency of a planar solar cell.
η_{3D}	Efficiency of a 3DCNTPV cell.
η_{μ}	Free carrier segregation and collection.
η_{Abs}	Short circuit current.
η_{gen}	Exciton generation.
η_{SQ}	Shockley-Queissier efficiency.
η	Solar cell efficiency.
γ	Density.
$\hat{\delta}, \hat{\omega}, \hat{\psi}$	Radial, azimuthal and zenith spherical coordinate unit vectors.
$\hat{\mathrm{L}}$	Incident light vector.
$\hat{\mathrm{N}}$	Unit normal vector.
$\hat{\mathrm{x}}, \hat{\mathrm{y}}, \hat{\mathrm{z}}$	Unit vectors in cartesian coordines.
κ	Grain growth constant.
λ_{F}	Fermi wavelength.
λ_{g}	Wavelength of light equal to material bandgap.
λ	Wavelength.

ν	Subband number in CNT.
ω_δ	Non-point source angular diameter in the ω direction.
ω	Azimuthal angle.
ψ_δ	Non-point source angular diameter in the ψ direction.
ψ	Zenith angle.
ρ	Resistivity.
σ	Conductivity.
τ	Injection coefficient.
θ	Carbon nanotube chiral angle.
ϱ	Aperture radius of lamp.
$\mathrm{a-Si}$	Amorphous silicon.
a	Carbon-carbon bond length.
b	Number of conducting subbands.
$\mathrm{c-Si}$	Crystalline silicon.
c	Velocity of light.
dist	Distance from stage to lamp.
d	Distance between vertically aligned carbon nanotube structures.
f	Carbon nanotube areal density.
g	Mass.
h	Planck's constant.
h	tower height.
$\mathrm{k_B}$	Boltzmann's constant.
$\mathrm{m-CNTs}$	Metallic carbon nanotubes.
n	Diode ideality factor.
$\mathrm{p_s}$	Probability photon is absorbed by tower sidewalls.
$\mathrm{p_t}$	Probability photon is absorbed by tower tops.
q	Universal charge constant.

rpm	Revolutions per Minute.
$s-CNTs$	Semiconducting carbon nanotubes.
sccm	Standard cubic centimeters per minute.
t	Time.
v_F	Fermi velocity.
x_f	x-position of photon leaving system.
x_o	x-position of photon entering system.
$\vec{C_h}$	Chiral vector.
$\vec{\delta}$	Radial vectors.
$\vec{\epsilon}$	Electric field.
$\vec{a_1}$	First crystallographic vector for graphene.
$\vec{a_2}$	Second crystallographic vector for graphene.
$\vec{k_c}$	Circumferential wave vector.
$\vec{v_x}, \vec{v_y}, \vec{v_z}$	Velocity vectors in cartesian coordinates.
w	Tower width.

SUMMARY

Photovoltaic (PV) cells with a three dimensional (3D) morphology are an exciting new research thrust with promise to create cheaper, more efficient solar cells. This work introduces a new type of 3D PV device based on carbon nanotube (CNT) arrays. These arrays are paired with the thin film heterojunction, CdTe/CdS, to form a complete 3D carbon nanotube PV device (3DCNTPV). Marriage of a complicated 3D structure with production methods traditionally used for planar CdTe solar cell is challenging. This work examines the problems associated with processing these types of cells and systematically alters production methods of the semiconductor layers and electrodes to increase the short circuit current (I_{sc}), eliminate parasitic shunts, and increase the open circuit voltage (V_{oc}).

The main benefit of 3D solar cell is the ability to utilize multiple photon interactions with the solar cell surface. The three dimensionality allows photons to interact multiple times with the photoactive material, which increases the absorption and the overall power output over what is possible with a two dimensional (2D) morphology. To quantify the increased power output arising from these multiple photon interactions, a new absorption efficiency term, η_{3D}, is introduced. The theoretical basis behind this new term and how it relates to the absorption efficiency of a planar cell, η_{2D}, is derived.

A unique model for the average number of multiple photon impingements, Γ, is proposed based on three categories of 3D morphology: an infinite trench, an enclosed box, and an array of towers. The derivation of η_{3D} and Γ for these 3D PV devices gives a complete picture of the enhanced power output over 2D cells based on CNT array

height, pitch, radius, and shape. This theory is validated by monte carlo simulations and experiment.

This new type of 3D PV devices has been shown to work experimentally. The first 3DCNTPV cells created posses I_{sc} values of 0.085 to 17.872mA/cm^2 and V_{oc} values in the range of 2 to 122mV. These figures of merit are low for CdTe cells, so planar cells without CNTs and planar cells with unpatterned CNTs were developed. The planar cells had figures of merit about the same as the 3DCNTPV cells, indicating that the low efficiency of the 3DCNTPV cell is due to processing and not inherent to the 3D structure.

The CdTe/p-Si interface used as a back contact was determined to provide a rectifying barrier opposite normal current flow. This had the effect of inverting the normal curvature of the IV curve in the fourth quadrant. This problem was eliminated by replacing the CdTe/p-Si interface with a CdTe/metal interface.

CNTs were successfully grown directly on an Ag underlayer, but the growth reproducibility and the CNT height was not sufficient for use in 3DCNTPV devices. Therefore, CNTs were grown on a SiO_2 passivated Si wafer and then metallized. This eliminated the CNTs as the back contact and used them only as a structure to provide the 3D morphology. These cells exhibited low shunt resistances on the order of 300Ω, causing a straight line IV curve.

This shunting was found to be caused by the ion assisted deposition of ITO. This plasma process etched away semiconducting layers and caused pinholes in the CdTe/CdS film. Many different strategies were utilized to try and eliminate this shunt and induce curvature in the IV curve, including adding sacrificial metal layers before the ITO deposition, using electron beam evaporated ITO, and using RF sputtered ITO. The addition of metal layers before ITO deposition did not result in cells which could reliably demonstrate both photocurrent and IV curvature. Electron beam

deposition of ITO resulted in cells with excellent IV curvature, but the ITO deposited in this manner was too resistive and absorptive to create well functioning cells.

RF sputter was found to be an acceptable method of ITO deposition if an intrinsic ZnO layer was deposited beforehand. This high resistance and transparent ZnO layer was deposited in order to passivate any pinholes or inhomogeneities present in the CdTe/CdS layer. Cells with this ZnO layer exhibited I_{sc} values slightly less than 1mA/cm^2 with V_{oc} values of up to 350mV. This represents an order of magnitude increase in the I_{sc} and a 300% increase in the V_{oc}.

The cells with this ZnO layer also exhibited good IV curvature. Unfortunately, the increase in I_{sc} was not enough to catch this curvature in the fourth quadrant. In order to further increase the I_{sc} of the cells so that IV curvature could be measured in the fourth quadrant, a $CdCl_2$ anneal was attempted. A $CdCl_2/CH_3OH$ solution-based anneal resulted in delamination of the CdTe layer due to penetration of the liquid beneath the semiconductor layers. Soaking the cells in a $CdCl_2/CH_3OH$ solution and air drying before anneal eliminated this delamination, but did not increase the I_{sc} values of the cells. To determine if the $CdCl_2$ could not penetrate through the CdS layer, annealing with only the CdTe layer present was attempted, but did not result in an I_{sc} increase. To investigate if intermixing of CdS into the CdTe layer during annealing was preventing an increase in cell I_{sc}, a two-stage (pre- and post-anneal) CdS deposition was attempted. This did not result in an increase in cell I_{sc}. Finally, soaking cell substrates in the $CdCl_2/CH_3OH$ solution before CdTe/CdS deposition was attempted, but also did not result in an increase in I_{sc} values of the cells.

The output power of the cells at varying incident angles of light was measured. The cells show an increase in the normalized power output compared to similar planar cells when the solar flux is at off-normal angles. The power output vs. incident angle curve takes an inverted C-type curve as predicted by the theory developed here. The complete theory of 3DCNTPV presented in this work describes the power output vs.

incident angle of a 3DCNTPV cell based only on cell morphology. The experimental power output vs. zenith angle was compared to the theoretically calculated power output with very good agreement between the two.

This work has made a number of contributions to the field of 3D PV device research, including:

1. Developing one of the first Generation III inorganic PV devices to use CNTs as a charge collector
2. Developing a simple-cost effective way to texture thin film solar cells using a "bottom up" substrate-configuration approach
3. Developing a complete theoretical model of the 3DCNTPV cell
4. Creating working proof-of-concept devices using the 3DCNTPV structure
5. Increasing I_{sc} by an order of magnitude and V_{oc} by 300%
6. Demonstrating viable techniques towards eliminating shunting resistances and inducing IV curvature
7. Confirming theoretical model with experimental data of power output vs. incident angle

CHAPTER I

MOTIVATION

There are two main motivations for the decarbonization of the United States' energy supply and the development of renewable energies. The first is the further domestication of US energy resources. Currently, while 84% of US energy is derived from fossil fuels and the US consumes 25% of worldwide petroleum resources, only 3% of known petroleum supplies lie within US borders [1]. This has two main consequences, the first being a trade deficit due to petroleum purchased from foreign countries and the second being a dependence on the security, stability, and economies of the foreign nations which control petroleum reserves. While the United States does not have a large percentage of the world's petroleum resources, it has ample wind and solar energy resources. The research and development of these resources will create jobs, balance the trade deficit, and eliminate threats to energy security.

The second motivation for the development of renewable energies is the abatement of adverse, man-made climate effects [2]. In order to significantly abate climate change, it is estimated that the world must derive 10 TW/year of energy from carbon neutral sources by the year 2035, many times the current renewable energy output of 0.28TW/year [3]. This is known as the "Terawatt Challenge". The currently available carbon neutral energy technologies which do not utilize carbon feedstock are nuclear, wind, and solar power [4].

Commercial nuclear energy technology has been well known and utilized for over 50 years [5]. However, the real or imagined environmental impacts of nuclear energy weigh heavily on the public's mind. With such events as the tragedy at the Fukushima Daiichi nuclear plant in Japan, it is unlikely that the United States will break ground

on a large number of new nuclear reactors in the near future, an event which has not occurred since 1974. Therefore, it is unlikely that one 1GW nuclear plant could be built everyday for the next 50 years in order to supply 10TW of energy [2].

In many areas of the United States and the world, steady, heavy winds are prevalent. Wind has been calculated to provide as much as 72TW of energy worldwide [6]. However, practical considerations may limit that to only 2TW or less of available wind kinetic energy [4].

Solar energy is abundant, cheap, and regular. At any moment, 1,366 W/m^2 of solar energy is incident on the earth. The average insolation on the earth's surface is approximately 250 W/m^2 per day [1]. Over the earth's surface, this means there is a total available power of 1.2×10^5 TW, (8,000 times human energy consumption) over the entire year [4]. Covering only 0.1% of the Earth's surface with commercially available, 10% efficient solar cells would provide enough energy for the entire human population [7]. Solar energy is the only extensive renewable source which can provide the majority of the necessary 10TW power. Although photovoltaics (PV) research has come a long way since its introduction in the 1950s [8], there must be an order of magnitude decrease in the price per watt in order to economically compete with conventional non-renewable power sources. This means that future research must focus on cells which can be manufactured and installed quickly, cheaply, and easily [9].

While PV is one of many technologies available in the terrestrial power production portfolio, extraterrestrial power production for earth-orbit satellites has been almost exclusively produced by PV modules. While the figure of merit for a terrestrial solar module is cost per watt peak produced ($\$/W_p$), the figure of merit for a module going into space is specific energy (W/kg) because the cost of the PV modules is much less than the cost of the fuel and rockets to launch these modules into space. Therefore,

future research in PV for space based applications must focus on cells which can be manufactured with as high an efficiency and as lightweight as possible.

Three dimensional (3D) carbon nanotube (CNT) based PV devices (Figure 1) are a type of next generation solar cell, possessing unique properties which are advantageous to both terrestrial and space based applications. 3DCNTPV consist of large scale, periodic arrays of vertically aligned CNTs over which thin film PV material is then deposited. CNTs act as both the scaffolding, providing the three dimensionality, and the back contact to collect charge carriers. These types of cells have two main advantages over planar thin film PV devices.

The first advantage is that while conventional devices are produced in a superstrate configuration, 3DCNTPV are produced in a substrate configuration. Substrate configuration cells are produced on top of a flexible metal foil. These cells are more lightweight, flexible, and cost efficient, which makes them ideal for both terrestrial and space applications [10].

Although all substrate configuration cells, planar or otherwise, have the previously mentioned advantages, 3DCNTPV have a unique advantage over all other types of planar cells. All planar solar cells have maximum power output when oriented normal to the solar flux and fall off as a cosine function at off-normal angles. In order to maximize the power output of an array of planar cells, machinery is used to orient the array and track the solar disc. However this machinery is heavy, bulky, occasionally unreliable, and extremely expensive to produce and install, drastically increasing both a module's $\$/W_p$ and W/kg figures of merit. 3DCNTPV have been designed in order to create cells which can produce more power at off-normal angles of incidence without this tracking machinery.

Because of the 3D geometry provided by the vertically aligned CNTs, these cells allow for multiple photon impingements when the solar flux is at off-normal angles compared to the cell substrate. These multiple photon impingements lead to an

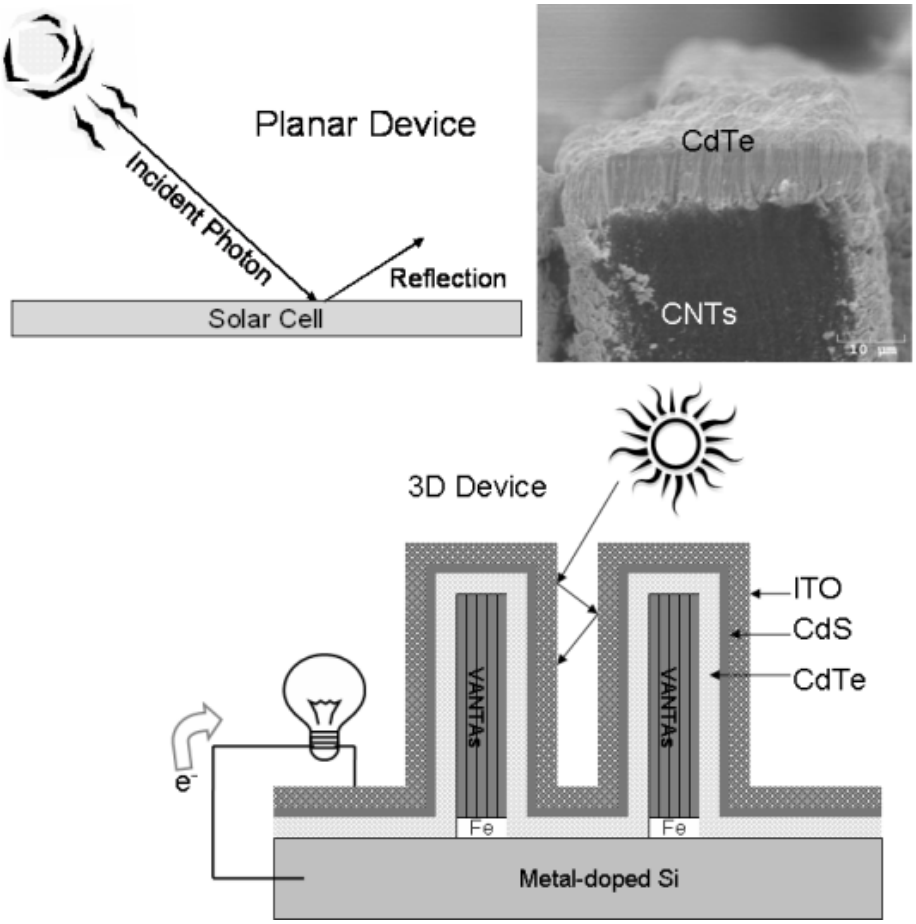

Figure 1: (Top left) Ray diagram of a conventional planar cell without texturing or anti-reflective (AR) coating. After one impingement the photon exits the system. (Top right) Scanning electron micrograph of a bisected vertically aligned carbon nanotube (VACNT) tower with semiconductor deposit showing good adhesion between the CdTe semiconductor and CNTs. (Bottom) A 3D carbon nanotube based photovoltaic (3DCNTPV) cell. Arrays of VACNTs provide a scaffolding and collection electrode over which PV materials are deposited. The VACNTs allow for multiple photon impingements and an increased photon absorption.

increased number of interactions between a photon and the solar cell surface. An increased number of interactions leads to an increased photocurrent and a higher power output than for similar planar cells. 3D cells actually have their highest efficiency at off-normal angles, so no complicated machinery is needed to orient the cells. As the sun subtends all zenith angles, this increased power output yields an increased energy output of many times that of a planar cell throughout the day.

The power output of these 3DCNTPV cells depends on tower orientation, height, and shape, along with the direction and intensity of the solar flux. In order to determine the optimum tower size, spacing, and shape, a comprehensive theory to account for increased power output of 3DCNTPV cells over planar cells has been developed. In order to test this theory, computer simulations and prototype development and testing were carried out.

Although this type of cell offers advantages, such as multiple photon impingements, some disadvantages of the 3D morphology must be overcome. The three dimensionality and intricate structure of the towers can introduce a high defect density and void spaces in the semiconductor layers as they adhere to the towers. This leads to a high series resistance, low shunt resistance, and lower efficiency. The deposition of photoactive materials and top electrode overtop of complicated 3D structures is a challenging topic from a processing point of view. This research advances the processing methods of these cells to eliminate many of these inefficiencies and make 3DCNTPV more production ready.

CHAPTER II

BACKGROUND

2.1 Introduction to Photovoltaics

2.1.1 History of Photovoltaics

The PV effect was first discovered in 1839 by Henry Becquerel when he observed current flow from a chemical solution when illuminated with light. In 1873, selenium was the first solid material found to exhibit the PV effect [11]. After the pioneering works of Einstein [12] and Schottky [13] in 1905 and the 1930's, respectively, the first PV devices were developed.

The first device to convert sunlight to energy through the use of crystalline Si ($c-Si$) was patented in 1946 by Russel Ohl in Bell Labs [14]. The development of solar cells proceeded quickly and the May 3, 1954 Time Magazine proclaimed that Bell's "solar batteries" could produce a power density of 50 W/yd^2, for an efficiency of around 5% [1].

Today, solar cells are classified into three distinct generations based on their working principles [15] (Figure 2). Generation I devices are made of c-Si. This class of devices is the oldest and most mature technology and account of 90% of solar cell production [1]. Crystalline Si cells, with a bandgap of 1.12eV have a record efficiency in the lab of 24.4% [16], which is reasonably close to the highest achievable efficiency of 33% [17]. By definition single crystals contain very few defects, leading to fewer losses due to recombination and a higher efficiency than most other cell types. However, ingots of single crystal Si are expensive to produce and compete for resources with the microelectronics industry [1]. In addition Si is an indirect bandgap

semiconductor, so it suffers from a low absorption coefficient, meaning that thicker (50 to 100 μm) layers and more material must be used.

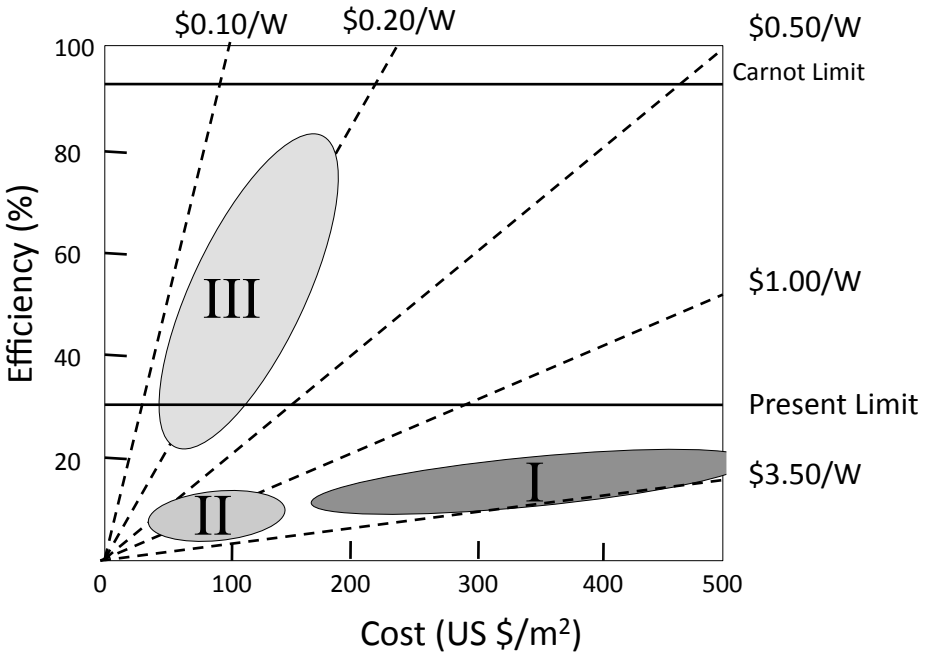

Figure 2: Efficiency vs. cost per watt of three generations of PV devices. Generation I devices are made up of crystalline Si. Generation II devices are composed of thin films and, due to the drastically decreased amount of material, have a lower cost per watt produced. Generation III are devices still in the developmental stage which increase power output or decrease cost by a number of different ways. This grouping contains polymer, Graetzel, quantum dot, and nanowire PV devices. From [15]

Second generation PV devices utilize thin film, polycrystalline inorganic materials [18] which can be deposited in either a substrate or superstrate configuration. These types of cells include $CuIn_{1-x}Ga_xSe_2$ (CIGS), amorphous Si (a − Si), and CdTe cells.

CIGS is a thin material with a bandgap in the range of 1.5eV [1]. These solar cells are usually paired with a CdS window layer. Efficiencies on flexible substrates have been demonstrated at 19.9% [19].

Amorphous Si cells, unlike c-Si cells, show no long range order [1]. The large scale disorder and dangling bonds caused by the amorphous character causes a short carrier lifetime. However, by hydrogen passivation of the dangling bonds, a-Si becomes a direct band semiconductor with a bandgap of 1.7eV. So devices can be made very thin, which reduces cost [20]. Flexible cells demonstrating high specific power have been demonstrated. Amorphous Si cells would seem to dominate solar cell technology however, light degrades the H-passivated bonds in a mechanism known as the Stabler-Wronski effect [21], decreasing both their efficiency and lifetime.

The final generation II device is a CdTe cell. This type of cell was first developed in 1972 by Bonnet with a working efficiency of 5-6% [22]. CdTe cells were developed extensively in the 1980's [23, 24, 25] because of CdTe's near ideal bandgap of 1.5eV (as shown by Loferski in 1956 [26]) and better space-based radiation tolerance than either Si or GaAs modules [27]. The current efficiency record for CdTe cells is 16.5%[28], just 2/3 of the highest theoretical efficiency of 30.6% [10, 29]. The cells which reach such high efficiencies are laboratory cells with active areas usually much less than $1cm^2$. The best commercial CdTe cell available is 11% with the majority of commercially available cells having efficiencies of 7-9% [30].

Generation III devices are relatively nascent and include a wide variety of materials and operational principles. This group includes devices such as polymer, Graetzel, quantum dot, and nanowire PV. This class of devices is composed of two groups of cells. The first group is composed of devices such as quantum dot and nanowire cells, which seek to decrease $\$/W_p$ by increasing the efficiency of cells above Generation I and II devices through the use of novel absorption, separation, or collection mechanisms. The second group is composed of devices such as polymer or Graetzel cells, which seek to decrease $\$/W_p$ by decreasing the cost of cells well below both Generation I and II devices by using extremely cheap materials and manufacturing methods.

2.1.2 Basic Operating Principles

Solar cells are very simple devices and consist entirely of a junction between n-type and p-type semiconductors. These semiconductors have different Fermi Energies (E_F). When a junction is formed by putting these two semiconductors together, holes diffuse from the p-type to the n-type semiconductor and vice versa for electrons. The diffusion of these majority carriers unscreen the ionized acceptors in the p-type and the ionized donors in the n-type semiconductor (Figure 3). These unscreened charged impurities set up an electric field which eventually reaches equilibrium with the diffusion field and no net current flows. The region where this electric field is present is known as the depletion region (because there are effectively no free carriers) or the space-charge region (SCR) and the potential difference in the region is known as the built-in voltage (V_{bi}). The distance the SCR extends into the semiconductor layer is directly related to the dopant density of that semiconductor. The less doped a semiconductor is, the farther the SCR extends. If the semiconductor layers are large enough, there is a quasi-neutral region outside of the SCR where the effects of the other semiconductor are not felt and V_{bi} has no effect [31].

One contact to the semiconductor is made of either a transparent material or a metal mesh in order to allow photons to pass and interact with the junction. The semiconductor layer which is connected to this connection is known as the window layer and it is either made as thin as possible or of a material with a higher bandgap in order to minimize photon absorption. The semiconductor material opposite this contact is known as the absorber and consists of the majority of the photoactive material.

A photon possessing an energy less than the bandgap of the absorber layer will pass through the material without absorption. A photon with an energy much greater than the bandgap will be weakly interacting, due to the relatively small density of states at higher energies. A photon with an energy equal to or slightly larger than

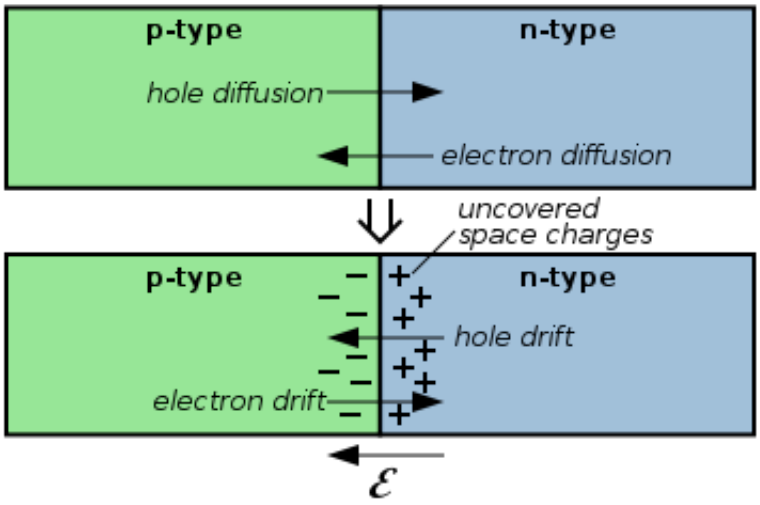

Figure 3: The difference in Fermi energies in a n- and p-type semiconductor cause the diffusion of free carriers. These carriers unscreen ionized acceptors which uncover an electric field, $\vec{\epsilon}$, opposite the direction of diffusion. The region near the junction where there is an electric field is known as the depletion region, since it has no free carriers, or the space charge region

the bandgap of the absorber layer can create an electron-hole pair by promoting an electron from the valence to the conduction band.

If this pair is generated in the quasi-neutral region of the p/n-junction, then the electron and hole will diffuse randomly until eventually recombining. If, however, the electron and hole is generated within a diffusion length of the depletion region, then the electric field will separate the pair, causing electrons to go down the potential towards the n-type semiconductor while holes flow up the potential towards the p-type semiconductor (Figure 4) [32]. Collection of these charges and flow through a circuit yields a current.

There are thus three different processes that must occur for a photocurrent to be generated. (1) A photon must be absorbed. (2) An exciton pair must be dissociated. (3) The respective carriers must propagate through the junction to the contacts. The efficiency (η) of the solar cell then becomes the product of all three of these processes,

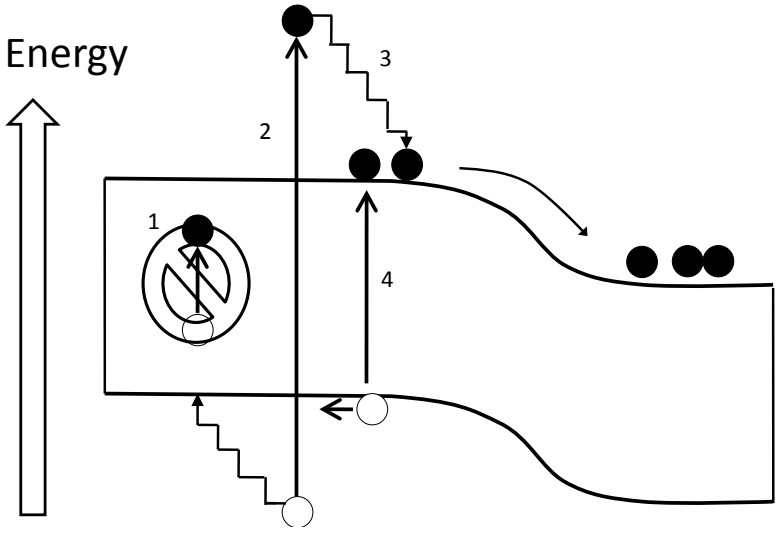

Figure 4: Absorption and loss mechanisms in a homojunction solar cell. The low photons do not have enough energy to excite electrons from the valence to the conduction band and are not absorbed by the cell (1). Photos with energy higher than the bandgap of the material may be absorbed by the junction (2), but the excess energy of these "hot carriers" is lost to lattice thermalization (3). Photons which have an energy about equal to the bandgap of the material efficiently created electron hole pairs (4). From [15]

$$\eta = \eta_{Abs} \times \eta_{gen} \times \eta_{\mu} \tag{1}$$

Where η is the overall cell efficiency, η_{Abs} is the efficiency of absorbing a photon, η_{gen} is the efficiency of generating an exciton pair, and η_{μ} is the efficiency of segregation and collection of free carriers in the solar cell.

When the window layer and absorber layer are made from the same material which has been n- and p-doped, then the cell is known as a homojunction. If, however, the window layer is a different material than the absorber layer, the device is known as a heterojunction. Heterojunctions have an advantage over homojunctions because the window layer may be chosen to have a wider bandgap than the absorber layer. This means than the window layer is totally transparent to any photons which would be absorbed by the absorber layer [33].

In a homojunction, the difference in doping results in a difference in the Fermi energy between the window and absorber layers. In a heterojunction, the difference in Fermi energies is determined by the work functions (energy required to remove an electron from E_F) and bandgaps of the materials. Therefore, a heterojunction does not necessarily require any external doping or modifications of any kind to set up a SCR [33]. A complete working junction could be formed simply by bringing together the window and absorber layers and adding contacts to each side (Figure 5).

Heterojunctions do have two distinct disadvantages. The first is that since the window and absorber layers are composed of different materials, they most likely exhibit atomic disregistry from the mismatch of lattice parameters. If this disregistry is large enough, it can induce strain and form defects which act as recombination sites, reducing the efficiency of the device. The second is that for a wide bandgap window layer and narrow bandgap absorber layer (such as a CdS/CdTe junction), discontinuities in the conduction and valence band ($\Delta \mathrm{E_c}$ and $\Delta \mathrm{E_v}$, respectively) develop due to the difference in bandgaps between the materials. These discontinuities are described by

$$\Delta E_C = \chi_p - \chi_N \tag{2}$$

$$\Delta E_V = E_{gN} - E_{gp} - \Delta E_C \tag{3}$$

These discontinuities can cause spikes in the band diagram which provide a barrier to current flow. However, if ΔE_c is relatively small or negative, then the obstruction to electron flow is negligible [33]. The CdTe/CdS band heterojunction band diagram in Figure 5 shows ΔE_C= -0.22 and ΔE_V=1.18. Since ΔE_C is negative and ΔE_V is positive, there is no spike in the conduction of valence band and current may flow freely in this heterojunction [35].

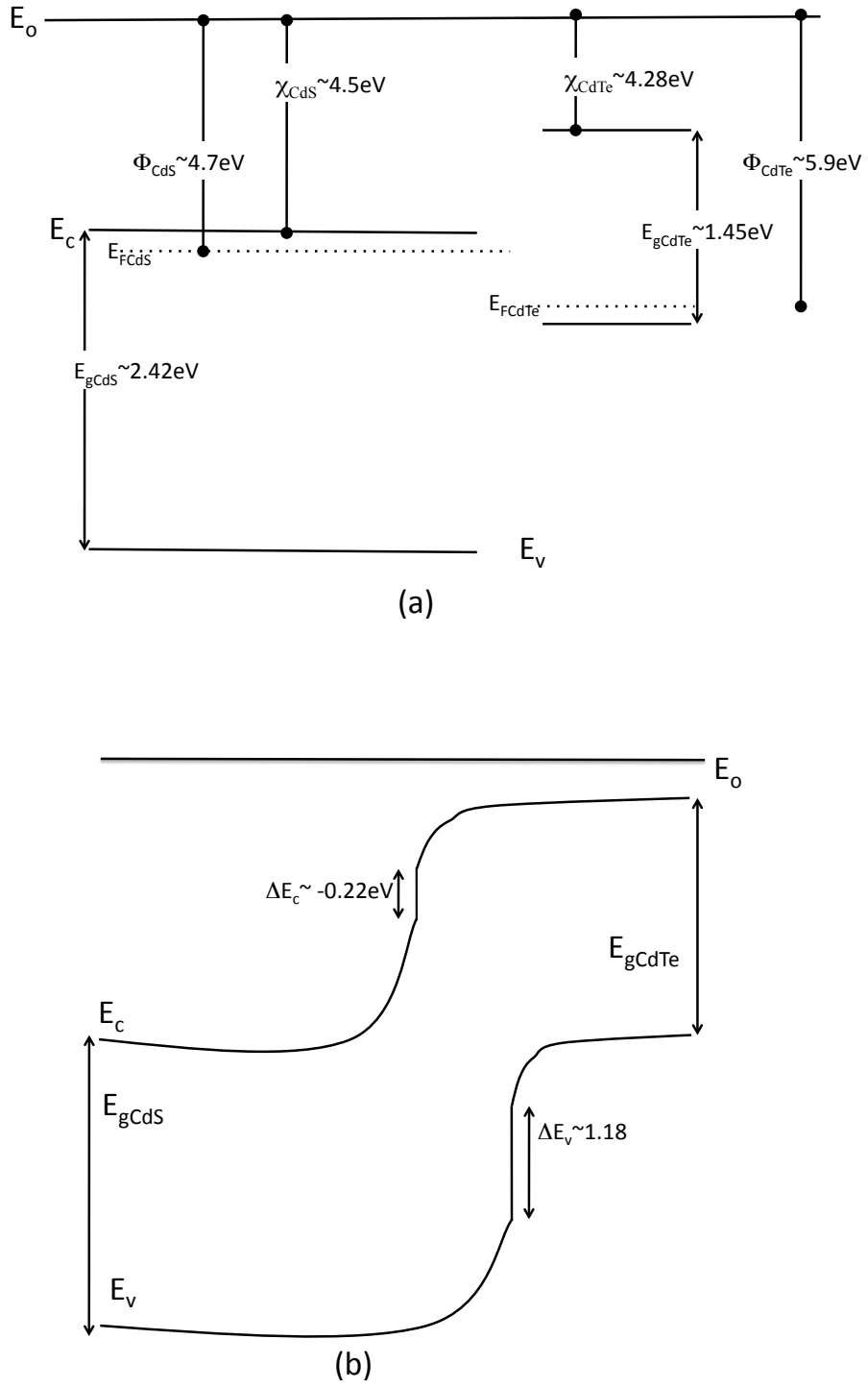

Figure 5: Band diagram of the p/N CdTe/CdS heterojunction with a large bandgap n-type semiconductor and small bandgap p-type semiconductor of different materials (a) electrically separated and (b) in electrical contact. The differences in bandgap and electron affinity cause a discontinuity in the conduction, ΔE_c, and valence, $\Delta \mathrm{E_v}$ bands. From [34]

2.1.2.1 IV Curves and Figures of Merit

The figure of merit for both a diode and a solar cell is a current-voltage (IV) curve. In the dark, an ideal solar cell acts exactly like a regular diode. Under negative or small positive biases, the diode acts as an insulator and current is prevented from flowing. When the applied bias is larger than the built in potential of the p/n-junction, current is no longer prevented from flowing. The difference between a diode and a solar cell is that under illumination, the solar cell produces a current flow. This causes a current offset, I_L, in the IV curve so that the diode curve exists in the fourth quadrant. The IV curve in the fourth quadrant (positive Voltage and negative current) has a negative product. This negative power indicates a power output (Figure 6).

Several benchmarks are used to describe the light curve of a solar cell. These are the short circuit current (I_{sc}), open circuit voltage (V_{oc}), and power at max point (P_{mp}). The short circuit current is defined as the output current from the cell under an applied bias of zero. This is the maximum possible output current from a cell for a given illumination. The open circuit voltage is defined as the applied voltage corresponding to zero output current, or the point where the IV curve crosses the positive voltage axis. The power at max point is defined as the maximum output power (power is the product of the applied voltage and output current) of the cell. For well behaved cells this point occurs at the "knee" of the IV curve, or the point where the output current begins to rapidly decrease. In a circuit diagram, an ideal solar cell can be described as a simple diode in parallel with a current source.

The I_{sc}, V_{oc}, and P_{mp} are used to find the efficiency of the cell by:

$$\eta = \frac{P_{mp}}{P_{in}} = \frac{I_{mp} \times V_{mp}}{I_{sc} \times V_{oc}} \tag{4}$$

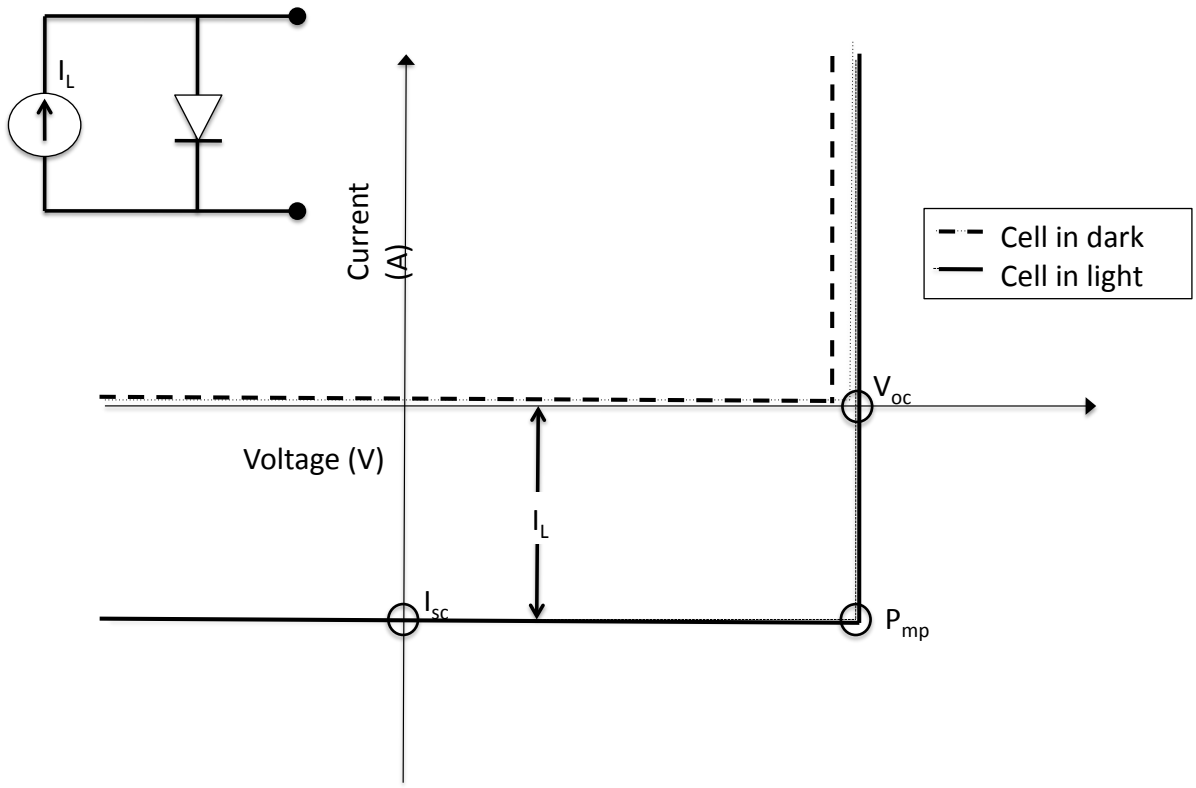

Figure 6: In the dark, a solar cell acts like a diode. In the light, however, it produces a current, which shows up as an offset, I_L, in the fourth quadrant of the IV curve. An ideal cell is described by three points, the short circuit current (I_{sc}), the open circuit voltage (V_{oc}), and the power at max point (P_{mp}). The circuit diagram for an ideal cell is simply a current source in parallel with a diode.

where I_{mp} and V_{mp} are the current and voltage values at the P_{mp}.

2.1.2.2 Nonidealities

No solar cell is perfect and these nonidealities will alter the IV curve for the devices, sometimes quite noticeably, and will result in parasitic effects which drain power from the cell. The first of these are electron/hole recombination. Recombination has three main modes, radiative recombination, Auger recombination, and Shockley-Reed-Hall recombination.

Radiative recombination (Figure 7 left) is an equilibrium process and therefore is inherent in any p/n-junction. In this type of recombination an electron in the conduction band is demoted and combines with a hole in the valence band. This results in the emission of a photon with an energy equal to the semiconductor bandgap and is effectively the "opposite" process of photon absorption. This process is the least detrimental to cell performance since only a small percentage of photons which are emitted from the semiconductor are not later reabsorbed.

Auger recombination (Figure 7 middle) becomes important when semiconductor doping levels are above $10^{17} cm^{-3}$, due to the large number of free carriers [36]. In Auger recombination an electron recombines with a hole, just as in radiative recombination. However, instead of emission of a photon, the excess energy is used to promote a hole to higher energy levels. This hole then sheds this excess energy by lattice thermalization.

Shockley-Reed-Hall (SRH) recombination (Figure 7 right) is when an electron and hole recombine via traps located in the bandgap. The energy from the recombination of the electron and hole is released to the semiconductor lattice in the form of phonons. These mid-gap traps are present due to unwanted impurity atoms, dislocations and defects, or disregistry between the n- and p-type semiconductors.

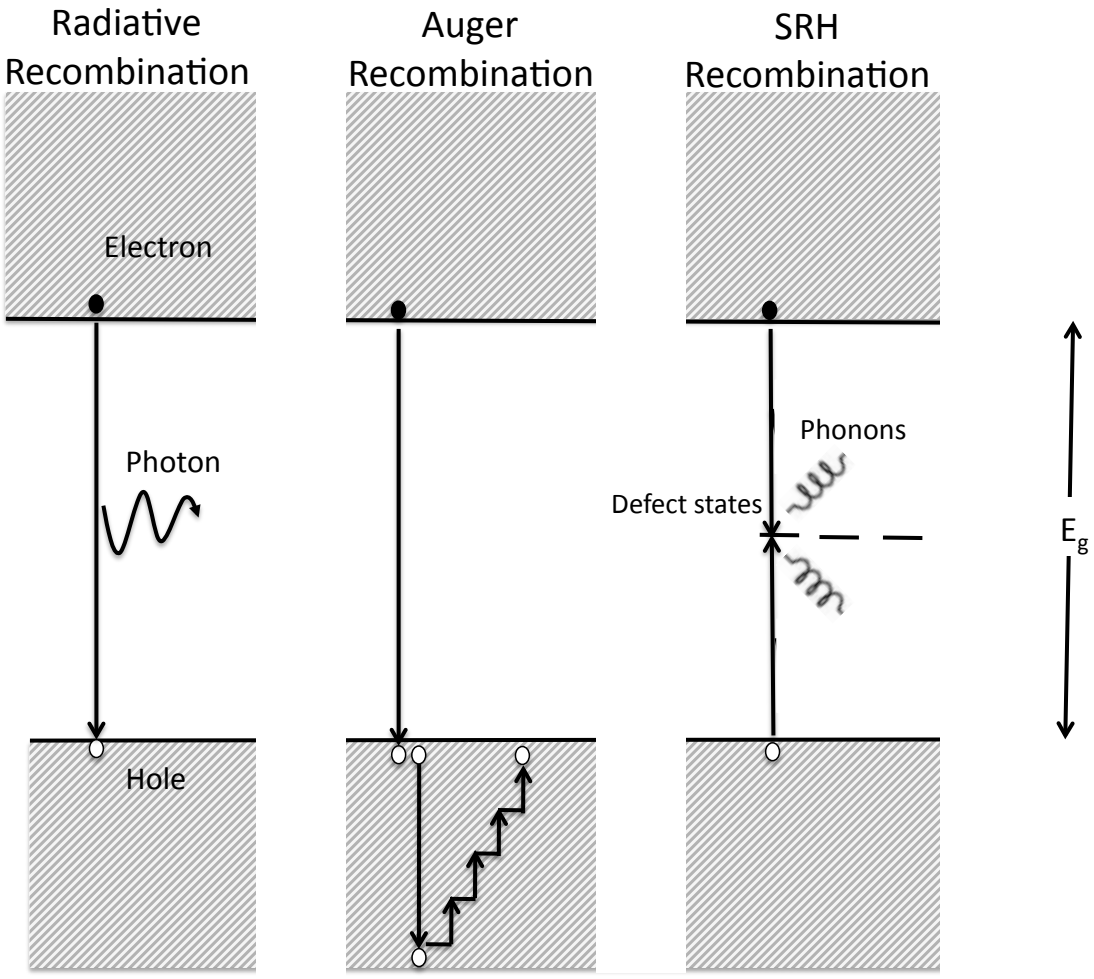

Figure 7: Diagram of the valence band and conduction band showing three mechanisms of carrier recombination. The mechanisms are, from left to right, radiative recombination, Auger recombination, and SRH recombination. In radiative recombination an electron in the conduction band is demoted and combines with a hole in the valence band. In Auger recombination, an electron recombines with a hole and the excess energy is used to promote another carrier to higher energy levels. In SRH recombination, an electron and hole recombine via mid-gap traps and two photons are emitted with an energy less than the bandgap energy. From [36]

There are also two parasitic resistances commonly associated with non-ideal solar cells. These terms are series resistance, (R_s), and shunt resistance, (R_{sh}). The series resistance is mainly due to the bulk resistance to carrier flow in both the n- and p-type semiconductors and the metal contacts [37]. R_s rapidly decreases the I_{sc} of a cell with little influence on the V_{oc} (Figure 8 top). A modest increase in R_s from 1 to 5 Ω reduces the overall efficiency of the cell by 20% [37]. For well-behaved cells, R_s may be approximated by taking the inverse slope of the IV curve at voltages much larger than V_{oc}.

The second resistance, R_{sh}, is due a leakage current across the p/n-junction and around the edge of the cell. These shunt pathways are frequently caused by crystal defects and foreign impurities in the junction [31] and decrease power output by decreasing the V_{oc} while leaving the I_{sc} unchanged (Figure 8 bottom). For well-behaved cells, R_{sh} can be approximated by taking the inverse of the IV curve slope at slightly negative voltages.

These non-idealities decrease the power output of a real cell. In the ideal solar cell presented in Figure 6, P_{mp} is simply equal to the product of the I_{sc} and the V_{oc}. Because a non-ideal IV curve is not perfectly "squared off," but has a rounded knee, there is a ratio between the real P_{mp} value for that cell and the theoretical max P_{mp} value for an ideal cell. This ratio is called the fill factor (FF) and is defined as

$$FF = \frac{P_{mp}}{V_{oc} \times I_{sc}} \tag{5}$$

By combining these non-idealities, a more complete model for a simple cell is shown in Figure 9. This cell is composed of a light dependent current source in parallel with two "leaky" diodes. The first diode has a leakage current, I_{01}, with a diode ideality factor, n, of 1. The diode ideality factor is a fitting parameter used to account for

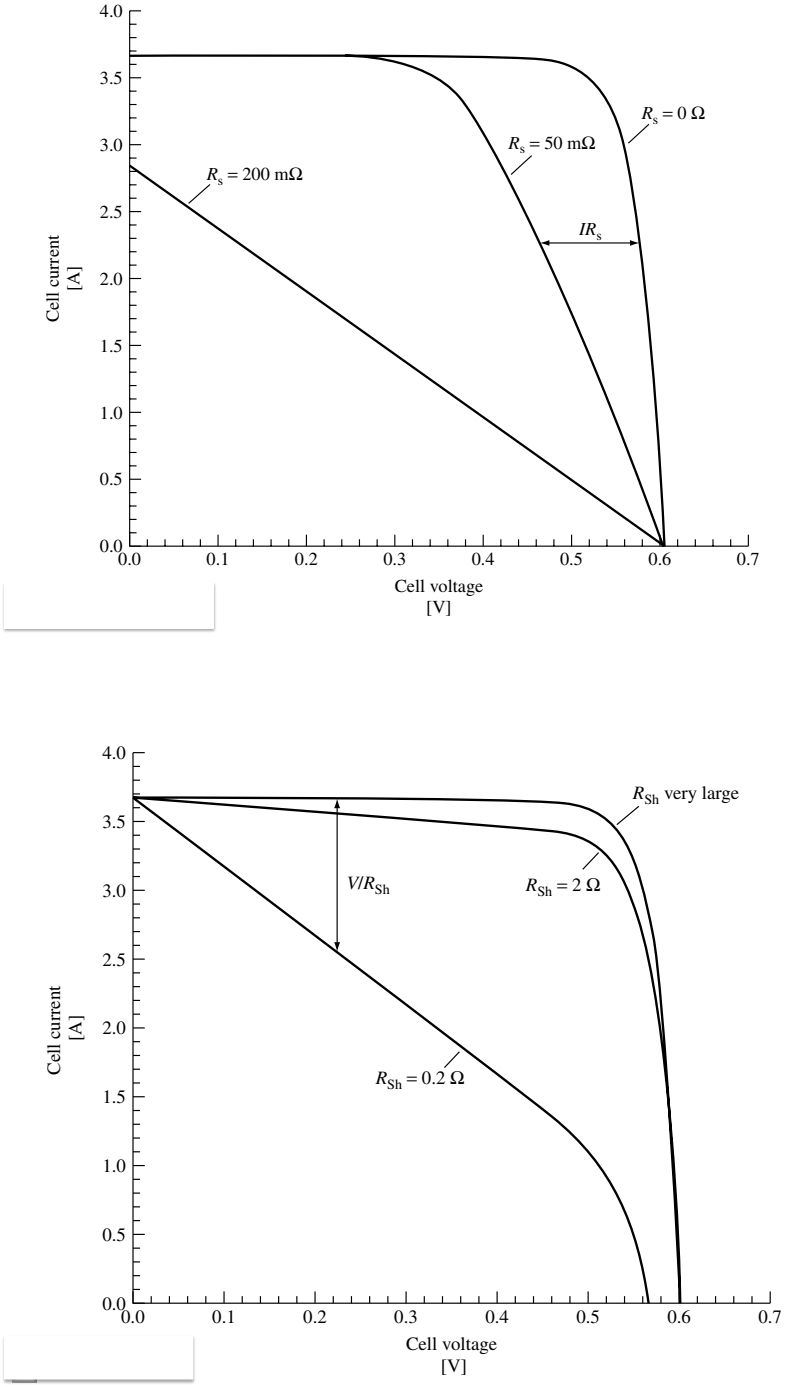

Figure 8: (Top) Effect of R_s on a solar cell IV curve. A series resistance close to zero has an IV curve which is close to ideal. Increasing resistances affect the solar cell power output by decreasing the short circuit current. (Bottom) Effect of R_{sh} on a solar cell IV curve. A shunt resistance of infinity yields a near ideal IV curve. Decreasing values of R_{sh} yield lower power by decreasing the open circuit voltage. From [31]

discrepancies between the curvature of real and ideal diodes, since real diodes are not "squared off." This diode with ideality factor 1 represents a recombination current in the quasi-neutral regions and contacts. The second diode has a leakage current, I_{02}, with a diode ideality factor of 2. This diode represents a recombination current in the depletion region. The final two circuit elements represent the parasitic resistances, R_s and R_{sh}.

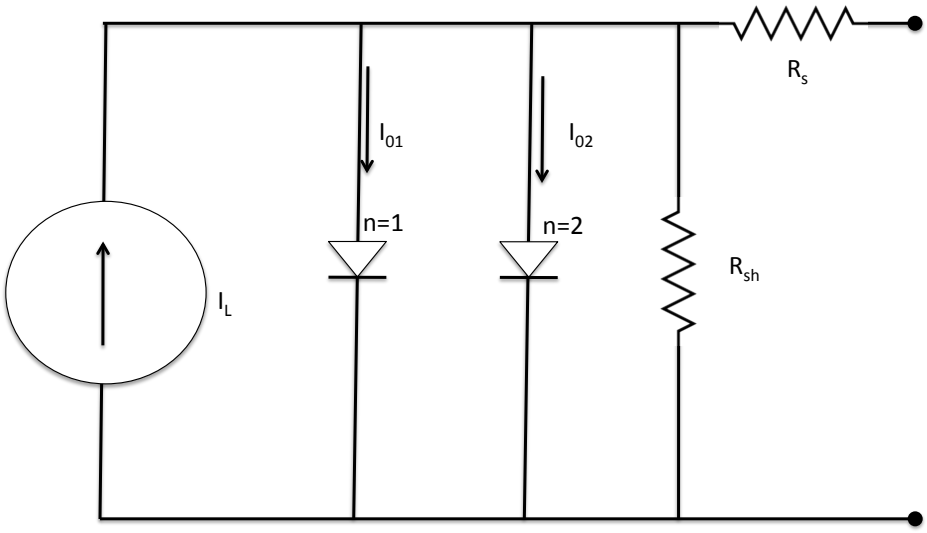

Figure 9: Circuit diagram for a non-ideal solar cell. The cell consists of a current source, I_L, two leaky diodes, I_{01} and I_{02}, and two parasitic resistances, R_s and R_{sh}. The first diode with current I_{01} represents recombination current in the quasi-neutral regions. The second diode with current I_{02} represents recombination current in the depletion region. R_s represents a parasitic resistance due to the inherent resistance to carrier flow in the bulk semiconductor and contacts. R_{sh} represents a parasitic resistance due to shunting conduction pathways from one contact to another around the depletion region. From [31]

Using Kirchoff's Circuit Law an equation for a simple, nonideal solar cell can be developed. The overall current can be described as the sum of the light, I_L, and dark, I_D, currents.

$$I = I_L + I_D = I_L - I_{01}(e^{\frac{q(V+IR_s)}{k_B T}} - 1) - I_{02}(e^{\frac{q(V+IR_s)}{2k_B T}} - 1) - \frac{V + IR_s}{R_{sh}} \qquad (6)$$

Where q is the universal charge constant, V is the applied voltage, I is the current flow, k_B is Boltzmann's constant, and T is the temperature.

The value of I_D is the sum of three different terms called the diffusion current (the term starting with I_{01} in Equation 6), recombination current (the term with I_{02}), and the shunt current (the final term). Equation 6 is not analytically solvable without several simplifying assumptions. Therefore to determine the values of the non-ideal terms exactly, this equation must be solved numerically. This is typically done by measuring the solar cell IV curve under dark conditions, giving a I_L value of zero and separating out any light induced effects, and then using a least squares fit to find the values of I_{01}, I_{02}, R_s, and R_{sh}.

Dark IV curves are typically viewed on a semilog scale in order to more easily determine the effect of the I_D parameters on the device. Figure 10 shows an example of how the recombination, diffusion, and shunt currents affect the behavior of a solar cell on a semilog plot. The shunt current dominates in the low voltage regime of the dark IV curve. The shunt current increases rapidly at voltages near zero before flattening. As the voltage increases towards and past the knee of the curve, the measured current increases rapidly as the recombination and diffusion currents begin to dominate. The exact behavior of the curve at this point is determined by the relative strengths of the two currents. At very large voltages, the dark IV curve flattens out again as series resistance effects dominate.

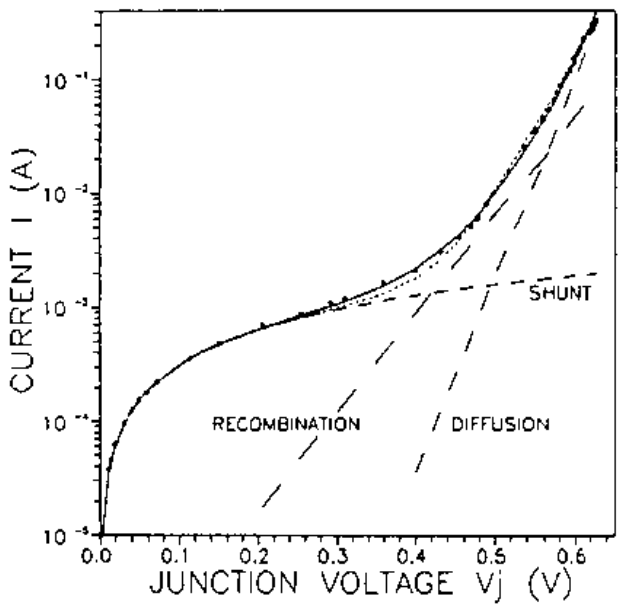

Figure 10: Dark IV curve on a semilog scale of a well-behaved Si cell. Equation 6 can be used to fit the curve as a sum of three currents. The diffusion current term is determined by I_{01}, the recombination current by I_{02}, and the shunt current accounts for the last term. The shunt current has a major effect on low voltages and flattens the IV curve. For higher voltages, the current increases dramatically as the recombination and diffusion currents are dominant. At very large voltages series resistance effects are dominant, flattening out the IV curve. From [38]

2.1.3 CdTe Cells

Solar cells composed of cadmium and tellurium thin films were first created in 1972 when Bonnet and Robehorst composed the first completely thin film device and demonstrated an efficiency of 6% [39, 40]. CdTe is thought to be a near ideal solar cell material because the direct bandgap of 1.45eV is a good match to the solar spectrum (495nm), has a high optical absorption coefficient, can be manufactured quickly and cheaply in a polycrystalline state, can be prepared as n- or p-type, and can be made as this as possible to ensure homogeneity without using high dopant levels.

2.1.3.1 Maximum efficiency of CdTe cell

With a E_g of 1.45eV, a CdTe solar cell can possibly absorb 66% of the solar spectrum power (Figure 11). For the AM1.5 global solar spectrum incident on an ideal CdTe cell, the ultimate efficiency, η_{u}, can be calculated assuming no recombination or reflection. This perfect cells absorbs each photon with an energy greater than the bandgap. Thermalization losses cause all absorbed photons to have a final energy equal to E_g. For this perfect CdTe cell, η_u is 46.5% and is defined as

$$\eta_u = \frac{E_g \int_0^{\lambda_g} N_{ph}(\lambda)\, d\lambda}{\int_0^{\infty} N_{ph}(\lambda) E(\lambda)\, d\lambda} \tag{7}$$

Where λ_{g} is the photon wavelength at E_g, $\mathrm{N_{ph}}$ is the number of incident photons given wavelength, h is Planck's constant, c is the velocity of light, and $\mathrm{P_{in}}$ is the total incident power over all wavelengths [41] .

Of course no cell is perfect and, in accordance with the Laws of Thermodynamics, electron-hole pairs are randomly created and destroyed at any temperature greater than absolute zero. So, any cell in the real world must undergo recombination. This

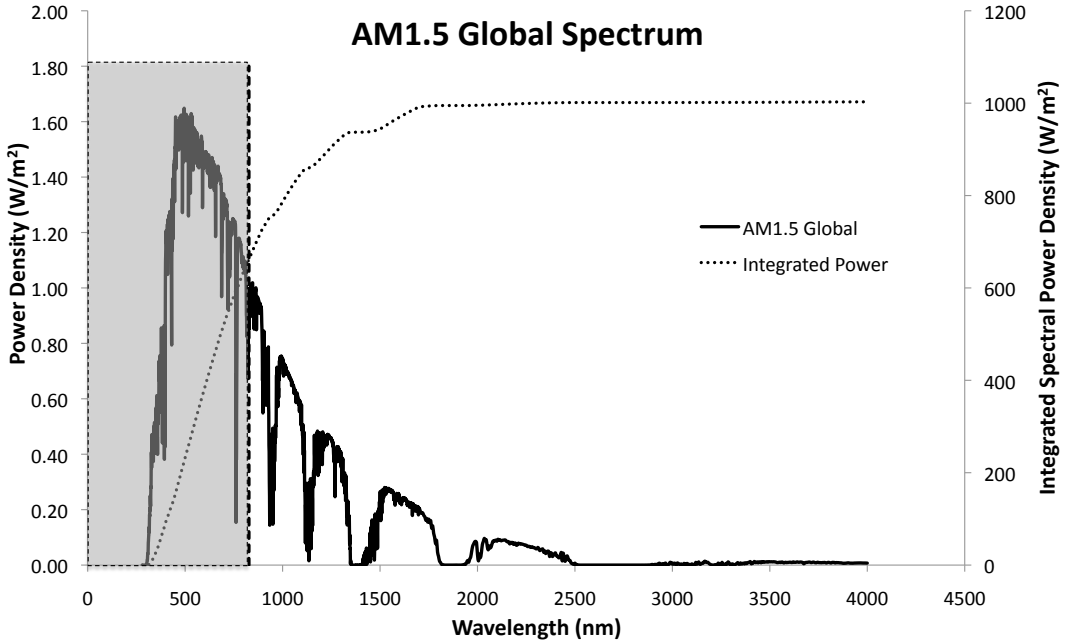

Figure 11: Standard test conditions for terrestrial solar cells require the ASTM AM1.5 global solar spectrum (black line). This solar spectrum can be approximated by black body radiation at a temperature of 5762K. The sharp declines in power density at certain wavelengths are due to absorption by H_2O, CO_2, and other trace molecules in the atmosphere. The integrated power of the spectrum is denoted by the dashed line. A CdTe solar cell with a E_g of 1.45eV can absorb photons with an energy larger than E_g (shaded box). For an ideal CdTe solar cell, this would mean that 66% of the maximum integrated power density of the solar spectrum can be harnessed.

thermodynamic maximum efficiency for a solar cell is called the Shockley-Queissier efficiency, η_{SQ} [41].

The η_{SQ} may be calculated by considering a cell which absorbs all incident photons and undergoes only radiative recombination. If this cell is in thermal equilibrium in the dark under zero applied voltage, then the difference in the quasi-Fermi levels is zero. Assuming the cell is a perfect blackbody above E_g and a perfect white body below E_g, then the equilibrium radiative recombination rate, $\mathrm{RR_o}$, can be described by the equation

$$RR_o = \frac{2\pi}{c^2 h^3} \int_{E_g}^{\infty} \frac{E^2}{e^{\frac{E}{k_B T}}} \mathrm{d}E \tag{8}$$

Where k_B is Boltzmann's constant, c is the velocity of light, h is Planck's constant, and T is the cell temperature [31].

For a cell in the light that is under an applied voltage, the largest possible split in the quasi-Fermi levels is equal to V. In this case, the recombination rate will increase from RR_o to RR according to the equation

$$RR = qRR_o e^{\frac{qV}{k_B T}} \tag{9}$$

If all photons incident with E> E_g are absorbed and contribute one electron to current flow, then the current, I, is defined as

$$\begin{aligned} I &= q\left[\int_0^{\lambda_g} N_{ph}(\lambda)\mathrm{d}\lambda - RR + RR_o\right] \\ &= q\left[N_{Tph} - RR_o(e^{\frac{qV}{k_B T}} - 1)\right] \end{aligned} \tag{10}$$

Where N_{Tph} is the total number of photons with an energy greater than E_g.

Since $RR_o \ll N_{Tph}$, equation 10 can be simplified to

$$I \approx q\left[N_{Tph} - RR_o e^{\frac{qV}{k_B T}}\right] \tag{11}$$

The IV curve of such a CdTe cell is shown in Figure 12. Taking thermodynamics into account causes the knee of the IV curve to no longer be a right angle and the FF value of the curve to be less than 1. The open circuit voltage for such a cell can be found by solving equation 11 for I=0. In this case I_{sc} and V_{oc} would be equal to

$$I_{sc} = q\left[N_{Tph} - RR_o\right] \tag{12}$$

$$V_{oc} = \frac{k_B T}{q} \ln \frac{N_{Tph}}{RR_o} \tag{13}$$

The highest possible efficiency of this cell, η_{SQ} is then found by solving equation 4. For a solar cell composed of a CdTe absorber with an E_g of 1.45eV and a temperature of 300K, η_{SQ}=32.65%. Such solar cell would have a V_{oc} of 1.18V, an I_{sc} of 30.84mA/cm^2, and a FF of 89.66%. CdTe has one of the highest possible values of η_{SQ} and matches well with the AM1.5 spectrum (Figure 13).

The value of FF for a real CdTe cell has a ceiling of 89.66%. On the other end of the spectrum, the lowest possible FF value would correspond to a straight line IV curve. Such a curve is possible for a cell with a very small value of R_{sh}. For shunted, straight line IV curve, the current can be approximated by a linear relationship with $-I_{sc}$ as the y-intercept and V_{oc} as the x-intercept

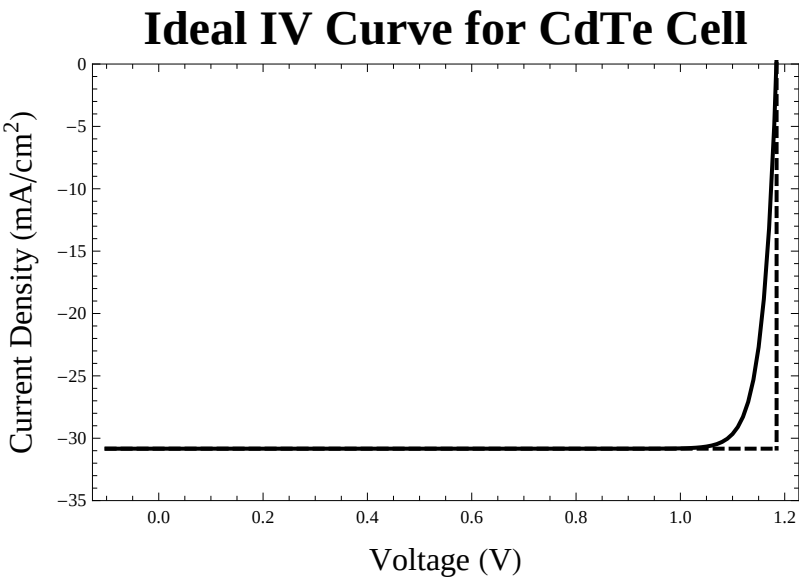

Figure 12: IV curve of a CdTe cell exhibiting only radiative recombination. Since this radiation is thermodynamically required, this cell constitutes the highest possible efficiency, 32.65%, possible from a real-world cell. Such a cell would have an I_{sc} of 30.84mA/cm^2, a V_{oc} of 1.18V and a FF of 89.66%.

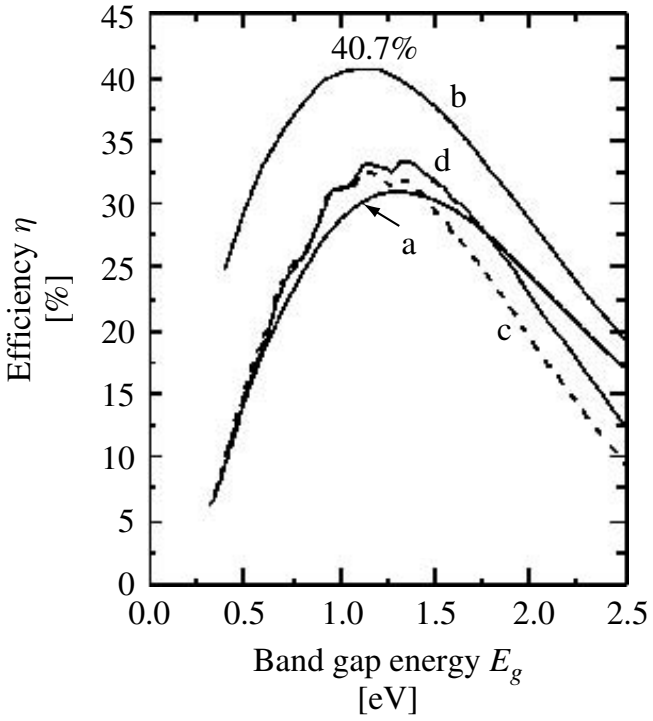

Figure 13: Shockley-Queissier efficiency limit for cells composed of absorbers with different bandgaps. (a) 6000K blackbody radiation (b) concentrated 6000K blackbody radiation (c) AM1.5 Direct spectrum (d) AM1.5 Global spectrum. From [31].

$$I = \frac{I_{sc}}{V_{oc}} V - I_{sc} \tag{14}$$
$$= I_{sc} \left(\frac{V}{V_{oc}} - 1 \right)$$

The power, P, and the partial derivative of the power with respect to the voltage is described by

$$P = IV \tag{15}$$
$$= I_{sc} \left(\frac{V^2}{V_{oc}} - V \right)$$
$$\frac{\partial P}{\partial V} = I_{sc} \left(\frac{2V}{V_{oc}} - 1 \right) \tag{16}$$

The voltage at max power, V_{mp}, is found by solving for the voltage at which equation 16 is equal to zero

$$0 = I_{sc} \left(\frac{2V_{mp}}{V_{oc}} - 1 \right) \tag{17}$$
$$V_{mp} = \frac{V_{oc}}{2} \tag{18}$$

By substituting equation 18 into equation 14, the current at maximum power, I_{mp}, can be found and P_{mp} calculated

$$I_{mp} = I_{sc}\left(\frac{V_{mp}}{V_{oc}} - 1\right) \tag{19}$$
$$= I_{sc}\left(\frac{V_{oc}}{2V_{oc}} - 1\right)$$
$$= \frac{I_{sc}}{2}$$
$$P_{mp} = I_{mp} \times V_{mp} \tag{20}$$
$$= \frac{I_{sc}V_{oc}}{4}$$

FF can then be easily calculated

$$FF = \frac{P_{mp}}{I_{sc}V_{oc}} \tag{21}$$
$$= \frac{I_{sc}V_{oc}}{4I_{sc}V_{oc}}$$
$$= \frac{1}{4}$$

(22)

Therefore, FF values around 25% indicate a totally straight line shunt. FF values can range anywhere from between 25 and 89.66% for a CdTe cell.

2.1.3.2 Makeup

A typical CdTe/CdS production cell in use today (Figure 9) has a metal rear contact for hole collection, CdTe layer which acts as the absorber and contains the majority of the depletion region, CdS window layer, transparent conducting oxide (TCO) for electron collection, and soda-lime glass top for protection.

2.1.3.3 Substrate vs. Superstrate Configurations

CdTe cells can be manufactured in two configuration, superstrate and substrate. The superstrate configuration means that photoactive material is deposited on top of

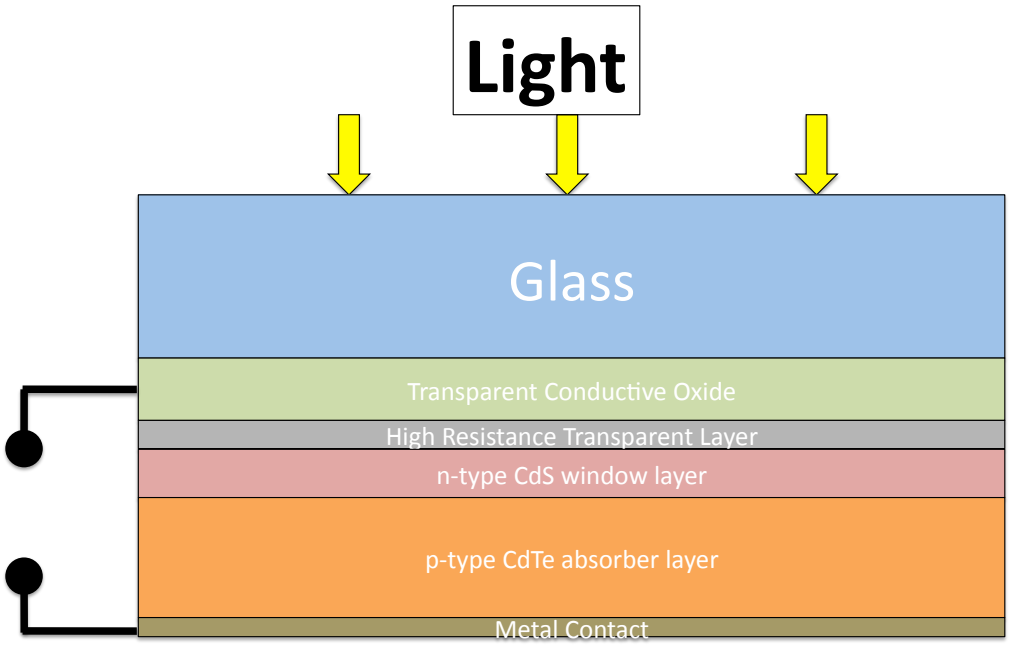

Figure 14: Schematic of the layers of a CdTe cell. The cell is composed, from top to bottom, of a soda lime glass, transparent conductive oxide top contact, high resistance transparent buffer layer, CdS window layer, CdTe absorber layer, and metal back contact.

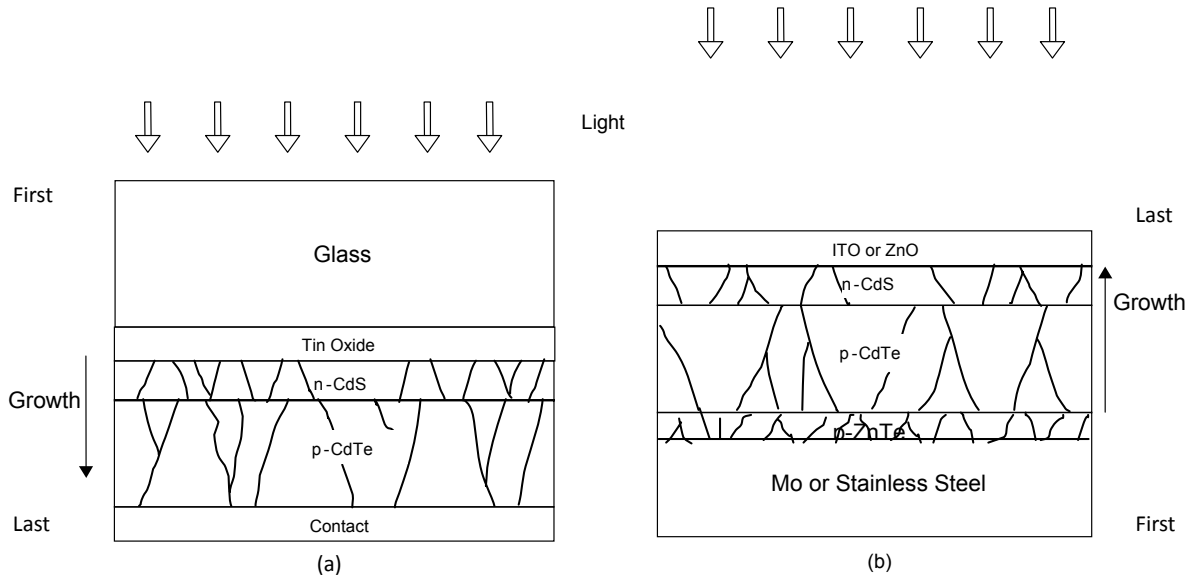

Figure 15: Difference in thin film solar cells deposited in a (a) superstrate configuration versus cells deposited in a (b) substrate configuration. Superstrate cells are grown starting with the transparent layer and the semiconductor/metal contact is the last interface deposited. Substrate cells are grown starting with a metal layer. The last layer deposited is the transparent conductive oxide. From [42]

glass and the metal back contact is the final production step. Contrastingly, a cell produced in the substrate configuration has the PV materials deposited on a metal layer and finished with a transparent and conductive top electrode (Figure 15).

While superstrate configurations have the advantage of allowing more processing (chemical etching, diffusion, or interfacial layers [43]) of the photovoltaic/back contact interface (the source of many parasitic losses), they have large disadvantages. The largest of these is that the vast majority of both the weight and volume of these cells is taken up by encapsulating glass, decreasing their specific power. Secondly, the glass layer allows no shape adaptability [44] for uses in building integrated PV, or other applications which require flexible power sources.

Without the glass layer, substrate configuration cells have a much higher specific power and can easily be deposited on conductive metal foils or polymers, using a low cost roll-to-roll manufacturing method [45]. The fact that substrate configuration

cells, such as 3DCNTPV cells, are lightweight, flexible, and utilize low cost substrate materials makes them ideal for both terrestrial and space applications [10].

However, the challenges of making substrate configuration cells as efficient as similar superstrate configuration cells are large. In substrate configuration cells, a low V_{oc} and FF result due to poor contact between the CdTe and metal underlayer. While superstrate configuration cells regularly reach efficiencies of over 15%, the highest recorded efficiency for a substrate configuration is only 11.4% [46] on cells with very small areas.

2.1.3.4 Transparent conductive oxide

The three transparent conductive oxides (TCO) used in cell manufacture today are indium tin oxide (ITO), fluorine-doped tin oxide (SnO_2:F), and aluminum-doped zinc oxide (AZO). Cadmium stannate ($CdSnO_2$) has also been used in record setting CdTe cells, but is not considered a manufacturable TCO [47, 48, 49].

ITO is more stable at higher temperatures and is widely used in high temperature processes. For most applications today, ITO is the industry standard even though there is a movement towards other available TCOs due to the expense and toxicity of indium [50]. The only specifications for the TCO are that it must be transparent (>90%) and conductive ($\rho < 10 \times 10^{-4}$ Ω /cm) [51, 52].

ITO was first reported as a TCO as far back as 1907 [53] and is one of the most extensively studied and most commonly used TCOs in optoelectronics [54, 55, 56, 57, 58]. Tin (Sn_{In}^{3+}) is used to extrinsically dope indium oxide (In_2O_3). In_2O_3 has a lattice parameter of 10.118 Å[59] and occurs in the cubic bixbyite structure with one unit cell being composed of 16 formula units [60]. There are many possible deposition methods including sputtering, thermal evaporation, spray pyrolysis, pulsed laser deposition, ion assisted deposition (IAD), dipcoating, electron beam evaporation, and screen printing [61, 62, 63, 64, 65, 66, 67, 68, 69], but most methods require either high

energy densities or high temperatures in the presence of oxygen in order to deposit high quality ITO films.

Spray pyrolysis, screen printing and dip coating require a crystallization process at temperatures up to 600^{o}C. Since In and Sn have such disparate vapor pressures, thermal evaporation must be reactive, and is extremely difficult to get films with the correct stoichiometry [60]. Films deposited by direct current (DC) sputtering tend to be amorphous [70] and have a very low transmittance, as grain boundaries (GBs) and dangling bonds absorb light [71]. For solar cell applications, this leaves radio frequency (RF) sputtering, electron beam evaporation, and IAD. RF sputter and IAD have the best results for large area and low temperature ITO deposition [72].

ITO is a degenerate wide bandgap (E_g= 3.75 [73]) semiconductor. The large bandgap gives rise to the transparency of the ITO because it means that the majority of photons are not absorbed and only UV or near UV photons are absorbed [62]. Oxygen vacancies (V_o) and tin doping (Sn_{In}) give rise to n-type doping [33, 72] with the carrier concentration described by:

$$n = [Sn^{\cdot}] + 2[V_o^{\cdot\cdot}] \tag{23}$$

ITO conductivity has been demonstrated as low as $1.5 \times 10^{-4}\Omega/cm$ for N_D= $10^{21}cm^{-3}$ [62].

It would be advantageous for a TCO to be both completely transparent and highly conductive. However, there must be compromise between resistance and transparency [74]. High O_2 incorporation during deposition results in relatively few oxygen vacancies. The lack of oxygen vacancies yields a highly resistive film, but also one that has a large bandgap, so it is very transparent [74]. During deposition

the critical parameter is the O_2 concentration, which changes conductivity [75, 76], workfunction [77, 78], and transmission [79] of the deposited film.

2.1.3.5 High Resistance Transparent Layer

In order to create high efficiency cells, it is necessary to avoid shunting of the cell from CdS pinholes. There are two ways to accomplish this, the first is the addition of a high resistance transparent (HRT) layer between the low resistivity TCO layer and the CdS layer. The second is to deposit a larger CdS layer [27]. Using a larger CdS layer is simpler from a processing standpoint, however, it decreases the efficiency of the cell for high energy photons due to parasitic absorption from the CdS layer (E_g=2.42eV, λ_g=513nm).

The HRT layer was specifically developed in order to counteract the existence of shunts [80] in the CdTe cell and increase both device uniformity and yield [81, 82]. Cells which have an HRT layer exhibit higher V_{oc}, I_{sc}, and FF [43]. This layer also, in a superstrate configuration, shields against adverse K^+ and Na^+ diffusion into the semiconductor layers from the glass top [39], helps CdS to adhere during deposition and form large grains, and acts as a final etch stop barrier during back contact formation.

Small thicknesses (20-200nm) of undoped ZnO, undoped SnO_2 [83], and a mixture of Zn_2SnO_4 and $CdSnO_4$ [28], have all been used as an HRT layer in high efficiency cells. These materials are used because they have an ideal resistivity of 1-10k$\Omega/\square$ [84], which is higher than a TCO, but low enough to still be considered a metal since the Fermi level of the HRT (ϕ=4.45 [85]) is above that of the CdS (ϕ=4.7eV) [80]. The HRT layer does add to the R_s of the cell, but due to the small thickness, does not adversely affect the IV curve properties of the cell. It is thought that this higher R_s is necessary because it causes lateral current to decay and thus to mask nonuniformities and pinholes which can drain energy [43].

2.1.3.6 CdS

The ITO/HRT bi-layer is deposited adjacent to the top semiconductor layer, Cadmium Sulfide (CdS). Relatively little is known about this junction, since, when produced in the more popular superstrate configuration, it is buried. The picture is further muddled by the fact that the CdS/ITO junction is seldom pristine and a barrier oxide or impurity layer exists [86], though it is known that in certain cells, the depletion region may extend over the entire CdS layer and even into the ITO. So the ITO can affect the main junction characteristics I_D and V_{oc} [86].

When deposited, the CdS/ITO junction starts as a ohmic contact (Φ_{CdS}=4.5, Φ_{ITO}=4.2-4.5) [86]. This junction starts to be rectifying after annealing at 400^{o}C for 10 min and becomes fully rectifying after 20 minutes [87]. This is because oxidative treatments can raise the workfunction of ITO up to 5eV [62]. The raising of the ITO workfunction is deleterious to the ITO/CdS interface, however, it does increase ITO transmission and conductivity [75, 76].

CdS acts as the window layer in the CdTe cell and is natively n-type due to sulfur vacancies [1]. The CdS layer can be applied by any number of methods e.g., close spaced sublimation (CSS), thermal evaporation, chemical bath deposition (CBD), sputtering, molecular beam epitaxy (MBE). But good quality CdS has a suitable dopant concentration ($>10^{16}cm^{-3}$), high transmission, and good uniformity [88]. CBD has been shown to make better devices in the superstrate configuration [89], though thermal evaporation is more effective for the substrate configuration [10].

Stable CdS is usually in the wurtzite structure, though some deposition methods can form a zincblende lattice or a combination of the two [90]. CdS is deposited in the cubic structure below temperature of about 100^{o}C and in the hexagonal structure at temperatures above 300^{o}C [89]. MBE CdS is typically deposited in a metastable cubic structure, which converts to the hexagonal form during an anneal of at least 300^{o}C [91]. The cubic structure of CdS is preferred to match the structure of the CdTe

layer, though good junctions are commonly formed even with mismatched crystal structures [92].

The main purposes of the CdS window layer are to increase the quality of the depletion region [39] and decrease the number of surface states present in CdTe [93]. This layer is not a perfect window layer and attenuates higher energy light (λ= 300 to 514nm) due to the large bandgap of CdS (E_g=2.42eV) [94, 95]. The minority carrier lifetime in the CdS is too low for carrier collection, so the photocurrent from this parasitic optical absorption is ultimately lost [84]. Therefore, this layer should be as thin as possible to maximize photocurrent, while avoiding pinholes, voids, and nonuniformities, which act as centers for light scattering and decrease R_{sh} [90, 96].

2.1.3.7 CdTe

CdS forms the main semiconductor junction with the CdTe absorber layer. CdTe/CdS interface defects act as major recombination sites and the SCR of the semiconductor is a major exciton sink [97, 98]. The reduction of this SCR recombination and an increase in the V_{oc} of the cell is a major direction in future thin films research [99].

CdTe is the p-type absorber layer and contains most of the depletion zone due to a low level of doping [100]. This layer is typically 2-10μm thick in order to obtain homogeneity [94], with the optimum thickness being 2-6μm. A larger layer sacrifices a degradation of FF due to an increase in R_s while a smaller layer is not thick enough to ensure generation of exciton pairs and produces less photocurrent [101].

CdTe can be deposited in a wide variety of manners, similar to those available in CdS deposition [94]. Deposition in most methods occurs in a columnar grain structure with an average grain size less than 1 μm in a preferential {111} orientation [100]. A large grain size is preferable because the volume to surface ratio is larger, which decreases recombination at grain boundaries (GBs).

The doping of the CdTe layer is not well known, but there are empirical recipes for making good p/n junctions [102]. Controlled doping is difficult because of compensation effects in grains and segregation of dopants at GBs [100]. Since the doping temperature is less than 600^oC, dopant levels at the GBs are several orders of magnitude higher than in the bulk. If these dopants are metallic or conductive they tend to shunt the CdTe layer [39].

For most processes natively p-doped CdTe is used. Maximum conductivity of the CdTe layer has been shown to occur at a Te/Cd precursor ratio of 6 [93]. Conductivity is also heavily influenced by oxygen, indicating that V''_{Cd} is the primary native doping species [39, 51] and acts as an acceptor 0.21eV above the valence band maximum [31].

2.1.3.8 CdTe Back Contact

Another important area of research is the formation of a back contact to the CdTe layer. An ohmic junction is an ideal junction where the work function of the metal is equal to the work function of the semiconductor and there is no barrier to carrier flow [90]. A Schottky diode junction forms when the work function of the semiconductor is larger than the work function of the metal. This sets up a potential barrier

$$V_b = (\chi + E_g) - \Phi_m \tag{24}$$

Where V_b is the barrier, χ is the semiconductor electron affinity, E_g is the semiconductor bandgap, and Φ_{m} is the work function of the metal.

This barrier limits forward current. CdTe has such a high electron affinity ($\chi_{CdTe} = 4.28eV$ [31]) that no metal has a high enough work function to give a zero Schottky barrier [103]. Current research is instead trying to limit the potential barrier to <200meV [51]. The materials used to limit the barrier are Cu, Au, Ag, Ni, Mo, C, or Pt electrodes [104].

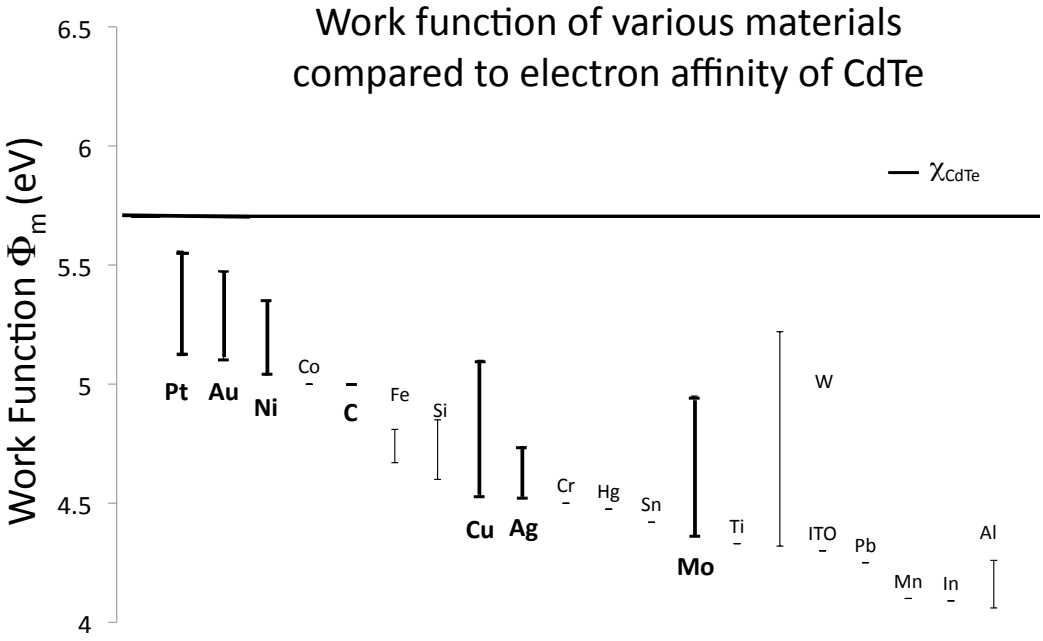

Figure 16: Electron affinity of CdTe compared to the work function of common materials. The difference between the χ of CdTe and Φ of the metal is the Schottky barrier. Few common materials can form a truly or near ohmic contact to CdTe.

This back contact is important to the operation of the solar cell because, if the thickness of the depletion region approaches that of the thickness of the CdTe layer, then the back contact can impact the IV curve in the 4th quadrant [105]. Since a truly ohmic contact to CdTe with a pure metal is impossible, the back contact barrier is modeled by a diode in the opposite direction from the main junction diode [106]. This contact barrier limits current flow in the 1st quadrant when the primary junction diode is forward biased (Figure 17). Instead of an exponential increase in current flow in the 1st quadrant, these cells have a current flow which remains nearly constant for even large voltages, a condition known as roll-over (RO). RO is nearly unavoidable in substrate configuration cells, though it might not always be seen because it can be masked by a large R_s [107].

In the superstrate configuration, roll-over is typically attenuated by using post-deposition processing to create a heavily doped p^{++} Te-rich layer. This allows for tunneling through the barrier to the back contact [84]. This layer is typically formed either by an etch before deposition of the metal back contact or by the use of dopants. If an etch is used, it is either accomplished by a nitric/phosphoric acid mix or Bromine. This etch not only leaves a Te-rich layer, it also eliminates a thin oxide barrier which can be very deleterious. Even a small $CdTeO_3$ oxide layer on the order of $20\mathring{A}$ can increase R_s, block free carriers, and lead to increased recombination [86, 104].

A p^{++} layer can also be formed by the diffusion of certain dopants such as Te, Cu, Au, and Ag [86, 107]. For instance, diffusing a thin layer of Cu into the CdTe has been shown to improve the characteristics of the main junction and increase the CdTe conductivity [108, 109, 110]. Though Cu is beneficial as an acceptor level in the CdTe, if it migrates to the junction or into the CdS, it becomes one of the major degradation sources by poisoning the depletion region. The metal then forms a metal-insulator-semiconductor MIS structure which decreases efficiency [51, 93, 94, 111]. However,

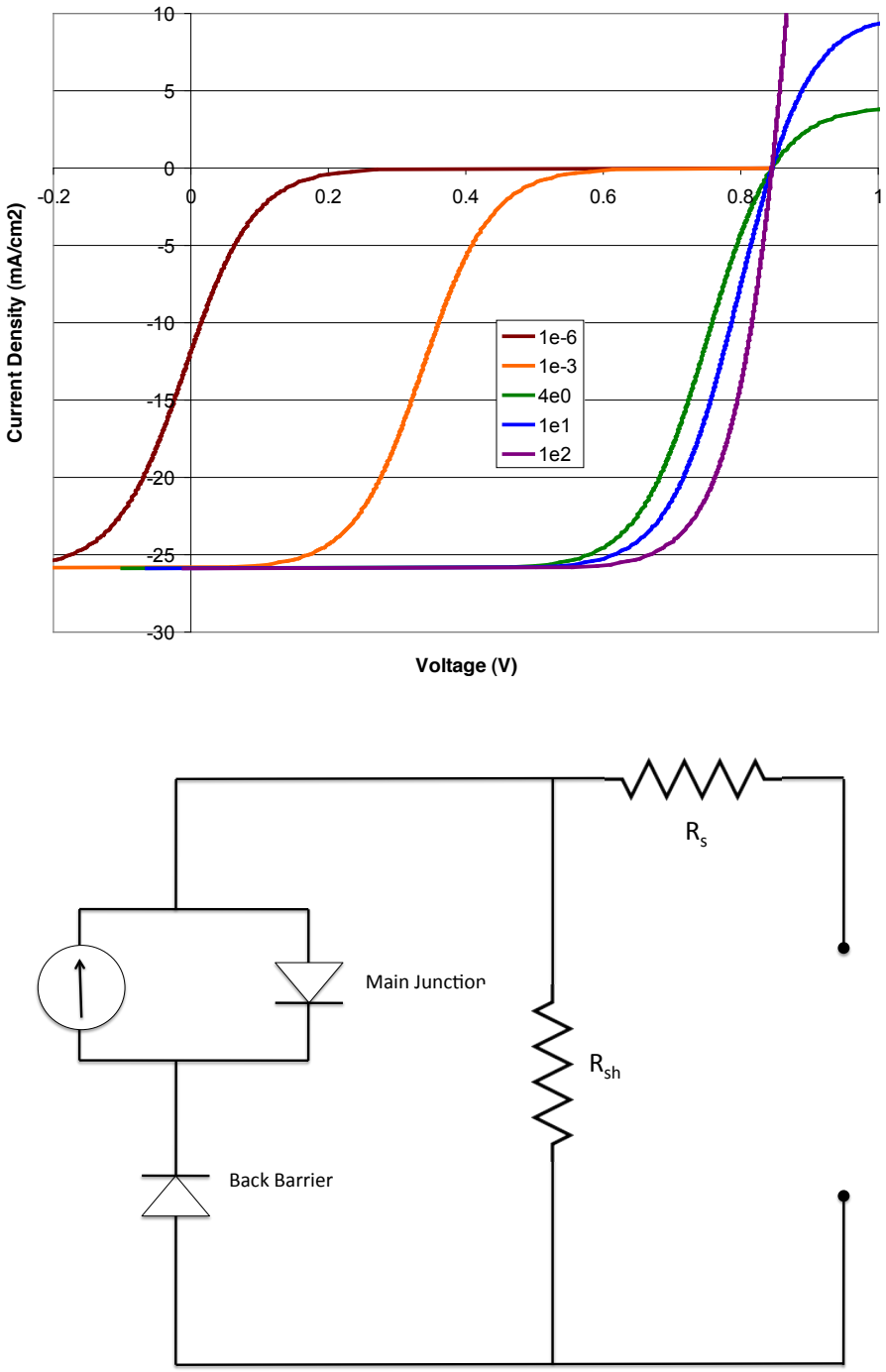

Figure 17: (Top) Roll-over of IV curves from an idealized CdTe cell with different strengths of back-contact barrier. The current through the back contact ranges from 1×10^2 for a weak barrier, to 1×10^{-6} for an exceptionally strong back contact barrier. For very strong schottky barriers, the roll-over can occur in the fourth quadrant, causing an inversion of curvature compared to a normal IV curve. From [1] (Bottom) Circuit diagram of a CdTe solar cell taking into account a back contact barrier. The barrier is in series with the main junction, but opposes current flow. This limits current flow in the forward direction.

few long term studies have been done and almost every record setting CdTe cell has had a Cu back contact (usually graphite doped with Cu) [100].

The major disadvantage of the substrate configuration of cells is that the back contact is a buried contact, so that many of the post-processing methods used in the superstrate configuration are unusable. This leads to abnormally low V_{oc} values ($\sim$300-600mV) for substrate configuration cells [112]. The best materials for use in back contacts for the substrate configurations have shown to be pure or alloyed forms of Cu, Ag, Au, or Ni. While each of these form near ohmic contacts, they each have disadvantages. Ag, like Cu, can act as a p-type dopant. However, it is prone to electromigration along GBs leading to shunts and non-uniformities which can degrade the junction quality [113, 114, 107]. Au has been shown to be an acceptable contact, though it does not eliminate adverse back contact effects [115, 116]. Ni can form an insulative Ni_3Te_2 at the back contact which increases the R_s and degrades the device [107].

2.1.4 $CdCl_2$ Post Treatment

One treatment which all high efficiency (>10% [93]) CdTe solar cells undergo is $CdCl_2$ annealing in which a $CdCl_2$:CH_3OH solution is applied, dried, and then heat treated at $\sim$ 400^oC [101]. This treatment corresponds to an order of magnitude increase in the overall efficiency, V_{oc}, and I_{sc} of the cell [51]. While the kinetics of this process are not well understood and the process is more of an optimization of a recipe that has been shown to be affective [100], it is widely believed that GB changes are very important due to carrier recombination and transport changes during the $CdCl_2$ treatment [102]. It is generally thought that at least three distinctive processes which act to optimize the cell, (1)grain growth, densification and recrystallization, (2) semiconductor inter-diffusion, and (3) electrical changes at GBs [37].

$CdCl_2$ treatment causes grains to go through the classic stages of recovery, recrystallization and growth [102]. It is thought that $CdCl_2$ acts as a fluxing agent which increases the atomic mobility of Cd [117, 29] and X-ray diffraction studies (XRD) have shown little or no grain growth without it. However, growth is only demonstrated for CdTe films with grain sizes of less than 1μm and show a grain growth factor of around ten. The grain growth in CdTe during $CdCl_2$ anneal follows a near ideal Burke and Turnbulls Parabolic Grain Growth formula

$$\sqrt{D^2 - D_o^2} = \kappa t^{1/2} \tag{25}$$

For 350^{o}C< T < 385^{o}C where $D^2 - D_o^2$ is the difference of the squares of the original (D_o) and final (D) grain sizes, κ is a constant, and t is time [51].

The recrystallization of grains has been shown by XRD to have an activation energy of 2.5±0.3 eV (comparable to Cd diffusion 2.44-2.67eV) and AFM measurements confirm that the recrystallization occurs at grain interstices [51]. This recrystallization and growth is accompanied by minimization of porosity of the structure [118], grain boundary passivization [51], formation of deep crevasses at GBs, and grain direction randomization from as-grown {111} [100]. These affects all help with the crystallinity of the bulk, increasing the diffusion coefficient of carriers and decreasing defects, inclusions, and traps which aid in electron-hole recombination.

As with all annealing procedures, diffusion is a significant contribution to the kinetics of the process. In CdTe cells, the increase in temperature during the $CdCl_2$ treatment is marked by Te diffusion into the CdS layer to form $CdS_{1-y}Te_y$ and S diffusion into the CdTe layer to form $CdTe_{(1-x)}S_x$ (where y≈x≈0.05) [118]. The sulfur diffusion consumes a significant amount (∼0.02-0.05 nm/s at 420^{o}C [119]) of the CdS layer and sets a lower limit to the CdS deposition thickness [118]. The Te

diffusion into the CdS layer lowers the bandgap of CdS and thus reduces the window transmission properties in the red wavelength region [51, 1]. Alternatively sulfur diffusion into the CdTe layer raises the bandgap and beneficially extends the spectral response to higher wavelengths.

The primary result of diffusion in the CdS system is strain reduction, which improves carrier transport by eliminating defects [1]. XRD shows that as deposited CdTe is slightly strained with a lattice parameter 0.13% greater than pure CdTe [118]. As sulfur diffuses into the CdTe matrix, the smaller S atoms substitute Te atoms, forming CdS and reducing the average lattice parameter, helping to accommodate the strain of the CdTe layer. Methods include using a two stage anneal to limit Te diffusion into the CdS layer prior to the primary $CdCl_2$ treatment in order to reduce the unwanted lowering of the CdS bandgap [51].

Conventional wisdom states that polycrystalline semiconductors are inherently less efficient than single crystals because GBs contain localized states. These states act as traps and centers of electron-hole pair recombination. However, $CdCl_2$ treatment decreases the density of these surface recombination sites due to grain growth and increased grain volume [51]. Although the process is not well understood, it is thought that $CdCl_2$ changes the GBs so they do not act as recombination sites, but instead as efficient photocurrent collectors and transporters.

It is thought that Cl_{Te} (0.35eV below conduction band minimum [31]) segregation near GBs causes a valence band deformation known as band bending which results in an inversion of the semiconductor and an electrostatic potential barrier [51]. This causes a barrier for hole transport across grains and a hole depleted region forms 100-300nm from GBs [120]. The effective segregation of electrons along the grain edges and holes along the bulk does not allow for effective recombination and electrons are rapidly transported by GB diffusion against the electric field gradient while holes are transported down the gradient along the bulk of the CdTe grains [120].

In the superstrate configuration the only layers which are present during the treatment are the CdTe/Cds, TCO, and glass encapsulant. These layers stay relatively static during the heat treatment so oxidation and diffusion effects can be largely ignored.

The $CdCl_2$ treatment in substrate configuration cells is much more problematic from a processing standpoint. The layers present are CdS/CdTe and a metallic back contact. These layers present two distinct problems. The first is that the $CdCl_2$ solution must be applied to, and diffuse through, the CdS layer during the heat treatment. Studies have shown that the presence of a CdS layer >100nm thick may inhibit $CdCl_2$ diffusion into the junction [43]. To work around this problem, it may be necessary to alter the heat treatment in order to sublimate enough sulfur so that the effective thickness of the CdS film is reduced. This enables diffusion of the $CdCl_2$ to the junction [10]. Otherwise, it may be necessary to complete a two stage CdS deposition, where a thin, sacrificial CdS layer is deposited before the $CdCl_2$ anneal followed by another CdS deposition in order to restore the rectifying characteristics of the junction.

The second problem is that the CdTe/metallic back contact interface is not static throughout the heating process. In addition to the thermal stresses caused by the difference in expansion coefficient, diffusion of metal atoms into the CdTe and possibly the CdS occurs. Some metal ions may have a deleterious effect if found in the junction and that impurity can change the back contact from an ohmic to a rectifying contact [43].

2.1.5 Solar cell texturing

One of the reasons c-Si cells have efficiencies of up to 24.4% is the use of anti-reflective coatings and surface texturing to increase power output. The reflection of photons away from a solar cell surface causes a major decrease in efficiency due

to the relatively large difference between the index of refractions of air and a solar cell's photoactive material. Both texturing and anti-reflective (AR) coatings increase power output through one or more of these processes: (1) increasing the number of interactions between a photon and the photoactive surface, (2) increasing the path length of the photon through the device, and (3) decreasing the amount of reflection from the solar cell front [121].

AR coatings have been used in creating high efficiency devices. These coatings are applied on top of the front surface charge collector. They reduce the reflection of light from the solar cell by matching the thickness and index of refraction of a coating so that $\frac{1}{4}\lambda$ destructive interference occurs. However, this destructive interference can only occur for a relatively small spectral range of wavelengths. More layers of anti-reflection coatings must be added to eliminate reflection over a larger range of wavelengths. This can result in a large cost or number of processing steps to create a broad spectral response. The coatings are also only effective for near-normal incidence angles of light. Increased angles of incidence result in diminished AR capabilities [122].

Texturing lowers reflection of the cell for both a wide range of wavelengths and large range of incident angles [123]. By far the most successful application of texturing in Si cells is the use of pyramidal shapes. This type of texturing was first proposed in the 1960s and 70s [124, 125]. The angle of the pyramid face causes multiple interactions with the solar cell surface and light rays entering the cells are refracted to a shallower angle, increasing internal reflections.

In order to form pyramids on the Si surface, KOH or some other alkali hydroxide is used to isotropically etch the $\langle 100 \rangle$ surface. This etch continues until reaction slows nearly to a stop at the $\{111\}$ planes. This family of planes, at an angle of 54.7^o to the $\langle 100 \rangle$ in Si, forms a pyramid with a typical base size of around $10\mu\text{m} \times 10\mu\text{m}$ [126]. If a bare $\langle 100 \rangle$ surface is submerged in KOH, random pyramidal structures are

formed. Inverted, periodically spaced pyramids can be formed using an etch mask on portions of the Si surface.

The inverted pyramidal texturing has been used to set a record efficiency in c-Si cells of 24.4% [16]. However, since this method utilizes the etching of single crystal Si, it is unable to be used for many other material systems. This is especially true for thin film cells such as polysilicon and CdTe which are polycrystalline [122]. Texturing would be useful to increase the power output for many other types of solar cells, but there is no simple, cost effective way to texture of the surface of thin film solar cells.

Some "top-down" techniques, those which involve removal of material to produce texture, have been attempted for polycrystalline solar cells. These include mechanical grooving [127], laser scribing [128], defect etching [129], and reactive ion etch (RIE) [130]. However, all of these methods have significant disadvantages. Mechanical grooving, which involves micromachining texture into the solar cell surface through the use of a dicing saw, and laser texturing, both result in surface damage of the cell and more processing steps are required in order to passivate the solar cell surface. Since it is dependent on the local defect density, defect etching both requires a highly defective semiconductor layer and is extremely inconsistent from device to device. RIE results in a large parasitic absorbance and there exists problems in passivating the etched surface.

It is only within the past few years that thought has been given to texturing thin film solar cells via a "bottom up" approach where material is added instead of etched away. These methods include moth eye texture [131], photonic crystals [132], microspherical texturing [122], and the 3DCNTPV approach. These methods show great promise in increasing the power output of thin film solar cells for a wide range of incident spectral wavelengths and angles.

Second generation CdTe cells have been around for over thirty years. Although they remain one of the more studied PV devices, many of the device structures and

materials processing conditions must be further understood and optimized in order to realize the full efficiency of these devices. There are currently many active research areas regarding all the second generation thin film solar cells. However, many recent research thrusts spurred by recent advances in nanotechnology are exploring a new generation of solar cells. These many nascent and largely unproven types of cells are lumped together as third generation PV devices.

2.1.6 Third Generation Solar Cells

Third generation solar cells encompass a wide variety of different technologies. There are, however, three main types. The first are those which mimic photosynthesis using donor-acceptor molecular assemblies and clusters. The second are those which use semiconductors and photocatalysts to produce fuels. The third, and most promising, are nanostructure semiconductor based solar cells [2]. Nanostructured solar cells try to improve upon efficiencies of current solar cells by facilitating photon absorption, electron transport, or carrier collection [133]. Of these nanostructured PV devices, the largest share of work has been done using 1D materials such as nanotubes, nanowires (NW), and nanorods.

2.1.6.1 1D nanostructured solar cells

Nanowire devices are defined by the type of junction. They can have either radial junctions [134, 135], axial junctions [136], or thin-film embedded junctions [137] (Figure 18).

Radial junctions and thin-film embedded junctions have one major advantage over traditional planar devices. In planar films, absorption and collection are in competition [138, 139]. This means that the absorber must be thick enough to absorb incident photons, but still thin enough to collect generated free carriers [136]. This competition is known as the "thick-thin conundrum" and is especially important in thin films because of the high recombination velocity due to grain boundaries,

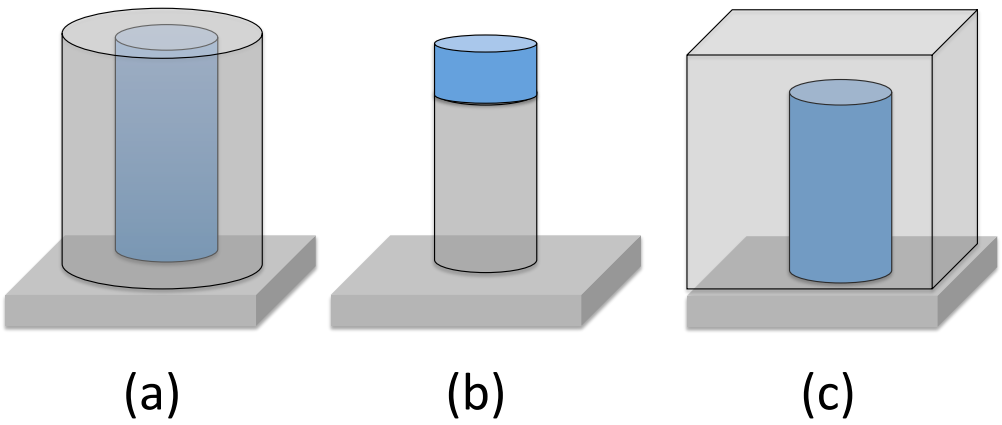

Figure 18: Three broad classes of 1D nanostructured solar cells of nanowires with a (a) radial junction, (b) axial junction, and (c) thin-film embedded junction of an absorber (blue) and window (gray) material.

vacancies, and impurities [20, 140, 139, 141, 142, 143, 144]. 1D nanostructures solve this conundrum by orthogonalizing the light absorption and carrier collection processes [138] (Figure 19). So it is possible to optimize the device absorption length (device thickness, L_A) independently of the optimization for carrier diffusion length (radial diameter, L_C) [136].

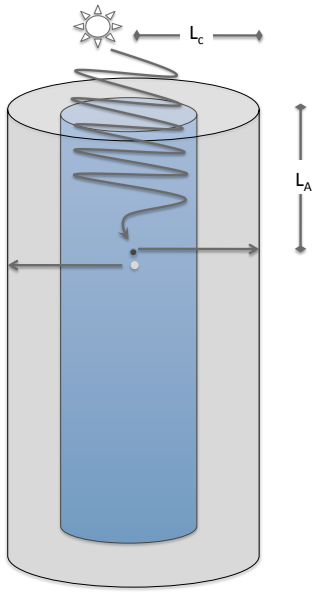

Figure 19: The "thick-thin conundrum" inherent in the device architectures of conventional solar cells can be solved by using 1D nanostructured solar cells. This means that the absorption length (L_A) of the structure can be optimized independently of the optimization for the carrier collection length (L_C) for a device such as a radial junction 1D nanowire. This device is composed of two co-axial cylinders which act as absorber (blue) and window (gray) layers.

The radial junction 1D nanostructures show the most promise for fully developed solar cells. Such cells have been accomplished by growing p-doped nanowires of Si or GaAs followed by atomic layer deposition (ALD) of Si or GaAs to create a radial p-i-n junction. A single p-i-n junction has been shown to have high efficiencies (34% in the case of Si [145] and 45% for GaAs [146]. Large area arrays of these structures suffer from very low efficiencies, however, 0.33-0.46% in the case of Si [147].

The efficiencies of these Si and GaAs devices are limited at large scales. Nanowire solar cells show significant enhancement of junction area with no increase in collection length and geometrical enhancement of absorbance. However, due to the increased surface area they show an increase in surface recombination events. Therefore, they are most useful for materials with a low surface recombination velocity [136], for which the dominant recombination mechanism is in the bulk [138]. For instance, c-Si and GaAs have high recombination velocities, so are not perfectly suitable for nanowire applications.

It is also necessary for the nanowires to have a large minority carrier lifetime in order to have efficient charge collection. However, there exists a problem with impurities from the nanowire growth causing high defect densities in the nanowire cells. Nanowires are grown from a metallic catalyst (for Si NW, Au is used [145]) nanoparticle. Impurities from these particles diffuse into the nanowire and form deep level traps. The traps greatly reduce the minority carrier lifetime by SRH recombination.

In 2005, Kayes et. al. first proposed using thin film deposition techniques to create a 3D solar cell made from densely packed nanorods with a radial junction [138]. It was soon afterwards, in 2006, that the Ready group demonstrated the 3DCNTPV concept utilizing arrays of VACNTs coated with CdTe/CdS thin films [148]. Ready holds patents in China, South Korea, and Australia (pending in US, Europe, and elsewhere) for a 3D solar cell device utilizing 1D conductors which are created using additive processes. The first forays into 3DCNTPV cells taken by the Ready group has spurred other publications using CNT scaffolding for a-Si [149] and other types of solar cells [150, 151].

CNTs as a 1D nanostructure paired with CdTe/CdS is an ideal material system for 3D cells. CNTs coated with CdTe can act as an ideal channel to collect and transport charges with minimal loss [133]. This is because CNTs are preferentially hole

conducting with extremely large hole velocities (v=0.6×10^6m/s), equal to electron velocities [152, 153]. CNTs have been used as an efficient back contact for CdTe [154] solar cells and p^+ Si [155, 156] transistors with little or no rectifying barrier.

A rigorous treatment of a CNT/semiconductor or CNT/metal junction must be determined quantum mechanically, due to the small number of available states in the CNT compared to the macroscale bulk of the semiconductor or metal. This mismatch in the number of states leads to a high contact resistance that can be modelled using a nonequilibrium Green's function [157]. However, it is possible to get an empirical sense of the junction through analytical equations to determine barrier heights [158]. Tzolov et al. used the Anderson Model [159] to model the p^+ Si/CNT interface as a semiconductor heterojunction and found an interface batter between 0.44 and 0.51eV [156]. Kawano et. al. modelled the CNT as a metallic contact to the p^+ Si and found a barrier of 0.37 to 0.67eV. However, the contact functioned as ohmic as the thin barrier width permitted hole tunneling [155].

The bandgap of a CNT falls as the inverse of the tube diameter. Semiconducting tubes with diameters of approximately 30nm have bandgaps on the order of thermal energy (≈20meV) and can be considered as conductors. For 3DCNTPV cells, the CNTs used have an average outer diameter of ∼17.5nm. The semiconducting version of these tubes have bandgaps around half the thermal energy at 300K. This, combined with the voltage difference across the CNT during solar cell operation, is enough to approximate the CNT as a conductor.

Using the same formulism as Kawano et al., it is possible to find an approximate barrier for the CNT/CdTe contact. For modeling the junction as a metallic/semiconductor junction, the barrier height can be calculated using Equation 24 with χ_{CdTe}=4.28eV, E_{gCdTe}=1.45, and ϕ_{CNT} ≈4.95 [160]. This gives a barrier height of V_b≈0.78eV (Figure 20). For CNTs as a back contact to CdTe, there will be a rectifying barrier associated with the CNT/CdTe interface. However, this barrier is

only slightly larger than the Ni/CdTe barrier and is lower than the barrier CdTe forms with many metals (Cu, Ag, Ti) used in CdTe cells. Other carbon electrodes, such as graphite paste, have shown great promise for high efficiency, stable back contacts for CdTe cells [104].

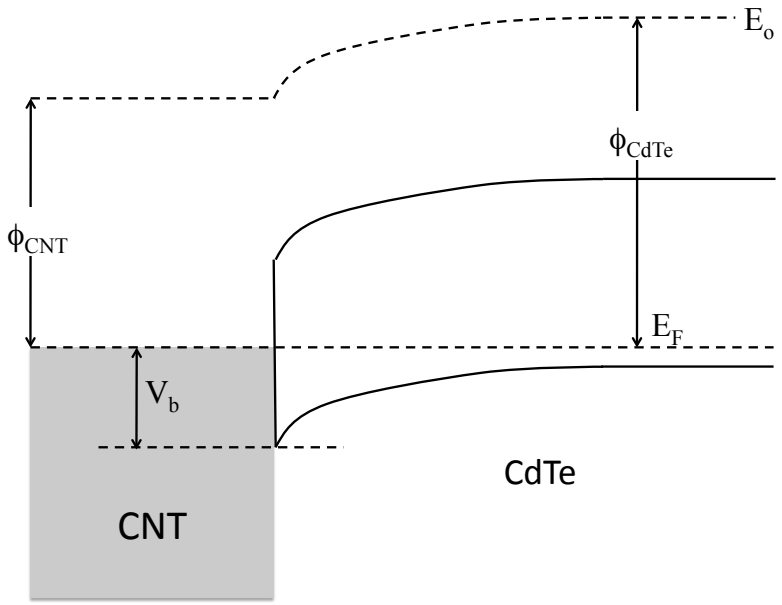

Figure 20: Band structure of a CNT/CdTe junction ignoring mismatch in the density of states and assuming the CNT is large enough to ignore the bandgap. The barrier formed by this junction opposes hole flow and has a value of 0.78eV. This value V_b is the on the order of those formed by interface of CdTe with Au and is smaller than the barrier formed by CdTe with Cu and Ag.

While NW growth exhibits poisoning related to the metal catalyst used for growth, the growth of CNTs do not exhibit the same problems. If CNTs are grown in a root growth mechanism, the metallic nanoparticle is separated from the semiconductor layer and thus the deep level traps can be mitigated. Traditional NW must be purified, though it cannot be totally cleaned of metal impurities due to some catalyst atoms diffusing into the NW. This can have deleterious effects on efficiencies and carrier lifetimes [136].

CdTe and CdS are ideal semiconductor materials system for 3D cells. In Si and GaAs cells, the added power output from texturing is always balanced by increased surface recombination. This is due to the high surface recombination velocity of those materials. Surface recombination is especially problematic for nanostructured solar cells due to the very large surface area. CdTe/CdS 3D solar cells should also have higher efficiencies than similar Si or GaAs systems because untreated CdS and CdTe have relatively low surface recombination velocities [136], so advantages from the nanoscale texturing are not offset by increased surface recombination.

2.2 Introduction to CNTs

2.2.1 History

The world of carbon was thrown into relative disarray upon the discovery of a new stable room temperature (RT) allotrope of carbon in 1985 [161]. These "curved graphite" balls with threefold coordination number were known as Fullerenes (Figure 21 (a-c)) and were discovered by accident while Smalley et al. were studying carbon production processes in stars. While graphite is composed of a repeating series of hexagons, a Fullerene contains pentagonal rings. These rings cause positive curvature of the molecule which leads to closure [162]. The first Fullerene discovered was C_{60} followed closely by C_{70}. This Fullerene is simply a bisected C_{60} molecule with a ring of ten carbon atoms inserted. By adding j such rings of these ten carbon atoms, it is possible to construct a cigar shaped structure consisting of C_{60+10j}. This produces a CNT (Figure 21 (d)).

Although Iijima is often credited with the discovery of CNTs in 1991 [164] due to his impressive transmission electron microscopy (TEM) images and the explosion of experimental and theoretical work that followed, work on nanoscale tubules of carbon had been occurring for a very long time. The first mention of carbon filaments occurred in 1889 from the thermal decomposition of methane [165]. The tools of the

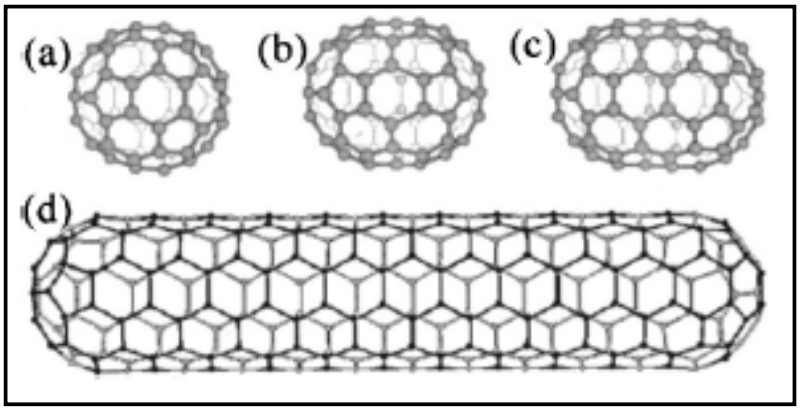

Figure 21: C_{60}, C_{70}, C_{80}, and C_{60+10j} Fullerene structures. The addition of C atoms between two C_{60} hemispheres forms high aspect ratio structures which resemble a CNT. From [163].

day were limited to optical microscopy and therefore it is impossible to tell if these tubules of carbon were actually of the nano scale. The first direct TEM observation of CNTs occurred in 1952 when a Russian journal first published a paper discussing the tubular nature of carbon [166]. However, this information was not disseminated in the western world due both to the nature of the cold war and the fact that the journal was in Russian [165]. Several other sources [167, 168, 169] detailed evidence of filamentous carbon deposits on the order of a micron or less before the celebrated 1991 paper by Iijima.

However, all of these tubules were greater than 5 nm in diameter and so are almost certainly multiple walled carbon nanotubes (MWCNTs). The first single walled carbon nanotubes (SWCNTs) were discovered very nearly simultaneously in 1993 by Iijima and Ichihashi [170] at NEC and Bethune et al. [171] at IBM, though Iijima et al. published slightly before Bethune et al. Since then, CNTs have overtaken fullerenes as the hottest research topic in science. With thousands of articles published every year in every aspect of science and engineering, the time is ripe for moving from research oriented aspects of these unique materials toward engineering consumer ready devices utilizing CNTs.

2.2.2 Structure and Bonding

Carbon contains four valence electrons in the 2s, $2\,p_x$, $2\,p_y$, and $2\,p_z$ orbitals. Since the energy difference in the 2s and 2p levels is much smaller than the binding energy of chemical bonds, the 2s orbital hybridizes with two 2p levels to form three equal sp^2 orbitals. In graphene, these orbitals form three strong, in-plane σ bonds to three equidistant neighbors 0.1421nm away. The remaining electron in the unhybridized $2\,p_z$ orbital forms weak π bonds with graphene sheets above and below to form graphite. The in-plane sp^2 bonds are the shortest and strongest single bonds found in nature [172]. Graphene sheets stack in an ABABA... order with an interplanar distance of 0.34nm to form a 3D hexagonal unit cell.

CNTs can be thought of as a long plane of graphene rolled into a seamless cylinder which can be left open or capped by two hemispheres of fullerenes [162, 173, 172]. The smallest diameter cap that is stable follows the isolated pentagonal rule and corresponds to a C_{60} molecule, which provides a lower limit of 0.7nm for the size of a CNT [50, 173]. The properties of CNTs vary widely and are highly dependent on two parameters, their size and chirality [9, 162]. The curvature of the CNT induces the sp^2 hybridization to mix with some sp^3 character in order to decrease strain energy.

This means that bonding around the CNTs circumference is slightly weaker than along the axis of the CNT [174]. The relatively small number of atoms along the circumference of the tube as compared to the axis causes confinement of the electron wavefunction along the circumference, but retains plane wave behavior along the axis, causing the CNT to behave like a one dimensional (1D) object [50]. Depending on the size and chirality, CNTs can act as 1D metallic wires or semiconductors with bandgaps inversely proportional to the diameter [173, 175].

2.2.3 Types of CNTs

CNTs can be first categorized by the number of walls present. SWCNTs are the simplest type of CNTs and are composed of a single rolled up graphene sheet with a diameter of 0.7-3nm. Although these types of CNTs can be quite rare, depending on the method of CNT synthesis used, the vast majority of theoretical work has been done on these types of tubes due to their simplicity, size, and ability to act as an almost ideal 1D quantum wire despite very large aspect ratios. MWCNTs are multiple layers of axially concentric SWCNTs with an average interlayer distance of 0.34 nm [162, 176]. The spacing between the cylinders increases with decreasing diameters due to the increasing curvature of the graphene sheets [172]. Each individual wall shows very little out of plane interaction with any other wall and transport methods and chiral parameters of one wall are very nearly independent of the others [177].

A further method of categorization is due to the chirality or helicity of the tube. If a given CNT were unrolled and laid out as a graphene sheet (Figure 22), a vector, $\vec{C_h}$, is formed by connecting two equivalent lattice points on each edge of the CNT cylinder. This chiral vector is defined as

$$\vec{OA} = \vec{C_h} = n\vec{a_1} + m\vec{a_2} \tag{26}$$

Where $\vec{C_h}$ is the chiral vector, $\vec{a_1}$ is the first crystallographic vector for graphene, and $\vec{a_2}$ is the second crystallographic vector for graphene.

The diameter of the CNT may then be defined by

$$D = \frac{\mid \vec{C_h} \mid}{\pi} = \frac{a\sqrt{n^2 + m^2 + nm}}{\pi} \tag{27}$$

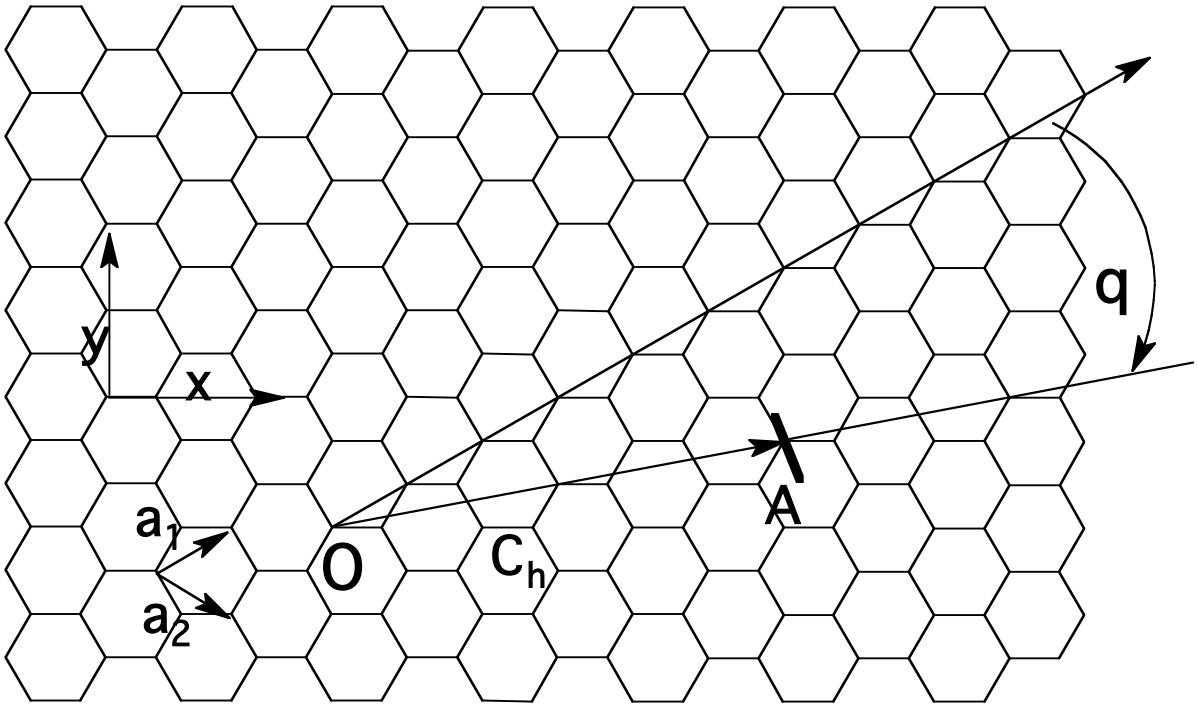

Figure 22: Chiral vector, $\vec{C_h}$, of a $(n = 4, m = 2)$ CNT with respect to a graphene lattice. Chirality is assigned by (n,m) number. The chiral angle, θ, is defined as the angle between C_h and $\vec{a_1} = (n, 0)$. From [173]

where a is the length of the carbon carbon bond.

This determines the chirality indices (n, m) of a CNT as the number of iterations of the real space crystallographic vectors $\vec{a_1}$ and $\vec{a_2}$ that must be used in order to traverse $\vec{C_h}$. Due to the highly symmetric nature of the hexagonal lattice, the only unique chiralities are generated by a $\frac{1}{12}^{th}$ wedge of the Bravais lattice [178].

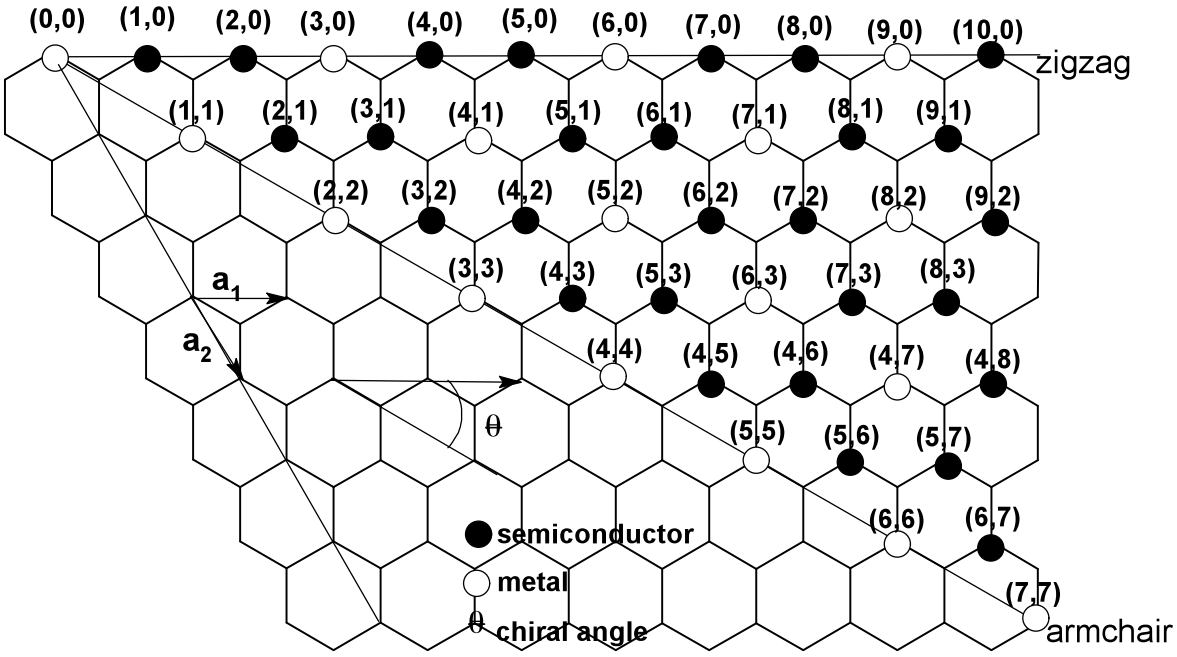

Figure 23: The value of the chiral vector determines whether a CNT is metallic or semiconductor. From [173]

Achiral CNTs, or those which are superimposable on their mirror images, are highly symmetric and contain a reflection plane [179, 180]. Those CNTs that result from a graphene plane bisected normal to its five-fold rotation axis have a chiral angle of 30^o and are labeled (n,n) [173, 178]. These CNTs are known as armchair and are always metallic in nature (Figure 23) [179]. If the graphene plane is, instead, bisected normal to its three-fold axis, then the chiral angle of the ensuing CNT will be 0^o and will be known as zigzag. These CNTs are labeled (n,0) [173]. CNTs which have a chiral angle between 0^o and 30^o contain a screw axis leading to the formation of

a helical structure with rows of hexagons that spiral along the CNT axial direction (Figure 24) [176, 180].

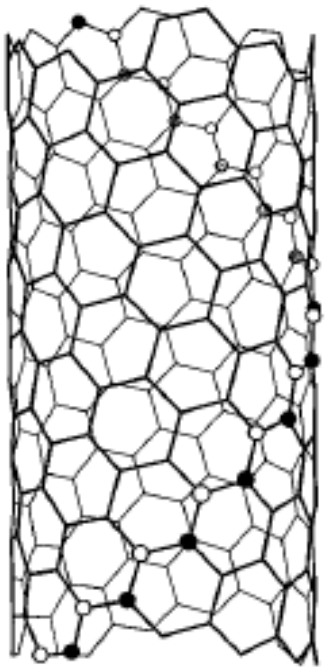

Figure 24: (10,4) chiral CNT with two independent helices (black and white dots). These are the only independent C atoms in the CNT and all others are translations from these. In general an (n,m) chiral CNT is made up of n-pairs of such helices. From [181].

CNTs can further be classified by whether they are metallic or semiconducting in nature. As in the band gap structure of graphene, the first Brillouin zone of a CNT is a hexagon. At the six corner points of this zone, known as the K-points, the valance band (π^*) and the conduction band (π) meet at E_F, creating a Fermi Point (Figure 25) [175]. Due to the repeating boundary condition of the circumference of the CNT, energy states are quantized by

$$\vec{k_c} \bullet \vec{C_h} = 2\pi\nu \tag{28}$$

Where $\vec{k_c}$ is the wave vector in the circumferential direction, $\vec{C_h}$ is the chiral vector, and ν is a quantization number.

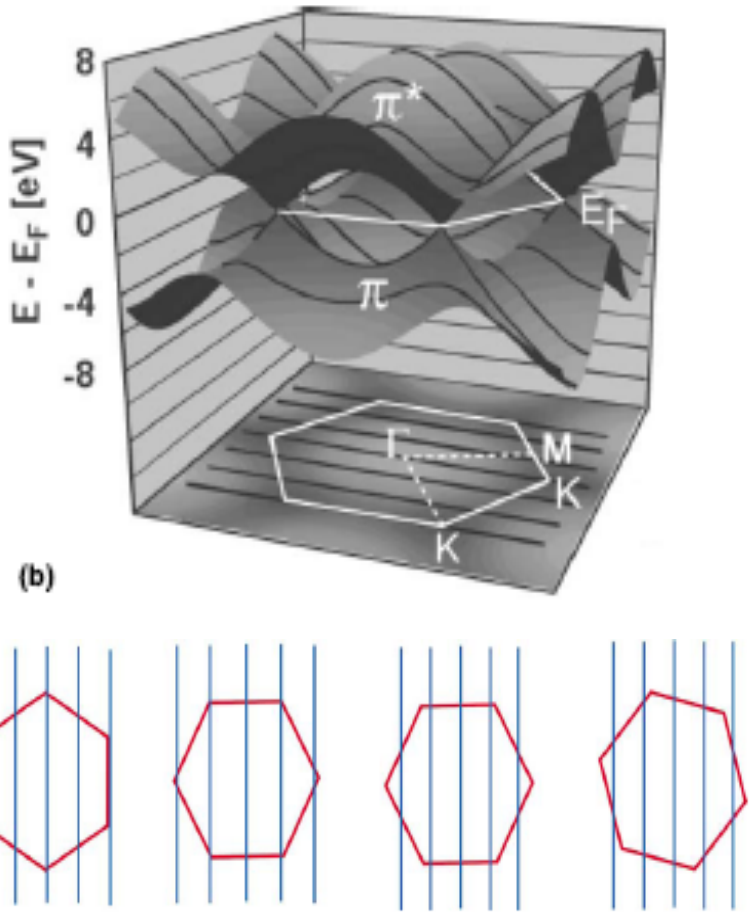

Figure 25: (Top) Electronic π and π^* bands of a graphene structure with the first Brillouin zone, BZ, of a (3,3) CNT (white lines). The allowed electronic states (black lines) shown intersecting the 1^{st} BZ at the K-points, passing through the Fermi points and indicating this CNT is metallic in nature. From [175]. (Bottom) The allowed electronic states of (from left to right) a (10,10) armchair metallic tube, (12,0) small band gap zigzag semiconductor tube, (14,0) semiconducting tube, and (7,16) semiconducting chiral tube. If an allowed electronic state intersects a K-point of the first BZ, then the CNT is metallic. If no allowed electronic state intersects a K-point, then the tube is semiconducting From [176].

If an allowed electronic state intersects one of the six vertices of the Brillouin zone at the K-points, it will intersect the Fermi Points and the CNT will be a zero bandgap metallic conductor with the Fermi level pinned to the band crossing [178].

If the allowed states do not intersect the Fermi Points, then the CNT will be a semiconductor with a finite bandgap.

Theory predicts that both armchair and zigzag CNTs should be metallic. In fact, any CNT where $n = m$ or $n+m = 3j$, where j is an integer, should be metallic. Armchair CNTs have been shown to be truly metallic, as described by theory. However, zigzag CNTs, which are predicted to have a bandgap of zero, actually have a very small band gap ($\sim$0.01eV). This is due to symmetry breaking through curvature of the CNT which induces an orbital rehybridization [182]. Although armchair CNTs are the only truly metallic CNTs with the symmetry necessary for zero bandgap, the very small bandgap of zigzag CNTs is almost unnoticeable at room temperatures. The opening of a bandgap due to symmetry breaking depends inversely on the square of the diameter, so the effect is very small for larger CNTs [174].

Armchair CNTs are truly 1D quantum conductors exhibiting ballistic electron flow (length of the CNT is less than the mean free path of the electron) and quantized conduction [183] with no energy dissipated in the CNT [184].

Semiconducting CNTs ($s-CNTs$) have a bandgap which is determined by the closest allowed electronic state to the Fermi Point [30]. This band gap, E_g is inversely proportional to the diameter (D) of the tube [5, 28] and is defined as

$$E_g = \frac{2hv_F}{\pi^2 D} \tag{29}$$

Where v_F is the Fermi velocity (velocity of electrons with E=E_F) in graphene ($\sim 1 \times 10^6$ m/s [185]) and h is Planck's constant.

This bandgap relation is inversely dependent on the CNT diameter and a 10nm semiconducting CNT would have an energy gap $E_g \approx$0.08eV. The bandgap of the tubes is independent of CNT chirality [173], though the transport mechanisms are

not well understood, especially compared to those of metallic CNTs (m − CNTs), which do not exhibit a bandgap [175]. It has been demonstrated that s-CNTs are natively p-doped due to oxygen sorption and are very sensitive to impurities, gases, and trapped charges [176, 175]. This can change the conductivity many orders of magnitude with only a small change in gas concentration as s-CNTs change from p-type to intrinsic to n-type semiconductors. For this reason, CNTs have shown great promise as gas sensors orders of magnitude better than current state of the art gas sensors.

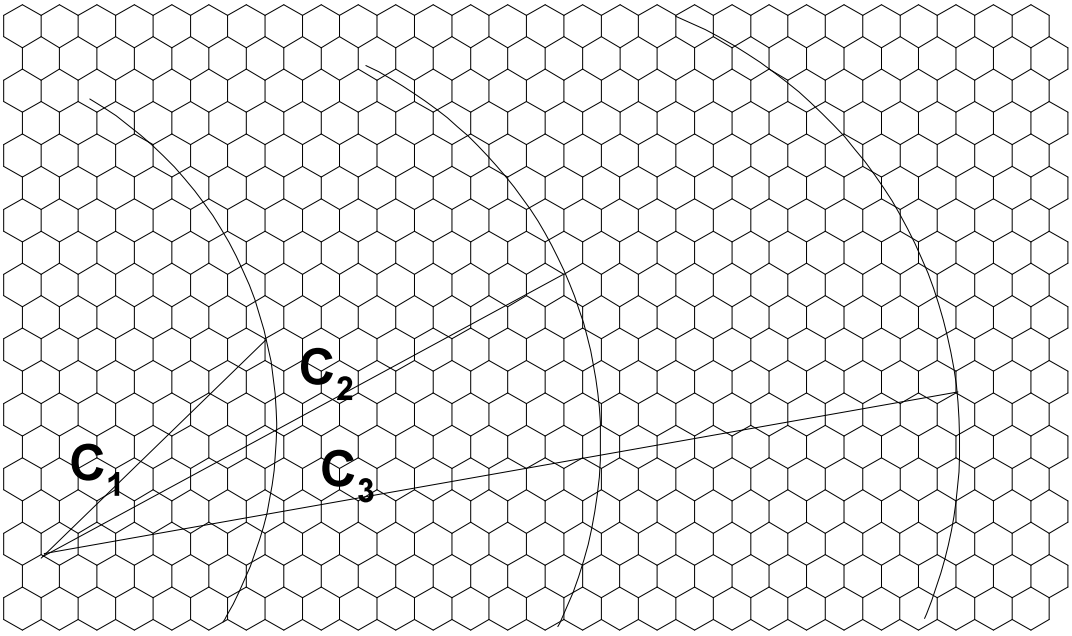

Figure 26: Successive CNT layers in a MWCNT showing the coupling of chiral angles in layers. Since the wall circumferences are fixed, only certain chiral angles are allowable

Although most of the theoretical and experimental work on charge transport has been done on SWCNTs due to their simple nature, MWCNTs are the majority of CNTs created using most experimental methods. The chiralities of CNT layers in MWCNTs are related to each other due to the fact that the circumference of each successive CNT layer increases by $0.34 \times 2\pi$ nm. This means that the chiral angles of shells are related and only certain chiral angles are allowable (Figure 26), although it is

unlikely that a carbon on one shell is commensurate with the carbon on a neighboring shell. It has been shown in TEM electron diffraction images where the number of chiral angles in a MWCNT is much less than the number of walls, indicating the possibility of sequential formation of MWCNT walls at a constant chiral angle and a relaxation of intershell distance until strain considerations force a change [162]. Two shells will have commensurate carbon atoms and thus will show interlayer coupling if the ratio translational vectors, T(n, m), of the two shells is a rational number [186]. Therefore a (9,0) CNT would couple with an (18,0) shell, but not with a (10,0) shell [174].

2.2.4 Electronic Conduction in CNTs

CNTs have been researched for use in electronic devices due to their unique properties. Theoretically, they are 1D room temperature ballistic conductors, meaning that the distance between scattering centers is smaller than the length of the CNT itself. Therefore no process alters the electron momentum and the resistance of the CNT is independent of length [174]. Due to the ballistic nature of the conduction, no heat is dissipated in the CNT and they are able to carry much higher current densities than other metals (10^9 A/cm^2 for CNTs compared to 10^6 A/cm^2 for Cu) [187]. They also do not suffer from electromigration degradation as do metallic wires. These unique properties make CNTs ideal for current carrying applications.

2.2.4.1 One Dimensional Conductors

Conduction occurs when an electron passes from a source to a drain. Resistance is caused when an electron's momentum is changed so that it is ejected from the source, but then is scattered back towards the source. In a macroscopic conductor, where the width, W of the conductor is large, this change in momentum may occur due to many small angle scatters which slightly alter the electron momentum until the momentum of the electron is completely reversed (Figure 27) [188]. The conductance (inverse of

resistance) of the system, G, scales linearly with the width of the conductor, following ohm's law.

$$G = \sigma \frac{W}{L} \tag{30}$$

The conductance is a function of is conductivity (σ), a material parameter, and W and L, which are defined in Figure 27.

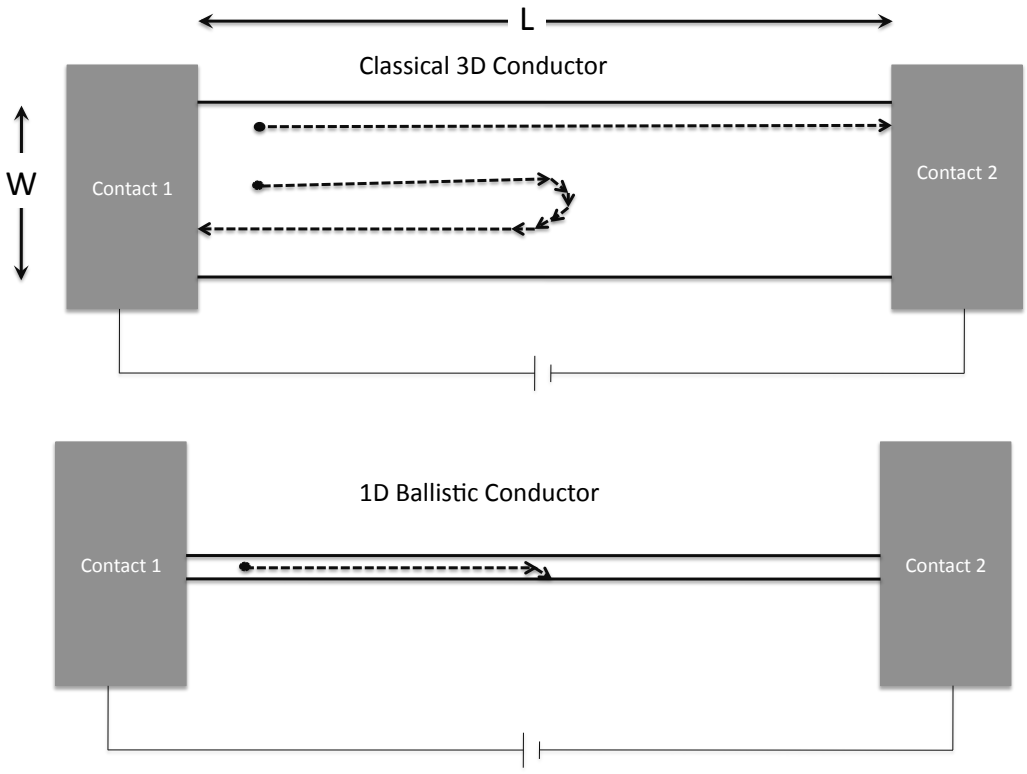

Figure 27: (Top) Resistance in a classic conductor of width, W, and length, L, occurs when an injected electron undergoes many small angle scattering events until it is backscattered back to the source. (Bottom) in a 1D conductor, small angle scattering is geometrically disallowed, and scattering must completely invert the momentum of the electron. In most systems, phonons with this much momentum are not present so electrons can pass through the entire length of the conductor without being scattered.

As W begins the approach the size of the deBroglie wavelength at the Fermi Energy, λ_F , the wavevectors are quantized and separated by $\frac{2\pi}{W}$ [174]. The conductance is no longer proportional to W, but depends on the number of available conduction bands. For an electron traveling in a 1D conductor, since there are constraints in two simultaneous directions, the only way an electron may be redirected back towards the source is by a single collision which totally reverses the electron momentum. The probability of this type of collision occurring is effectively zero in 1D systems because acoustic phonons, which are the primary scatterers in conductors do not carry enough momentum to completely backscatter an electron and optical phonons are too energetic for any significant population to exist at operating temperatures [189]. Since electrons are not scattered, the mean free path of the electron is longer than L, the length of the conductor [174].

For these 1D conductors, the conductance, G_C, does not decrease monotonically as W decreases, but in discrete conductance steps. In this 1D limit, the conductor becomes a ballistic conductor and its conductance is described by the Landauer Formula [190].

$$G_C = G_0 b \tau \tag{31}$$

Where b is the number of available conducting subbands inside the conductor, τ is the average probability that an electron injected into the conductor will transmit to the other end, and G_0 is the conductance quantum and is defined as

$$G_0 = \frac{2e^2}{h} = 12.9 k\Omega^{-1} \tag{32}$$

The relatively small value of conductance per conducting subband is due to the interface between the conductor and the contact. Scattering takes place at the interface because the current must redistribute at the contact/conductor interface as it transitions from the contact with a large number of available conduction bands to the 1D conductor with a very small number of available conduction bands [184]. No energy is dissipated in the conductor, only in the electrical contacts [183].

2.2.4.2 Conduction in SWCNTs

Due to their small size and quantization around the circumference, SWCNTs act as ideal 1D conductors [174]. The theoretical band structure of two zigzag CNTs (one a s-CNT with n,m=227, 0 and E_g=47.94meV and the other a m-CNT with n, m=228, 0) is shown in Figure 28. The bandstructures consist of many subbands with a separation inversely dependent on the diameter of the CNT.

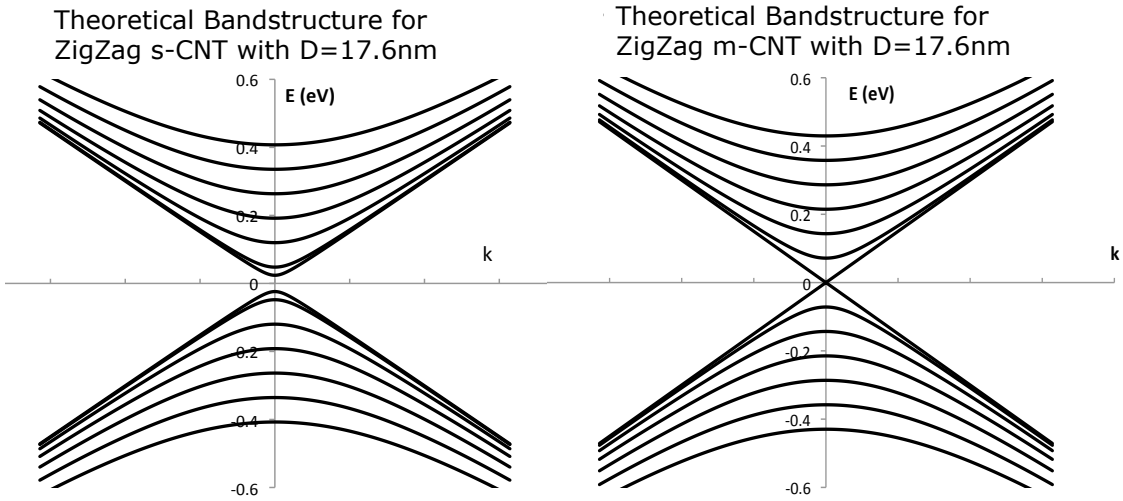

Figure 28: (Left) Ideal bandstructure and first 7 subbands calculated for a s-CNT with (n,m)=(227,0). The diameter of the tube is 17.6nm with an E_g of 47.94meV. The spacing of subbands is constant with increasing energy. (Right) Ideal bandstructure and first 7 subbands calculated for a m-CNT with (n,m)=(228,0). The first subband crosses E=0, so the CNT has no bandgap. At 0K and no applied voltage, the m-CNT would have a conductance of $2G_0$. The s-CNT would have a conductance of zero.

If the m-CNT and s-CNT described above are used as a wire with ohmic metal contacts (τ=1) at each end and held at a temperature of 0K, the E_F would be equal

to zero with no applied voltage. The conductance of the metallic tube would be $2 \times G_0$ (6.45kΩ). The conductance of the semiconducting tube would be zero because the E_F does not cross any subbands.

If a positive voltage difference is applied to the ends of the s-CNT, the value of E_F will decrease. For an applied voltage which is larger than the bandgap of the s-CNT, the subbands with a maximum energy greater than E_F contribute to conduction. The number of subbands contributing to conduction is approximately linear with applied voltage and the change in conductance for the s-CNT takes on a characteristic staircase pattern with the increase in each step having a value of $2 \times G_0$ (Figure 29). As the temperature increases from 0K, the square nature of the steps is rounded off as thermal promotion of carriers is taken into account.

2.2.4.3 Conduction in MWCNTs

While the conduction of SWCNTs has been more commonly studied due to their relative theoretical simplicity, the conduction of MWCNTs may be more useful for real-world applications. This is because MWCNTs are the primary result of the high throughput CNT growth methods necessary for inexpensive electronic devices.

There is much discussion in the literature over whether the inner walls of a MWCNT contribute to the transport properties. Statistically, an outer wall which is metallic has only a one in three chance of having a metallic nearest neighbor. Since the probability of high interlayer coupling is very low, metallic and semiconducting CNTs of different chiralities are predicted to have only a weak interlayer coupling between layers independent of all non-adjacent layers [177]. The presence of interior semiconducting tubes in MWCNTs is predicted to have no affect on the current transport of the CNT and current is relegated to the outside walls only [183, 191, 192, 193].

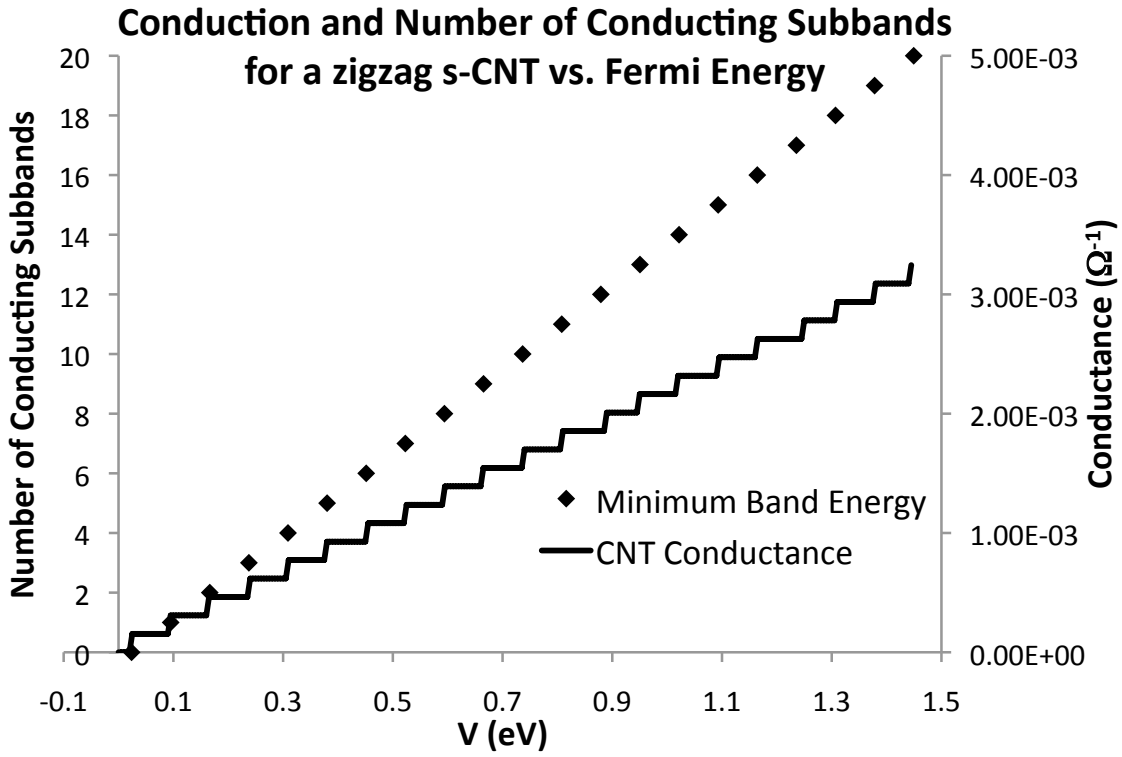

Figure 29: Number of conducting subbands for a s-CNT with D=17.6nm and E_g=47.94meV vs. applied voltage. The spacing of subbands is constant with energy. As the applied voltage is increased, the E_F decreases and more subbands begin to conduct. Each conducting subband increases the CNT conductance by a value of $2G_0$. As voltage is increased, the conductance of a CNT will take on a stairstep pattern with the rise being equal to $2G_0\Omega^{-1}$ and the flat equal to $3E_g/2$eV

There have been other studies, however, which have demonstrated that current conducting in MWCNTs occurs through multiple semiconducting and metallic layers [175, 194] even in the low bias regime [195]. These experiments show a stair step pattern in the current (Figure 30) at high voltages as the MWCNTs thin due to shell failure [194].

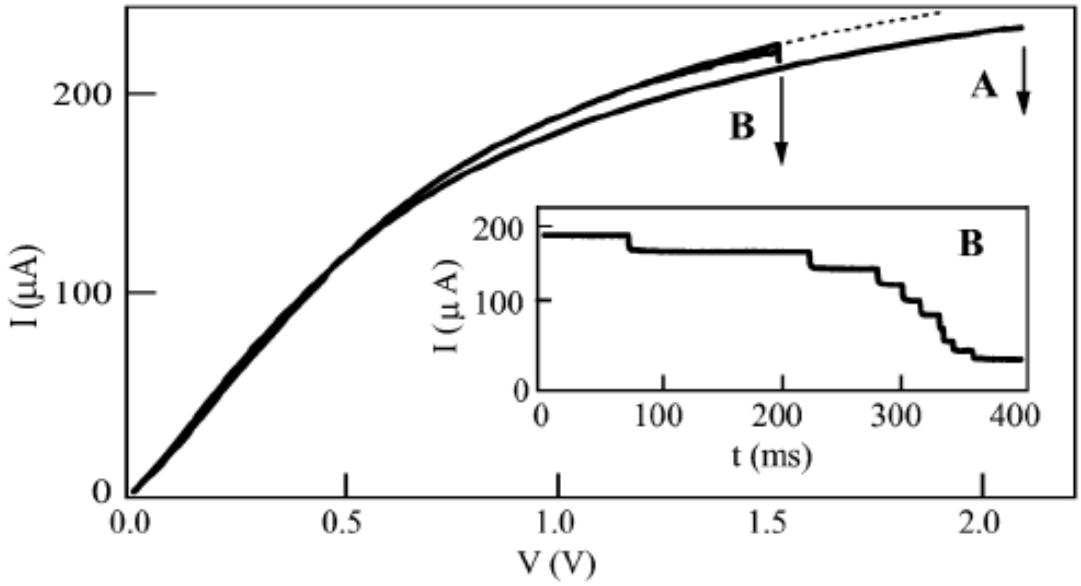

Figure 30: IV curve on a single 8μm MWCNT which demonstrates current transport in multiple layers. Steps (inset) of $\sim$12μA can be seen as individual layers fail and the MWCNT thins. From [194].

The reason for the ambiguity in these results is probably due to sample preparation. Transport properties are highly dependent on CNT preparation conditions, purity, presence of defects, and any residual solvents present [174]. The activation energy of transport in MWCNTs has been found to be 21meV for oxidatively purified MWCNTs, which is less than the $\sim$80meV bandgap of the MWCNTs studied [196]. The low barrier to conduction is caused by thermally activated interlayer hopping between layers, allowing electrons to move from the outer to the inner walls [197]. This interlayer hopping is actually facilitated by defects in tube walls as they allow short circuit pathways from one tube to the other. Compared to the E_a for current

transport in purified MWCNTs of 21meV, in as-grown MWCNTs with defects, the E_a was found to be only 5meV as electrons were easily able to hop from wall to wall through defects. This small activation energy means that most walls in a MWCNT should conduct even at very low biases, though due to the amount of defects, the conduction is not ballistic and energy is dissipated in the tube, eventually resulting in the shell failure seen in Figure 30.

Although defects may allow for intershell hopping as a mode of conduction, it also destroys ballistic conduction. For a defect-ridden CNT, assuming an equally spaced distribution of scattering centers over the entire CNT length with each defect having an electron transmision of τ, the total transmission may be described by

$$\tau = \frac{L_o}{L_o + L} \tag{33}$$

In this equation, L_o is on the order of the mean free path of an electron and L is the total length of the CNT. For $L \leq L_o$, the conduction is ballistic. For $L \geq L_o$ the conduction is ohmic and decreases with length. In CNTs, the mean free path of an electron has been found to be approximately 1μm [198].

Interconnect applications of CNTs typically use bundles of CNTs. These bundles tend to have a gaussian distribution of sizes with 33% m-CNTs and 66% s-CNTs. Naeemi et. al. [199] and Haruehanroengra et. al. [200] have both discussed the conductivity of MWCNT bundles at great length. These works assume that electrical contact is made to each shell in a MWCNT bundle and the applied voltage to the MWCNT bundle is low enough to so that only the first subband is conducting. By integrating over all of the available conducting subbands in all available shells of the MWCNTs, it was found that densely packed MWCNT bundles outperformed similarly sized Cu wires for lengths greater than L_o.

Figure 31 shows the conductance vs. length of densely packed SWCNT and various diameter MWCNTs compared to copper wires. For CNT lengths greater than L_o, the conductivity of the CNTs is greater than the Cu wire. For interconnect applications, the longer the channel, the larger the CNTs desired. At interconnect lengths greater than 50μm all CNTs have a greater conductance than traditional Cu wires. These works provide a low estimate for the use of CNT interconnects in solar cells and other devices because the increased operation voltages mean numerous subbands are involved in conduction. This will increase the CNT conduction to even larger values.

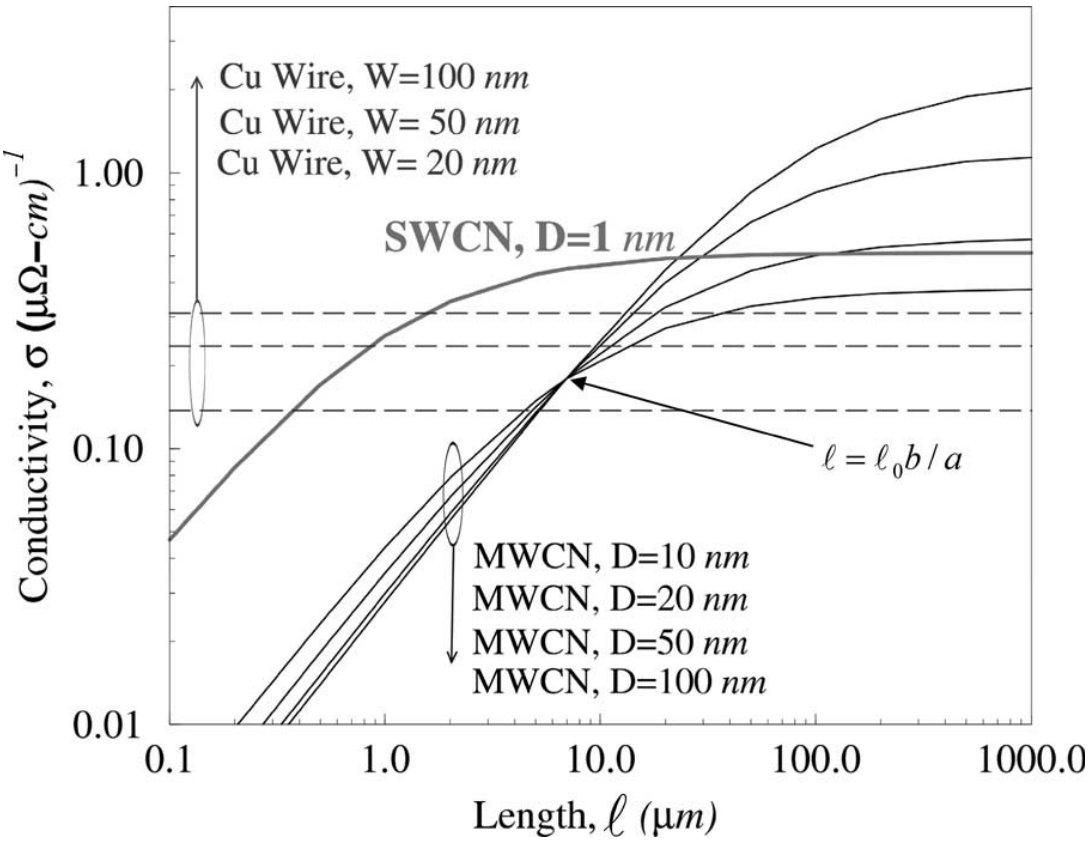

Figure 31: Conductance vs. length for a bundle of SWCNTs with diameter of 1nm, MWCNTs with diameters from 10-100nm, and Cu wires of widths of 20-100nm. The arrow indicates the crossover point between ballistic and ohmic conduction for the CNTs. For longer interconnect lengths, larger MWCNTs are desired. However, for lengths greater than 50μm all CNTs have greater conductance than the Cu wires. From [199]

Although real CNT bundles used in devices may not exhibit ballistic conduction for lengths above the micron scale, they are still very promising for a variety of device and interconnect applications. Experiments have shown that for even defect laden MWCNTs the electric transport properties exceed those of SWCNTs and metal conductors [201] with extremely high current densities $\sim 10^8$-10^9 A/cm^2 [183]. The unique properties of CNTs highlight the possibility of using SWCNT or MWCNT conduction bundles in various microelectronics applications [175].

2.2.5 CNT Synthesis

CNTs have been shown to be produced in an extremely large number [9] of manufacturing processes (Carbon-arc discharge, laser ablation, CVD, PECVD, etc) with a number of metal catalysts and temperature ranges.

2.2.5.1 Chemical Vapor Deposition

Of CNT production methods, plasma enhanced chemical vapor deposition (PECVD) or thermal CVD are the synthesis methods with the most easily controlled parameters and ability for manufacturing related scaleup and throughput. CVD produces a majority percentage of MWCNTs in large quantities. They are characterized by a high density of defects (small-angle twist boundaries and sidewall pentagons and heptagons introducing positive and negative curvature, respectively [172]) and lengths up to the millimeter range [176].

Thermal CVD (Figure 32) is a method which utilizes the pyrolytic decomposition of hydrocarbon feedstock gases at temperatures ranging from 550-900^{o}C (850-1000^{o}C for SWCNT due to their smaller size, lower defect density, and higher strain energy [176]). The hydrocarbon gas, usually ethylene (C_2H_4), methane (CH_4), or acetylene (C_2H_2) is flowed into the furnace chamber under a reducing atmosphere (necessary so the metal does not oxidize, possible in even a 10^{-6} Torr vacuum [202]). A thermal heat source provided by plasma flame or heated coil decomposes the feedstock into its

carbon and hydrogen components. CNTs then form on a substrate coated with metal catalyst. Cobalt, nickel, and iron are the only pure metals which have been found to produce CNTs. Alloys of these metals are also suitable catalysts [203]. Growth yield, rate, and morphology can largely be controlled by varying temperature, gas flow, metal catalyst, or precursor gases. The as-grown CNTs can then be purified to remove amorphous carbon and leftover catalyst through oxidation, acid wash, or solvent wash and then annealed in an inert gas atmosphere at $T > 2500^o$C to remove defects.

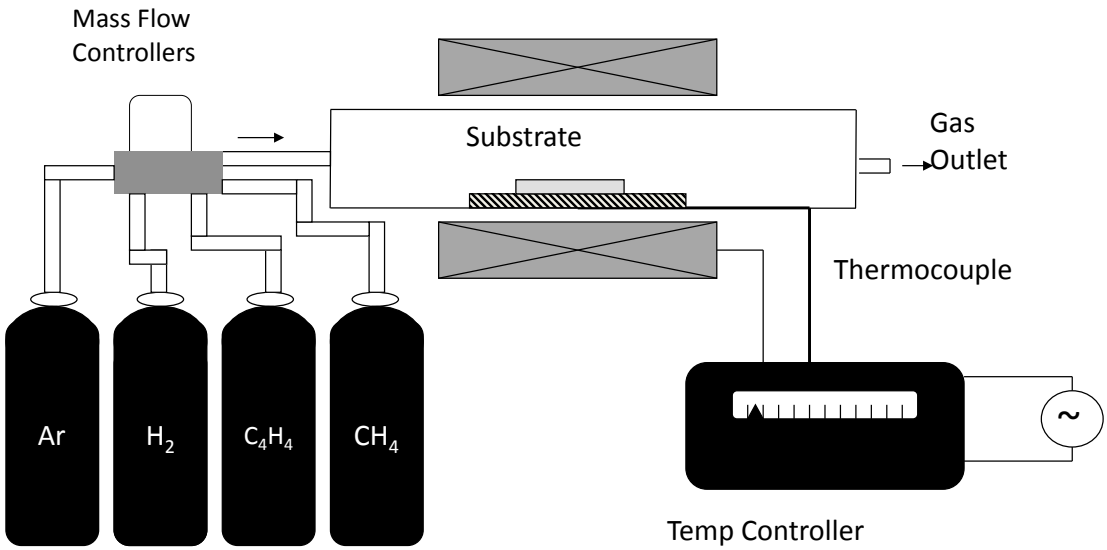

Figure 32: Schematic of a thermal CVD setup for pyrolytic decomposition of carbon feedstock (C_4H_4 and CH_4) to form CNTs. The carrier gas is Ar while H is used as the reducing gas.

PECVD uses high energy electric fields to force CNT growth in a certain direction. A plasma, consisting of an ionized and rarified atmosphere of hydrocarbons is formed through RF, microwave, or DC bias [204]. As the hydrocarbons break down, they are assembled on a substrate in the form of CNTs preferentially grown in the direction of the electric field of the plasma. PECVD not only has the advantage of alignment of single CNTs and low defect density, but since only the plasma is energized, growth can occur at low ($<300^o$C) temperatures, allowing for CNT growth on glasses and

plastics [205]. This method will be of increasing importance as CNTs are incorporated as field emitters in viewing displays and electronic interconnects, two applications which require low temperature synthesis.

2.2.6 CNT Growth Mechanism

The two proposed mechanisms of CNT growth are tip growth and root growth (Figure 33). Many studies show a tip growth method [167, 206, 207, 208]. They argue that base growth methods are unstable and a catalyst particle must be present at the tip to stabilize dangling bonds and that if CNTs form in highly packed structures then the hydrocarbon feedstock cannot reach the bottom and that even and linear growth as is observed would be unlikely [31, 51]. There is a similar amount of SEM and TEM evidence for root growth [206, 209]. The method of growth and their relative percentages seems to be dependent on growth equipment and parameters, including substrate/catalyst adhesion.

In CVD production, both methods of growth, base and tip mode, start with the same three steps. First, the temperature is ramped, and the metal catalyst layer forms nanoscale droplets. The nanoscale formation does not occur necessarily through melting, but through strain relief [210]. If the catalyst metal is actually melted, the mobility on the substrate surface becomes too high and the droplet size increases through Ostwald ripening, eventually creating non-nanoscaled catalyst particles which form graphite, not CNT, structures [187]. The hydrocarbon feedstock is then dissociated into carbon and hydrogen. The carbon dissolves into, and forms a saturated solution with the metal nanoparticle before it precipitates in CNT form. The growth continues through addition of small C−C particles until the catalyst

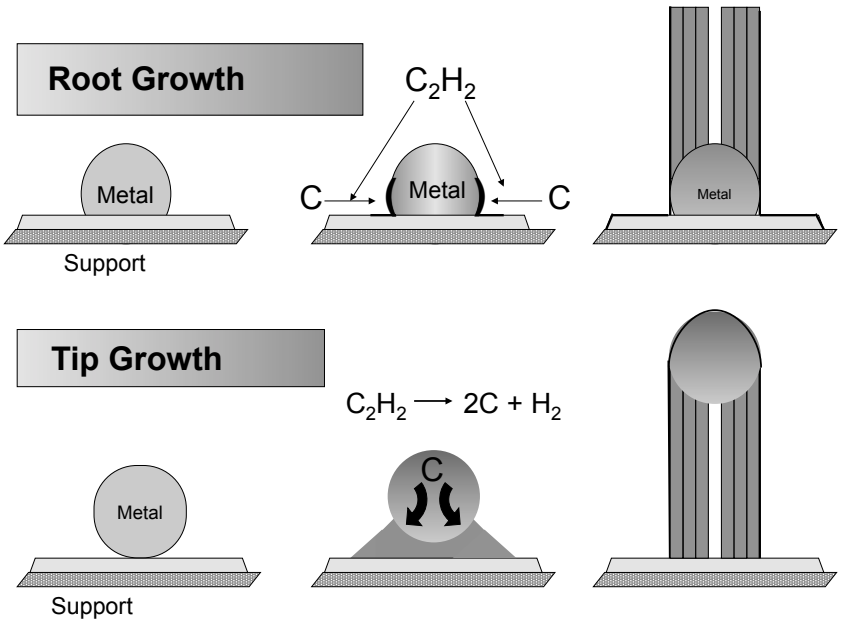

Figure 33: Schematic of the two mechanisms for CNT growth on a catalyst bed. (Top) Good adhesion between the catalyst nanoparticle and substrate results in a CNT being extruded from the top of the catalyst nanoparticle. Since the nanoparticle remains at the base of the CNT, this process is known as root growth. (Bottom) Poor adhesion between the catalyst nanoparticle and the substrate results in the CNT being extruded from the bottom of the catalyst nanoparticle. Since the nanoparticle remains at the CNT tip as the CNT grows, this process is known as tip growth. From [167].

particle is eventually poisoned by impurities or stable carbide formation [172]. It is thought that Fe, Ni, and Co catalysts are the preferred transition metal catalysts because at high temperatures they have a finite solubility for carbon and form a solid state solution. Tubule formation is favored for small carbon structures (< 1000 C atoms) over graphene sheets for energetic reasons [180].

Potential energy calculations done by Sinnott et al. have shown that for structures of less than 1000 C atoms, CNTs are the stable form of carbon due to the large density of dangling bonds. By wrapping a graphene layer into a tube and eliminating the dangling bonds along the outside, the overall energy of the system can be decreased. CNT stability increases with length and number of shells with little regard to chirality [179] due to increased Van der Waals forces. As the number of carbon atoms grows, the strain of the CNT increases. From 1000-6000 carbon atoms, graphene is the stable form of carbon due to the constantly decreasing fraction of edge atoms and constantly increasing strain energy [180].

It has been shown that both the diameter of CNTs and growth rate are a function of size of the metal catalyst particles [211, 206] , the former due to physical capping of the CNT and latter due to a shorter carbon diffusion length as shown by an inverse square root relationship between growth rate and particle size [167, 211, 212]. The size of the catalyst particle can be changed by varying the parameters of the system. Several studies have shown that it is possible to control the diameter of CNT formation through the thickness of the metal catalyst film [211, 208], the use of a reducing pretreatment step such as NH_3 or H_2 [202, 213] or the control of the Fe:C ratio in the catalyst bed [180].

2.2.7 Vertical Alignment of CNT

Vertically aligned growth of single CNTs or blocks of CNTs has been aggressively pursued in CNT research due to its numerous industrial uses for organic PV devices,

field emission displays, and gas sensors. Vertically aligned CNTs (VACNT) were first fabricated by Fe nanoparticles on porous silicon wafers. The CNTs grew out of the pores, but only those CNTs growing from vertically directed pores were not sterically hindered by the growth of neighboring CNTs [94]. Today the growth of VACNTs occurs through two main modes. The first is through the patterning of catalyst islands through photolithography or similar technique. Catalyst islands can be patterned in any type array or column shape through the use of lithography or some other etching technique in scales as small as a few microns (Figure 34). The CNTs form a rigid bundle through Van der Waals forces. This bundle of CNTs is vertically self aligning because it sterically hinders CNT growth in non-vertical directions [176, 206]. This method is known as a CNT forest or carpet. The other technique for forming aligned CNTs is the use of PECVD which preferentially grows CNTs in the direction of an applied electric field. In this way single CNTs can be grown for use with field emission displays.

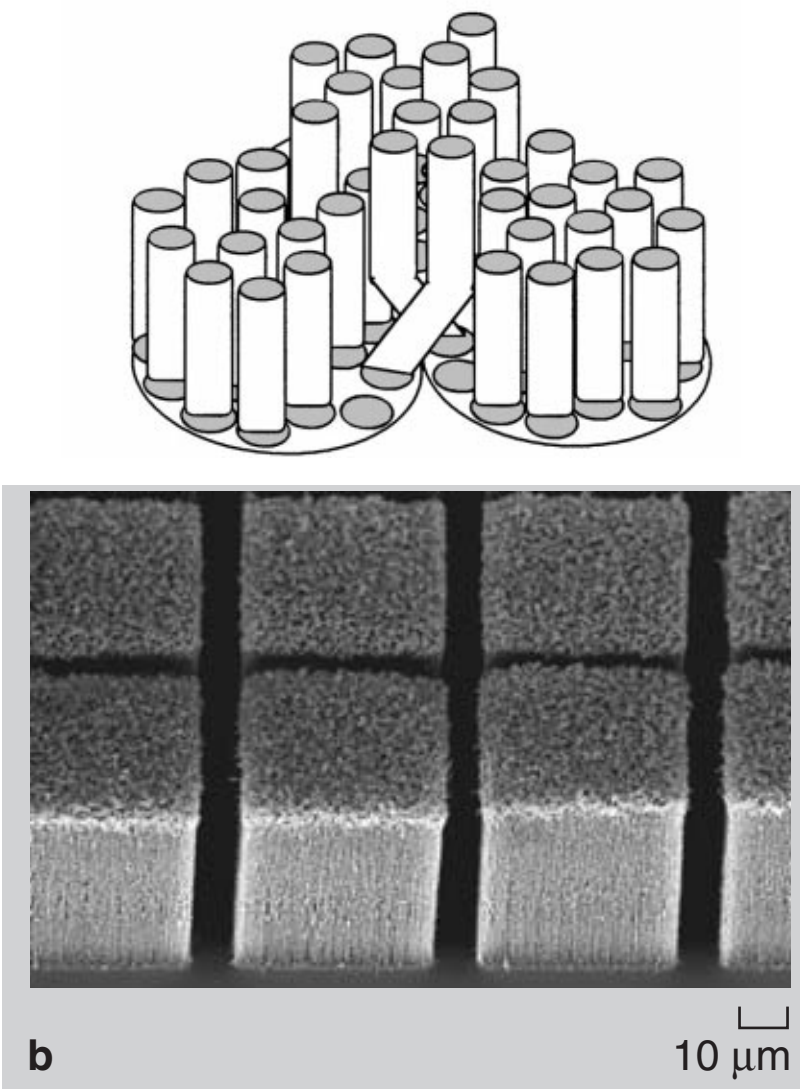

Figure 34: (Top) Schematic of VACNT growth through Van der Waals forces and steric hindrance. The general direction of growth of the CNT film is vertical. Individual CNTs may grow in non-vertical directions, though they eventually run into competing growth from other CNTs. From [206]. (Bottom) A rigid self-orienting film VACNTs patterned into blocks through lithography. From [148]

2.3 Introduction to 3DCNTPV cells

3DCNTPV devices consist of a conductive Si wafer substrate, on top of which are grown vertically aligned arrays of CNTs. These CNTs act as the back contact to the CdTe semiconductor (or other semiconductor material) and provide the three dimensionality of the cell. On top of these towers is deposited a CdTe/CdS heterojunction and a top contact of ITO (Figure 35). The main advantages of this type of substrate configuration cell are (1) the utilization of multiple photon impingements and (2) the decoupling of the carrier generation and extraction processes.

In traditional planar cells, a photon which is incident on the surface is either reflected, in which case it travels back off to infinity, or it is absorbed, in which case it is added to the photocurrent produced by the cell. There is only one interaction with the photoactive layers per photon and the maximum photocurrent occurs when the solar flux is coincident with the normal of the solar cell surface and falls off as a cosine function as the solar flux subtends off-normal angles. Many different things have been done in order to avoid this disadvantage inherent in planar cells including etching, texturing, and anti-reflectance coatings. However, these processes add either significant processing costs or make use of harmful caustic solutions [214, 215].

The topography added by the VACNTs allows for multiple interactions between a photon and the solar cell surface. When the solar flux is orthogonal to the solar cell surface, the apparent height of the CNT towers is zero, so there is no difference between the morphology of the 3DCNTPV and planar devices. In this configuration, the planar cell power output is at a maximum. As the solar flux subtends different angles throughout the day, the apparent height of the VACNTs increases. This non-zero height allows multiple reflections by a photon off the parallel faces of neighboring towers. This "pinball" effect means that if a photon is reflected from the solar cell surface, there may be multiple other interactions and chances for absorption. Therefore, while a planar cell has a power output which monatomically falls from a

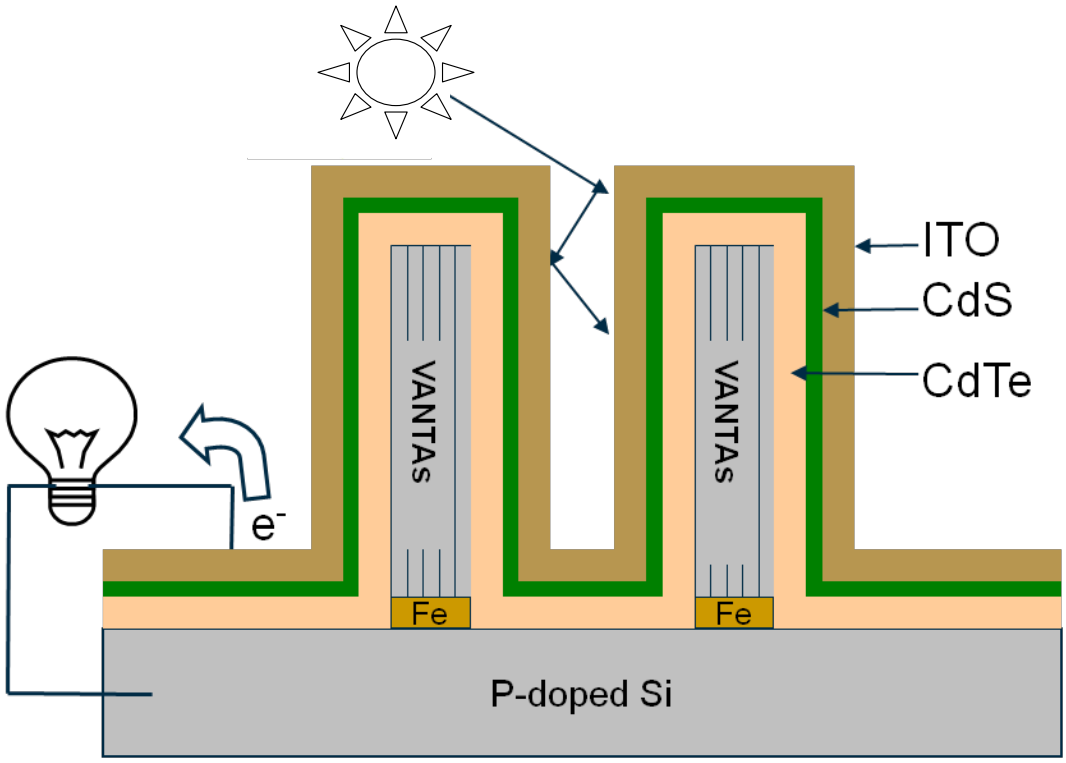

Figure 35: Schematic for a 3DCNTPV cell. The cell utilizes vertically aligned CNT towers as a back contact and three dimensional scaffolding. A CdTe/CdS heterojunction is deposited on these towers followed by a top contact of ITO. This three dimensionality allows for multiple photon impingements as the photons "pinball" between parallel faces of the towers, thereby increasing the power output over traditional planar cells.

maximum, a 3DCNTPV cell should have the same power output when the solar flux is coincident with the substrate normal, but have an even higher power output as the solar flux makes some off-normal angle with the solar cell surface.

3DCNTPV devices are grown in a substrate configuration. This means that they have a higher specific power and a more cost effective process flow than similar cells made in the planar superstrate configuration. This also means that virtually any semiconductor material can be used to coat a 3DCNTPV cell. So, while in this work, a CdTe/CdS heterojunction is used to coat the VACNTs, other semiconductor materials such as GaAs, a-Si, QDs, and polymers can be used.

3DCNTPV cells have a greater energy output than planar cells with a similar efficiency. Planar cells have their highest power output when the solar flux is coincident with the substrate normal. Power generation falls off monatomically as the solar disc subtends different angles. For 3DCNTPV cells, the power output at off-normal angles is always greater than that of a 2D cell with a similar efficiency. The maximum power output occurs when the solar flux is at an off-normal angle. This greater power output at different angles means that, as the sun subtends all angles throughout the day, more energy is produced from the 3DCNTPV cell than a similar planar cell.

Due to this greater energy generation, 3DCNTPV cells have no need for the orientation machinery used to orient solar cells to a maximum power position. The elimination of this orientation machinery decreases the cost of the cells both for terrestrial and extraterrestrial uses. For terrestrial systems, the orientation machinery is a large part of the balance of system cost. In extraterrestrial uses, the orientation machinery consists of a large percentage of the weight, and therefore the launch cost, associated with the energy producing solar panels.

CHAPTER III

EXPERIMENTAL PROCEDURE

The process flow to create a 3DCNTPV device includes a positive photolithography step, CNT growth, catalyst deposition, semiconductor deposition, and finally deposition of a transparent top contact (Figure 36).

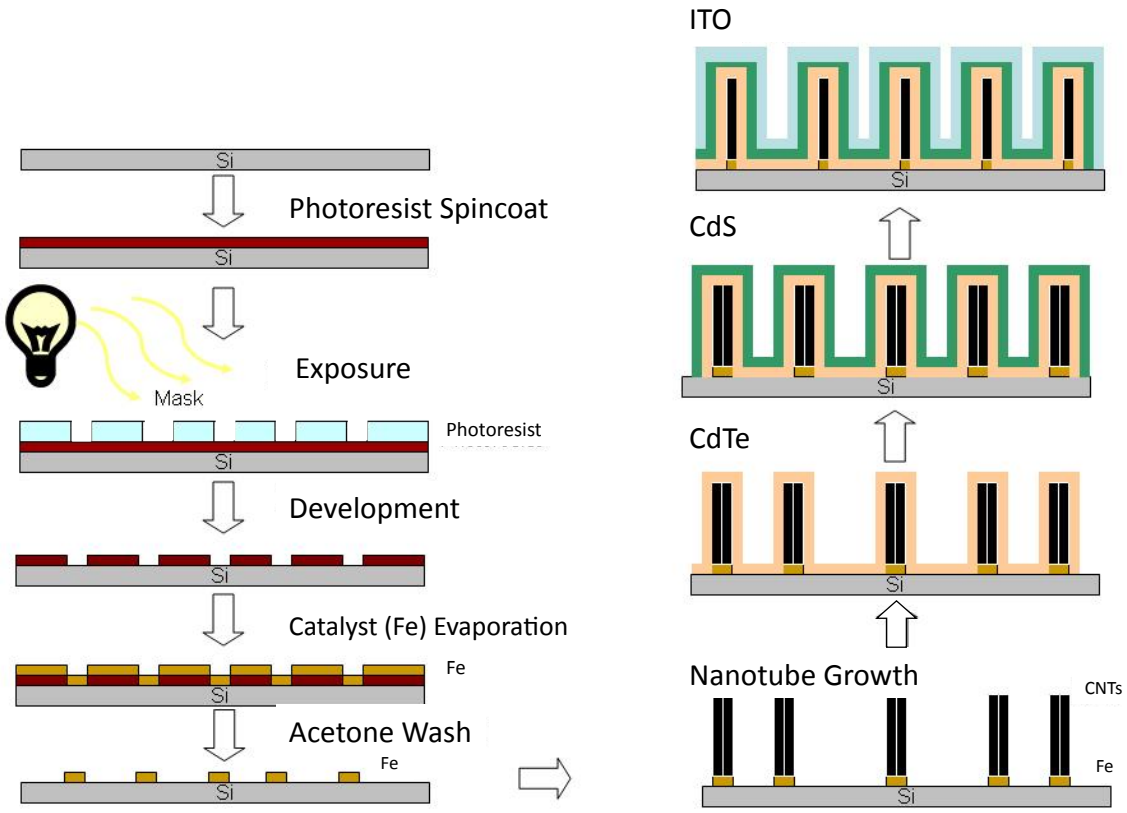

Figure 36: The process flow for creating a 3DCNTPV cell. Photoresist is spincoated on a p-type low resistivity Si wafer. That resist is then exposed and developed. Iron catalyst is evaporated on the wafer and the excess Fe and photoresist are removed by acetone wash. CNT are grown via thermal CVD. The CdTe/CdS heterojunction is then deposited on top of the CNTs and the top contact is made with ITO.

3.1 Photolithography

In order to create patterned arrays of CNTs, positive photolithography is carried out on a heavily p-doped Si wafer (University Wafer; Boston, MA) with a resistivity of 47.5-66.4 mΩ/cm. This wafer acts as the back contact for the 3DCNTPV solar cell. A p-type wafer is required as a contact to the p-type CdTe layer. If an n-type wafer were used, the n-Si/CdTe/CdS would form an npn-transistor type structure. A second depletion region would originate at the n-Si/CdTe interface and no current could flow at low voltages.

Photolithography takes place in a class 10 cleanroom. The Si substrate is first serially cleaned with trichloroethanol, methanol and de-ionized (DI) water. The wafer is then blown dry with dry nitrogen gas and baked at 95^{o}C for 5 minutes to ensure solvent evaporation. Microchem Photoresist 1818 (Newton, MA) is spincoated onto the wafer at 5000 rpm for 25 seconds before the substrate is softbaked at 95^{o}C for 25 minutes.

After the softbake, the substrate is patterned with the desired chrome darkfield mask and exposed to ultraviolet light from a Karl Suss MJB (Garching, Germany) exposure system for 6 seconds at a power density of $274mW/cm^2$. The patterned wafer is then immediately soaked in chlorobenzene for 10 minutes. After the soak, the wafer is blown dry with nitrogen gas and baked at 95^{o}C for an additional 10 minutes.

The wafer is then developed in a mixture of 140mL DI H_2O and 40 mL Microchem Developer AZ 351. The developer is agitated during the developing process for 60 seconds before the wafer is vigorously washed with DI H_2O to stop photoresist development. The wafer is then visually inspected via a Olympus AH2 (Tokyo, Japan) optical microscope with orange light filter. If the pattern is fully clear and developed, the wafer is then taken for catalyst deposition. If the pattern is not fully clear and developed, the wafer is developed for an additional 20 seconds or until it is clear.

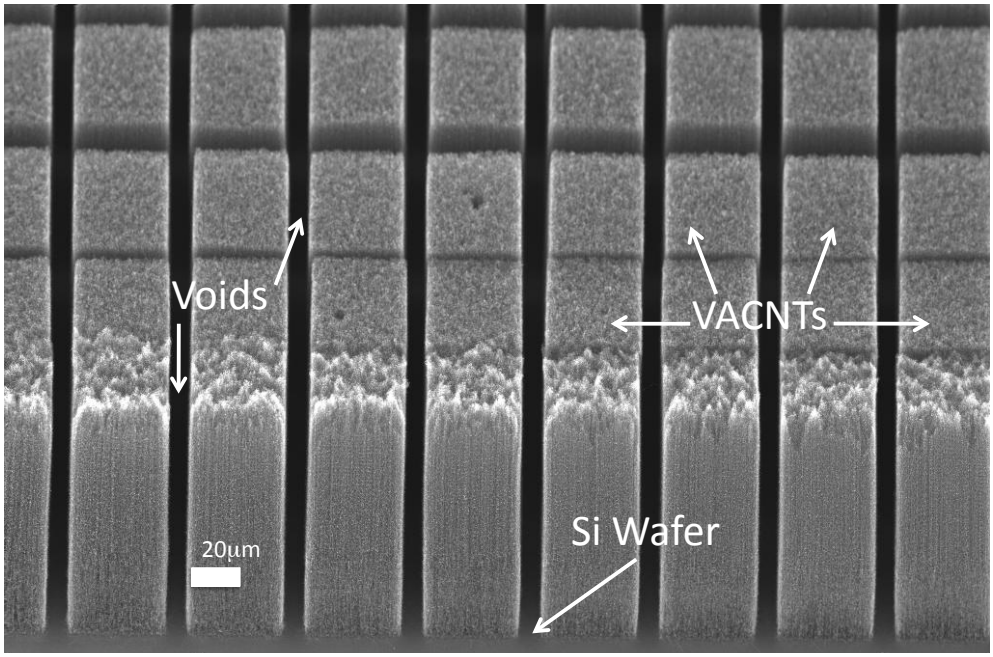

Figure 37: CNTs grown from a photolithographically patterned Si wafer patterned in a series of repeating blocks. The blocks of VACNTs are 40μm$\times 40\mu$m with 10μm between each block.

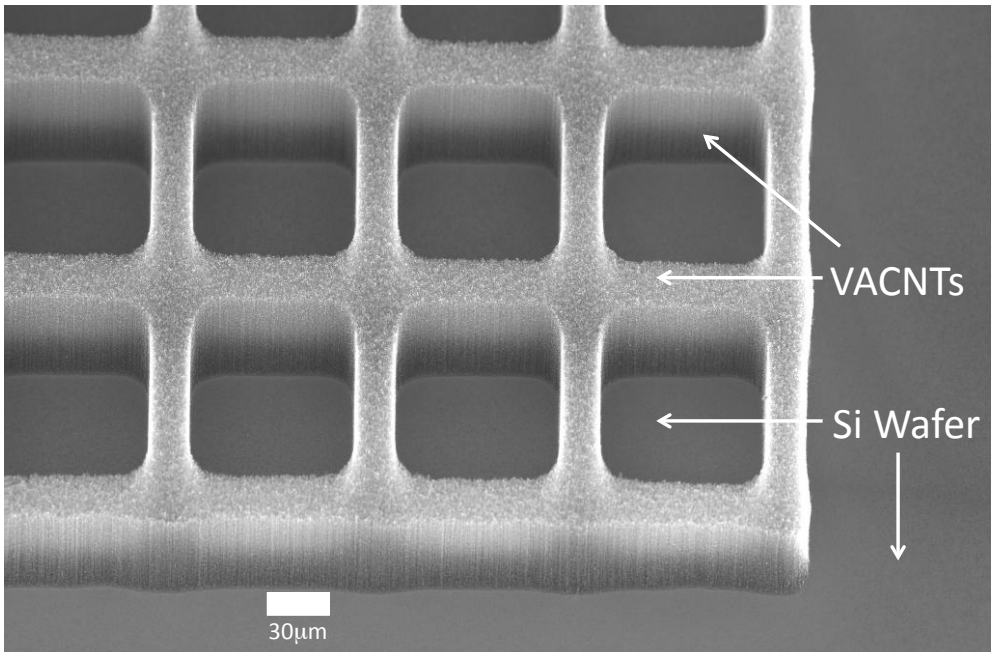

Figure 38: CNTs grown from a Si wafer with Fe catalyst patterned in a waffle pattern. The VACNTs on the crossbars have a thickness of 25μm. The pores where no CNTs are grown is 75μm$\times 75\mu$m

There are two complementary patterns which are used in the production of the 3DCNTPV. The first is a pattern of repeating blocks (Figure 37). Each block is 40μm$\times 40\mu$m and is separated on each side from the next block by a 10μm pitch. The pattern permits CNTs to be grown inside the blocks, but not in the 10μm inter-block spaces. When completed into a cell, the active area of this pattern is 1.2cm $\times$ 1.2cm.

The second pattern is a waffle pattern (Figure 38). This pattern is a near negative image of the block pattern. Photolithography allows CNTs to be grown between blocks while CNTs are prevented from being grown in the blocks themselves. In this pattern, the blocks are 75μm $\times$ 75μm and the inter-block spaces where CNTs are grown are 25μm. The active area of this type of cell is 0.75cm $\times$ 0.75cm.

3.2 Catalyst Deposition

After successful photolithography on the wafer, A nanoscale iron catalyst film is deposited via thermal evaporation using a Denton Vacuum (Moorestown, NJ) DV-502 system (Figure 39). This system pairs a mechanical pump and water cooled diffusion pump to reach a base pressure in the 1×10^{-7} Torr range. The pressure is measured via two Hastings thermocouple gauges, the gross for pressures greater than 1 mTorr and the fine for pressures in the range of 1×10^{-4} to 1×10^{-7} Torr. The DV-502 system can operate with a voltage between the electrodes of 0 to 24 volts and a total apparent power of 1kVA.

The source iron used is 0.005" diameter 5N (99.999%) purity wire from ESPI Metals (Ashland, OR). 0.01 grams of Fe is measured out using a Mettler (Columbus, OH) AE260 analytical balance with sub-milligram resolution.

The filament used in the evaporator is a tungsten 4 coil filament made of a twist of 3 wires and measuring 4" long from Kurt J Lesker (Clairton, PA #EVF23030W). The Fe wire is twisted around the center of the filament as tightly as possible in order

Figure 39: (Left) Denton DV-502 thermal evaporator system used to thermally evaporate Fe wire onto a Si substrate to create an Fe catalyst film. (Right) Interior of the Denton system belljar showing electrodes with tungsten 3-wire filament and rotating stage assembly.

to approximate a point source. The wire wrapped filament is then placed between the electrodes of the Denton DV-502 system and the wafer is placed on the stage.

The bell jar is lowered and the system is pumped down to at least 4×10^{-6} Torr. To evaporate the wire, the sample stage is set to rotate at 100 rpm and the voltage is turned on and ramped up to 12V over 3 seconds. The voltage is then held at 12V for an additional 3 seconds before quickly being brought to zero. After a period of time to cool, the system is vented and the wafer is removed.

Liftoff of the unexposed photoresist is accomplished by soaking in acetone and agitating via a sonicator for 15 minutes. The wafer is then diced into single samples measuring approximately 1cm^2.

3.2.1 Results of catalyst deposition

The above procedure was used to determine the catalyst deposition thickness by measuring the thickness with a Veeco (Plainview, NY) NT2000 optical profilometer. The profilometer was calibrated with an optical flat and has a resolution of 3$\mathring{A}$. Data was taken in phase shift interferometry mode with a modulation threshold of 7, a vibration detection of 7, and a signal averaging of 5 scans. The results (Figure 40) were analyzed by composing a histogram of the averaged data. The results of the optical profilometry scans show an average thickness of 14.74±1.77nm, which is in good agreement with calculations of a point source in this system configuration (radius = 7cm, vertical distance = 5cm).

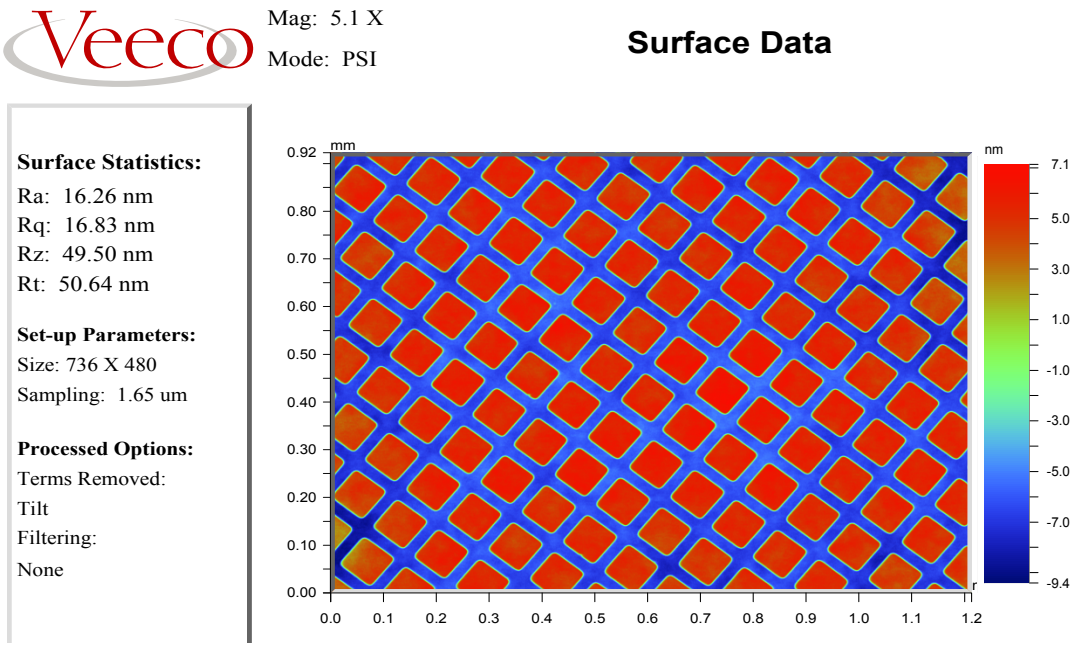

Figure 40: Single scan from optical profilometer using phase shift interferometry showing a block pattern of iron. For this scan, the iron deposition thickness is approximately 16nm.

3.3 CNT Growth

CNTs are grown on the single samples via thermal CVD using a First Nano Easy Tube 1000 (ET1000) system (Figure 41) by the CVD Corporation (Ronkonkoma,

NY). The Easy Tube 1000 is composed of an insulated 2-inch quartz tube furnace with a mechanized quartz loading platform. The ET1000 is capable of reaching temperatures of 1200^{o}C with a 0.6^{o}C accuracy, measured via thermocouple, using multiple resistive heating coils. The maximum heat rating is 73.33^{o}C/min.

Gas cylinders are supplied by Aigas Inc. (Radnor Township, PA). The ET1000 has four gas inputs controlled by MKS (Andover, MA) #2179 mass-flow controllers. These controllers are normally closed and are controlled by nitrogen (NUHP300 5N purity) with a flow accuracy of 1%. The carrier gas utilized is argon (ARUHP300 5N purity). Hydrogen (HYUHP300 5N purity) is used as the reducing gas. Methane (MEUHP300 5N purity) and acetylene (ACAA5 2N6 purity) are used as the carbon feedstock gases.

Figure 41: The First Nano Easy Tube 1000 system by the CVD Corporation. The system is composed of an insulated tube furnace with a mechanized loading platform. The temperature and gas rates are controlled by a computer running Labview. The system utilizes Argon as the carrier gas, hydrogen as the reducing gas and acetylene and methane as the carbon feedstock.

The operation of the mass-flow controllers and heating coils is accomplished through a computer running the Windows 2000 environment with a National Instruments (Austin, TX) Labview program. This program is packaged with the ET1000 from CVD Corp.

The recipe used grows CNTs at 820^{o}C and is called AcUHYCNT820. The program consists of four stages (Figure 42), a temperature ramp from ambient to 820^{o}C under 1000 standard cubic centimeter (sccm) Argon flow, followed by a constant temperature soak. During the soak period, a mixture of acetylene, methane and hydrogen gasses at 120, 1000, and 500 sccm, respectively, is fed into the chamber. After a thirty minute soak at 820^{o}C, the chamber is quenched to 676^{o}C in ten minutes under a 1000 sccm flow of Argon. The chamber is then allowed to cool to room temperature with no gas flow and the samples are removed.

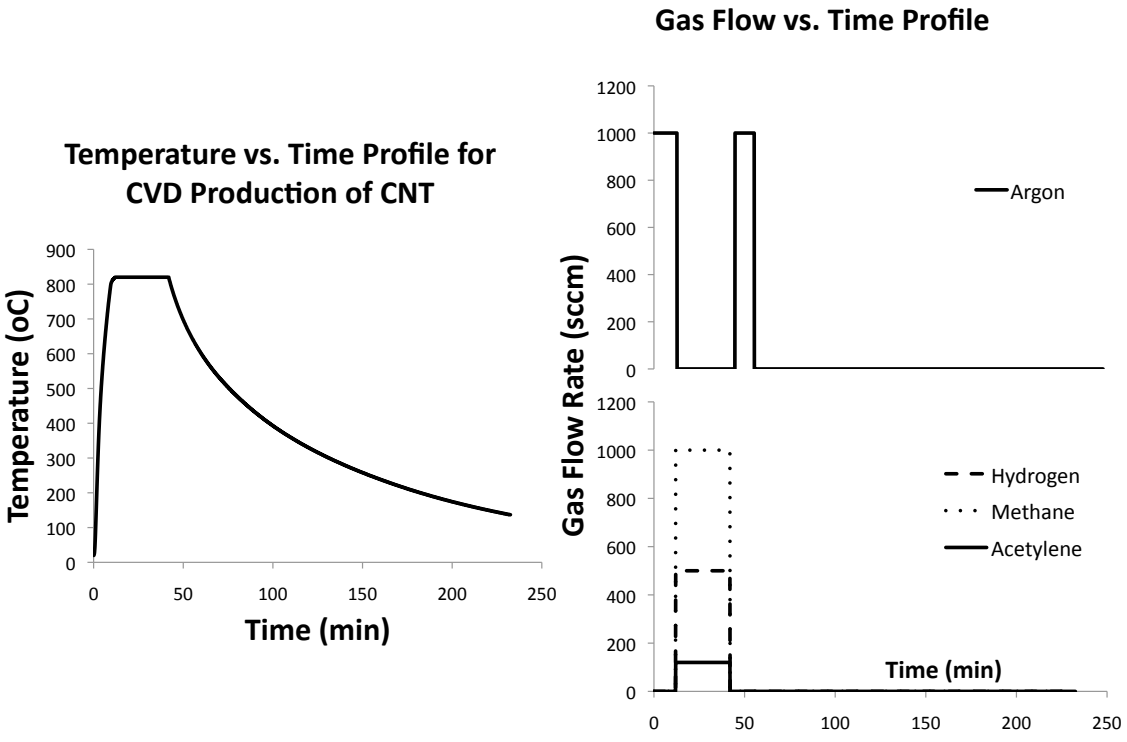

Figure 42: Temperature vs. time profile (left) and gas flow vs time profile (right) for the program AcUHYCNT 820^{o}C used to grow VACNT structures via chemical vapor deposition for PV devices.

3.3.1 Results of CNT growth

This growth process produces a high yield of MWCNTs which are highly vertically aligned in the microscale, but very defect ridden and tortuous in the nanoscale (Figure

43). The vertical height of the MWCNTs can vary widely from sample to sample. However, in a single sample, the deviation in vertical height is typically $\sim$10 μm.

The vertical height of CNTs grown from this recipe on different samples was calculated. This was done based on the average height of CNTs from SEM micrographs taken at different locations on the sample. The SEM images were obtained after dicing individual samples into quadrants and measuring the vertical height along the previously unexposed side edges. The height was obtained by averaging more than 40 measured points for each sample. The vertical height of CNTs grown using the AcUHYCNT820 recipe was found to be 88.67$\pm$30.05μm across 10 samples, but only has a spread of around $\pm$10μm across a single sample. The nonuniformity in the CNT height is associated with the misalignment and other defects [216] from sample to sample.

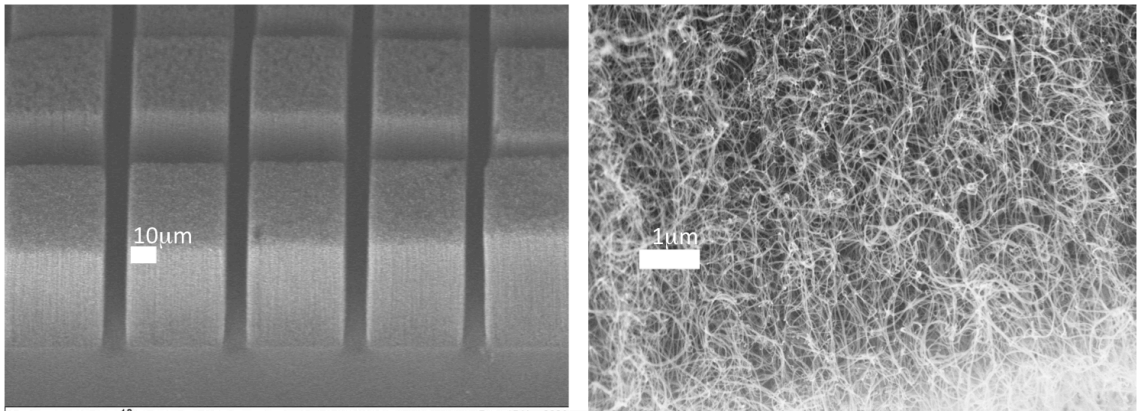

Figure 43: Scanning electron micrographs of VACNTs. (Left) These CNTs were photolithographically patterned into the block pattern and at the micron scale (scale bar is 10μm) CNTs look straight and well aligned. (Right) A close up of the nanostructure of the CNTs (scale bar is 1μm) show that, while aligned and straight in the microscopic regime, in the nanoscale regime the CNTs are tortuous and not well aligned.

The diameter of the as-grown MWCNTs was measured via TEM by scraping the CNTs from the silicon substrate onto a lacey carbon grid (#01881-F) from Ted Pella (Redding, CA) and imaging on a JEOL (Tokyo, Japan) 100CX2 TEM operated at

100keV. The average diameter of the CNTs was determined to be 17.5±4.0nm (Figure 44).

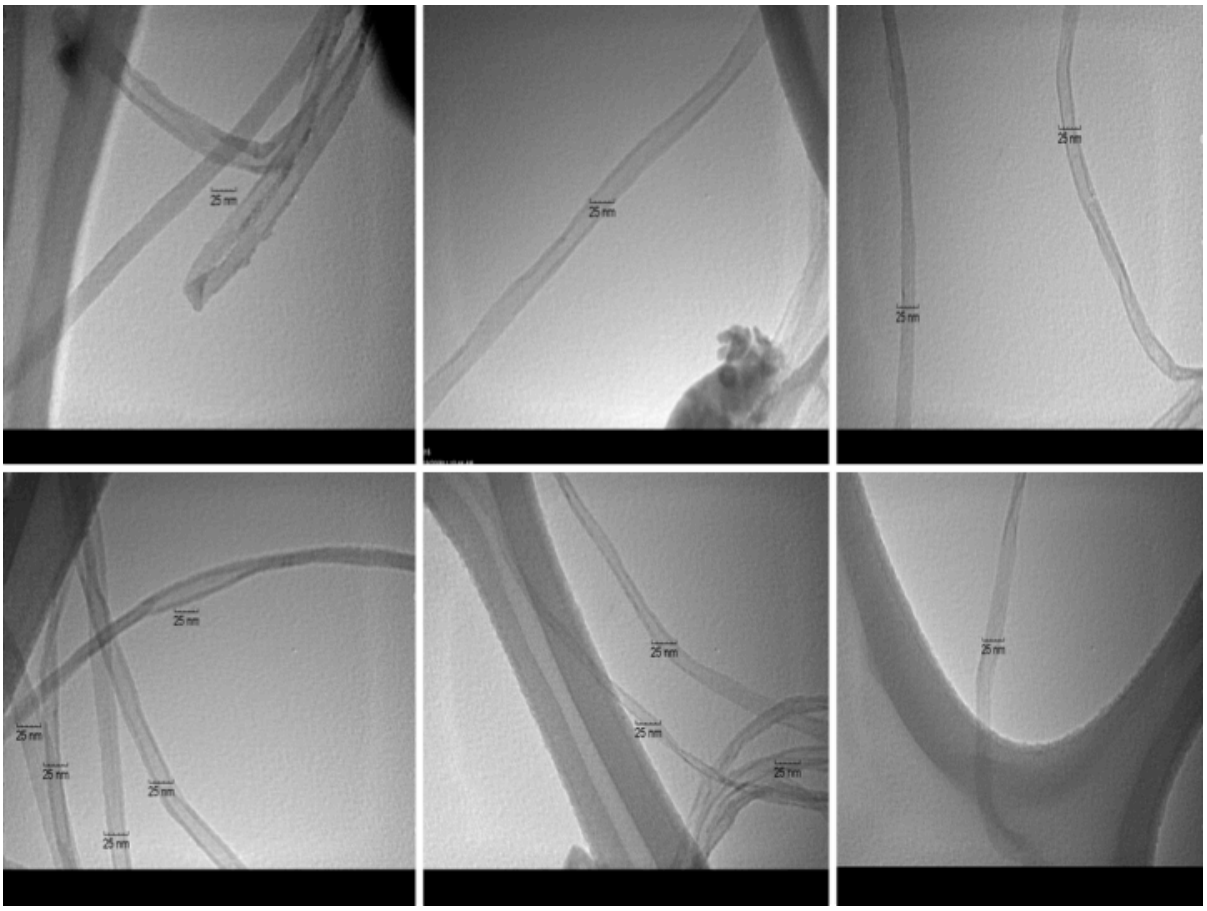

Figure 44: Variety of transmission electron micrographs showing CNTs grown using the AcUHYCNT820 recipe and detached from the Si substrate. Images were obtained with a JEOL 100CX2 TEM operated at 100keV. All scale bars are 25nm. The diameter of the CNTs is 17.5±4.0nm.

The areal density of the CNTs was calculated by measuring the vertical height, h, and area, A, of the CNT mat. The CNTs were then removed from the Si substrate with a razor. The mass, g, of the separated CNTs was measured with a Mettler AE260 analytical balance. If it is assumed that the density, γ, of the MWCNTs is the same as graphite (2.2 g/cm^3) then the areal density ($\#/cm^2$), f, can be approximated by the CNT mat weight (g), height (h), density (γ), and diameter (d).

$$f = \frac{4g}{h \times A \times \gamma \times \pi \times d^2} \tag{34}$$

For this recipe, the average areal density was found to be $2.31 \times 10^{10} \pm 2.18 \times 10^{10} cm^{-2}$, which is in line with measurements from other groups [217, 218, 219, 220]. However, the reliability of this number can be questioned since the standard deviation is almost as large as the average. This is due to uncertainty in the weight measurement and catalyst and particulate impurities on the CNT mat.

3.4 Molecular Beam Epitaxy

Molecular beam epitaxy (MBE) was chosen as the deposition method for the CdTe/CdS heterojunction because purity and controllability of the layers was of paramount importance while scalability was of less importance.

Molecular beam epitaxy is a subcategory of ultra high vacuum (UHV) evaporation techniques [221]. Elemental or compound materials are heated (or just introduced, if gaseous) in pseudo-Knudsen effusion cells [222]. Since these cells have a small exit aperture compared to the mean free path, a molecular beam is formed. This beam is directed towards, and condenses on, the substrate. The high vacuum requirements are necessary to control doping and impurity concentrations. UHV is also necessary so that the flux of the source materials have a mean free path [223] larger than the size of the chamber. If the mean free path is large enough, the gas molecules may have ballistic flow towards the substrate surface (a pressure of 1×10^{-6} Torr gives a mean free path of 10 meters).

MBE has many advantages, the most important of which are the high precision of resultant composition and doping with low impurity levels (as low as 10 parts per billion). However, there are a number of drawbacks including slow growth rate.

Films grow at a rate of approximately one atomic monolayer/second (assuming 1×10^{14} to $1 \times 10^{15} atoms/cm^2$ and a source gas pressure of $\sim 7.5 \times 10^{-7}$ Torr). Other disadvantages are low throughput and difficulty in producing products of scale [221]. Although rotation of the substrate is used in order to improve uniformity [224, 225], the inability to put the substrate through any other complex motions due to the limitation of lubrication techniques in UHV, means a near line of sight material deposition.

The most common method of flux monitoring use an ionization gauge to measure beam equivalent pressure (BEP) of individually shuttered sources [226, 227]. A nude Bayard-Alpert type gauge [228] is capable of measuring BEPs down to 7.5×10^{-12} Torr range. A common arrangement is for the gauge to be mounted on the back of the substrate manipulator so it is not constantly in the beam flux. For species which stick to the first surface they meet (sticking coefficient $\sim$1), like cadmium and sulfur compounds, it is sufficient to measure the difference in the steady-state signal with the source shutter closed and then open to determine the BEP.

The MBE system used in this work was a self-fabricated system produced by Dr. Wusheng Tong of the Georgia Tech Research Institute (Figure 45) [215]. It is composed of a 16" stainless steel growth chamber with a continuous azimuthal rotation sample holder which rotates at 3 rpm. The chamber is connected to a turbomolecular pump. The BEP and internal pressure are monitored by ionization gauges controlled by a #929 MKS gauge controller. The effusion cells are #3230 K-type cells from EPI (now a subsidiary of Veeco; Plainview, NY) with a 40 cm^3 pyrolytic boron nitride crucible (#200628). These sources are isolated from the growth chamber by pneumatically operated tantalum shutters. The temperature of the cells is monitored by an Omega (Stamford, CT) C-type thermocouple attached to a Eurotherm (Richmond, VA) #832 Temperature controller. The effusion cell heating uses an Hewlett-Packard (Palo Alto, CA) #6286A DC Power Supply.

The sources for the effusion cell are 5N purity 3-6mm pieces of CdTe (#C-1023) and 4N purity 3-6mm pieces of CdS (#C-1255-5) provided by Cerac Inc. (Milwaukee, WI).

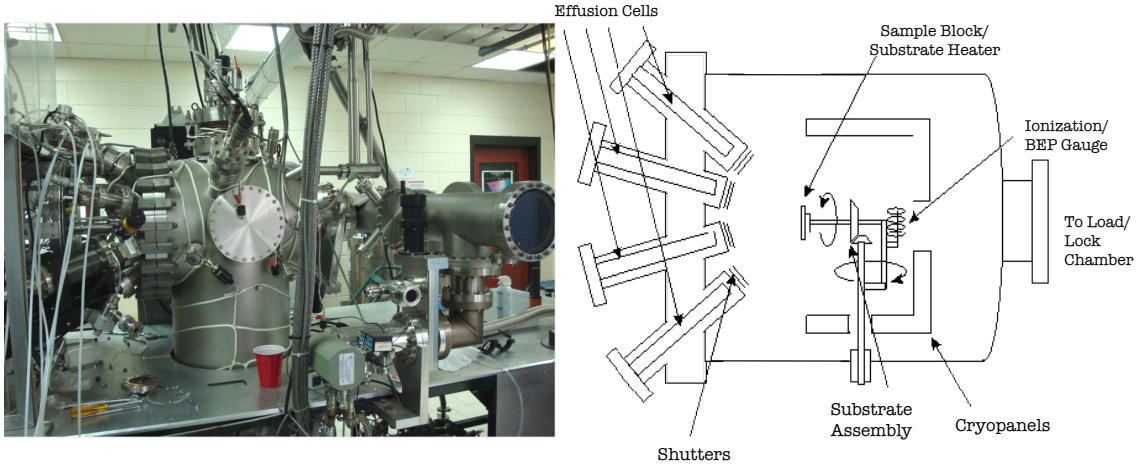

Figure 45: (Left) Image of MBE growth chamber and effusion cells used to deposit semiconductor heterojunction for 3DCNTPV work. (Right) Schematic of interior of growth chamber showing substrate assembly and effusion cells.

In order to deposit the semiconductor heterojunction onto the 3DCNTPV cells, the cryoshield of the MBE system is pumped with a Danielson (Lombard, IL) TD-100 Tribodyne turbopump for at least 45 minutes. The Si substrates with CNTs grown on them is attached to a 2" molyblock substrate holder with molybdenum clips. The molyblock is placed into the load/lock, which was pumped down to the sub-μTorr scale with a Tribodyne turbo pump. The isolation valve between the growth chamber and load lock is opened and the mechanical load arm is used to transfer the sample holder to the continuous azimuthal rotation apparatus. Liquid nitrogen is then continuously flowed through the cryoshield. The BEP ionization gauge is turned on and the CdTe effusion cell is heated to a suitable temperature ($\sim 650^{o}$C). Once the CdTe effusion cell has stabilized at the final temperature, the pressure reading of the BEP ionization gauge is noted. The effusion cell shutter is then opened for three seconds. Before closing the effusion cell, the new pressure reading of the BEP

ionization gauge is noted. If the difference between these two readings (the BEP) is not 4.3-4.5$\times 10^{-6}$ Torr, then the effusion cell temperature is adjusted either, higher or lower and a new BEP reading is taken until it is within the parameters.

If the BEP is within the pressure parameters, then the CdS effusion cell is heated to a suitable temperature ($\sim$ 350^{o}C). Once the CdS effusion cell temperature is stabilized, then the same procedure is used to find the BEP for the CdS flux. The target BEP for CdS is 3.3-3.5$\times 10^{-6}$ Torr. Once both effusion cells have a flux which is within the required BEP ranges, the BEP ionization gauge is turned off and the sample rotation assembly is rotated to be in line with the effusion cell flux.

The sample assembly is heated to 280^{o}C. The sample rotation is turned on and the CdTe shutter is opened. Deposition is carried out for 45 minutes. After CdTe deposition is completed, the sample temperature is decreased to 200^{o}C. Once the temperature stabilizes, the CdS effusion cell shutter is opened and CdS deposition is carried out for 75 minutes.

After CdTe and CdS deposition, the sample, CdTe effusion cell, and CdS effusion cell are allowed to cool. After the sample is completely cooled, it is transferred into the load/lock and taken out of the chamber.

3.4.1 Results from CdTe deposition

This process, including the BEP values and substrate temperatures were chosen because the CdTe and CdS adhered well to both CNTs and the Si substrate (Figure 46). To determine that CdTe and CdS were deposited via MBE, electron dispersive spectroscopy (EDS) was carried out on CdTe and CdS coated VACNTs samples (Figure 47). EDS spectra was taken with an Oxford Instruments (Oxford, England) INCA EDS system connected to a Carl Zeiss (Oberkochen, Germany) LEO 1550 SEM operated at 15keV. Xray maps were taken with a Thermo-Scientific (Waltham, MA)

Noran 7 EDS system connected to a Hitachi (Tokyo, Japan) S-800 SEM operated at 5keV. Both show the presence of Cd, Te, and S on top of VACNTs.

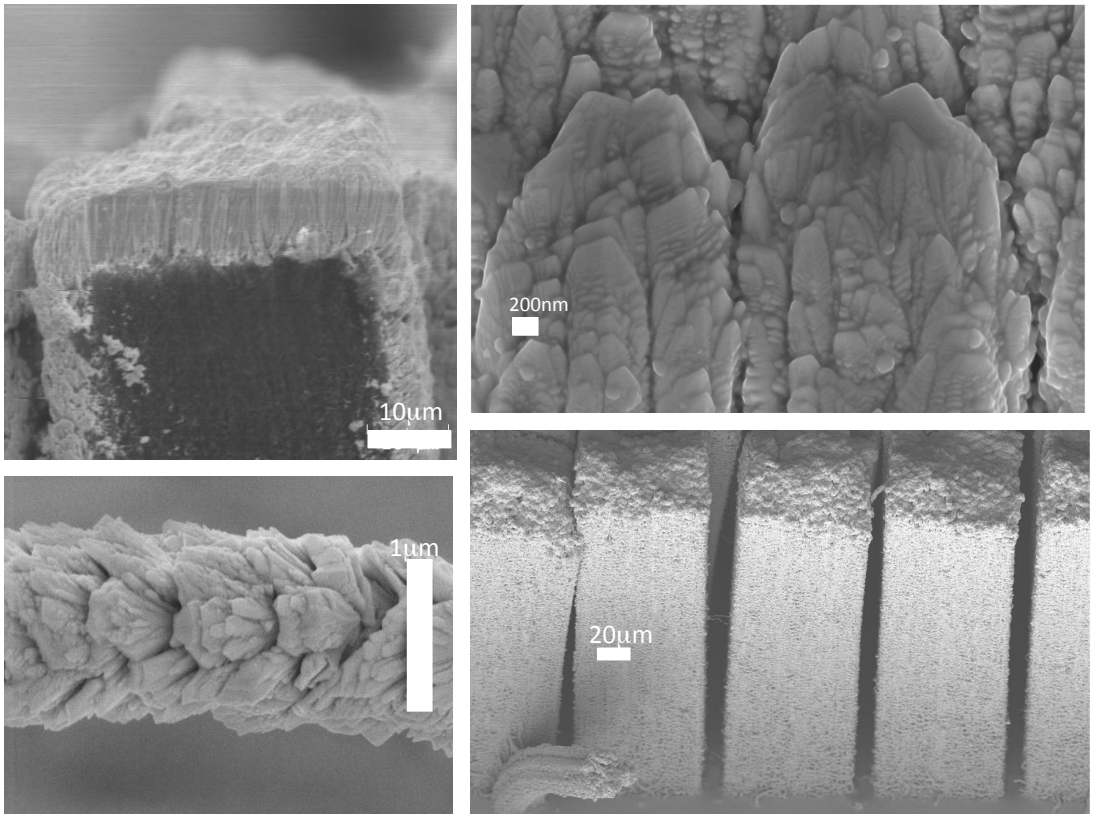

Figure 46: (Top left) Bisected VACNT tower showing complete CdTe coverage on top and on sides. Snowcapping has occurred (thicker on top than sides), but there is CdTe deposited on non line-of-sight faces and occurs for a depth of tens of microns from the VACNT top. The CdTe shows a columnar grain structure. (Top right) Closeup of CNT deposited on CNT. (Bottom left) CdTe well-adhered on multiple sides to a single stray CNT. (Bottom right) SEM micrograph showing CdTe completely covering both external and internal facing VACNTs for their entire length.

CdTe/Si samples were created. By bisecting samples and viewing edge on in a Hitachi S-4700 SEM, it was determined that the deposition rate for CdTe was approximately $5.02 \pm 0.30 \mu$m/hour.

In order to determine the bandgap of CdTe, the reflection spectra from a CdTe/Si sample was measured. A Hamamatsu Photonics (Hamamatsu, Japan) L7893 Series

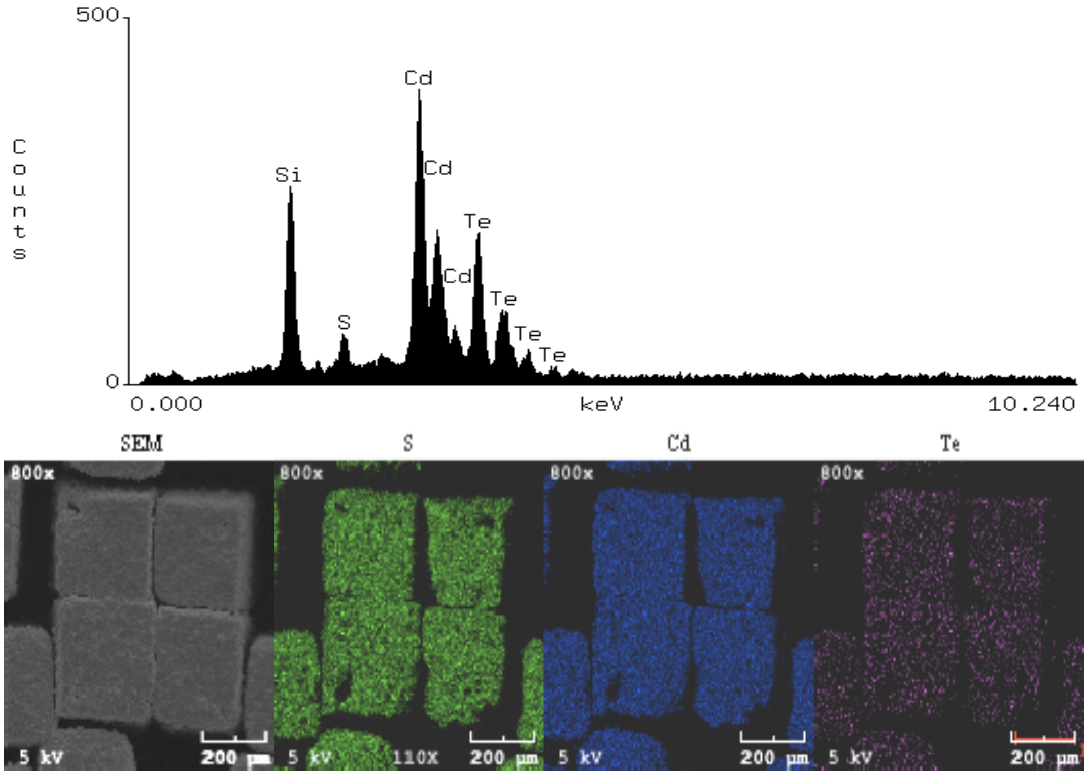

Figure 47: (Top) EDS of CdTe/CdS coated VACNTs showing presence of Si, Cd, Te, and S. (Bottom) EDS map of CdTe/CdS coated VACNTs showing Cd, Te, and S adhering to CNT towers.

halogen and deuterium lamp and Filmetrics (San Diego, CA) F20 series Thin Film Analyzer was used to find the absorption spectrum for wavelengths from 220 to 845nm, compensating for both background illumination and reflection from the Si wafer. From this, the absorbance value was calculated by subtracting the reflectance from unity (Figure 48). The CdTe has a wide absorbance band from about 2.5 to 4.75eV. A linear fit to the front edge of the absorption band to the x-axis gives a room temperature bandgap for this material of 1.36eV.

This value for E_g is smaller than the literature value for the E_g of CdTe (1.43eV at 300K) by 0.07eV [229]. This discrepancy may be explained by possible electronic differences in the MBE deposited CdTe or by localized heating of the CdTe sample during measurement. As CdTe increases in temperature, the bandgap decreases. If the lamp were focused on the sample for too long, it is possible that the sample temperature could increase, yielding a smaller value of E_g than would be expected at room temperature.

X-ray diffraction (XRD) characterization was performed on the MBE deposited CdTe with a PANalytical (Almelo, Netherlands) X'Pert PRO MRD Diffractometer with a Copper $K\alpha$ Xray tube operated at 1.8kW. The resultant pattern was analyzed and peaks were identified (Table 3.4.1) with MDI (Livermore, CA) Jade 8 and then matched with 2011 International Center for Diffraction Data (ICDD) (Newton Square, PA) Powder Diffraction File (PDF). A good match was obtained with PDF #01-76-8794 for cubic CdTe.

Figure 49 shows the X-ray diffraction pattern compared to the X-ray lines from the PDF file. The peaks in the diffraction pattern from the MBE deposited CdTe match very well with the (111), (220), (311), (331), and (422) peaks found in the ICDD database. Peaks corresponding to (hkl) indices of (200), (222), and (420) were of insufficient intensity to be resolved from the background of the scan. The peak

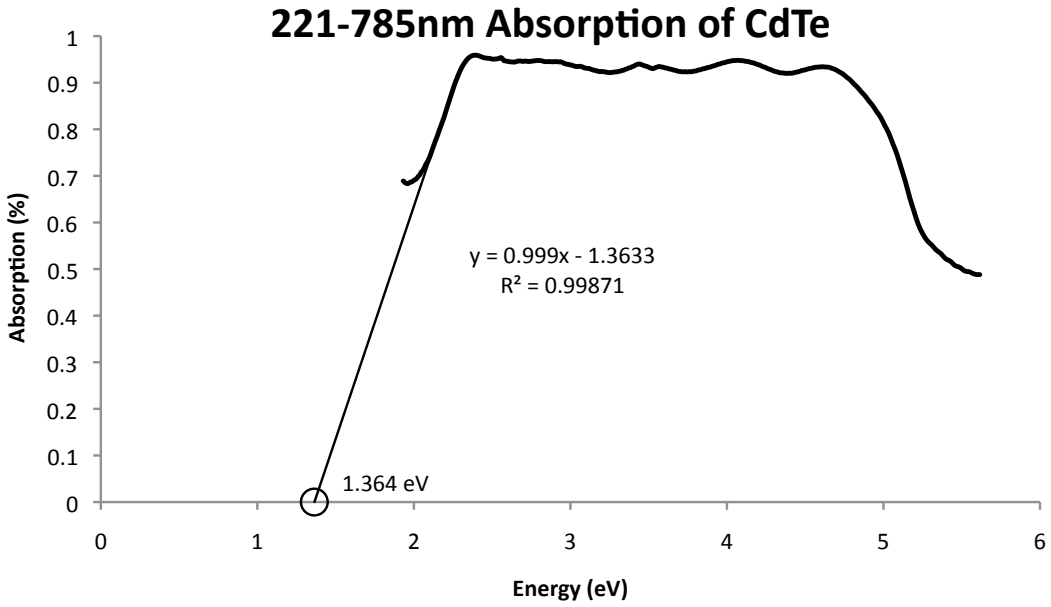

Figure 48: Percent absorption for CdTe on a Si wafer, corrected for background effects and the absorption of the wafer, but not scattering. There is a large absorption region from 2.5 to 4.75eV. A linear fit to the front band edge of the CdTe gives a room temperature bandgap of 1.36eV.

corresponding to (400) was not detected, though it should result in a peak of similar size to the (422) and (331) peaks, both of which were detected.

There also exist two anomalous peaks (denoted by arrows in Figure 49) in the spectrum which cannot be matched to any CdTe peak. The low angle peak is small and rests on the low angle shoulder of the (111) peak. This peak has a 2θ value of 22.38^o. The higher angle peak is a very broad peak (indicating a phase with an amorphous or nanoscale grain structure) located between the (220) and (311) peaks. The crest is located at a 2θ value of 41.22^o. These extraneous peaks indicate that there may be an impurity phase in the MBE deposited CdTe layer.

3.4.2 Results from CdS deposition

CdS/Si samples were created. By bisecting samples and viewing edge on in a Hitachi S-4700 SEM, it was determined that the deposition rate for CdTe was approximately 241.1 ± 41.9nm/hour.

Table 1: Peak list for x-ray diffraction pattern of MBE deposited CdTe. The 2θ values for the peaks (both ICDD and measured values) are listed, along with d-spacing (ICDD and calculated) for Cu $K\alpha$ radiation. The (hkl) indices are from ICDD PDF #01-76-8794 for cubic CdTe

$2\theta(^o)$		d-spacing ($\AA$)		Intensity		
ICDD	Measured	ICDD	Measured	ICDD	Measured	(hkl)
23.7780	23.66	3.73892	3.76	1000	1000	(111)
27.5238	-	3.23800	-	4	-	(200)
39.313	39.26	2.28961	2.29	583	85.33	(220)
46.4685	46.42	1.95259	1.96	311	101.73	(311)
48.6653	-	1.86946	-	3	-	(222)
56.8197	-	1.61900	-	65	-	(400)
62.4584	62.18	1.48570	1.49	87	18.65	(331)
64.2722	-	1.44808	-	5	-	(420)
71.2817	71.22	1.32191	1.32	89	24.02	(422)

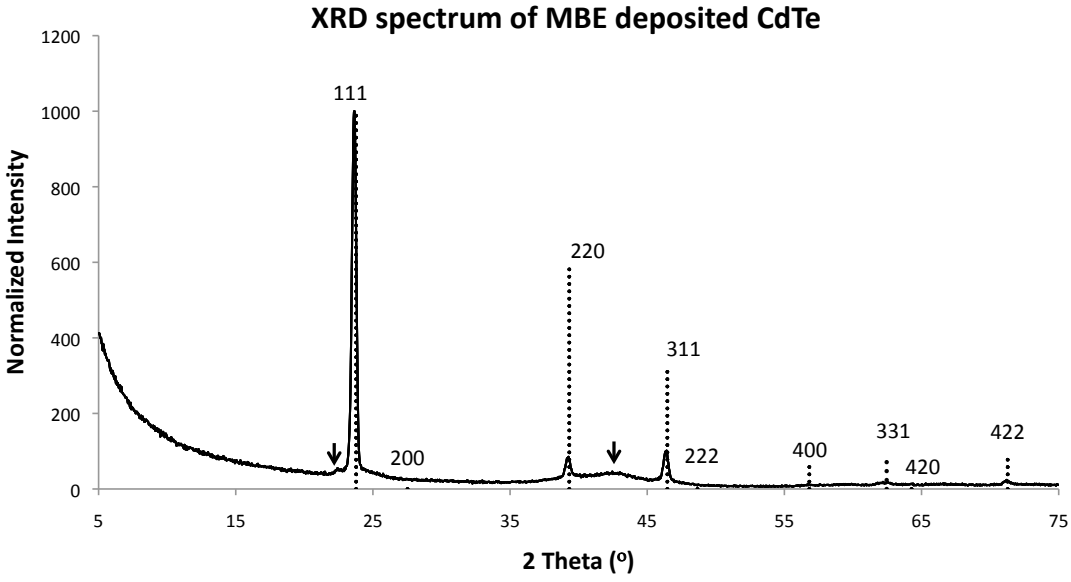

Figure 49: X-ray diffraction pattern obtained for MBE deposited CdTe using a PANalytical X'Pert Pro MRD with a Cu Kα x-ray tube. The peaks in the pattern (solid) match very well with peaks in the ICDD PDF database (#01-76-8794) for cubic CdTe (vertical hashed lines). The (hkl) planes of the ICDD database are labeled. Good matches between the experimental spectrum and the ICDD standard were found for the (111), (220), (311), (331), and (422) peaks. Other peaks were not intense enough to resolve over the scan background. The (400) peak is expected to show up in the scan, but was absent for unknown reasons. Two extraneous peaks, denoted with black arrows, were found in the CdTe spectrum. This indicates an impurity phase in the MBE deposited CdTe layer.

Photoluminescence (PL) was used to determine the bandgap for the CdS window layer. To do this, a Spectralab Physics (Santa Clara, CA) Model 2085 ($\lambda = 275nm$ 35mW) UV laser was focused on a 3DCNTPV cell without the ITO top contact (ITO absorbs UV light). The sample was mounted to an Air Products (Allentown, PA) Displex DE-202 cryostat, which was temperature controlled by an APD Cryogenics (Allentown, PA) HC-4 MK1 helium compressor. The PL spectrum was measured by a Spex (Edison, NJ) 1000M spectrometer controlled by Labview and operated with 10μm slit width.

The sample was cooled and spectra were taken at temperatures of 290, 225, 175, 104, and 74 Kelvin. Figure 50 shows the spectra in the region of the valence to conduction band edge recombination energy (1.85-4.00eV). As temperature decreases, the spread in the band gap energy begins to decrease, due to less thermal energy in the system. The median band gap also shifts to the left, indicating an increase in the bandgap energy as temperature decreases. In the spectra taken at higher temperatures, the band gap peak is a symmetrical gaussian peak. At lower temperatures, this peak is asymmetrical and it is possible to see that that band gap gaussian peak is actually the convolution of two peaks, one due to the radiative recombination between the conduction and valence band edges and the other due to radiative recombination of a bound exciton. The difference in these peaks at 74K is approximately 60meV and indicates the binding energy of the exciton.

By fitting the position of the radiative recombination peak at different temperatures (Figure 51) it is possible to find the 0K bandgap of CdS. For this sample, it was determined that the bandgap at 0K is 2.54eV with a $\frac{dE}{dT}$ value of -3.33×10^{-4} eV/K. At a temperature of 290K, the E_g was measured to be 2.447$\pm$0.035eV, which is slightly lower than the literature value of 2.47eV [229].

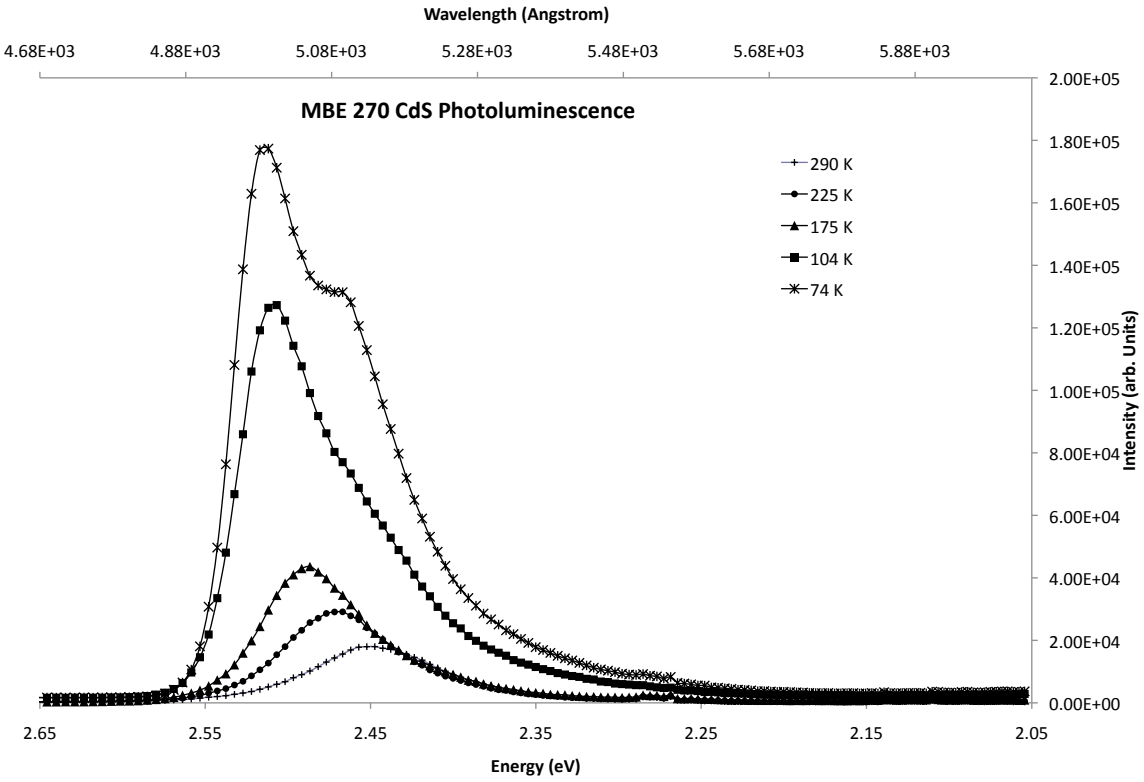

Figure 50: PL spectra of CdS at different sample temperatures. The peak shown is due to radiative recombination between the conduction and valence band edges. As temperature increases, the peak position moves to higher energies, indicating a widening of the bandgap. At 74K, it is possible to see that the gaussian peak has become asymmetric. This is due to the separation of two gaussian peaks, one due to radiative recombination between the band edges, and the other from radiative recombination from a bound exciton pair. The difference between the two peaks at 74K is approximately 60meV.

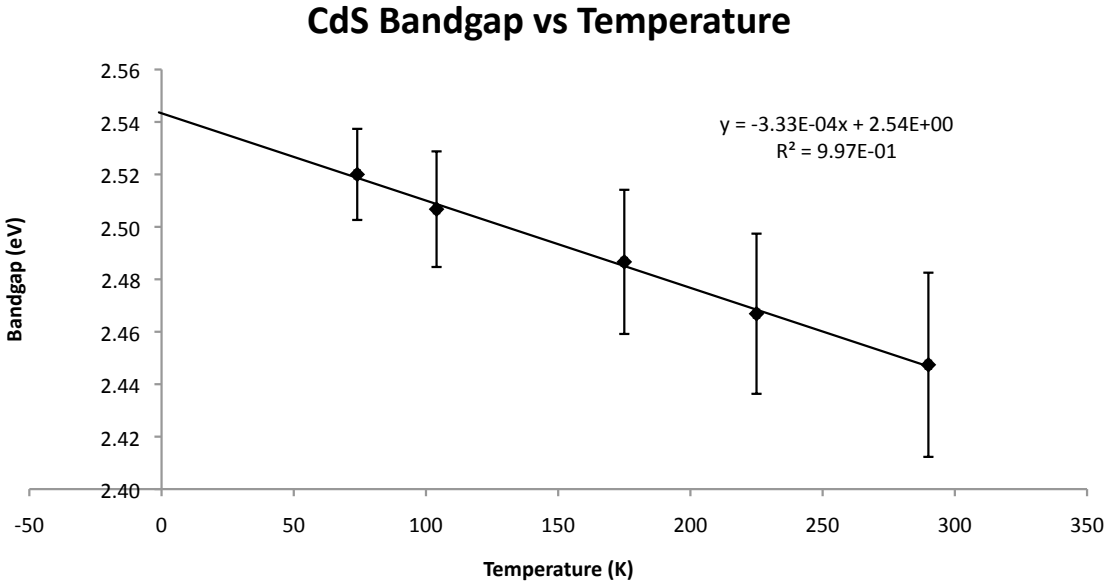

Figure 51: By fitting the peak position vs temperature, it is possible to perform a linear fit to determine the 0K bandgap. For this CdS sample, it was determined the 0K bandgap was 2.54eV with a $\frac{dE}{dT}$ value of -3.33×10^{-4} eV/K.

XRD characterization was performed on the MBE deposited CdS with a Rigaku (Tokyo, Japan) D/Max-11B X-Ray Powder Diffraction System utilizing Cu $K\alpha$ radiation. The resultant pattern (Figure 52) was analyzed and peaks were identified (Table 3.4.2) with MDI Jade 8 and then matched with ICDD PDF. Table 3.4.2 shows the ICDD and measured 2θ and d-spacing values along with the (hkl) indices of the lines. A good match to the spectrum (Figure 52)was obtained with PDF #01-074-9665 for hexagonal CdS. The peaks in the diffraction pattern from the MBE deposited CdS match with the (100), (002), (101), (102), (110), (103), (112), (201),(004), (202), (203), and (114) peaks found in the ICDD database, though the peaks are shifted in the low theta/high d-spacing direction. This may indicate that the MBE deposited CdS is in tensile strain. No peaks were found matching the positions of the (200), (104), and (211) lines.

One of the most interesting features of this spectrum is that the intensities of the peaks from the spectrum are very different from those values listed in the PDF. For

Table 2: Peak list for x-ray diffraction pattern of MBE deposited CdS. The 2θ values for the peaks (both ICDD and measured values) are listed, along with d-spacing (ICDD and calculated) for Cu $K\alpha$ radiation. The (hkl) indices are from ICDD PDF #01-074-9665.

$2\theta(^o)$		d-spacing ($\mathring{A}$)		Intensity		
ICDD	Measured	ICDD	Measured	ICDD	Measured	(hkl)
25.1163	25.060	3.54265	3.55	645	8.77	(100)
26.8266	26.692	3.32055	3.34	458	32.23	(002)
28.5330	28.902	3.12573	3.09	1000	1000	(101)
37.0771	36.96	2.42270	2.43	252	3.93	(102)
44.2465	43.896	2.04535	2.06	416	6.68	(110)
48.4484	48.112	1.87732	1.89	397	7.43	(103)
51.5527	-	1.77133	-	59	-	(200)
52.5028	52.090	1.74149	1.75	289	6.13	(112)
53.4956	53.144	1.71149	1.72	125	2.16	(201)
55.2844	54.844	1.66027	1.67	18	2.16	(004)
59.0582	59.026	1.56286	1.56	46	133.10	(202)
61.6435	-	1.50337	-	18	-	(104)
67.6887	66.948	1.38306	1.40	106	2.40	(203)
70.2364	-	1.33900	-	34	-	(210)
71.8668	-	1.31258	-	75	-	(211)
73.3902	72.592	1.24368	1.30	34	2.36	(114)

example, the ratio in intensity between the (101) and (100) peaks should be 64.5%. However, in the spectrum obtained from the MBE deposited CdS, this ratio is 0.87%. Similar discrepancies in the line intensities between the experimental spectrum and the ICDD PDF are numerous throughout the spectrum. This may indicate texturing of the CdS film. Texturing may explain why the (200), (104) and, (211) lines are unable to be resolved above the background.

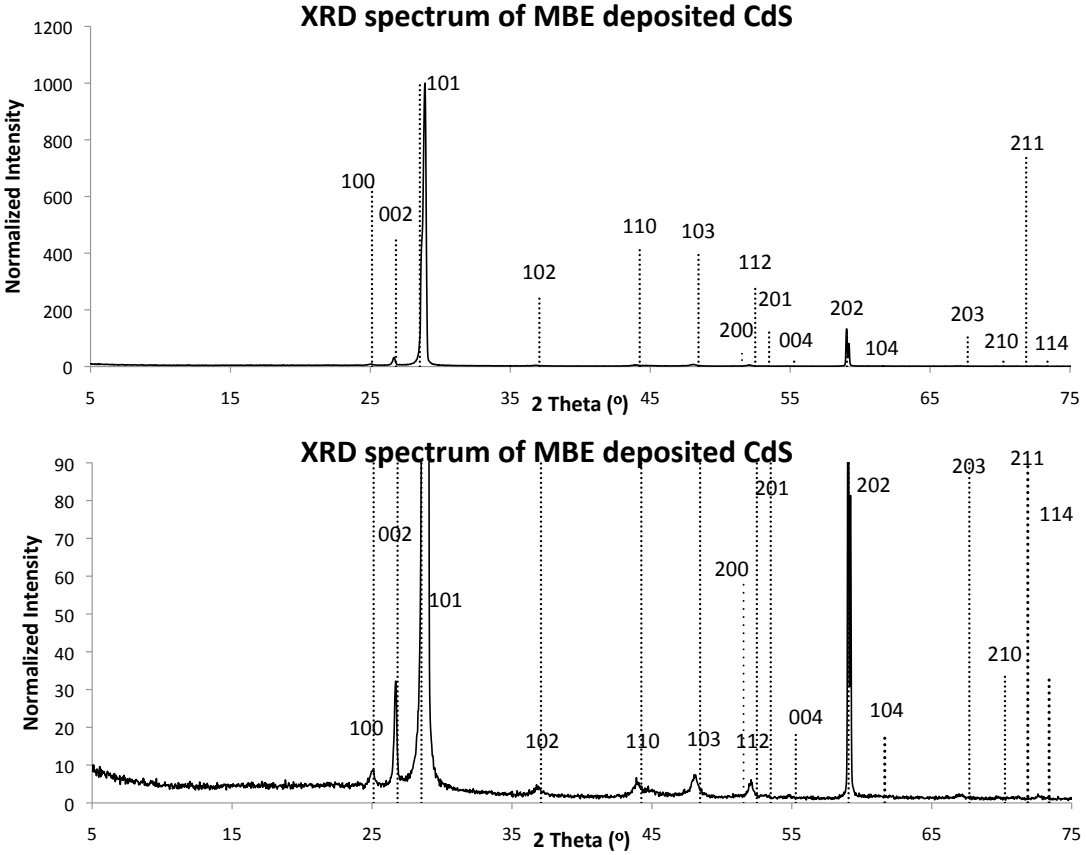

Figure 52: X-ray diffraction pattern obtained for MBE deposited CdS using a Rigaku D/Max-11B X-Ray Powder Diffraction System utilizing Cu $K\alpha$ radiation. The top spectrum shows the entire CdS diffractogram. Since the intensity of the (101) peak makes the smaller peaks difficult to discern, the bottom shows a close up of the low intensity region of the top spectrum. The peaks in the pattern (solid) match well with peaks in the ICDD PDF database (#01-074-9665) for hexagonal CdS (vertical hashed lines), though there is a shift toward the low theta/high d-spacing region. This may indicate the CdS is in tensile strain. The (hkl) planes of the ICDD database are labeled. The intensities of the peaks for the experimental spectrum are vastly different from those listed in the ICDD database. This may indicate texturing of the CdS film.

3.5 Ion Assisted Deposition

Ion assisted deposition (IAD), also known as ion beam assisted deposition (IBAD), was the method chosen to deposit the transparent conductive oxide, ITO, because it has been shown to create high quality, transparent, optoelectronic films at a lower temperature than other methods [230].

IAD uses a plasma-generated ion beam in combination with standard electron beam evaporation. This is desirable because, unlike other methods utilizing ion species, it is possible to control the deposition rate and ion energy independently. The plasma ion source has two main purposes. The first is that the source can etch or clean the sample surface by sputter-cleaning atmospheric contamination from the substate. The second is that the ions bombard the growing film with energetic inert ions to improve the deposited film qualities [231]. In order to achieve films of the highest optical quality, it is necessary to utilize a reactive mode deposition.

The deposition system used in this work is a Leybold (Pfäffikon, Switzerland) APS 1104 (Figure 53). The ITO source material is 4N purity ITO in $\frac{1}{8}$"to$\frac{1}{4}$" pieces from Kurt J Lesker.

After MBE deposition of the semiconductor heterojunction, the 3DCNTPV samples are fastened to the hemispherical sample holder of the APS 1104 with Kapton tape. Prior to deposition, the hemispherical sample holder is rotated and heated to a temperature of 200^oC. The ITO is then evaporated under 9sccm O_2 flow at a rate of $2\mathring{A}$/sec until a thickness of 150nm is measured with a quartz crystal deposition rate monitor. The argon ion assist is supplied by the APS operating at a bias of 80V and is operated at 4kW DC for deposition over the $\sim 9000cm^2$ surface area.

3.5.1 Results from ITO deposition

Sheet resistivity of the ITO films was measured via a linear 4-point probe technique using a Signatone (Gilroy, CA) #S-302-4 probe station with an #SP4-40085TFS SP4

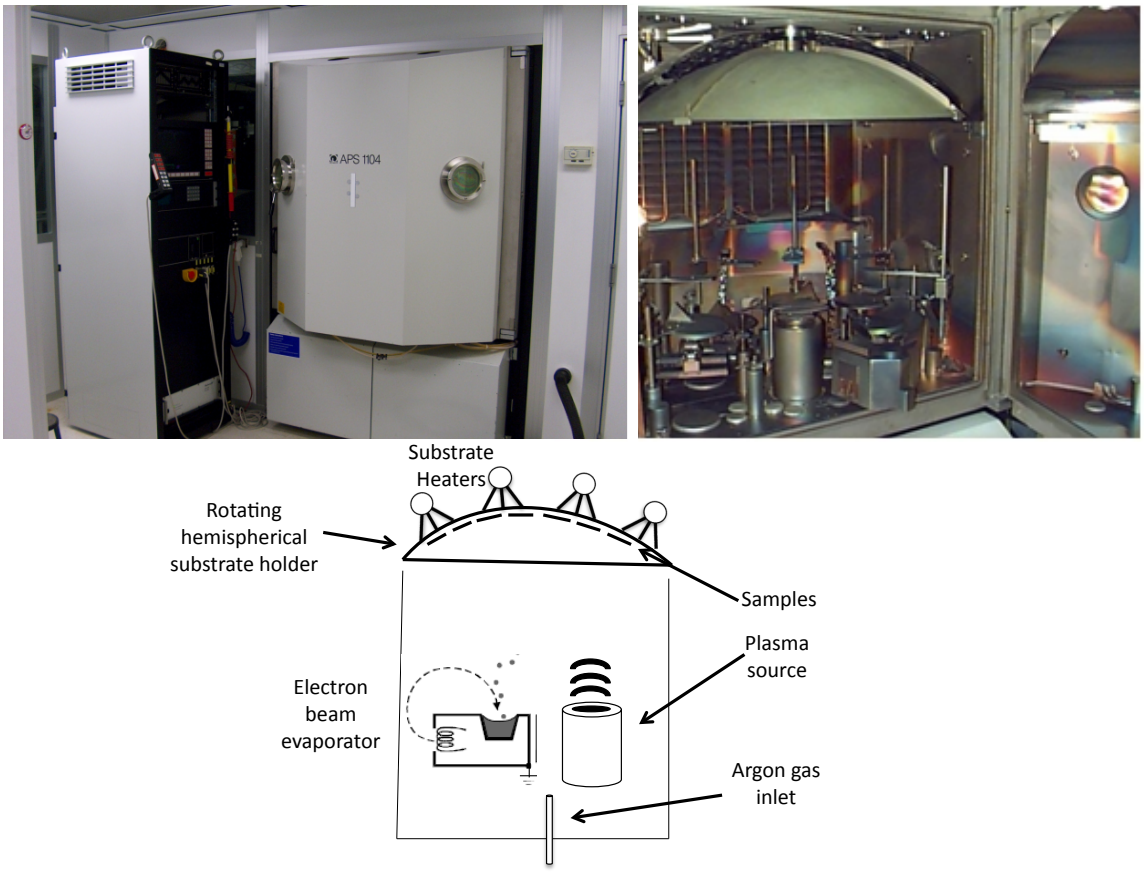

Figure 53: (Top left) External view of Leybold IAD chamber. (Top right) Internal view of Leybold IAD chamber. (Bottom) Schematic of IAD system components. The system is composed of a heated, rotating hemispherical substrate holder, an electron beam for evaporating source material, a gas inlet, and a plasma source.

probe tip connected to a Keithley (Cleveland, OH) 220 programmable current source and Keithley 2000 Multimeter. The Keithley products were controlled via GPIB interface with a PC running Labview 6i. The output current was set at 50mA. Before measuring any thin films, the setup was first calibrated with a VLSI Standard Inc. (Milpitas, CA) resistivity standard of 4.118 $\Omega/\square$.

In order to determine the sheet resistivity, the IAD recipe described above was used to deposit 150nm of ITO. The sheet resistivity was measured 5 times for each samples and multiple samples were averaged to get a sheet resistivity of $23.13 \pm 4.64 \Omega/\square$. This value is reasonably close to commercially available ITO films on glass substrates used for superstrate configuration cells, such as #CQ50IN0110 ITO lined quartz slides from Delta Technologies Inc. (Phoenix, AZ) with a sheet resistivity of $14.99 \pm 0.18 \Omega/\square$).

A transmission spectrum was obtained for IAD deposited ITO (Figure 54). The transmission data was taken with a Mikropack (Ostfildern, Germany) DH-2000 deuterium/halogen lamp chopped at 105.8Hz by a Spiricon (Logan, UT) chopper sync II system. The intensity of the lamp was measured by a Thorlabs (Newton, NJ) DET210 photodiode in line with an Oriel (Stratford, CT) Cornerstone 130 monochromator. The photodiode signal was passed to a Stanford Research Systems (Sunnyvale, CA) SR510 lock-in amplifier, which was interfaced via GPIB with a computer running Labview 7.1.

The IAD deposited ITO has lower overall transmission throughout the entire spectrum. However, the transmission of both is good. The transmission of the IAD deposited ITO is between 86 and 94% for the entire spectrum.

In order to determine the properties of the ITO in the 3DCNTPV cells, IAD was used to deposit ITO onto VACNTs without the CdTe/CdS heterojunction [232]. SEM was used to determine that ITO would adhere as a thin film to the VACNTs. These VACNTs were damaged to determine the penetration distance of ITO into the VACNTs. Figure 55 shows the deposited ITO completely covers the VACNTs and

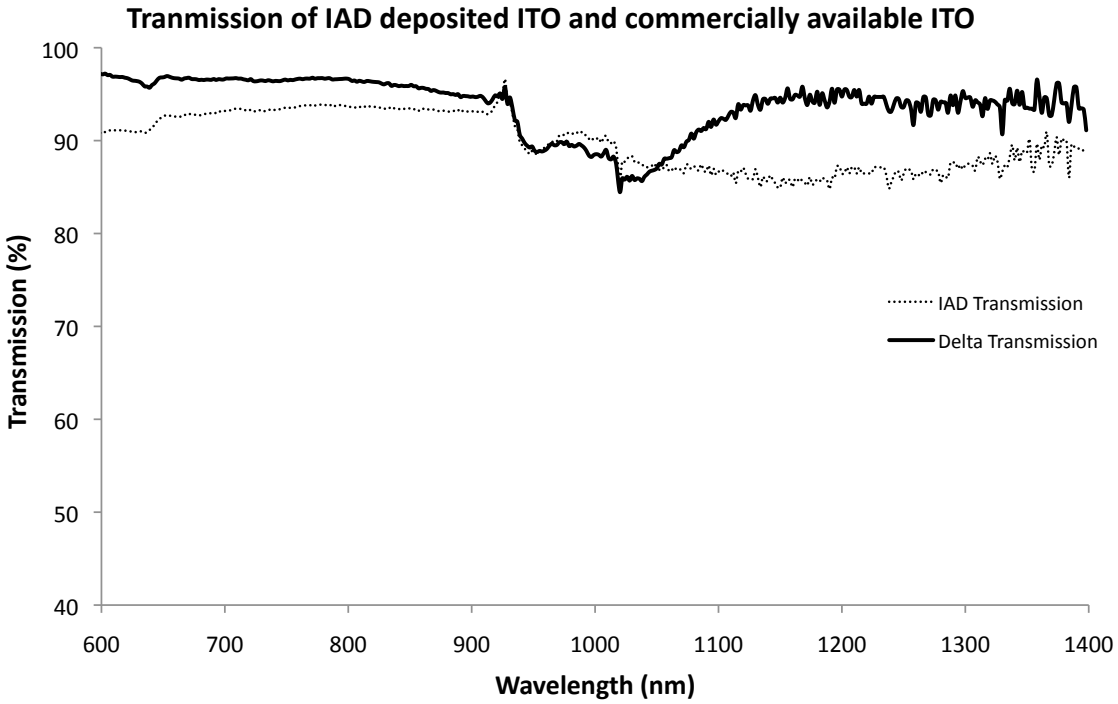

Figure 54: Transmission of IAD ITO compared to a commercially available ITO thin film from Delta Technologies, Inc. The IAD ITO has a slightly lower transmission than the commercially available film.

even penetrates into them for over a micron. It would be expected that the ITO would form a complete top contact on the VACNTs without voids and discontinuities.

TEM was carried out on the coated CNTs using a JEOL CX-2 TEM. The CNT were separated from the Si substrate by a razor blade and solvated in dichloromethane. This solution was then sonicated for ten minutes in order to ensure complete solvation of the CNT and discourage clumping. Lacey carbon TEM grids from Ted Pella were submerged in the dichloromethane and allowed to sit in the solvent overnight. The grids were imaged on a JEOL CX-2 TEM operated at 100 kV. The presence of indium, tin, and oxygen on the coated portion of the CNT was verified by electron dispersive spectroscopy measurement (Figure 56). The Fe peak is due to residual catalyst nanoparticles on the CNTs.

XRD characterization on these ITO covered VACNTs was performed with a Rigaku D/Max-11B X-Ray Powder Diffraction System (Table 3.5.1). XRD analysis shows peaks which can be attributed to the (211), (222), (400), (411), (420), (332), (134), (440), (433), (145), (622), (136), (44), (543), (633), and (156) indices of the ITO unit cell (Figure 57). The (200), (220), (123), (422), (125), (600), (611) (026), (046), (642), and (800) peaks were too small to be reliably differentiated from the scan background noise. The ideal peak positions are from PDF #01-089-4597 (93.75% In, 6.25% Sn).

The peak locations are shifted in the high theta/low d-spacing from their theoretical positions (Figure 57). This shift is due to either a strain in the ITO layer or differences in In/Sn composition (the IAD ITO has a 90%/10% composition) between the IAD ITO and the ICDD standard. If the shift is a result of strain in the ITO, it is most likely arises from the morphology of the ITO around individual CNTs. However, the sample was annealed at 350^{o}C for 1 hour in air and no appreciable strain relief was apparent after annealing.

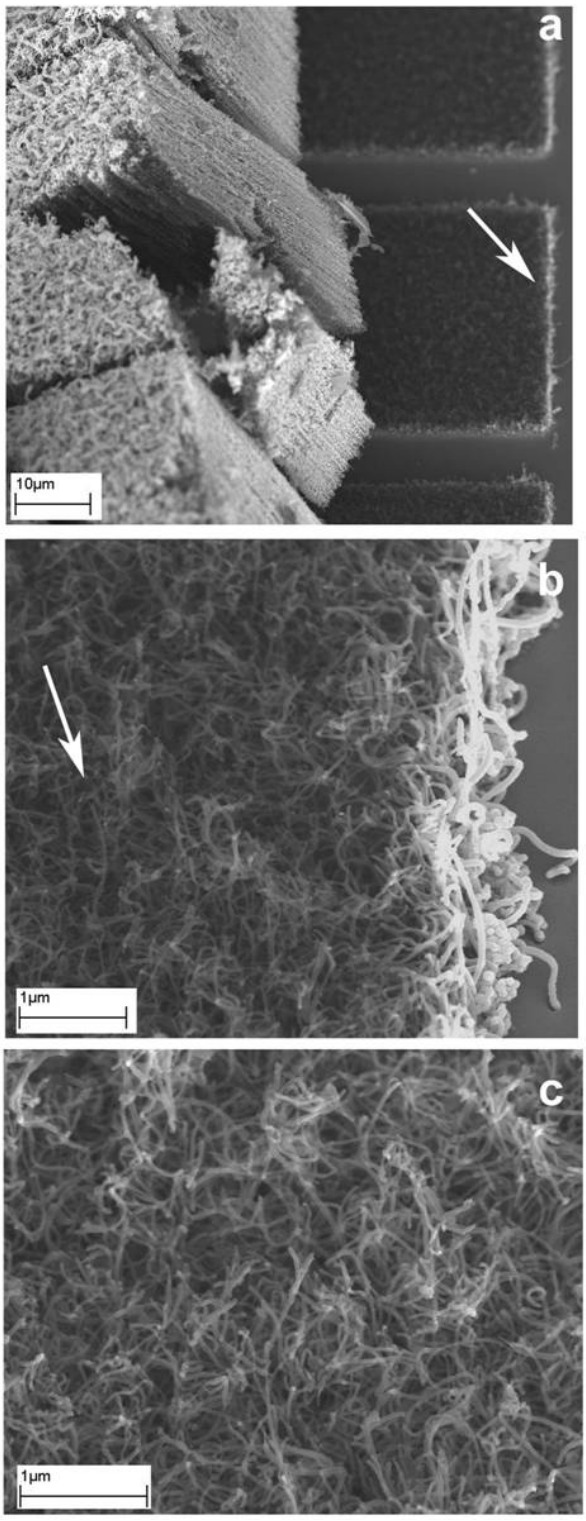

Figure 55: SEM images of ITO coated VACNTs showing (a) VACNTs removed from the substrate. Arrow in (a) indicates area of detail in (b). (b) Interior of VACNT showing penetration of ITO into VACNT interior. Arrow indicates area of detail shown in (c). (c) ITO coated CNTs in interior of VACNT.

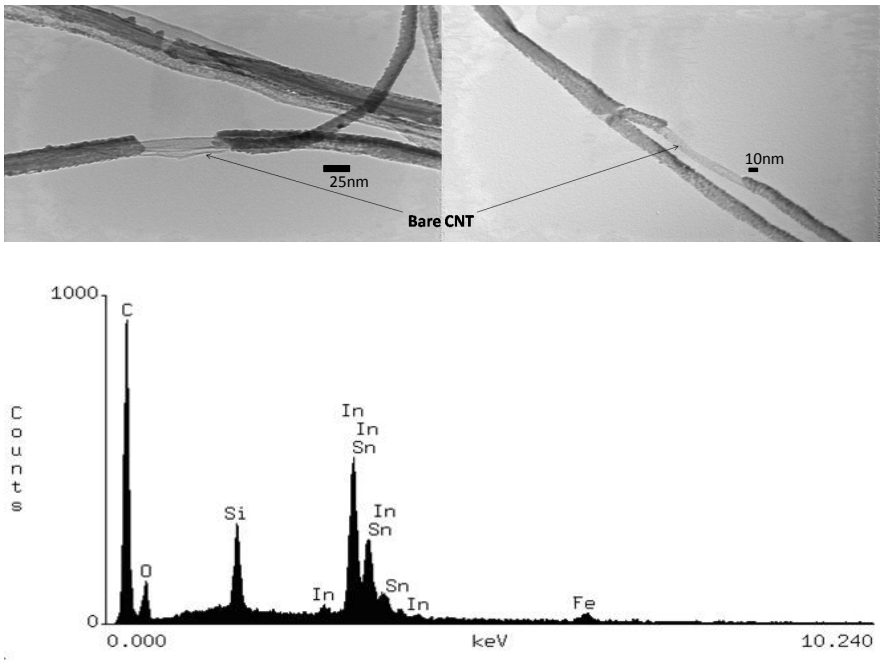

Figure 56: (Top) TEM micrograph of an ITO covered CNT. (Bottom) EDS spectrum of ITO deposited via IAD confirming presence of indium, tin, and oxygen.

The spectrum for ITO also exhibits a large, broad peak centered around the (211) peak at 21.98^o (denoted by arrows in Figure 57). This amorphous hump indicates material of poor crystallinity. The presence of amorphous ITO parasitically absorbs incident light and may explain why the transmission of the IAD ITO is lower than the commercially available ITO film.

Table 3: Peak list for x-ray diffraction pattern of IAD deposited ITO. The 2θ values for the peaks (both ICDD and measured values) are listed, along with d-spacing (ICDD and calculated) for Cu $K\alpha$ radiation. (hkl) indices are from ICDD PDF #01-089-4597. for 93.75% In/6.25% Sn composition ITO.

$2\theta(^o)$		d-spacing ($\AA$)		Intensity		
ICDD	Measured	ICDD	Measured	ICDD	Measured	(hkl)
17.5041	-	5.06235	-	3	-	(200)
21.4803	21.98	4.13339	4.04	113	696.60	(211)
24.8527	-	3.57962	-	1	-	(220)
30.5612	30.89	2.92275	2.89	1000	1000	(222)
33.0774	-	2.70594	-	13	-	(123)
35.4342	35.90	2.53117	2.50	294	259.12	(400)
37.6620	38.09	2.38641	2.36	47	159.65	(411)
39.7827	40.10	2.26395	2.25	10	131.28	(420)
41.8130	42.08	2.15859	2.15	39	153.10	(332)
43.7657	-	2.06670	-	8	-	(422)
45.6514	45.95	1.98562	1.97	74	164.33	(134)
49.2532	-	1.84851	-	21	-	(125)
50.9820	51.23	1.78981	1.78	331	366.70	(440)
52.6695	52.79	1.73637	1.73	19	135.33	(433)
54.3199	-	1.68745	-	4	-	(600)
55.9369	-	1.64244	-	41	-	(611)
57.5232	-	1.60086	-	9	-	(026)
59.0823	59.27	1.56228	1.56	33	145.93	(145)
60.6165	60.83	1.52636	1.52	234	132.52	(622)
62.1277	62.27	1.49281	1.49	45	147.80	(136)
63.6187	63.68	1.43185	1.46	44	158.72	(444)
65.0899	65.15	1.40404	1.43	16	148.11	(543)
66.5443	-	1.37780	-	9	-	(046)
67.9823	68.06	1.35297	1.38	22	146.24	(633)
69.4064	-	1.28584	-	11	-	(642)
73.6035	73.55	1.26559	1.29	17	149.36	(156)
74.9815	-	1.24626	-	29	-	(800)

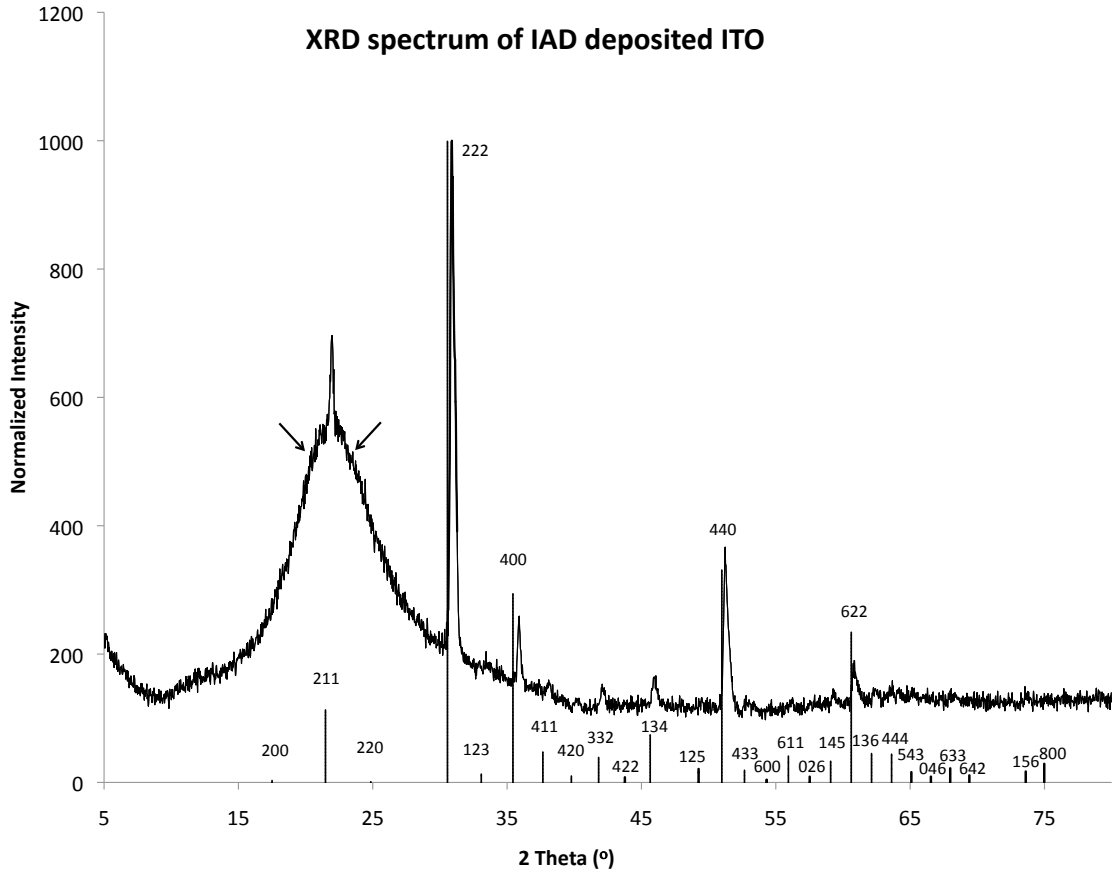

Figure 57: X-ray diffraction pattern obtained for IAD deposited ITO using a Rigaku D/Max-11B X-Ray Powder Diffraction System utilizing Cu $K\alpha$ radiation. The peaks in the pattern (solid) match well with peaks in the ICDD PDF database (#01-089-4597) for ITO composed of 93.75% In, 6.25% Sn (vertical hashed lines), though there is a shift toward the high theta/low d-spacing region. This may be due to the difference in Indium concentration in the ITO, since annealing at 350^{o}C did not alter the peak positions. There also exists a large broad peak denoted by arrows. This amorphous hump indicates the presence of amorphous or poorly crystalline materials. This lack of crystallinity may explain the decreased transmission of the IAD ITO compared to commercially available ITO. The (hkl) planes of the ICDD database are labeled.

3.6 IV characterization

Once the top ITO contact is deposited, the 3DCNTPV is ready to be tested. In order to test the IV characteristics of a cell, a Keithley 4200 semiconductor characterization station (SCS) is used to sweep applied voltage and measure output current. The 4200 SCS is capable of micro-volt and sub micro-amp resolutions.

In order to measure the IV curves for the 3DCNTPV, the leads of the SCS are connected to two Alessi Industries (Irvine, CA) micromanipulators capable of free motion along the x-, y- and z-axis. The top contact micromanipulator probe tip is covered with a 5N purity indium solder ball. This serves two purposes, the first is to prevent damage to the ITO top contact. The second is that indium is an ohmic contact to both ITO and CdS, so it ensures a good contact to the cell. Since the p-doped Si wafer is on the back of the cell, the back contact probe tip is contacted to a piece of single-sided Cu tape from McMaster-Carr (Atlanta, GA) which is taped to the testing platform and lies partially underneath the cell.

The cell testing is carried out on a CP12G05 Lytron (Warren, MI) cold plate. Cooling water, pumped by a submersible pump (#4182K2) from McMaster-Carr, is flowed through the cold plate tubing at a rate of 3.4 gallons per minute. This ensures a minimum temperature change while measuring the IV characteristics of the cell.

For light IV curves, a General Electric (Fairfield, CT) ELH 120V 300W halogen bulb is used. The intensity is this light can be changed by a Staco Energy Products (Dayton, OH) 3PN1010 variable autotransformer capable of altering the output voltage to the light from 0 to 140V. The transformer has a maximum apparent power of 1.4kVA. This light setup is on an angle calibrated circular track with the cold-plate at the center, so the incident angle of light can be changed from perpendicular to parallel to the cold plate.

In order to understand the overall quality of any 3DCNTPV cell created, two reference cells were obtained. The first is a substrate configuration CdS/CdTe cell

produced by Dr. Tim Gessert at the National Renewable Energy Laboratory (NREL). The cell has an area of 0.25cm^2 and is composed of a soda-lime glass substrate, a SnO_2:F layer (0.35μm) as the TCO, CdS (0.3μm), CdTe (4.5μm), ZnTe:Cu (1.0μm), and Ti (0.5μm) as the back contact. The cell was measured at NREL to have an efficiency of 10.18% (I_{sc}=5.0236mA, V_{oc}=0.7559V) with a fill factor of 66.77%.

Figure 58 shows the dark IV curves of the CdTe cell taken on the Keithley 4200 system (dashed line) and on NREL equipment (solid line). The dark IV curve of the cell taken on NREL equipment shows good curvature. It is relatively easy to see that for voltages greater than about 0.3V the recombination and diffusion currents begin to dominate the output of the cell. These currents dominate for most of the voltage range until there is a small flattening around 0.8V due to series resistance. The same cell measured on the Keithley system does not show the rapid increase in current around 0.3V. This flattening of the dark IV curve is most likely due to a parasitic resistance in the 4200SCS setup. The resistance could either be from the wires running to the 4200 or the contact resistance between the CdTe cell and the Alessi Industries micromanipulators. From the dark IV curve on the 4200SCS system, the R_{sh} value of the cell was found to be 9.89kΩ. The value of R_s was determined to be 207.9Ω.

The CdTe cell from Dr. Gessert is a dual back contact cell. The IV characterization equipment used in this work is unable to gather light IV curves with this type of cell structure, so analysis of the NREL cell is limited to dark IV curves. In order to obtain light curves from a reference cell, a GaAs cell was purchased from PV Measurements Inc. (Boulder, CO). The 4cm^2 GaAs homojunction cell is completely encapsulated with prefabricated wire-contact leads, eliminating the need for contacting using the micromanipulators. Figure 59 shows the results of testing this GaAs cell on the 4200SCS system. The left of Figure 59 shows the light IV curve of this cell as measured by NREL (solid line). Using standard AM1.5 illumination

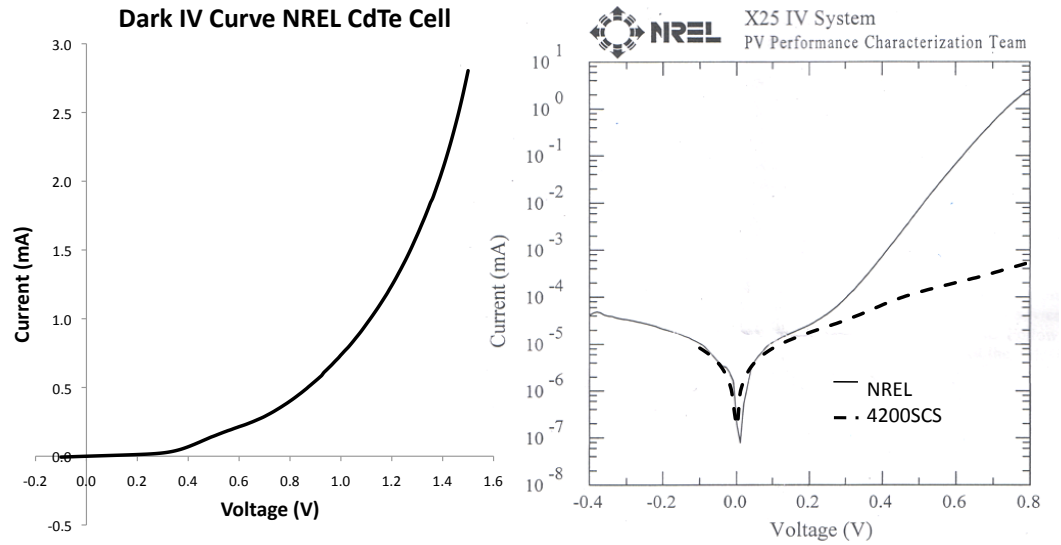

Figure 58: (Left) Dark IV curve taken of an NREL CdTe solar cell with the setup described in this section. The cell shows curvature, but not a very well defined knee. (Right) Semilog plot of the dark IV curve taken on the 4200SCS (dashed line) and by NREL (solid line). The curve taken on the 4200 is much flatter with much less curvature over the range of voltages than the curve from the same device measured using NREL's equipment. This flattening of the IV curve indicates an increased resistance added by the 4200SCS system. This resistance is either due to the wires leading to the 4200SCS system or is from a contact resistance between the micromanipulator probes and the CdTe cell.

at NREL, this cell was determined to have an efficiency of 17.70% (I_{sc}=89.10mA, V_{oc}=1.101V) with a FF of 77.5%.

The ELH bulb is not an AM1.5 light source, however, the power of the lamp can be tuned to match the I_{sc} value of the GaAs cell as measured at NREL. An input voltage of around 52% to the lamp matches the I_{sc} value of the GaAs cell to the value measured under AM1.5 illumination. The IV curves with input voltages of 50 and 55% are shown as dashed lines. For lamp voltages both above and below the voltage matched to the AM1.5 spectrum, the V_{oc} values measured by the 4200SCS system are about 100mV less than those measured at NREL. One cause for the decrease in V_{oc} may be due to parasitic absorption by the measurement equipment.

The right of Figure 59 shows the dark IV curve of the GaAs cell. The solid line with the right axis is the curve on a linear scale. The dotted line with the left axis is the dark IV curve on a semilog plot. In the semilog plot, the dark IV curve demonstrates more curvature than was seen in the CdTe cell. Instead of being flat for all voltages, the IV curve has an inflection point around 0.45V where the recombination and diffusion currents begin to dominate. When measuring the GaAs cell, it is not necessary to use micromanipulators to contact the cell since it was totally encapsulated with flying leads. The increased curvature of the GaAs cell may be due to a better contact than could be achieved with the CdTe cell. While measuring the IV characteristics of experimental 3DCNTPV cells, it is important to keep in mind the parasitic effects of the measurement equipment.

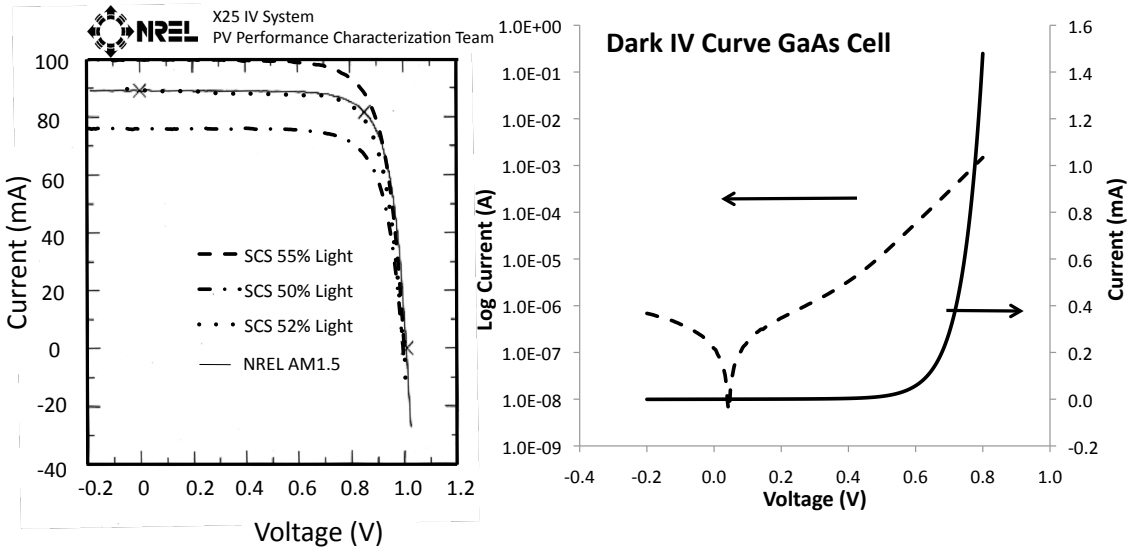

	NREL AM1.5	SCS 50% Light	SCS 52% Light	SCS 55% Light
I_{sc} (mA)	89.10	76.17	89.56	100.2
V_{oc} (V)	1.1010	0.995	0.995	1.00
FF (%)	77.50	75.79	76.14	75.22
P_{mp} (mW)	69.71	57.43	67.85	75.37
η (%)	17.70	14.57	17.22	19.19

Figure 59: (Left) Light IV curves from the GaAs cell tested at NREL (solid line) and tested on the 4200SCS (dashed lines) with lamp voltages of 50 and 55%. The lamp voltage needed to reproduce the I_{sc} value achieve under a AM1.5 spectrum is 52%. Both the NREL and 4200SCS curves demonstrate similar curvature. However, the V_{oc} values of the cell measured on the 4200SCS are 100mV less than the V_{oc} measured by NREL. This decrease in the V_{oc} may be due to parasitic absorption in the 4200SCS wiring. (Right) Dark IV curve of the GaAs cell. The solid line, paired with the right axis is a linear scale of the IV curve. The dotted line with the left axis is the IV curve on a semilog plot. The dark IV curve on the semilog scale, shows better curvature than was obtained with the CdTe cell. The curve is not flat, but shows an inflection point around 0.45V where the diffusion and recombination currents begin to dominate.

CHAPTER IV

THEORY OF OPERATION

For 3DCNTPV cells, the traditional term for efficiency, η , may vary widely for different geometries and incident angles of light. Therefore, a new efficiency for this 3D topology, η_{3D}, has been proposed. This treatment for cell efficiency assumes that a model cell is infinite in extent and therefore, all photons, except those traveling parallel to the cell surface, will impinge the surface. It is also assumed that all surfaces are non-rough and that specular reflection occurs at each impingement. Finally, it is assumed that at each impingement a photon of light is either reflected or absorbed and that the characteristic dimensions of the topological features are significantly larger than both the absorption distance of the material and the wavelength of the impinging photon, so that transmission and refraction through and around features may be ignored.

The general equation for the maximum power output of a well-behaved solar cell is [233, 234]

$$P_{mp} = \eta \times I_d \tag{35}$$

The power per unit area extracted from the device is simply the product of the cell efficiency and the solar insolation per unit area, $\mathrm{I_d}$, which varies as the cosine of the zenith angle of sunlight, ψ , according to Lambert's cosine law [235]. The efficiency of a solar cell, η, is a combination of multiple efficiencies. These include the efficiency of absorption, collection, and dissociation. Except for the absorption efficiency, these efficiencies have no, or a very small, dependence on the external texture of the solar

cell. Therefore the power output for an imperfect solar cell will be proportional to the absorption efficiency

$$P_{mp} \propto \eta_{ABS} \times I_d \cos\psi \tag{36}$$

The proportionality constant is determined by the products of the internal efficiencies. For simplicity, if the internal efficiencies are taken to be unity, the proportionality can be changed to an equality.

It has previously been stated that 3DCNTPV cells will have a higher power output over planar cells, due to the multiple interactions of photons with the solar cells surface. This "pinball" effect will lead to a higher efficiency, which is introduced as $\eta_{3\mathrm{D}}$. The following sections lays down the theoretical derivation for η_{3D} and compares that the the absorption efficiency of 2D devices, $\eta_{2\mathrm{D}}$. This treatment also quantifies the increase power output of these types of cells. Simulations, which are compared to the theory, are performed to compare the two types of cells, and later, experimental results are used as well.

4.1 Derivation of η_{3D}

The efficiency of a 3DCNTPV device, η_{3D}, is modeled by an idealized device, Figure 60 [236]. The 3D absorption efficiency is a combination of the absorption of two regimes of the cell, the absorption due to impingement at the "tops of towers and absorption inside the system, through tower side-wall and floor impingements. The combination of these two absorptions provides the overall absorption efficiency independent of number of particles incident on the system.

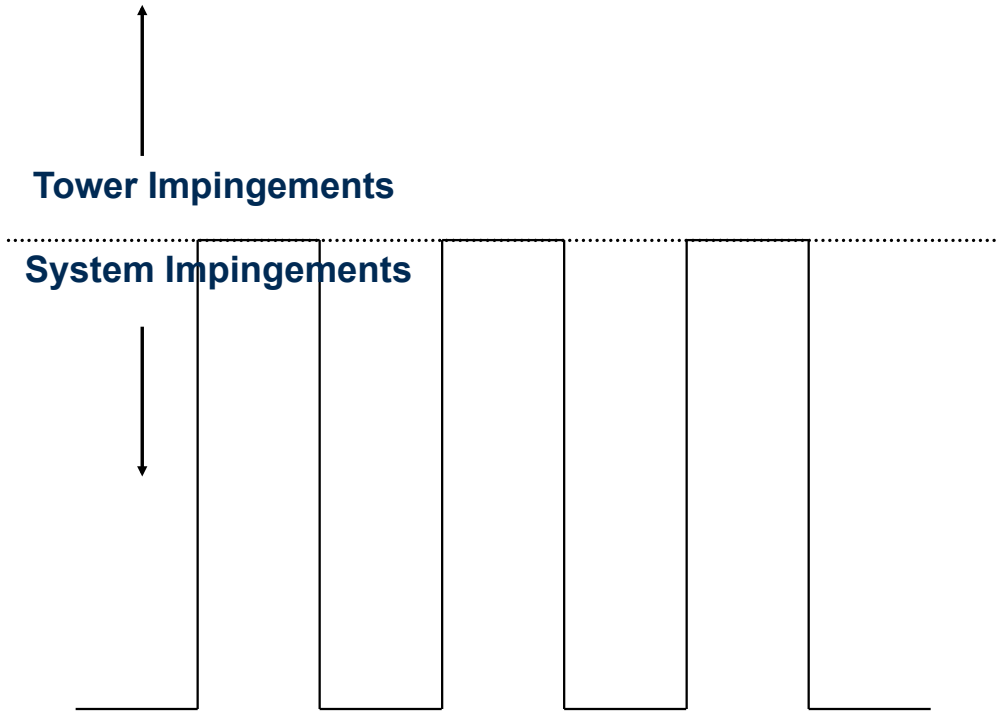

Figure 60: A 2D slice in the xz-plan of an idealized 3DCNTPV device used to model the efficiency and power production. The total absorption of the cell is defined by the absorption in two regimes. The first is the absorption of photons which interact only once with the tops of the towers. The second are photons which enter the system and interact with the sidewalls and floor of the cell. These photons have multiple interactions with the solar cell surface due to the "pinball" type effect.

$$\begin{aligned}\eta_{3D} =& \frac{\text{number of photons absorbed}}{\text{total number of photons}} \\ =& \frac{\text{photons absorbed by towers} + \text{photons absorbed by system}}{\text{total number of photons}} \\ =& \frac{p_t \times K + p_s \times S}{N_{ph}}\end{aligned} \tag{37}$$

p_t=probability a photons is absorbed by tower tops

p_s=probability a photon is absorbed by the system

K=number of photons impinging tower tops

S=number of photons entering system

N_{ph}=total number of photons

The number of photons entering the system (side-wall and floor impingements), S, is a function of the total number of photons, N_{ph}, the area fraction of space not occupied by towers, F_o, and the apparent area of the open spaces, determined by the cosine of the incoming zenith angle, ψ, where 0^o indicates photon travel colinear with the solar cell normal.

$$S = N_{ph} \times F_o \times \cos\psi \tag{38}$$

F_o=Open area fraction

ψ=zenith angle

The probability of absorbance is the probability of absorption (η_{2D}) for the 2D surface raised to the number of interactions (the number of reflections), Γ. After a repeated number of reflections, the probability of any one of Γ impingements resulting in absorption is the difference between unity and the probability that all the impingements resulted in a reflection.

$$p_s = 1 - \text{probability of continuous reflection} = 1 - R^{\Gamma} = 1 - (1 - \eta_{2D})^{\Gamma} \tag{39}$$

R=reflectance of surface

η_{2D}=absorption of surface

Γ=average number of reflections per photon

The number of photons impinging the tops of the towers is equal to the difference between the total number of particles and those entering the system. Due to the specular reflective nature of the tops of the towers, photons may interact only once and then proceed off to infinity.

$$K = N_{ph} - S = N_{ph}(1 - F_o)\cos\psi \tag{40}$$

$$p_t = \eta_{2D}^1 = \eta_{2D} \tag{41}$$

By substituting (38), (39), (40), and (41) into (37) an expression for the absorbance efficiency of a columnar solar cell device can be derived which is a function of fractional tower area, F_o, incident zenith angle, ψ, absorbance efficiency, η_{2D}, and the average number of reflections per particle, Γ.

$$\begin{aligned} \eta_{3D} &= \frac{\eta_{2D} \times N_{ph}(1 - F_o)\cos\psi + [1 - (1 - \eta_{2D})^{\Gamma}] \times N_{ph} F_o \cos\psi}{N_{ph} \times \cos\psi} \\ &= \eta_{2D}(1 - F_o) + F_o[1 - (1 - \eta_{2D})^{\Gamma}] \\ &= F_o[1 - \eta_{2D} - (1 - \eta_{2D})^{\Gamma}] + \eta_{2D} \end{aligned} \tag{42}$$

While F_o, ψ, and η_{2D} are all well defined or easily measured parameters, the function Γ is itself a function of multiple parameters including zenith angle, azimuthal angle, tower height, and cell geometry.

Although difficult to characterize theoretically, Γ has both a high and low limit. As the average number of reflections per photon approaches unity (planar cell limit) the efficiency approaches a constant value equal to the absorbance efficiency.

$$\begin{aligned} \Gamma &\to 1 \\ \eta_{3D} &= F_o[1 - \eta_{2D} - (1 - \eta_{2D})^1] + \eta_{2D} \\ &= F_o[0] + \eta_{2D} \\ &= \eta_{2D} \end{aligned} \tag{43}$$

As Γ, the number of impingements per photon, approaches infinity, the efficiency approaches a maximum. This value indicates a maximum for photon absorption for columnar solar cell morphologies. This absorbance, though larger than the plane cell limit, is limited through the one time reflection of incident photons off tops of columns which are then lost.

$$\begin{aligned} \Gamma &\to \infty \\ \eta_{3D} &= F_o[1 - eta_{2D} - (1 - \eta_{2D})^\infty] + \eta_{2D} \\ &= F_o[1 - \eta_{2D}] + \eta_{2D} \end{aligned} \tag{44}$$

Therefore, the study of the absorption efficiency of this type of solar cell necessarily becomes the study of maximizing Γ for the greatest number of zenith angles. The

determination of Γ is nontrivial since Γ is itself a function of photon incident direction, aspect ratio, and geometry (tower size, distribution, and shape) of the system.

As the value of Γ can be approximated as infinity for angles approaching ninety degrees, the maximum in the overall efficiency should track to higher angles. As the zenith angle approaches zero degrees, Γ must necessarily approach the planar cell morphology, since the apparent height of the towers is zero. Then the actual absorption efficiency diverges from the ideal maximum value and will approach the 2D absorption efficiency. The key is to determine the morphologies for which Γ can approximate infinity for the angles most near ψ=0^o. An ideal 3D cell would be one for which $(1-\eta_{2D})^{\Gamma} \rightarrow 0$ can be approximated for all angles up to ninety degrees. A non ideal cell deviates from this approximation and approaches $\Gamma = 1$, the planar cell limit, as the ψ approaches 0^o. The angle at which the non ideal cell deviates from the ideal cell approximation varies with the geometry of the system.

A non-ideal 3DCNTPV cell would have a Γ value which would not be approximated by infinity for all values of ψ so the P_{mp} vs. ψ curve would fall in between the planar cell and perfect 3D cell limit. This modeled power production for a real 3DCNTPV cell would take on an inverted C-curve type shape as seen in Figure 61. At small values of ψ, few photons enter the system due to the small apparent area between towers and P_{mp} is small. At near zero values of ψ, the 3D nature of the cell reduces to a planar morphology since a photon approaching from the infinite +z direction (axial direction of towers) shows an apparent tower height of zero and the number of reflections decreases towards unity. The angle at which the real power production curve deviates from the ideal power production is an important parameter. The study of these cells necessitates the optimization of VACNT layout and its contribution to the value of Γ in order to maximize this deviation angle.

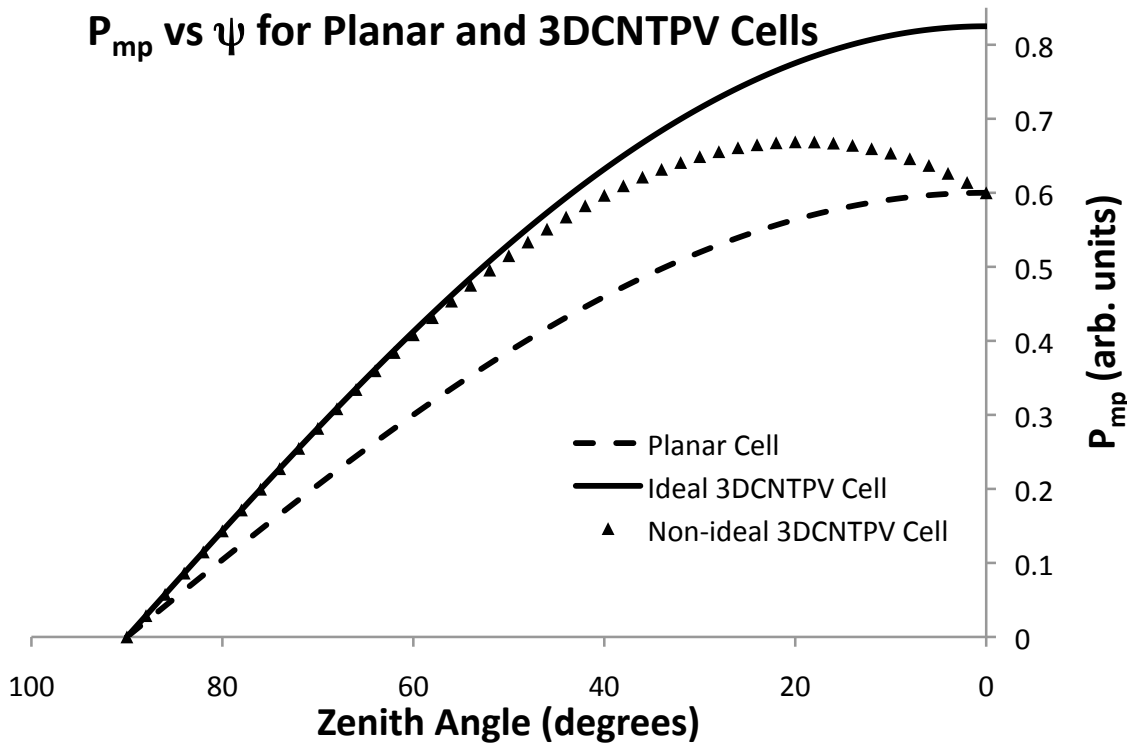

Figure 61: P_{mp} versus ψ for three types of cells. These are a planar cell (dashed line) which falls off as a cosine from a a maximum value at ψ=0^o, an ideal 3DCNTPV cell (thick line) for which Γ can be approximated as infinity for all ψ values, and a real 3DCNTPV cell (triangles) for which Γ can be approximated as infinity for $\psi \approx 90^o$ and unity for $\psi \approx 0^o$. The real 3DCNTPV cell forms an inverted C-curve. The specifics of this curve depends on the geometry of the VACNT system.

4.2 Derivation of Γ

At an average Earth to Sun separation distance equal to 93 million miles, the sun is an extended light source which subtends an apparent angular area of 0.5^o [237]. Photons coming from the sun have a divergence angle equal to half of this so are not truly parallel. However, this introduces limited error and for the purposes of deriving an expression for Γ, we ignore this divergence angle and consider the sun as a point source.

As a point source, the sun can be described as having a position determined by the radial vector, $\vec{\delta}$, the azimuthal angle, ω, and the zenith angle, ψ (Figure 62) [36]. The radial vector can take any positive value and is equal to zero at the origin. The azimuthal angle can take any value between zero and 2π and is equal to zero at the x-axis. The zenith angle can take any value between zero and π and is equal to zero at when collinear with the z-axis.

A photon which is emitted from the sun and travels towards the Earth, located at the origin of the coordinate system, has a velocity, $\vec{v}$, which is collinear with $\hat{\delta}$ and is equal to 3.0×10^8 m/s. This velocity can be broken down into x-,y-, and z-component velocities by the equation [238].

$$\vec{v} = \dot{\delta}\hat{\delta} + r\sin\omega\dot{\omega}\hat{\omega} + r\dot{\psi}\hat{\psi} \tag{45}$$

where $\hat{\delta}, \hat{\omega}, \hat{\psi}$ are the radial, azimuthal, and zenith unit vectors, respectively and $\dot{\delta}, \dot{\omega}, \dot{\psi}$ are the change in the radial, azimuthal, and zenith values, respectively.

Because the velocity of the photon is colinear with $\hat{\delta}$, with no velocity in the $\hat{\omega}$ or $\hat{\psi}$ directions

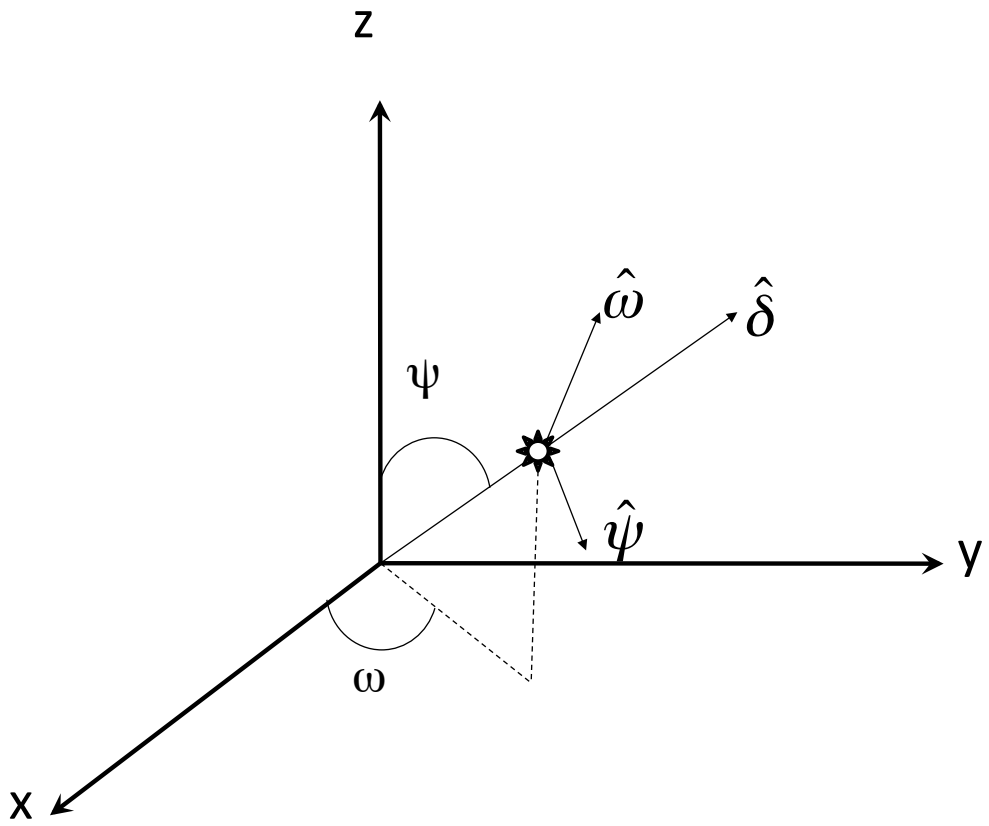

Figure 62: The sun (as a point source) can be described relative to the earth (origin) in a spherical coordinate system by the radial vector (δ), the azimuthal angle (ω), and the zenith angle (ψ). A photon traveling towards the earth has a velocity in the direction of $-\hat{\delta}$.

$$\dot{\omega} = \dot{\psi} = 0 \tag{46}$$

The velocity simply becomes

$$v = -\dot{\delta}\hat{\delta} \tag{47}$$

which can be transformed into cartesian coordinates $(\hat{\mathrm{x}}, \hat{\mathrm{y}}, \hat{\mathrm{z}})$, by substituting in

$$\hat{\delta} = \cos\omega \sin\psi\hat{x} + \sin\omega \sin\psi\hat{y} + \cos\psi\hat{z} \tag{48}$$

$$\dot{\delta} = speed = 3.0 \times 10^8 \frac{m}{s} \tag{49}$$

makes the velocity equal to

$$\vec{v} = -\dot{\delta}(\cos\omega \sin\psi\hat{x} + \sin\omega \sin\psi\hat{y} + \cos\psi\hat{z}) \tag{50}$$

The velocity can easily be separated into cartesian velocities $(\vec{v_x}, \vec{v_y}, \vec{v_z})$

$$\vec{v_x} = -\dot{\delta}\cos\omega \sin\psi\hat{x} \tag{51}$$

$$\vec{v_y} = -\dot{\delta}\sin\omega \sin\omega\hat{y} \tag{52}$$

$$\vec{v_z} = -\dot{\delta}\cos\psi\hat{z} \tag{53}$$

The distance travelled in the x, y, and z-directions (Δx, Δy, Δz) is equal to the velocity in those directions times the time, t, of travel.

$$\Delta x = |\vec{v_x}|t \tag{54}$$

$$\Delta y = |\vec{v_y}|t \tag{55}$$

$$\Delta z = |\vec{v_z}|t \tag{56}$$

In the three directions the time of travel is the same and is the basis for comparison between the three different directions.

$$t = \frac{\Delta x}{|\vec{v_x}|} = \frac{\Delta y}{|\vec{v_y}|} = \frac{\Delta z}{|\vec{v_z}|} \tag{57}$$

The maximum time of travel in the system is determined by the direction co-linear with the axial direction of the towers, which is denoted as the z-direction. In this direction a photon enters a space between towers at time zero and travels downward to the floor. After a time necessary to traverse a z-distance equal to the height of the towers, h, the photon then reflects off the floor and travels upward. Again after a time necessary to traverse a z-distance equal to h, the photon exits the system. From

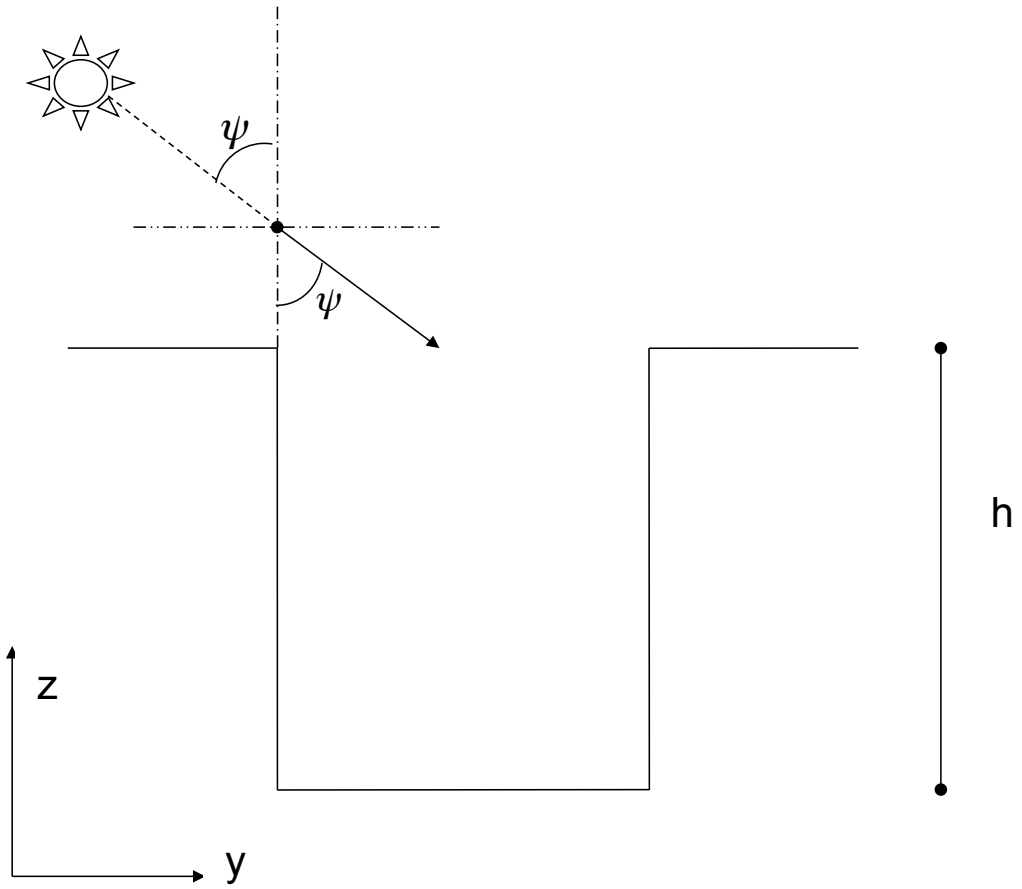

Figure 63: A photon which enters the system has a maximum dwell time in the system, t_{max}, which is determined by the velocity of the photon in the z-direction and the height of the VACNT towers, h.

the initial time zero when the photon enters the system, to the final time when the photon exits, the system, a z-distance of 2h has been travelled.

$$t_{max} = \frac{z}{\vec{v_z}} = \left| \frac{2h}{-\dot{\delta} \cos \psi} \right| \tag{58}$$

Solving t_{max} in the z-direction makes it possible to derive the x- and y-distances travelled in that time.

$$\begin{aligned} x = |\vec{v_x}|t &= \left| -\dot{\delta} \cos \omega \sin \psi \frac{-2h}{\dot{\delta} \cos \psi} \right| \\ &= |2h \tan \psi \cos \omega| \end{aligned} \tag{59}$$

$$y = |\vec{v_y}|t = |2h \tan \psi \sin \omega| \tag{60}$$

The value of Γ can be derived by considering a 3D system which is composed of a perfectly reflecting material. The simplest geometry for a 3D cell would be a single trench, infinite in the y-direction and bounded in the x-direction by two walls of height, h and separated by a distance d (Figure 64). A photon is considered which enters the system with a random y-position and an x-position located x_o from the rightmost wall and velocities in the x- and y-directions determined by the azimuthal angle, ω. Since the trench is considered infinite in the y-direction the velocity in that direction is inconsequential to the final determination of Γ and only the x-direction will be considered.

At time zero, the photon has travelled a distance of zero and the value of Γ is also equal to zero at that time. After a time period of t_1, the photon has traveled a

distance equal to x_o to impact the rightmost wall to give Γ a value of one. After a second time period, t_2, the photon has travel a distance of $x_o + d$ and impacted to the leftmost wall to give Γ a value of 2. This reflecting between walls continues until a time of t_{i+1}, which is the last interaction between a photon and a trench wall. At this point the photon has travelled in the x-direction a value of $x_o + id$ and reflected off the trench wall i+1 times. After this last interaction with the trench wall, the photon then travels a random distance in the x-direction, x_f, before it exits the system at t_f to give a value of Γ equal to i+1 (Table 4.2).

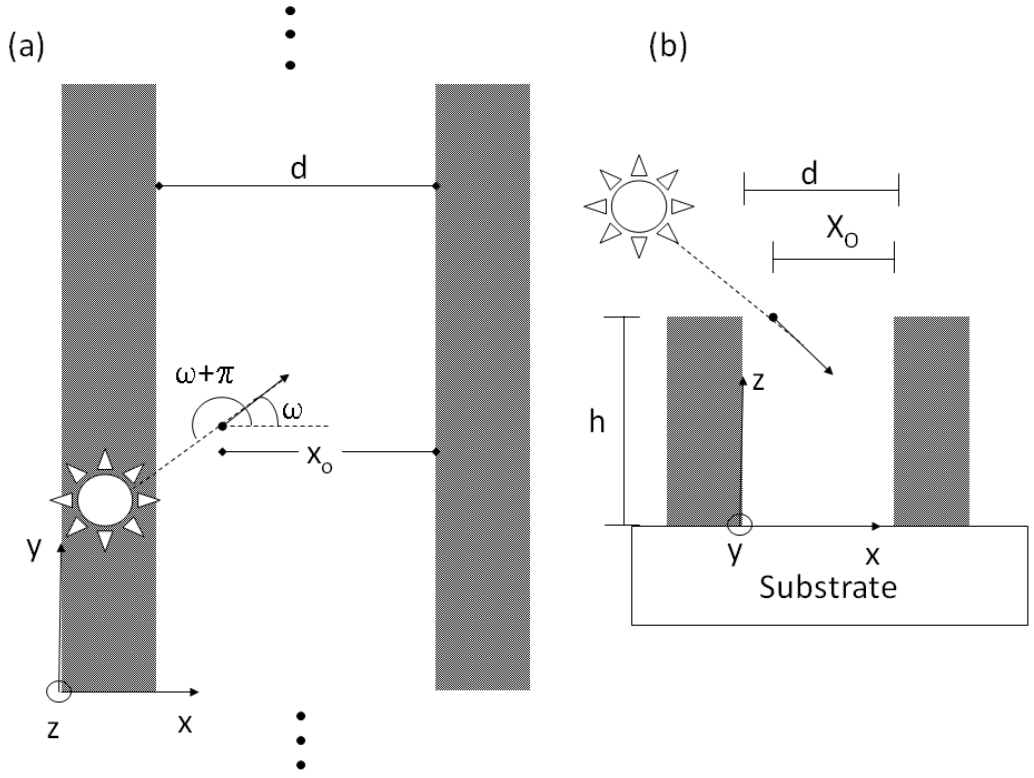

Figure 64: The simplest geometry for a 3D solar cell would be a single infinitely long trench. (a) A schematic shows a plan view of this geometry with a separation between walls of d. The grey portions represent smooth vertical sidewalls. (b) A schematic shows this geometry compressed in the y-direction. A photons entering this geometry from the top enters the system a distance x_o from the rightmost wall with an azimuthal angle of ω.

The total distance travelled by the photon in the x-direction after a time t_{max} is equal to $x_o + id + x_f$.

Table 4: The overall average value of Γ for a system may be determined for a single trench by tracking the distance travelled in the x-direction (x-distance), the elapsed time (t), and the number of interactions with a vertical sidewall (Γ) of a single photon.

x-distance	time	Γ
x_o	0	0
$x_o + d$	t_1	1
$x_o + 2d$	t_2	2
$x_o + 3d$	t_3	3
$x_o + 4d$	t_4	4
$\vdots$	$\vdots$	$\vdots$
$x_o + id$	t_{i+1}	i+1
$x_o + id + x_f$	t_f	i+1

$$\text{x-distance} = x_o + id + x_f = |\vec{v_x}|t = |2h \tan\psi \cos\omega| \tag{61}$$

Furthermore, since the starting position of the photon can be any value from zero to d some photons will enter the trench very close to the rightmost wall (x_o is small) while others enter the system very far away from the rightmost wall (x_o is large). As the number of particles approaches infinity, the average value of x_o will tend towards a value of $\frac{1}{2}d$. The same logic applies to the average value of x_f.

$$x_o \to \frac{d}{2} x_f \to \frac{d}{2} \tag{62}$$

A value of Γ can then derived for this x-trench, Γ_x, by solving for i+1.

$$\begin{aligned} \frac{d}{2} + id + \frac{d}{2} &= |-2h\tan\psi\cos\omega| \\ (i+1)d &= |-2h\tan\psi\cos\omega| \\ i+1 &= \left|\frac{-2h\tan\psi\cos\omega}{d}\right| = \Gamma_x \end{aligned} \tag{63}$$

The overall value of $\Gamma_{\mathrm{x-trench}}$ is equal to $\Gamma_x + 1$ due to a reflection off the floor of the trench which is not inherently accounted for.

$$\begin{aligned} \Gamma_{x-trench} &= \Gamma_x + 1 \\ &= \left|\frac{-2h\tan\psi\cos\omega}{d}\right| + 1 \end{aligned} \tag{64}$$

The same logic applies to a y-trench, which is infinite in the x-direction to give Γ_{y} and $\Gamma_{\mathrm{y-trench}}$

$$\begin{aligned} \Gamma_{y-trench} &= \Gamma_y + 1 \\ &= \left|\frac{-2h\tan\psi\sin\omega}{d}\right| + 1 \end{aligned} \tag{65}$$

An x-trench and y-trench which overlap will form a box. In this instance the photon in a box acts as two decoupled oscillators in the x- and y-directions, since the travel in the y-direction does not affect that in the x-direction. The average number of reflections, Γ_{box}, will be equal to the number of reflections due to movement in the y-direction plus those due to movement in the x-direction.

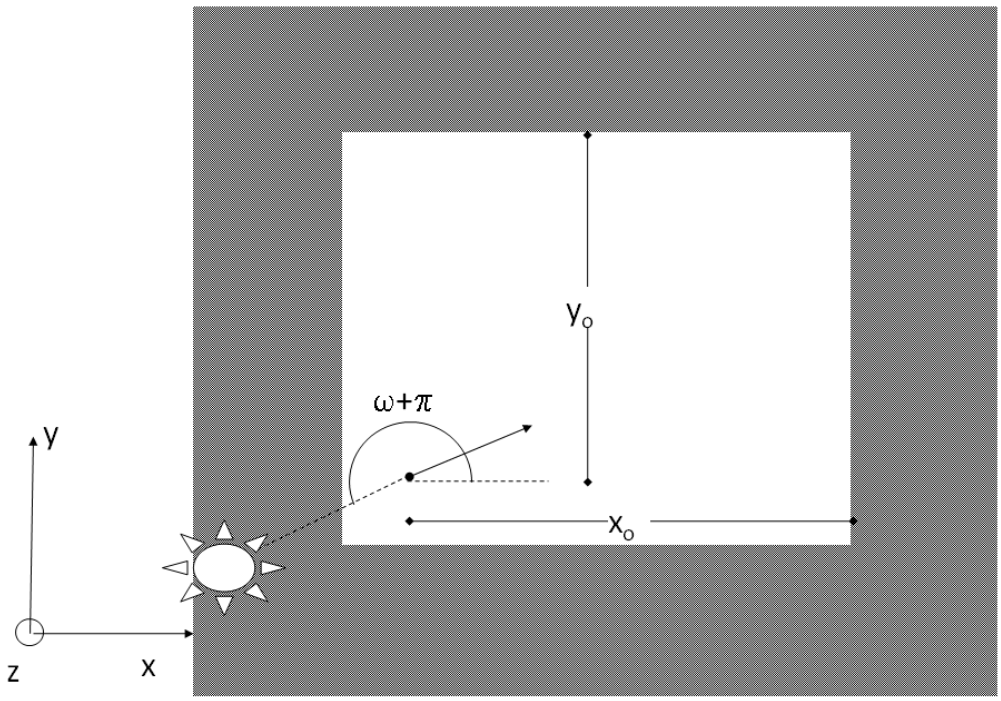

Figure 65: The overlap of an infinite trench in the x-direction with an infinite trench in the y-direction forms an enclosed square. The shaded portions indicated raised sidewalls. A photon enters the top of the system a distance x_o from the rightmost wall and y_o from the top wall. The photon has a velocity direction described by the azimuthal angle ω

$$\begin{aligned}\Gamma_{box} &= \Gamma_x + \Gamma_y + 1 \\ &= \left|\frac{-2h\tan\psi\cos\omega}{d}\right| + \left|\frac{2h\tan\psi\sin\omega}{d}\right| + 1\end{aligned} \tag{66}$$

Another pattern used for 3D solar cells is that of square towers, measuring a size of w on each side with a distance d in between the towers (Figure 66). For such a 2D array of towers, F_o is described by,

$$F_o = \frac{d^2 + 2dw}{(d+w)^2} \tag{67}$$

This 2D array can be reduced to a unit cell. The space in the unit cell between towers can be split into three separate regions. The first region, A, has a width of w and a length of 0.5d. A photon in this region behaves as if it is in a y-trench, as discussed earlier. The second region, B, has the same area as region A, however, a photon in this area will behave as if in an x- trench. The final region, C, is located at the corners of the tower and has a width equal to length equal to 0.5d. A photon in this region does not behave as in any previously discussed manner. A photon in this region may freely switch between the two types of trenches.

$$\text{Area A} = 2Nw\frac{d}{2} \tag{68}$$

$$\text{Area B} = 2Nw\frac{d}{2} \tag{69}$$

$$\text{Area C} = 4N\left(\frac{d}{2}\right)^2 \tag{70}$$

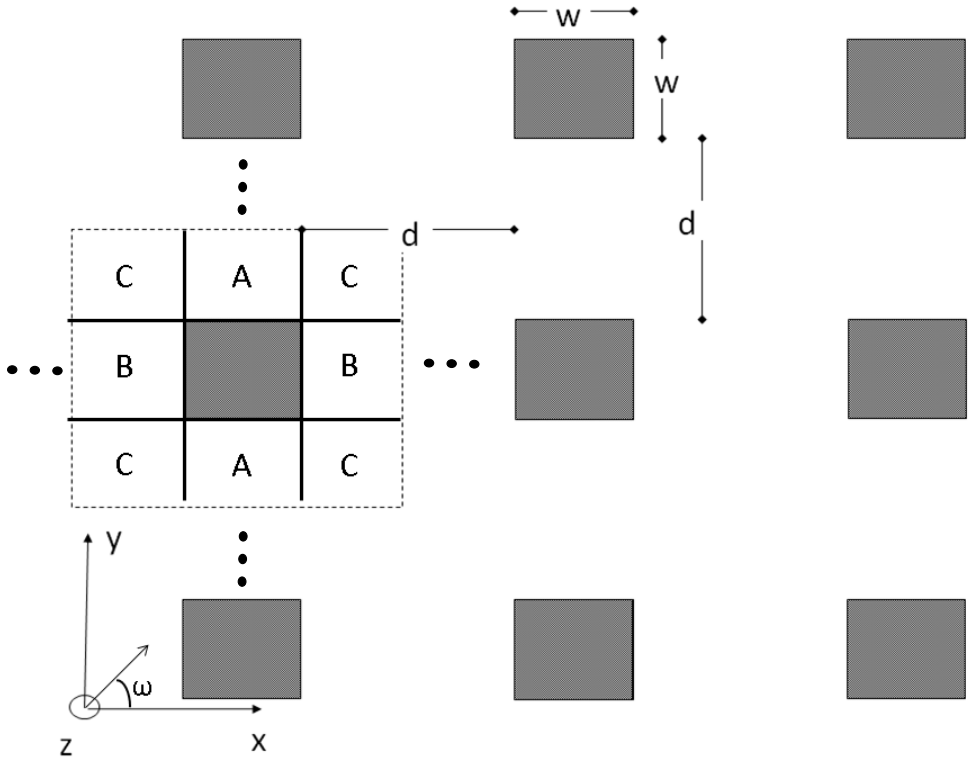

Figure 66: A portion of an infinite 2D array of towers. Each tower (indicated by shaded region) has a dimension on each side equal to w and is separated by a distance d. The hatched line indicates a single unit cell of this infinite array of towers. The unit cell can be split into three areas, A, B, and C. Region A can be considered to be a portion of an infinite (in the x-direction) trench. Photons which enter the system in this space will have Γ=0 if $\omega = 0^o$ or 180^o. If ω= 90^o or 270^o, $\Gamma = \Gamma_{x-trench}$. Region B can be considered to be a portion of an infinite (in the y-direction) trench. Photons which enter the system in this space will have Γ=0 if $\omega = 90^o$ or 270^o. If $\omega = 0^o$ or 180^o, $\Gamma = \Gamma_{y-trench}$. If a photon enters in region C and $\omega = 0^o, 90^o, 180^o$, or 270^o then $\Gamma = 0$.

where N is the number of unit cells.

For a random arrangement of photons with an azimuthal angle equal to 0^o, only those photons in the region marked as B will add to the number of reflections. Those photons in region B will act as if the towers were simply in an x-trench.

$$\Gamma_{towers} = \Gamma_{x-trench} \tag{71}$$

Photons in regions A and C will have no reflections

$$\Gamma_{towers} = 0 \tag{72}$$

So the distribution of reflections for this tower morphology,Γ_{tower}, will be composed of two delta functions with one peak at zero and one at $\Gamma_{x-trench}$. For a random distribution of photons over the entire area of the cell, the overall value of Γ_{towers} will be equal to the area weighted averages of each Γ value in that region.

$$\begin{aligned}
\Gamma_{towers}(\omega = 0^o) &= \frac{A(0) + B(\Gamma_{x-trench}) + C(0)}{A + B + C} \\
&= \frac{2Nw\frac{d}{2}(\Gamma_{x-trench})}{Nwd + Nwd + 4N\frac{d^2}{4}} \\
&= \frac{w(\Gamma_{x-trench})}{2w + d} \\
&= \frac{w}{2w + d} \times \left| \frac{-2h \tan\psi \cos\omega}{d} \right|
\end{aligned} \tag{73}$$

The same logic applies for an azimuthal angle equal to 90^o with a y-trench replacing an x-trench and the area of A replacing that of B.

$$\Gamma_{towers}(\omega = 90^o) = \frac{w(\Gamma_{y-trench})}{2w+d} = \frac{w}{2w+d} \times \left| \frac{2h \tan\psi \sin\omega}{d} \right| \tag{74}$$

Although we can know the values of Γ_{towers} exactly for $\omega = 90^o, 180^o,$ and 270^o, an exact solution of Γ_{towers} for any arbitrary ω cannot be derived. For any arbitrary value of ω, the simplest approximation of a 2D array of towers would be of a system of two independent, intersecting trenches. This would assume that photons which enter the system in area A would behave in the same manner as those in an y-trench ($\Gamma_{y-trench}$) and those photons which enter the system in area B would behave in the same manner as those in an x-trench ($\Gamma_{x-trench}$). This very simple approximation would ignore any photons which switch between the two types of trenches. Because of this, this approximation will overestimate the value of Γ because the travel distance to switch between trenches is larger than it would be for a reflection off a trench wall. The implications of this approximation will be discussed in the next section. With this approximation, the value of Γ_{towers} will be

$$\Gamma_{towers}(\omega) = \frac{w}{2w+d} \times (\Gamma_{x-trench} + \Gamma_{y-trench}) \tag{75}$$

$$= \frac{2hw \tan\psi}{d(2w+d)} \times (|\cos\omega| + |\sin\omega|) \tag{76}$$

To account for the single reflection off the substrate floor the overall number of reflections must be incremented by unity.

$$\Gamma = \Gamma_{towers} + 1 \tag{77}$$

$$= \frac{2hw \tan\psi}{d(2w+d)} \times (|\cos\omega| + |\sin\omega|) + 1 \tag{78}$$

4.3 Simulations

In order to determine what affects the various mask parameters have on the number of photon impingements and efficiency of a CNT based PV cell, a computer simulation was created. For ease of programming and utility of matrix mechanics, the simulation was written in Mathworks (Natick, MA) MATLAB 2009a. Simulations were run on both a Dell (Round Rock, TX) Optiplex GX620 3.0 GHz with 2GB RAM running Microsoft (Redmond, WA) Windows XP and the Georgia Tech Acme Unix kernel running SunOS 5.9 by Sun Microsystems (Santa Clara, CA). The program was a 2D simulation in the xy-plane with the z-direction mathematically coupled through ψ. The program investigates the average number of impingements of an incident photon due to different configurations of tower arrays before it exits the system. This average number of impingements per photon was used to determine the absorption of a 3D cell in various tower configurations.

A set of (N=100,000) photons were generated with pseudo-random positions seeded with the clock time and directions of motion in the XY-plane calculated using the azimuthal angle value. The impingements with each tower were recorded and, after each impingement, a unit reflection matrix was applied across the tower normal to alter the direction of motion and the new position was the site of impingement. The number of impingements for each photon was calculated and averaged over N photons to arrive at a value for Γ at each simulation condition.

4.3.1 Azimuthal Angle

The comparison between simulated data (points) and theory (lines) for Γ for the three type of 3D cells (trench, box, and 2D array of towers) for various azimuthal angles is shown in Figure 67. The data is shown for a tower height of 40μm, separation of 10μm, width of 40μm, zenith angle of 45^o and azimuthal angle ranging from 0^o to 90^o in 5-degree increments. For this configuration, the theory fits the simulation exceedingly well for all three models with a maximum relative error of 0.167% for the trench configuration, 0.736% for the box, and 0.613% for the 2D array of towers.

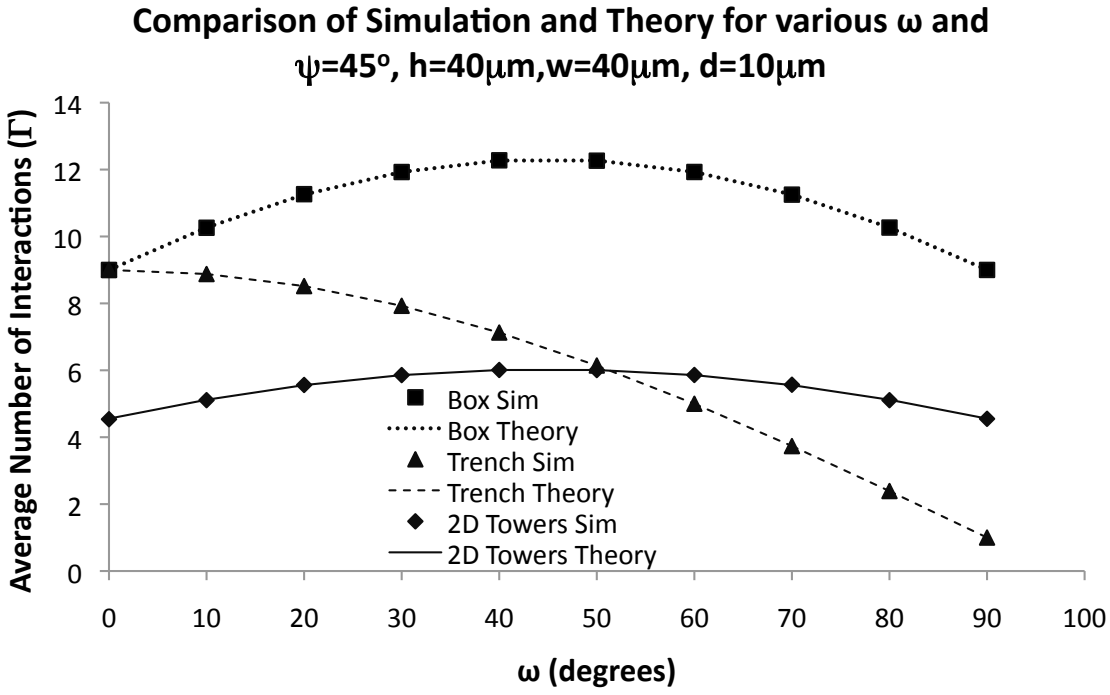

Figure 67: Comparison between simulation and theory of Γ for three types of three 3D cells, a single infinite trench, a box, and a 2D array of towers. Data shown is for photons with an incident zenith angle of 45^o and various azimuthal angles. Each cell was composed of 40μm towers 40μm×40μm in height separated by a distance of 10μm.

4.3.2 Tower Separation

The comparison between simulated data (points) and theory (lines) for Γ for the three type of 3D cells for various tower separations is shown in Figure 68 for d ranging

from 0.004 to 4000μm. The data is shown for a tower height of 40μm, width of 40μm, zenith angle of 85^o, and azimuthal angle of 35^o. For this configuration, the theory fits the simulation well for all three models for the entire range of d with a maximum relative error of 0.264% for the trench configuration, 1.15% for the box, and 3.47% for the 2D array of towers. The larger error for the 2D array configuration occurs for very small values of d where the value of Γ increases very quickly.

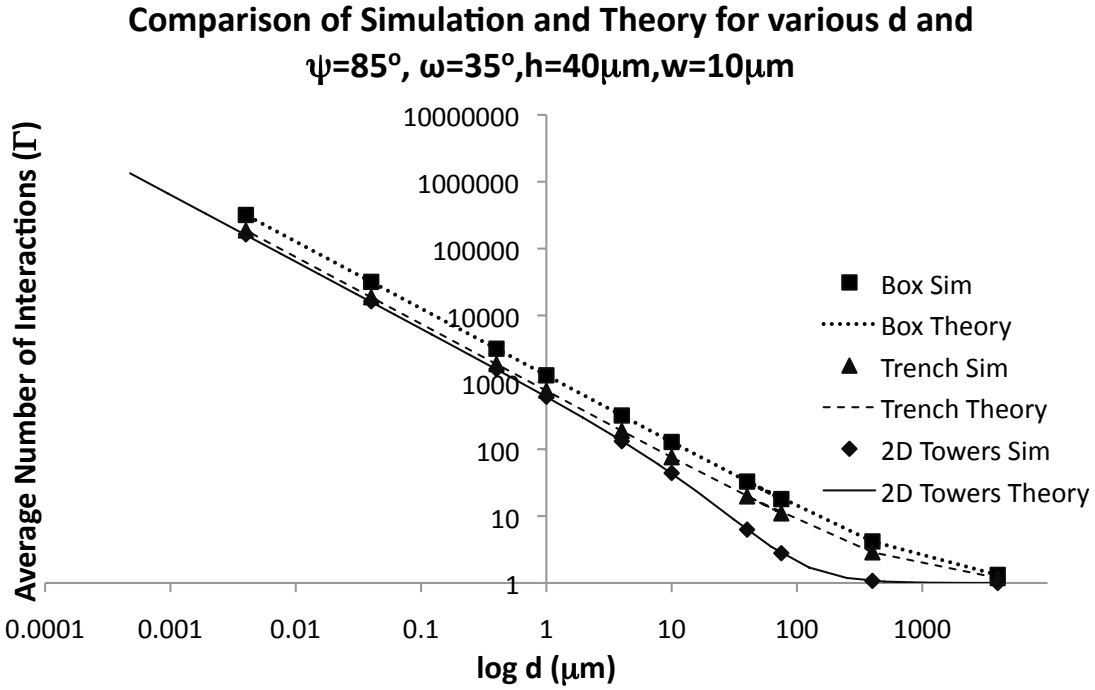

Figure 68: Comparison between simulation and theory of Γ for three types of 3D cells, a single infinite trench, a box, and a 2D array of towers. Data shown is for photons with an incident zenith angle of 85^o and an azimuthal angle of 35^o. Each cell was composed of 10μm$\times$10μm towers of 40μm height separated by a varied distance.

4.3.3 Tower height

The comparison between simulated data (points) and theory (lines) for Γ for the three type of 3D cells for various tower heights is show in Figure 69 for h ranging from 0.04 to 3250μm. The data is shown for a tower separation of 10μm, width of 4μm, zenith angle of 85^o, and azimuthal angle of 35^o. For this configuration, the theory fits the simulation well for two of the models for the entire range of h.

The box has a maximum relative error of 0.196% for all the simulations while the trench has a maximum relative error of 0.293%. For the case of the 2D array of towers, however, the theory overestimates the value of Γ due to the assumption of two intersecting orthogonal trenches. While the theory predicts a value of Γ which is linearly dependent on the tower height by a constant of 0.7075 (determined by substituting the values of w,d, ω, and ψ into the relevant equation), simulations have determined that the linear constant is actually closer to 0.56. For large values of Γ, this leads to an overestimation of around 26.5%.

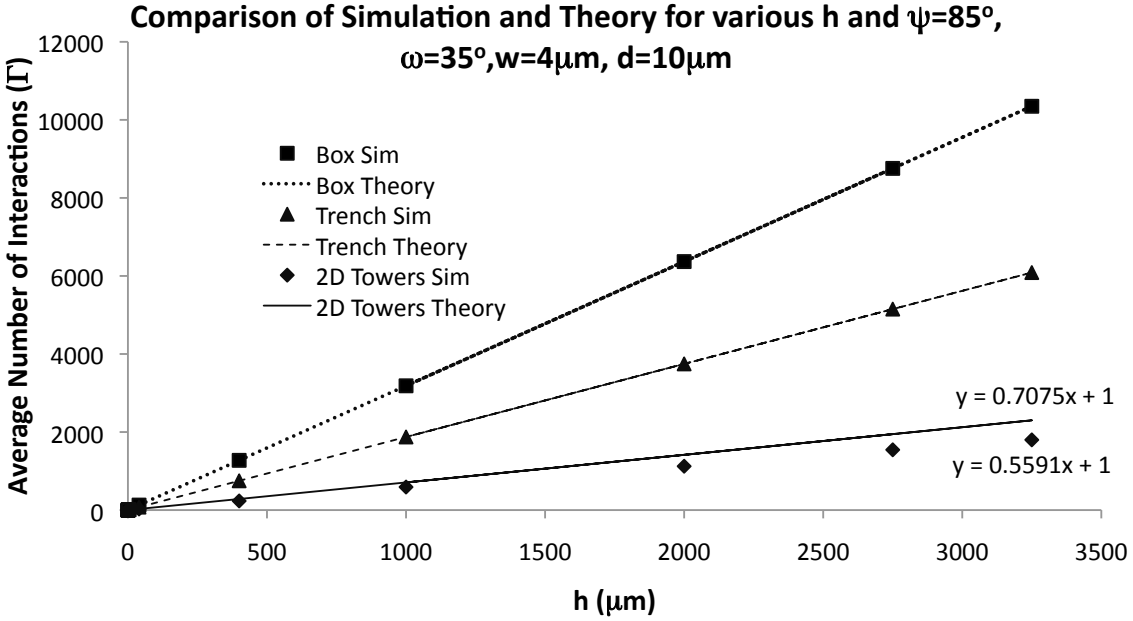

Figure 69: Comparison between simulation and theory of Γ for three types of 3D cells, a single infinite trench, a box, and a 2D array of towers. Data shown is for photons with an incident zenith angle of 85^o and an azimuthal angle of 35^o. Each cell was composed of 4μm$\times 4\mu$m towers of varied heights separated by a distance of 10μm.

The natural question would then be how much does an error in the value of Γ propagate to the actual measured power output of the cell. The values for η_{3D} were calculated from both the theoretical and simulated data for Γ for all previously simulated values of h, ψ, and ω. Two P_{mp} values were then calculated, one for the simulated data and one for the theoretical data. The relative power error is the

difference between the two P_{mp} values divided by the P_{mp} value from the simulated data [239].

$$RE_{P_{mp}}(\%) = \frac{|P_{theory} - P_{simulation}|}{P_{simulation}} \times 100 \tag{79}$$

After analysis, the propagation of error from Γ is highly dependent on η_{2D}, the absorption efficiency of a 2D cell composed of the same material. Figure 70 is a graph of how the maximum value of the error in P_{mp} changes as a function of η_{2D}. For η_{2D} equal or greater than 0.25, the maximum relative error in P_{mp} is less than 1%. All solar cells are composed of materials which have external quantum absorbance efficiencies well in excess of this value. For example, the quantum efficiency of a typical CdS/CdTe solar cell is approximately 80% for wavelengths ranging from 550-800nm [240]. Therefore, the error in the theory of Γ should be small enough that it should still accurately describe the power output from a 3D cell of this type.

4.3.4 Absorption Efficiency

The absorption efficiency, η_{2D}, of a cell is of primary importance to the power output of 3D cells. P_{mp} values were calculated for a 3D cell with η_{2D} of 0.01, 0.05, 0.15, 0.25, 0.5, 0.75, 0.9, and 1. P_{mp} vs. ψ results are shown in Figure 71.

From Figure 71 the power output of a 3D cell increases with increasing absorption efficiency. The maximum point in the P_{mp} vs ψ graph also occurs at higher zenith angles. This indicates that the $\Gamma \approx \infty$ approximation is valid for more zenith angles as η_{2D} increases. All of this would suggest that a 3D cell with as high an absorbance as possible would create the most efficient device.

However, the ratio between the maximum value of the P_{mp} vs. ψ curve and the value of P_{mp} at $\psi = 0^o$ decreases with increasing absorption efficiency. This indicates that the 3D morphology produces a lower power output when compared to a similar

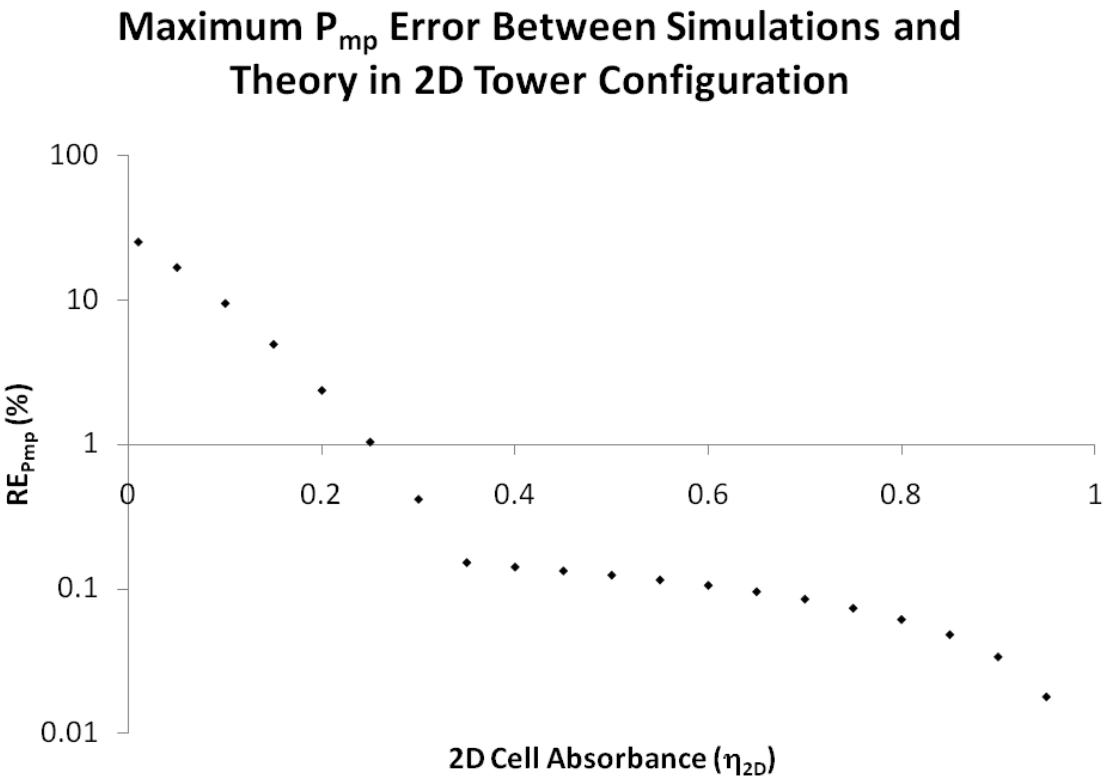

Figure 70: Maximum relative error between theory and simulation for a 2D infinite array of towers. The large error in Γ accounts for only a very small error in the actual power output of a cell.

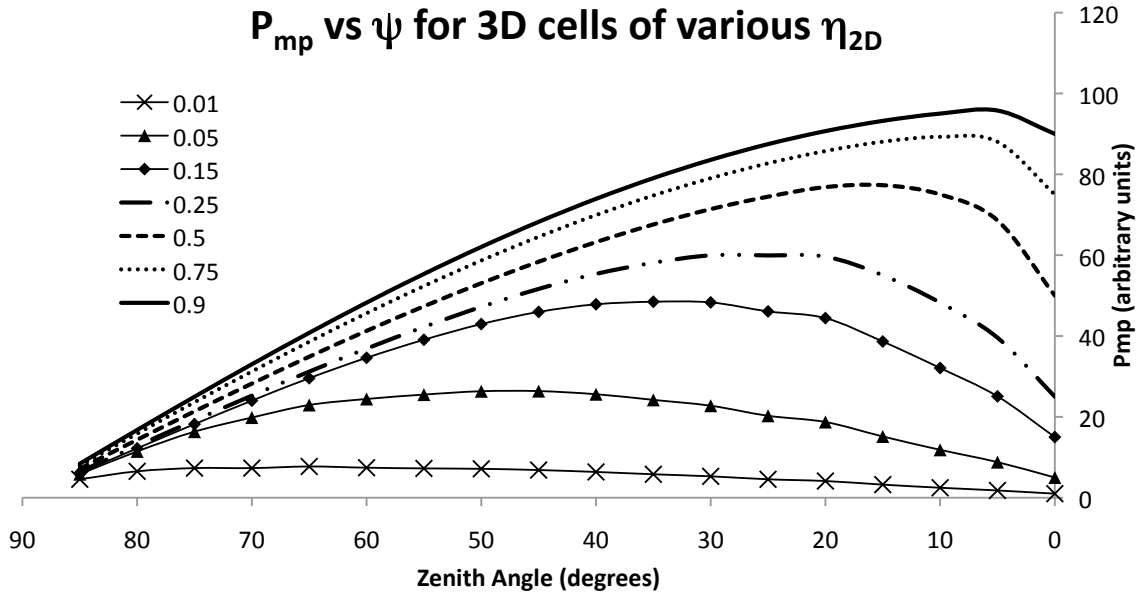

Figure 71: P_{mp} vs zenith angle for 3D cells with absorption efficiency, η_{2D} equal to 0.01, 0.05, 0.15, 0.25, 0.5, 0.75, 0.9, and 1. The power output of a 3D cell increases with increasing absorption efficiency. The maximum point in the P_{mp} vs ψ graph also occurs at higher zenith angles. This indicates that the $\Gamma \approx \infty$ approximation is valid for more zenith angles as η_{2D} increases, though the ratio of the power output for a 3D cell compared to a similar 2D cell actually decreases with increasing η_{2D}.

cell utilizing planar morphology. In other words, for higher absorption efficiency, the 3D morphology becomes less important and the gap between 3D cells and 2D cells closes. Qualitatively, this is understandable, because, for an η_{2D} value of unity, the first impingement results in absorbance and the multiple impingements of the 3D morphology is no longer useful.

This statement can be understood qualitatively. For simplicity, if an ideal 3D cell (one for which $\Gamma \approx \infty$ for all solar angles) located on the equator during the fall or spring equinox is considered, then it is assumed that the sun moves at a constant rate across the sky and there are exactly twelve hours of direct sunlight. The solar disc will travel at a constant rate of 15^o per hour. Using this conversion Figure 61 can be converted from a P_{mp} vs. ψ diagram to a P_{mp} vs. time diagram without a change in the relative shapes of the curves (Figure 72).

The integrated area underneath a power vs. time curve gives information about the energy generated. As can be seen from Figure 72, the ideal 3D cell has an increased area underneath the P_{mp} vs. time curve. The ratio of energy produced by an ideal 3D cell compared to a planar cell ($\mathrm{E}_{\frac{3D}{\mathrm{Planar}}}$) is given by

$$
\begin{aligned}
E_{\frac{3D}{Planar}} &= \frac{2 \times \int_0^{\frac{\pi}{2}} P_{mp}^{3D} d\psi}{2 \times \int_0^{\frac{\pi}{2}} P_{mp}^{planar} d\psi} \\
&= \frac{\int_0^{\frac{\pi}{2}} \eta_{3D} \times \cos\psi d\psi}{\int_0^{\frac{\pi}{2}} \eta_{2D} \times \cos\psi d\psi} \\
&= \frac{\int_0^{\frac{\pi}{2}} \left(F_o[1-\eta_{2D}] + \eta_{2D}\right) \cos\psi d\psi}{\int_0^{\frac{\pi}{2}} \eta_{2D} \times \cos\psi d\psi} \\
&= \frac{F_o \int_0^{\frac{\pi}{2}} \cos\psi d\psi}{\eta_{2D} \int_0^{\frac{\pi}{2}} \cos\psi d\psi} - \frac{F_o \times \eta_{2D} \int_0^{\frac{\pi}{2}} \cos\psi d\psi}{\eta_{2D} \int_0^{\frac{\pi}{2}} \cos\psi d\psi} + \frac{\int_0^{\frac{\pi}{2}} \eta_{2D} \cos\psi d\psi}{\int_0^{\frac{\pi}{2}} \eta_{2D} \cos\psi d\psi} \\
&= \frac{F_o}{\eta_{2D}} - F_o + 1
\end{aligned}
\tag{80}
$$

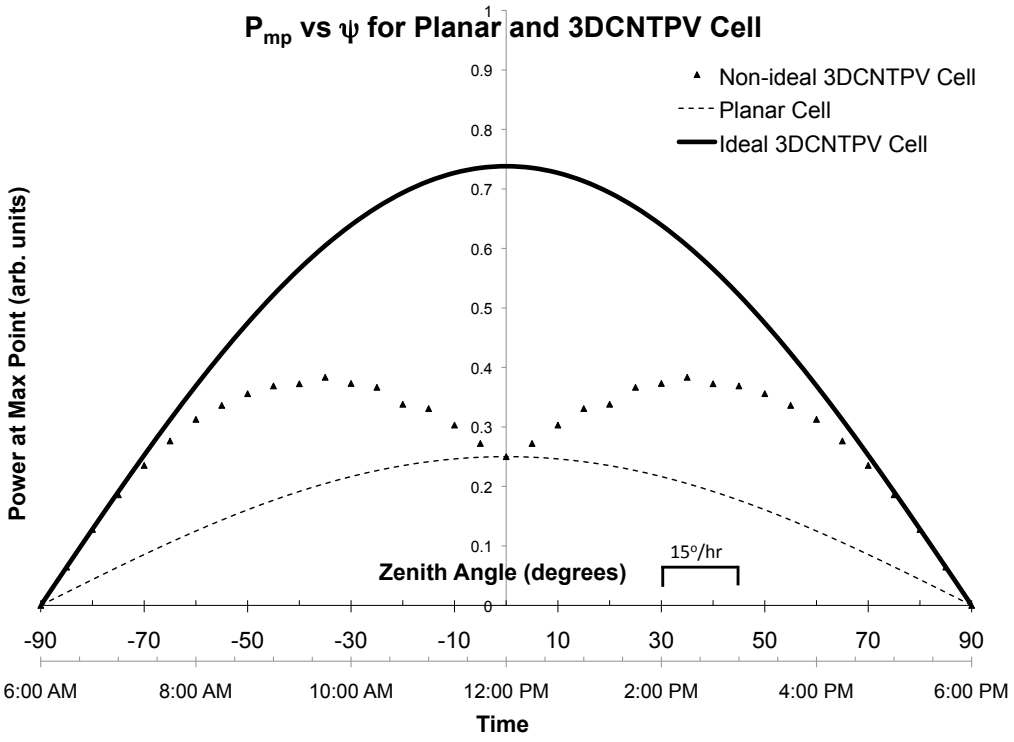

Figure 72: P_{mp} vs. time for a planar cell, ideal 3DCNTPV cell, and non-ideal 3DCNTPV cell for a day with a sunrise (ψ=-90^o) at 6AM and sunset (ψ=90^o) at 6PM. During the twelve hour day the sun has a constant ω value of 0^o and subtends zenith angles -90 to 90^o at a rate of 15^o per hour.

Since this 3D cell is ideal, this is the highest possible ratio of output energies from a 3D cell compared to a similar planar cell. η_{2D} and F_o are always less than one, this means that $E_{\frac{3D}{Planar}}$ is greater than one. Therefore the ratio of energy produced from a 3D cell to that of a planar cell will always be greater than one. For a constant F_o the ratio of the energy produced is inversely proportional to the absorbance efficiency (Figure 73). So an ideal 3D cell would be made of a material with a relatively low absorption efficiency. This would maximize the 3D morphology as compared to a similar cell in a planar configuration.

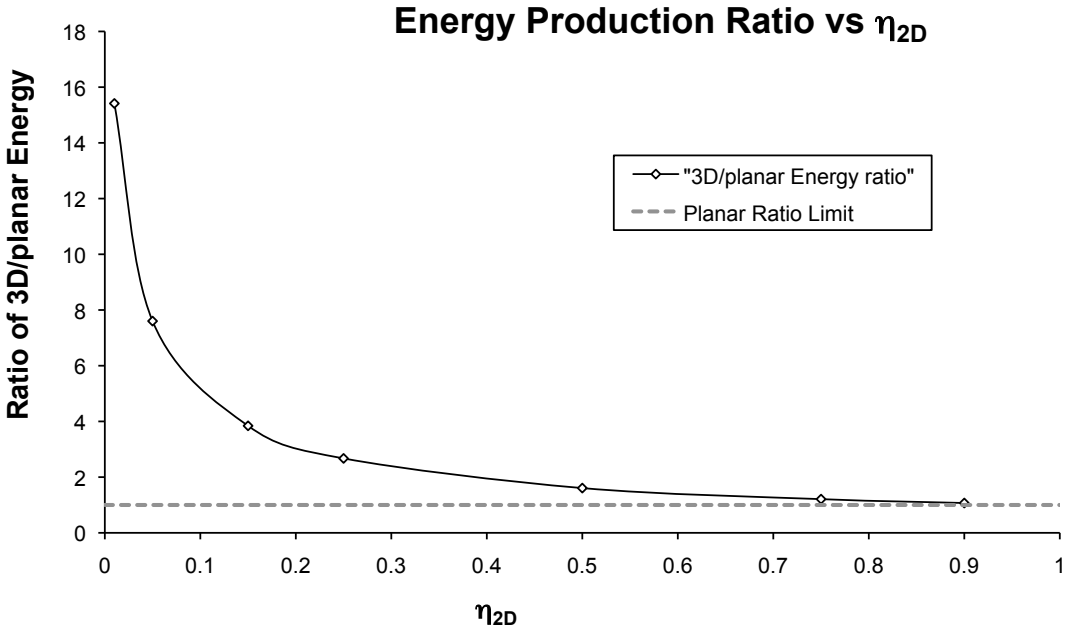

Figure 73: The maximum energy output ratio of a solar cell in a 3D vs 2D morphology. This maximum energy output ratio is inversely proportional to η_{2D} so to maximize the 3D morphology, the photoactive material should have a relatively low absorption efficiency.

4.3.5 Tower Shape

Various tower geometries for a 2D array of towers were simulated (Figure 74). A 2D array of circular towers, both staggered and uniform were simulated. Uniform 2D array of towers whose shapes were defined by the parametric equations for a

lam*é* curve, eight curve, rhodonea curve, asteroid curve, and Talbot's curve were also simulated.

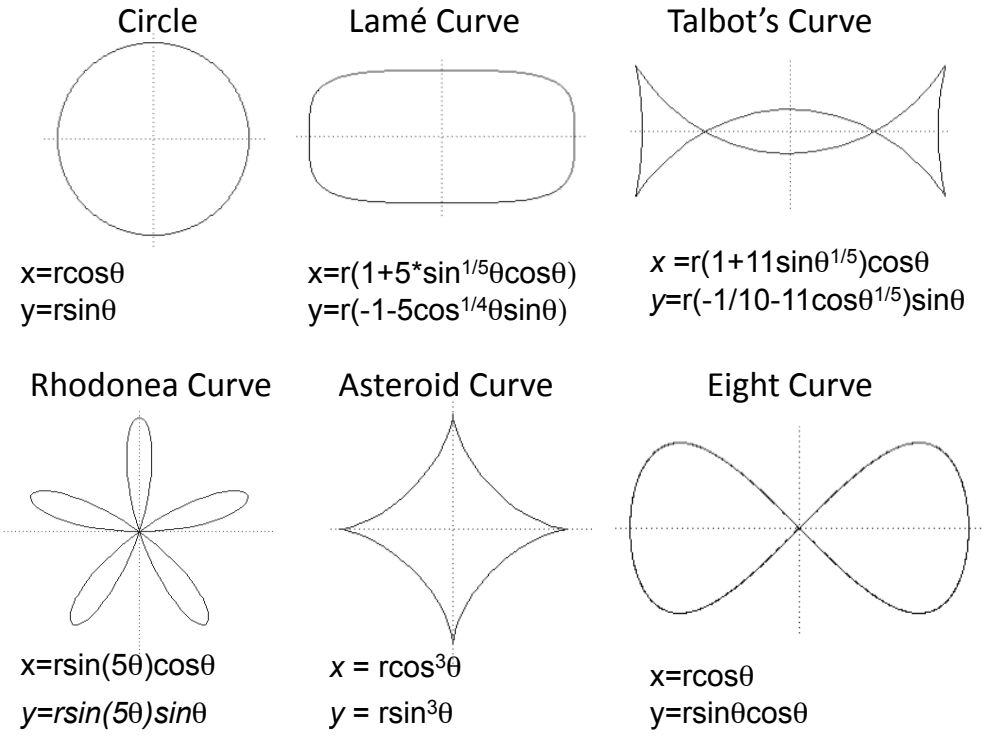

Figure 74: Tower geometries simulated with corresponding parametric equations. (Top left to right) Circle (both staggered and unstaggered arrays), Lam*é* Curve, Eight Curve (Bottom left to right) 5-pointed Rose (Rhodonea), Asteroid Curve, Talbots Curve

For all geometry simulations the aspect ratio was two, η_{2D} was 0.25, and F_o was 0.1963. The energy output for these curves was found by fitting the P_{mp} vs. ψ curve with a polynomial line using SPSS Inc TableCurve2D v 5.0 (Chicaco, IL) and then numerically integrating. It was found that an increase in perimeter/area ratio roughly corresponded to an increase in the energy output.

The energy output tends to increase with an increase in perimeter to area ratio, indicating an increase in the value of Γ. This is understandable, since a higher

perimeter to area ratio indicates a highly concave polygon. These polygons have many inlets and concavities where a photon may interact multiple times with a given tower. For a convex polygon, a photon will interact only once. This effect is the slightest of previously discussed parameters.

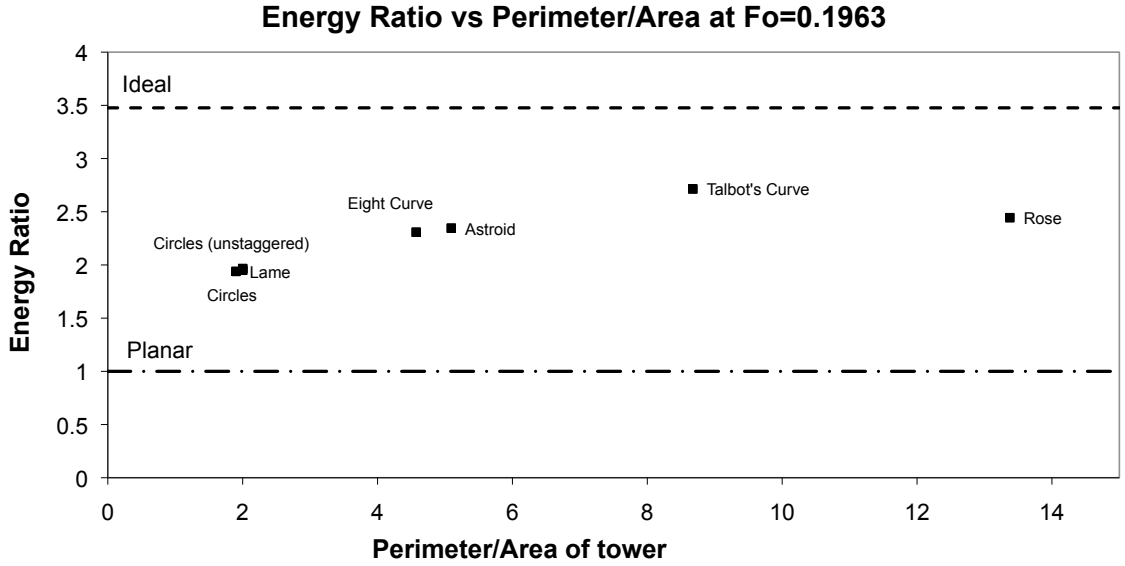

Figure 75: Energy output vs. perimeter to area ratio for various tower geometries. A higher perimeter/area ratio indicates a highly concave shape. A photon may pinball in these inlets and concavities, increasing the value of Γ over that of a purely convex tower. As the perimeter/area ratio increases, the energy output shows a slight increase, though the effect is the slightest of any of the previously discussed parameters.

4.4 Nonspecular Reflection

One of the major assumptions for a theory of η_{3D} is that the VACNTs specularly reflect incident light. However, as seen from the SEM images, the CdTe/CdS coated VACNTs are not smooth. The VACNTs are textured both by the grains present in the semiconductors, but also because the VACNTs are composed of many individual CNTs. Due to the presence of this texture, it would not be expected for the VACNTs to show completely specular reflection. So simulations were carried out for VACNTs which have nonspecular reflection.

One of the most common ways to represent diffuse reflection is through Lambertian reflection (Figure 76). While the incident and reflected angles are identical in specular reflection, in Lambertian reflection, the reflected ray varies as the cosine to the surface normal. In other words,

$$\begin{aligned} I_{diff} &\propto \hat{N}\hat{L} \\ &\propto \cos\alpha \end{aligned} \tag{81}$$

where $\mathrm{I_{diff}}$ is the diffusely reflected intensity, $\hat{\mathrm{N}}$ is the surface normal vector, $\hat{L}$ is the incident light vector, and α is the angle between the normal and the incident light vector.

The simulations carried out previously were altered so that photons interacting with the 3DCNTPV cell walls are not always reflected specularly. The percentage of specular vs. Lambertian reflectance is specified before the simulation so that at each interaction, a photon may be reflected either specularly or nonspecularly. If the particle reflects nonspecularly, then the probability of the direction of reflection is varied so that for many such interactions, the overall intensity will vary as the cosine seen in Lambertian reflectance. Figure 77 shows the results of this type of simulation for an infinite trench in the x-direction, wall height of 80μm, and a wall separation of 40μm. The percentage of specular reflection was varied from 0% to 100%.

While the shape of the curves stay constant. There is a decrease in the value for Γ as the amount of nonspecular reflection increases. For the system described above, the value of Γ at $\psi = 85^o$ from 38.4 for completely specular reflection to 30.9 for completely Lambertian reflection. As Lambertian reflection increases, the histogram for values of Γ changes from a near delta function to a function which can be approximated by a Gaussian with negative skew.

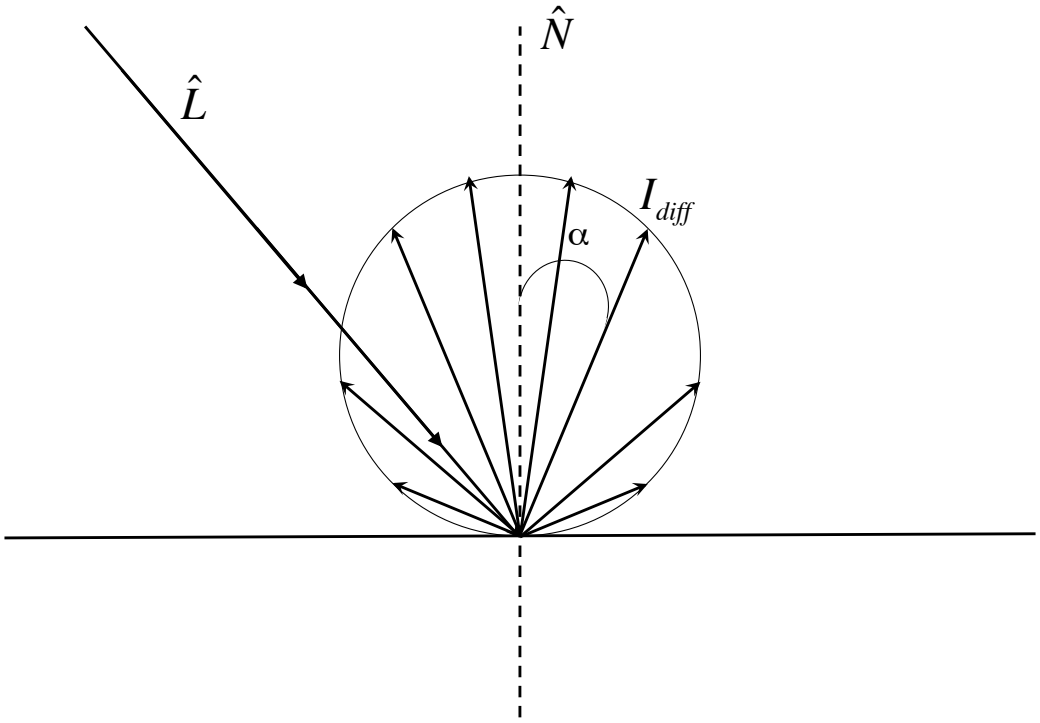

Figure 76: Lambertian reflection of an incident light ray, $\hat{\mathrm{L}}$, off a surface. The intensity of the diffusely reflected light, I_{diff}, varies as the $\cos\alpha$, where α is the angle between the light ray and the surface normal, $\hat{N}$.

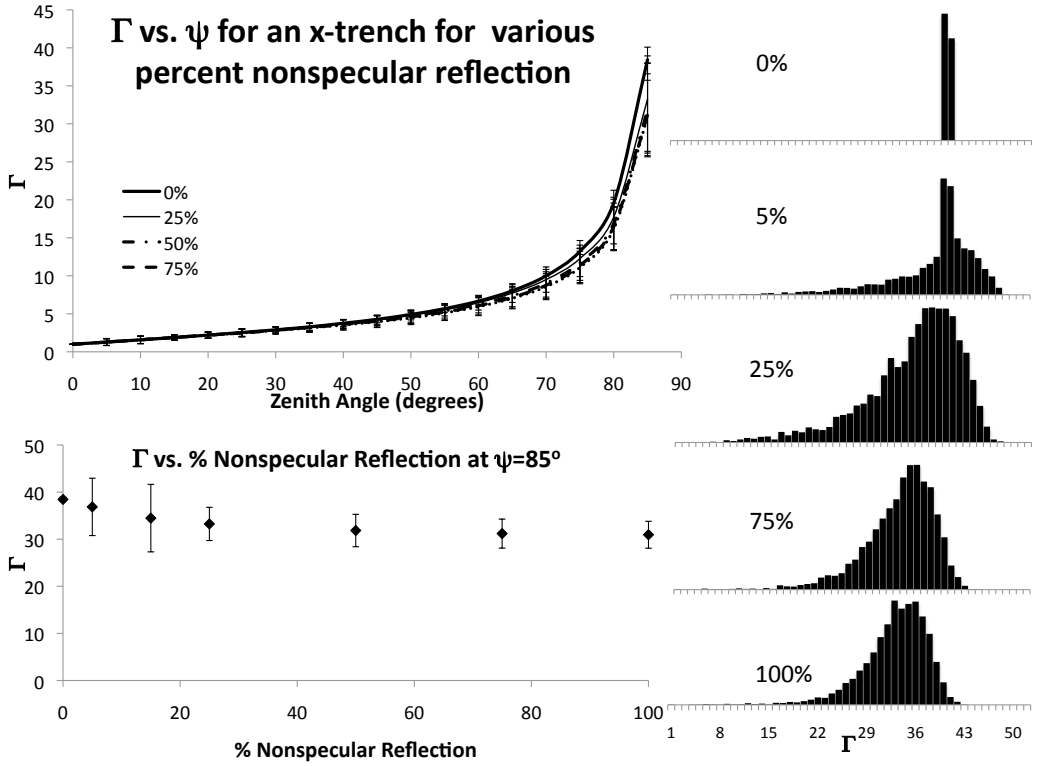

Figure 77: Results of simulations for various percentage Lambertian reflection in an infinite x-trench. (Top Left) The graph of Γ vs. ψ shows that the shape of the curves stay constant with different amount of diffuse reflection. In general, as the amount of diffuse reflection increases, the value of Γ slightly decreases with a larger standard deviation in the simulated values. (Bottom Left) Γ vs. percent nonspecular reflection at a constant azimuthal angle of 85^o. As diffuse reflection increases, there is a drop in the average value of Γ from 38.4 at 0% Lambertian reflection to 30.9 at 100% Lambertian reflection. The spread in the data also increases with increasing diffuse reflection. (Right) Histogram of Γ values for simulations at 0%, 5%, 25%, 75%, and 100% Lambertian reflection. The distribution of Γ goes from a near delta function at 0% to a distribution which is better approximated by a Gaussian with negative skew at 100% nonspecular reflection.

Although the mean value of Γ decreases as the percentage of specular reflection increases, this difference is difficult to detect when measuring the power output of a cell. Figure 78 shows the P_{mp} vs. ψ curves for a 3DCNTPV cell composed of a series of x-trenches with an F_o of 0.25, η_{2D} of 0.25, wall height of 80μm, and a wall separation of 40μm. The P_{mp} curves for different percentages of nonspecular reflection lie almost on top of each other. There is only a very slight difference in the power output for the zenith angles in the range of 25^o to 60^o.

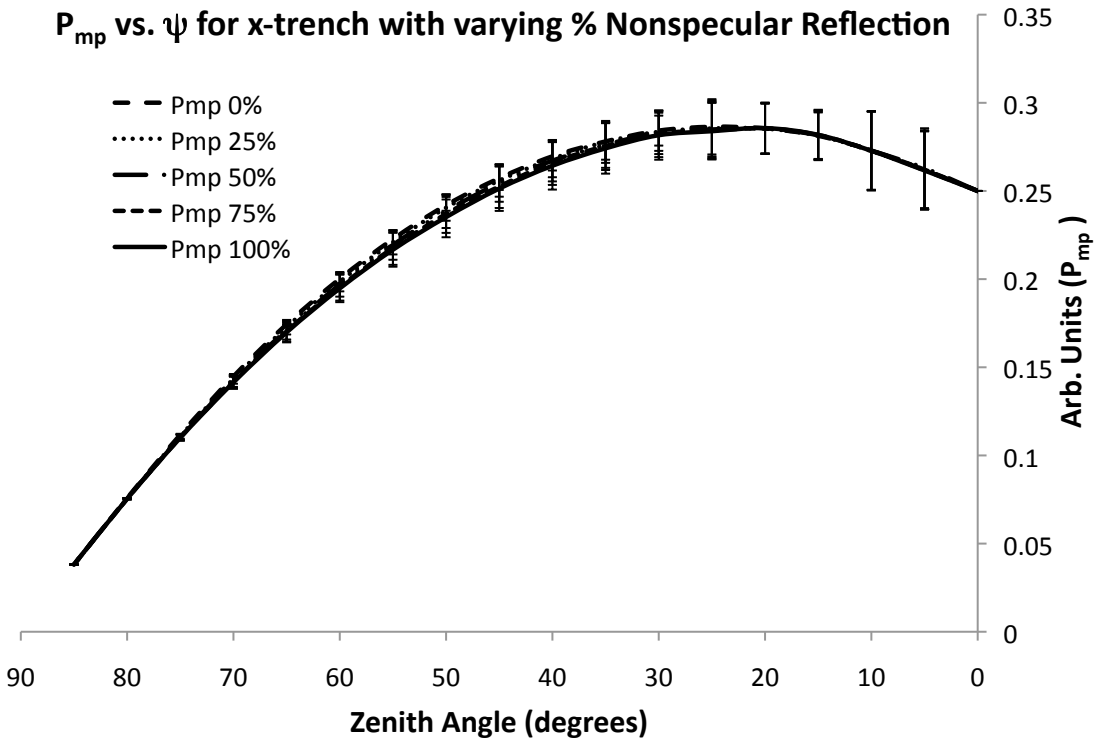

Figure 78: P_{mp} vs. ψ for 3DCNTPV cell exhibiting different amount of nonspecular reflection. The cells are composed of an array of x-trenches with an F_o of 0.25, η_{2D} of 0.25, wall height of 80μm, and a wall separation of 40μm. The power output of each of the cells is nearly identical even though there is a slight decrease in the value of Γ as nonspecular reflection increases.

4.5 Reflection at different angles

Another simplification in the development of η_{3D} is that the absorption of a material is constant with regard to incident angle of light. Fresnel's law states that the

reflectance of a boundary between two materials with different indices of refraction will vary as the angle of incident light changes. More specifically, for s-polarized (perpendicular to the plane of incident ray and surface normal) light, the reflectance ($\mathrm{R_{s-polarized}}$) will vary as

$$R_{s-polarized} = \left(\frac{n_1 \cos \alpha_i - n_2 \cos \alpha_t}{n_1 \cos \alpha_i + n_2 \cos \alpha_t} \right)^2 \tag{82}$$

where n_1 is the index of refraction of the first material, n_2 is the index of refraction of the second material, α_i is the incident angle of light relative to the surface normal, and α_t is the transmission angle of light relative to the surface normal (Figure 79).

Similarly, p-polarized (in the plane of the incidence ray and surface normal) light behaves in a similar manner, with the reflection, $\mathrm{R_{p-polarized}}$, described by,

$$R_{p-polarized} = \left(\frac{n_1 \cos \alpha_t - n_2 \cos \alpha_i}{n_1 \cos \alpha_t + n_2 \cos \alpha_i} \right)^2 \tag{83}$$

For unpolarized light, it is assumed that the light is composed of equal parts s- and p-polarized light.

$$R_{total} = \frac{R_{s-polarized} + R_{p-polarized}}{2} \tag{84}$$

For a 3DCNTPV devices, the incident angle of light relative to the surface normal is different for material located on tower tops and tower sidewalls. The surface normal for tower tops and the system floor is colinear with $\hat{z}$, so the incident angle of light is equal to the zenith angle ψ. The surface normal for sidewalls, however,

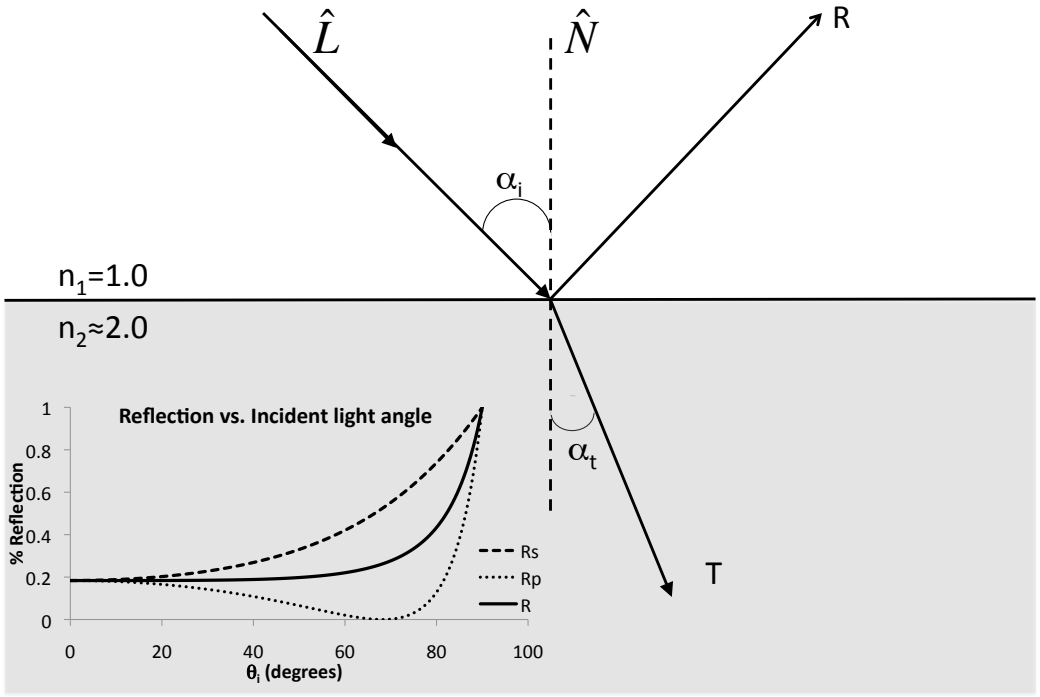

Figure 79: An incident light ray, $\hat{L}$, interacting with a material interface between air (n_1=1.0) and ITO ($n_2 \approx 2.0$) at an incident angle of α_i with the interface normal, $\hat{N}$. The ray is either reflected (R) or transmitted (T) through the material at an angle to the interface normal of α_t. The amount of light reflected or transmitted varies as the incident angle changes according to the Fresnel equations. The inset graph shows how the reflection s- and p-polarized light varies with incident angle. Assuming unpolarized light, the reflectance is the average of the two polarizations (solid black line).

is perpendicular to $\hat{z}$, so the incident angle of light is actually $90^o - \psi$. Therefore, equation 42, where it was assumed that η_{2D} was the same for all portions of the cell, must be altered so that tower tops, tower sidewalls, and the system floor all have different η_{2D} values.

By substituting separated absorption efficiencies for tower tops (η_{2D}^{Top}) and tower sidewalls ($\eta_{2D}^{Sidewall}$) into the appropriate equations, p_s becomes

$$\begin{aligned} p_s &= 1 - \text{probability of continuous reflection} \\ &= 1 - R_{Sidewall}^{\Gamma} \times R_{Floor} \\ &= 1 - (1 - \eta_{2D}^{Sidewall})^{\Gamma} \times (1 - \eta_{2D}^{Floor}) \end{aligned} \tag{85}$$

and p_t becomes

$$p_t = \eta_{2D}^{Top} \tag{86}$$

N, T, and S remain unchanged. So, allowing for Fresnel's equations, equation 42 becomes

$$\begin{aligned} \eta_{3D} &= \eta_{2D}^{Top}(1 - F_o) + F_o(1 - R_{Sidewall}^{\Gamma} \times R_{Floor}) \\ &= \eta_{2D}^{Top}(1 - F_o) + F_o(1 - (1 - \eta_{2D}^{Sidewall})^{\Gamma} \times (1 - \eta_{2D}^{Floor})) \end{aligned} \tag{87}$$

For this equation, Γ is no longer incremented by one in order to account for reflection off the device floor. Γ only accounts for interactions with tower sidewalls, so Γ=0 for $\psi = 0^o$. Figure 80 shows a P_{mp} vs. ψ graph for planar and 3D cells

accounting for Fresnel's equations. The dashed lines indicate planar and 3D cells accounting for Fresnel's equations while the solid line represents a 3DCNTPV cell P_{mp} without accounting for Fresnel's equations.

This 3D cell is represented by a interface between air and ITO with $n_1 = 1.0$ and $n_2 = 2.0$ (ITO has an index of fraction between 2.0 and 2.5 in the visible region [68, 60]). This 3DCNTPV cell is composed of towers with F_o of 0.5, a tower diameter of 40μm, tower spacing of 20μm, and tower height of 150μm. The planar cell no longer quite follows a cosine trend at higher angles due to the high reflectivity as ψ approaches 90^o. The 3D cell, accounting for Fresnel's equations, still displays a 3D inverted C-type curve. However, the maximum of this curve moves toward higher ψ angles with a slower rise to that maximum. This decrease in power output at angles near $\psi = 0^o$ is due to the near unity reflection at the sidewall interface. Over the entire range of zenith angles, the power output of the 3D cell is greater than the planar cell because, as ψ increases, the reflectance of the tower sidewalls rapidly decreases while the reflectance of the tower tops rapidly increases. This combination of tower tops and orthogonal tower sidewalls leads to a higher absorption over the entire range of ψ than is possible in a planar cell.

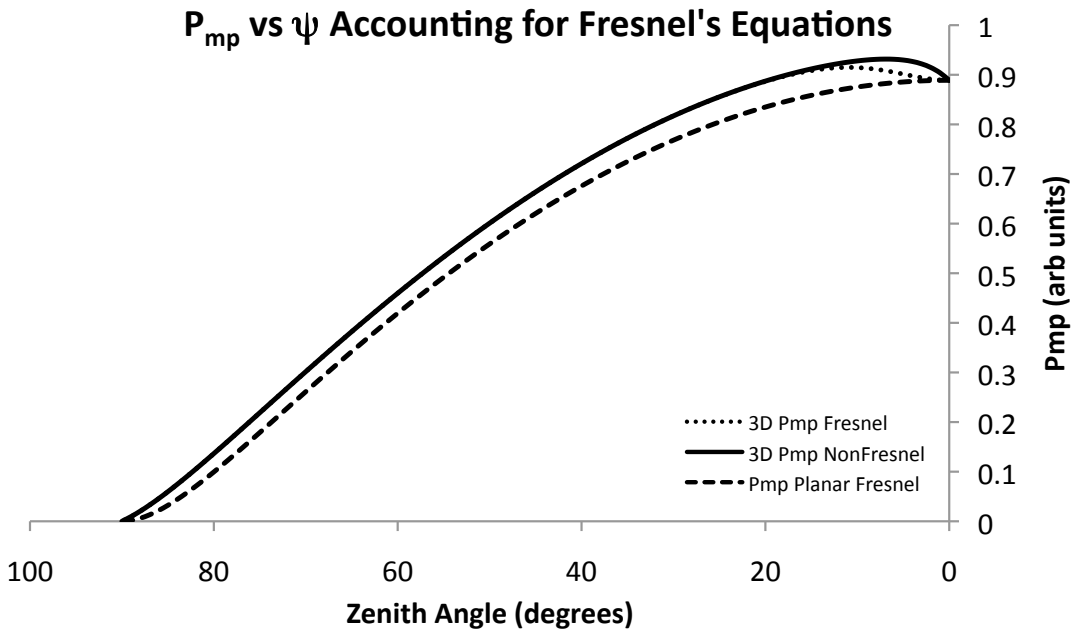

Figure 80: P_{mp} vs. ψ graph for planar and 3D cells accounting for Fresnel's equations. The dashed lines indicate planar and 3D cells accounting for Fresnel's equations while the solid line represents a 3DCNTPV cell P_{mp} without accounting for Fresnel's equations. The 3D cell is represented by a interface between air and ITO with $n_1 = 1.0$ and $n_2 = 2.0$. This 3DCNTPV cell is composed of towers with F_o of 0.5, a tower diameter of 40μm, tower spacing of 20μm, and tower height of 150μm.

CHAPTER V

RESULTS AND DISCUSSION

5.1 MBE Cells

A series of 18 3DCNTPV cells were created using the production process flow described in Chapter 3. These cells were labeled MBE xxx. Table 5 shows the figures of merit for 3DCNTPV cells created using this method.

These cells have a good yield, with only 1 cell (MBE 252) nonfunctional. They are characterized by low I_{sc}, with values varying from 0.85 to 178.72 μA/cm^2. These values of I_{sc} are small even for cells prior to any $CdCl_2$ postprocessing. They are also characterized by low V_{oc} values ranging from 0.31 to 122.21 mV and fill factors of approximately 25%.

Fill factors of 25% indicate a totally shunted cell and is the smallest FF possible without an inversion or curvature. R_{sh} and R_s values were calculated as described in §2.1.2.2, by taking the inverse slope of the IV curve at small negative voltages and at large positive voltages, respectively. R_{sh} varies from 5.3mΩ to 2.765 kΩ. This is several orders of magnitude lower than commercially available solar cells. Shunting is shown by the fact that the values of R_{sh} and R_s only nominally differ. For a working diode, these values should differ by orders of magnitude.

Figure 81 shows a dark IV curve for cell MBE 170 (solid line), which is typical of the series. The IV curve has very little curvature and more resembles a resistor. This IV curve has no diode character for the entire voltage range and demonstrates no noticeable knee. This is also indicative of a shunt. The dark IV curve on a semilog plot (dashed line) is clearly dominated by the shunt current with very little contribution from the recombination or diffusion currents. The light IV curve (Figure

Table 5: Figures of merit for 3DCNTPV cells manufactured according to the process flow in Chapter 3. These cells have low I_{sc}, on the order of $10\mu A/cm^2$. They are also characterized by V_{oc} values less than 150 mV and fill factors around 25%. The values of R_{sh} and R_s are of the same order of magnitude for all the completed cells. All of these factors indicate shunting present in the cells.

Sample Name	I_{sc} $\mu A/cm^2$	V_{oc} mV	FF %	P_{mp} nW/cm^2	R_{sh} Ω	R_s Ω
MBE 112	19.84	82.03	24.27	395.0	2,418.50	2,269.68
MBE 170	69.26	122.21	25.30	2,141.1	722.86	392.63
MBE 173	178.72	62.05	24.72	2,741.7	2,530.43	111.00
MBE 193	9.20	10.35	25.16	24.0	0.0053	0.0069
MBE 194	23.22	3.00	25.94	18.1	110.39	36.89
MBE 202	52.51	11.58	24.34	148.1	386.56	260.01
MBE 218	0.88	0.69	33.17	0.146	490.97	452.78
MBE 233	13.68	8.98	25.10	30.8	320.58	210.65
MBE 238	55.86	55.63	26.02	808.5	359.14	220.92
MBE 248	4.42	4.43	25.99	5,087.1	924.64	196.97
MBE 251	53.38	22.95	26.33	322.6	210.39	123.62
MBE 252	-	-	-	-	-	-
MBE 257	15.62	2.82	26.21	11.5	68.41	60.13
MBE 263	21.83	91.64	25.08	501.7	605.69	268.40
MBE 265	0.85	0.31	23.89	63.5	344.66	267.42
MBE 267	165.35	46.63	25.29	1,950.1	135.80	98.78
MBE 268	56.12	48.01	22.16	597.1	1,072.90	305.42
MBE 269	24.41	3.56	25.85	22.5	58.55	47.29

82) of MBE 170 similarly shows no curvature. The IV curve is simply a straight line offset into the fourth quadrant to indicate power production.

The creation of these working cells indicates that the 3DCNTPV structure can be used to create working solar cells. However, these cells are plagued by very low power output and massive shunting. The process flow of the 3DCNTPV cells was altered in order to identify the causes of these inefficiencies and then eliminate them.

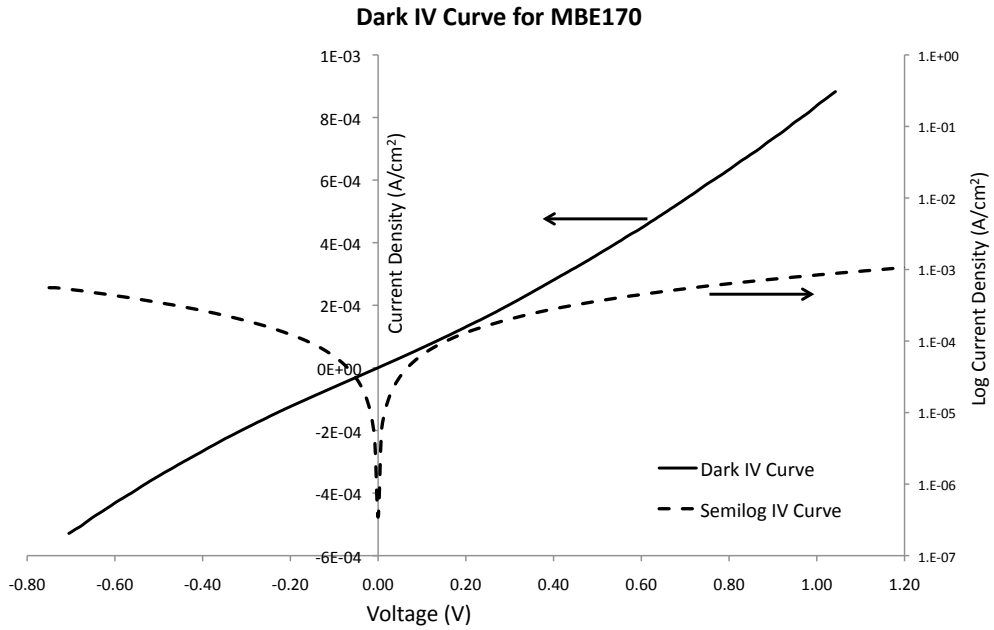

Figure 81: Dark IV curve (solid line) of MBE 170 under an applied voltage -0.75 to 1.5V. The IV curve is typical of all the cells created using this process flow and has little curvature. The IV curve more resembles that of a resistor than a diode. The lack of curvature is shown by the values of R_{sh} and R_s being nearly equal, indicating that the cell is shunted. This is more evident in the semilog dark IV curve (dashed line) which is dominated by the shunt current

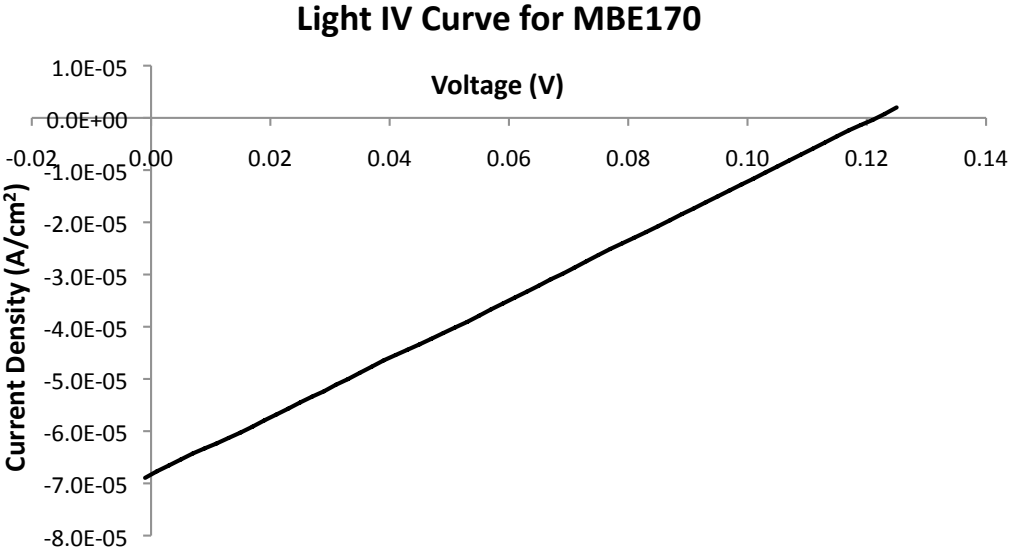

Figure 82: Light curve of MBE 170 showing an I_{sc} of 69.26μA/cm^2 and a V_{oc} of 122.21mV for a P_{mp} of 2,141.1nW/cm^2. The light curve, like the dark curve, shows no curvature, but is offset from the dark curve into the fourth quadrant, indicating power production.

5.2 Chemical Bath Deposition Cells

Chemical bath deposition CBD is the most commonly used method to fabricate CdS films for high efficiency cells [88]. It has the main advantages of being simple, easily controlled, and readily scaled to larger sized devices. In order to determine if the 3DCNTPV architecture was amenable to this manufacturing method, the CdS window layer was deposited via CBD in a number of cells. Table 5.2 lists the chemicals, their uses, and the concentrations used in the chemical bath.

Table 6: Chemical name, formula, concentration, and purpose of the materials used to deposit CdS via CBD.

Chemical Name	**Formula**	**Concentration**	**Purpose**
Cadmium Chloride	$CdCl_2$	0.0327 M	Cadmium source
Thiourea	$CS(NH_2)_2$	0.0686 M	Sulfur source
Ammonium Chloride	NH_4Cl	0.734 M	Buffer
Ammonium Hydroxide	NH_4OH	52.5% by vol.	Cadmium complexing agent

CBD cells are fabricated by using the process flow described in Chapter 3. However, after CdTe deposition via MBE, CBD is used to deposit the CdS window layer. The CBD method is modified from the process described in [241]. This process was chosen because the procedure used is simple and fastidiously explained. It also yields CdS films of high quality which have been used to create cells with demonstrable efficiencies of up to 15.4%, as measured by NREL. At the time of publication this efficiency was close to the record for a cell with a CBD CdS layer.

The CdS layer is created by mixing 100mL of the $CdCl_2$ solution with 200mL NH_4Cl solution and 250mL NH_4OH buffer. The mixture is heated to 85^{o}C and gently agitated with a magnetic stirrer. The CdTe covered 3DCNTPV samples are added to the bath. The samples are allowed to thermally equilibrate for 10 minutes. 24mL of the thiourea solution is added in 2mL increments every 10 minutes. During the thiourea addition, the solution turns from clear to a dark yellow color, indicating the

formation of CdS. After all the thiourea is added, the samples are removed from the chemical bath and dried. Following drying, ITO is deposited via IAD.

The overall CBD reaction is described by [242]

$$Cd(NH_3)_4^{2+} + CS(NH_2)_2 + 2OH^- \rightarrow CdS + CH_2N_2 + 4NH_3 + 2H_2O \qquad (88)$$

Ten samples were created using this CBD process to deposit CdS. Samples CBD 232A and CBD 241 were then air annealed in an oven for 60 minutes at 250 and 550^{o}C, respectively.

Table 7 shows the figures of merit for the cells created using this CBD technique.

Table 7: Figures of merit for 3DCNTPV cells created using a CBD step for the CdS window layer. The I_{sc} and V_{oc} values are similar in scale to the cells with MBE deposited CdS layer. The FF values are still approximately 25% and the R_{sh} and R_s values are on the same order, indicating a shunt still exists for the CBD cells.

Sample Name	I_{sc} μA/cm^2	V_{oc} mV	FF %	P_{mp} nW/cm^2	R_{sh} Ω	R_s Ω
CBD 172	-	-	-	-	-	-
CBD 191	0.84	60.56	27.68	16.1	86,482.74	768.70
CBD 221	-	-	-	-	-	-
CBD 230	-	-	-	-	-	-
CBD 231	50.0	62.03	24.91	772.1	1,349.27	997.70
CBD 232A	119.9	163.37	27.15	5,319.0	1,839.59	1,709.69
CBD 232B	0.47	0.90	24.59	0.10	1,962.09	880.36
CBD 241	90.43	114.05	25.64	2,643.9	990.59	578.17
CBD 243	0.061	1.02	25.17	0.016	8,711.56	1,528.30

The yield of the cells utilizing CBD of the CdS is lower than those only utilizing MBE. These cells were analyzed post mortem and it was discovered that the agitation of the stirrer bar in the chemical bath had a deleterious effect on the VACNTs. Even with gentle stirring, the VACNTs could be sheared off the solar cell surface of some of the cells. Figure 83 (Top) are two SEM micrographs of CBD 230 showing VACNTs present before the CBD, but notably absent after the deposition is complete.

The I_{sc} values for these cells are of the same order of magnitude at those created using the all MBE method with values varying from 0.61 to 119.9μA/cm^2. Except for CBD 231 and CBD 241, the I_{sc} values of the CBD cells are all lower than the MBE created cells. This is most likely due to thick, inhomogeneous coverage of the CdS layer, which parasitically absorbs incident light with no increase in output current. Figure 83 (Bottom) shows CBD 231 after CBD deposition. The CBD has left excess CdS in the form of platelike deposits. These layers are much too thick and parasitically absorb incident light, leading to an overall decrease in the I_{sc} values.

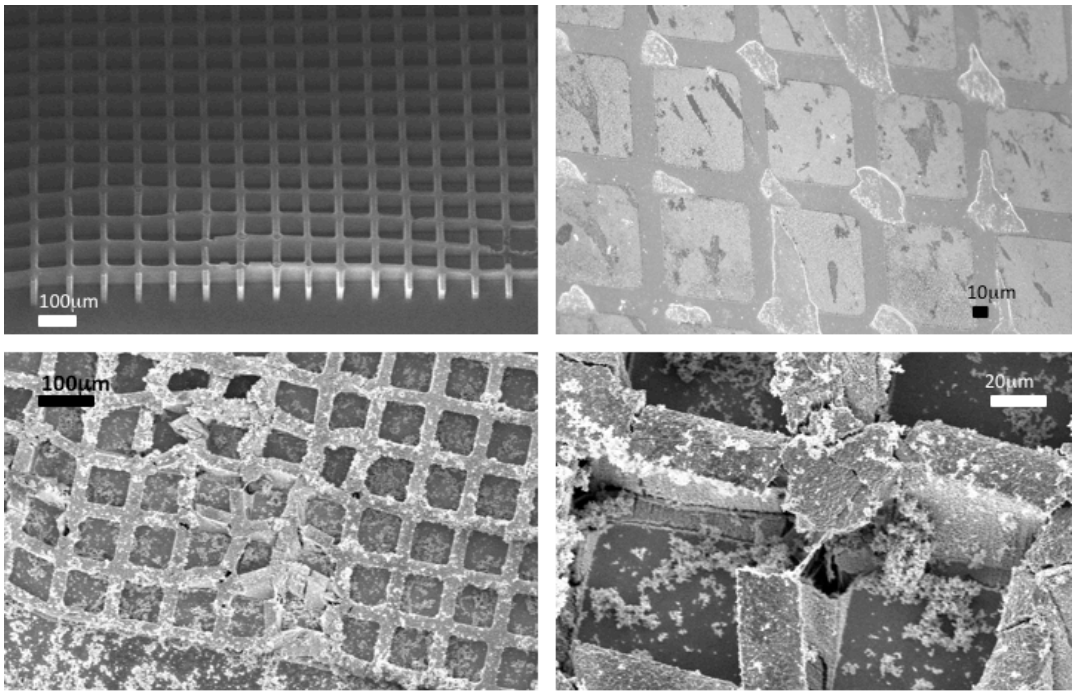

Figure 83: SEM micrographs illustrating two problems with CBD. The top images show MBE 230 before (top left) and after (top right) CBD of CdS. The VACNTs have been sheared off in the bath due to overagitation. The bottom images show inhomogenous CdS deposition in CBD 231 (bottom left). Thick plate-like deposits of excess CdS have formed on both the Si substrate and the VACNTs. These deposits are much too large and parasitically absorb incident light, decreasing from the power output of these types of cells.

The V_{oc} values are consistent with those created using the all MBE deposition method with values from 0.90 to 163.37mV. In order to more easily compare the CBD cells to those created using MBE, Figure 84 shows the MBE and CBD cells on

a graph with the I_{sc} density on the abscissa and the V_{oc} on the ordinate. The CBD cells are shown by triangles while the MBE cells are represented as diamonds. The CBD cells show lower I_{sc} values on the average and similar V_{oc} values as the all MBE cells. The lower I_{sc} is most likely due to inhomogeneous CdS deposition.

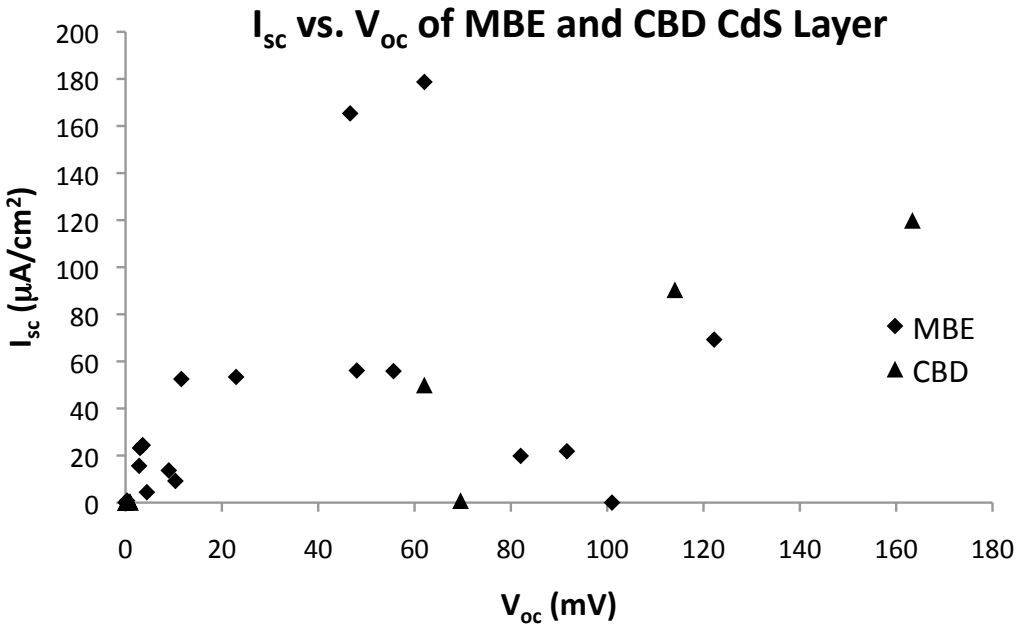

Figure 84: Graph of I_{sc} vs. V_{oc} for cells created using MBE deposition of both CdS and CdTe (diamonds) and using a CBD deposition step for CdS and MBE deposition for CdTe (triangles). The I_{sc} and V_{oc} values for each type of cell are fairly consistent with MBE having a higher average I_{sc}. This is most likely due to inhomogeneous deposition of the CdS layer during CBD which leads to parasitic absorption. Due to simplicity of deposition, MBE was chosen as the deposition method for both CdTe and CdS layers.

The FF values of the CBD cells are also consistent with the MBE deposited cells and are very nearly equal to 25%, indicating that these cells also suffer from a shunt. Figure 85 shows the dark IV curve from CBD 241. This curve is very similar to the curves taken from the other CBD deposited cells and displays very little curvature along the entire length. The semilog of the dark IV curve is dominated by the shunt current. This indicates that the shunting problem observed in the MBE cells is not alleviated by changing the CdS deposition method to CBD.

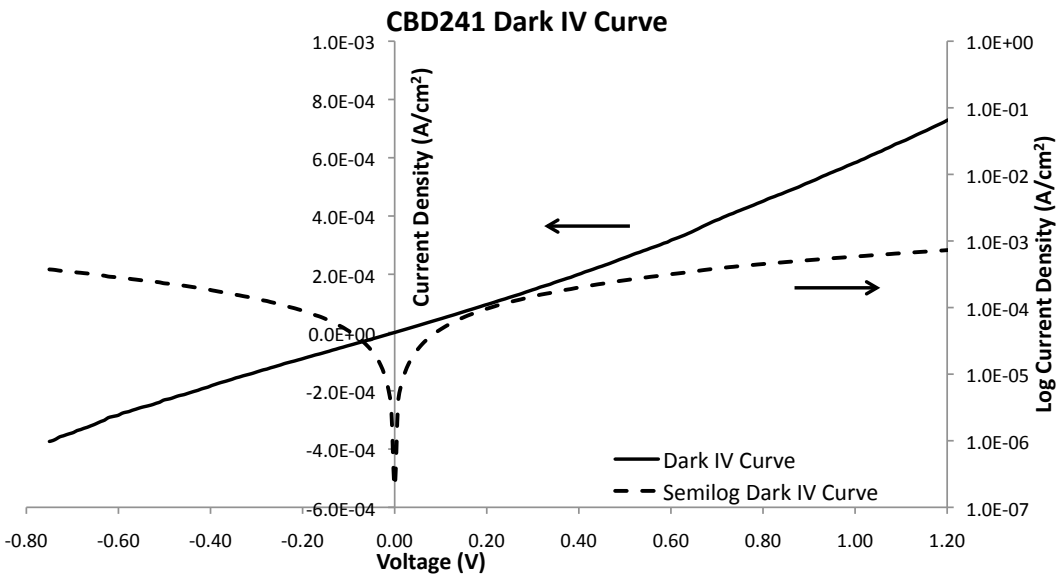

Figure 85: Dark IV curve of CBD 241 under an applied voltage -0.75 to 1.5V (solid line). The IV curve is typical of all the cells created using this process flow and has little curvature, much like the cells created using an all MBE deposition method. This indicates that the cell is shunted and the shunt is not alleviated by changing the CdS deposition method to CBD. The semilog of the dark IV curve (dashed line) shows that the shunt current dominates the IV curve of the cell.

The corresponding light IV curve for CBD 241 Figure 86 is very similar to the curves for the all MBE deposited cells. The curve is a single straight line with nearly zero curvature, indicating a massive shunting problem in the cell.

The creation of these working cells indicates that CBD can, with modifications, be used to deposit the CdS layer on 3DCNTPV cells. However, due to damage to the VACNT structures, inhomogeneous CdS deposition, the large amounts toxic liquid wastes produced, and the need to optimize yet another deposition method, it was determined that utilizing MBE for both CdTe and CdS deposition offered the greatest chance to improve the power output of the 3DCNTPV cells. While MBE may sacrifice sample scalability, it allows for much greater control and deposition simplicity than using MBE in conjunction with CBD. All of the following cells in this chapter have both the CdTe and CdS layer deposited via MBE.

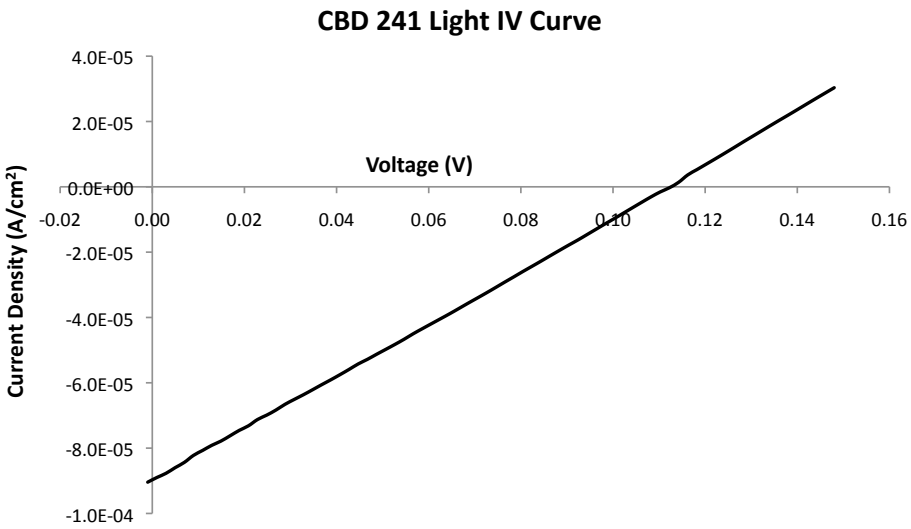

Figure 86: Light curve of CBD 241 showing an I_{sc} of 90.43μA/cm^2 and a V_{oc} of 114.05mV for a P_{mp} of 2,643.9nW/cm^2. The light curve, like the dark curve, shows no curvature, but is offset from the dark curve into the fourth quadrant, indicating power production.

5.3 Planar Cells

In order to determine if the low I_{sc}, V_{oc}, and FF values are due to the three dimensionality of the 3DCNTPV cells, and are therefore inherent in their architecture, or are a consequence of the processing methods used, a series of planar substrate configuration cells were created.

For three of these cells (CNT Planar 01, 03, and 08) an unpatterned carpet of VACNTs was created. To create these samples, a thin film of Fe catalyst is deposited via thermal evaporation as described in Chapter 3 without patterning by photolithography. VACNTs are grown via CVD using the AcUHYCNT820 recipe. Since no photolithographic patterning occurred, the VACNTs consist of a flat carpet of CNTs. These carpet CNT samples are planar, but have similar complex CNT geometry to the 3DCNTPV cells. After CNT growth, CdTe, CdS, and ITO are deposited as previously described.

Six of the cells (Planar 02, 05, 07, 08, 09, and 11) were created without CNT growth. For these types of samples, CdTe and CdS are deposited directly onto the p-Si substrate followed by ITO deposition via IAD. These planar cells do not have the complicated geometry of the CNTs. By comparing the MBE created cells with the planar cells of both types, it is possible to determine if the production processes or the CNTs are the cause of the low power outputs and the shorting of the cells. Table 8 shows the figures of merit for the CNT and planar cells.

Table 8: Figures of merit for planar cells created with an unpatterned CNT carpet on a p-Si wafer (CNT Planar) and a p-Si wafer without CNTs (Planar). The I_{sc} values for the planar cells are smaller than the 3DCNTPV cells previously created. This may be due to the inclusion of more defect and pinhole sites in the planar cells, which are of larger size. The V_{oc} values are similar to those of the 3DCNTPV cells and the FF values are still close to 25%. This indicates that the shunting in the 3DCNTPV cell is due to the processing conditions and is not inherently due to the 3D structure.

Sample Name	I_{sc} μA/cm^2	V_{oc} mV	FF %	P_{mp} nW/cm^2	R_{sh} Ω	R_s Ω
CNT Planar 01	25.6	111.63	26.79	764.5	2,420.84	1,995.97
CNT Planar 03	5.05	147.76	25.61	233.2	7,081.15	2,868.21
CNT Planar 08	41.0	150.69	25.65	1,582.6	343.28	223.02
Planar 02	1.69	36.75	23.65	14.7	2,958.23	3,600.10
Planar 05	1.86	35.81	23.90	15.9	5,327.08	5,905.279
Planar 07	1.41	63.37	26.80	24.0	12,231.82	5,330.20
Planar 08	0.25	35.47	21.34	1.90	30,857.53	7,735.75
Planar 09	1.69	103.35	18.42	32.2	5,150.92	11,014.55
Planar 11	0.39	28.58	23.77	2.65	39,025.91	11,998.75

The I_{sc} of both types of planar cells are comparable to the previously created 3DCNTPV cells. The I_{sc} values range from 0.25 to 41.0μA/cm^2, which is slightly lower than the 3DCNTPV cells. This may be due to the fact that since the 3DCNTPV cells are patterned, the size of the samples is determined by the photolithography mask and is $\sim$2.25 cm^2 after sample dicing. The planar cells are not limited by the dimension of the pattern and are made to to be approximately 6.5cm^2. The current density may not scale exactly with size since the larger size may mean the inclusion of more defects and pinholes, which ultimately will decrease the power more than the

increased size will raise it. Most of the high efficiency (<8%) substrate CdTe cells reported have very small areas, generally much less than 1cm^2.

The V_{oc} values for the planar cells are consistent with the 3DCNTPV cells with values from 28.58 to 147.76mV. Figure 87 shows the MBE and planar cells created cells on a graph with the I_{sc} density on the abscissa and the V_{oc} on the ordinate. The CNT planar cells are shown by triangles, the planar cells by squares, and the MBE cells are represented as diamonds. The planar cells, both CNT and p-Si show lower I_{sc} values on the average and similar V_{oc} values as the MBE cells.

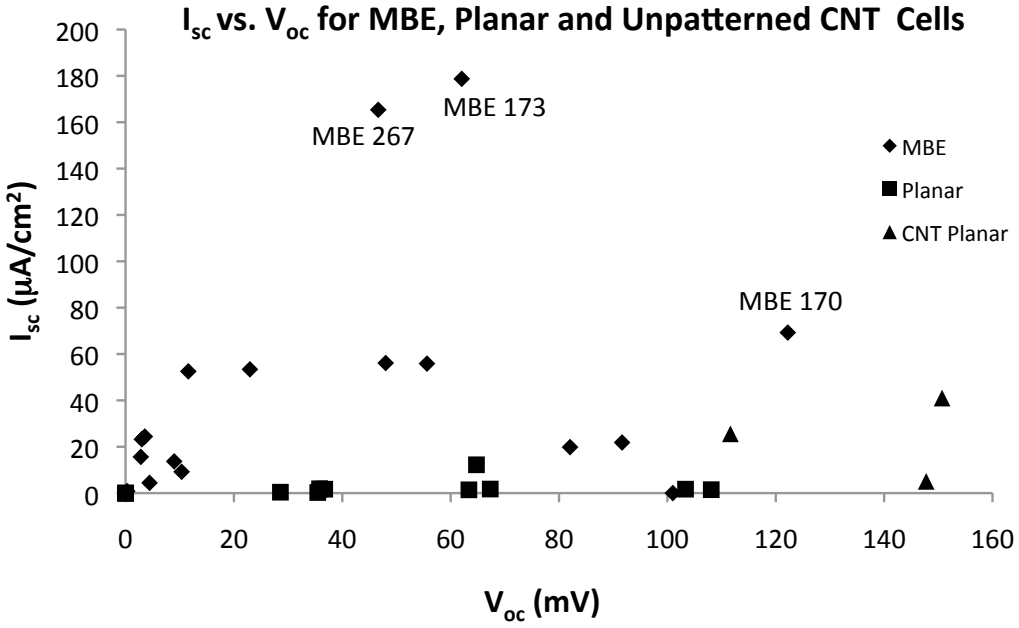

Figure 87: Graph of I_{sc} vs. V_{oc} for MBE cells with patterned VACNTs (diamonds), planar cells with unpatterned VACNTs (triangles), and planar cells with no CNTs (squares). The V_{oc} values for each type of cell are fairly consistent. The MBE cells have a higher average I_{sc} than the planar cells. This may be due to the increased size of the planar cells having more defects and pinholes, which could decrease the current density faster than the the increased area can compensate.

The FF values of the planar cells are also consistent with the MBE cells and are very nearly equal to 25%, indicating that these cells also suffer from a shunt. Figure 88 shows the dark IV curve from Planar 05. The linear curve (solid line) is very similar to the curves taken from the other planar cells. Unlike the previous IV curves which

showed no curvature along their entire voltage range, this cell has large curvature in the reverse voltage. The IV curve then becomes flat in the positive voltage direction. The curvature in the negative voltage region resembles diode breakdown, however, in this case it is completely reversible with no harm to the cell. The reason for this curvature is RO due to a Schottky barrier between the p-Si and CdTe, which became fully realized in a later series of cells. The portion of the semilog dark IV curve (dashed line) in the positive voltage regime looks much like the curves from other completed cells. The shunt current is dominant, though it is smaller than the values for the MBE and CBD cells.

The straight line in the positive voltage direction indicates that the planar cells are also shunted. Since the 3DCNTPV cells shows the same shunting, this indicates that the shunting and low power output problems observed in the MBE cells is not due to the 3D structure of the cell, but is being caused by the processing conditions.

The light curve of Planar 05 is similar to those from other 3DCNTPV cells. It is a straight line offset from the dark curve into the fourth quadrant.

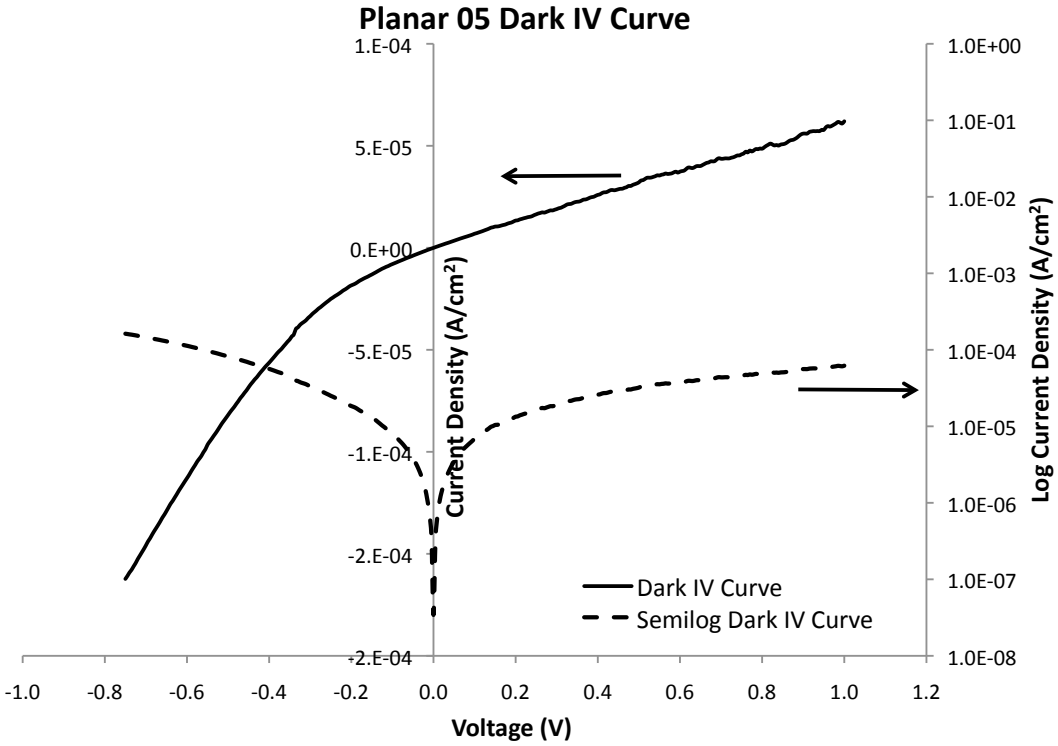

Figure 88: Dark curve of Planar 05 under an applied voltage -0.75 to 1.0V. The solid line represent the dark IV curve on a linear scale while the dashed line represents the curve on a semilog scale. The IV curve is typical of all the cells created using this process flow. In the negative voltage regime, there is a large negative curvature. This curvature resembles diode breakdown, but it is reversible and at only moderate negative voltages. It was realized during the production of a later series of cells that this curvature is due to RO caused by a Schottky barrier between the p-Si and CdTe. In the positive voltage direction, the IV curve have very little curvature and is dominated by the shunt current, much like the 3DCNTPV cells. This indicates that the cell shunting and low power output is not due to the 3D structure of the 3DCNTPV cell, but by subsequent processing steps.

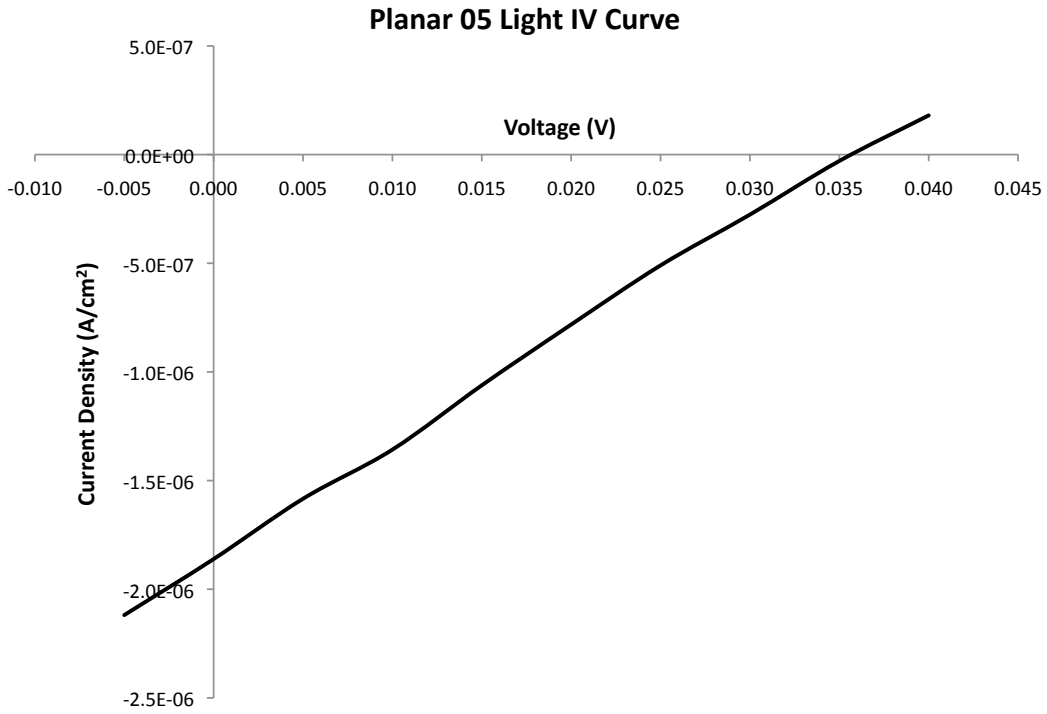

Figure 89: Light curve of Planar 05 showing an I_{sc} of 1.86μA/cm^2 and a V_{oc} of 35.81mV for a P_{mp} of 15.9nW/cm^2. The light curve shows no curvature, but is offset from the dark curve into the fourth quadrant, indicating power production.

5.4 MBEOx Cells

The shunting problem apparent in the MBE, planar, and CBD cells is most likely due to an electrical connection between the ITO top contact, and the doped Si wafer through pinholes and inhomogeneities. Cells with a passivating oxide layer over the Si wafer were constructed (Figure 90). By passivating the area in between CNT towers, the exposed surface area of the Si wafer is lessened. This should decrease the frequency of shorts in a given cell and the power output should correspondingly increase.

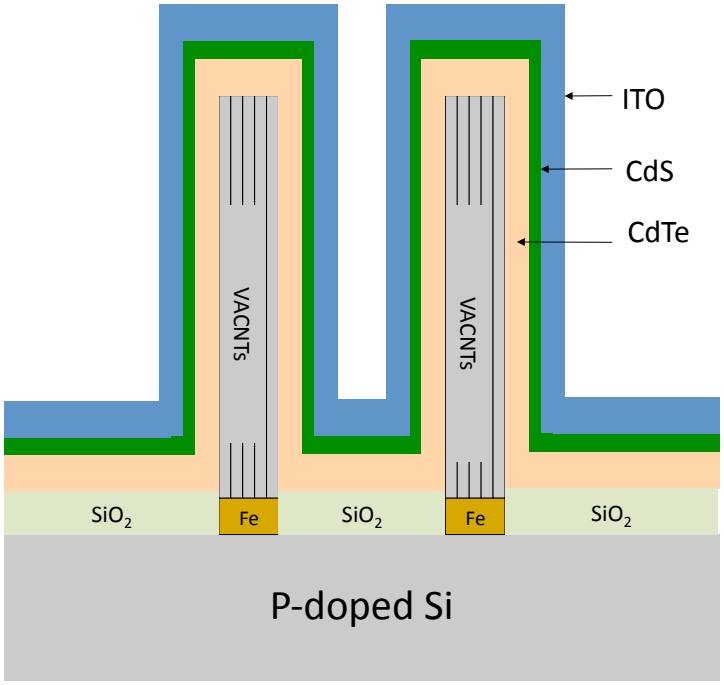

Figure 90: The shunting shown in previous 3DCNTPV cells is most likely due to an electrical connection between ITO and the p-Si wafer. By depositing an SiO_2 passivation layer between the VACNTs via PECVD, the exposed area of the Si wafer is lessened and the shunting should be abated.

These MBEOx cells are created by taking a p-doped Si wafer and depositing 321.6±7.2 nm SiO_2 via a PlasmaTherm (St. Petersburg, FL) PECVD system. 2%

SiH_4 in N_2 and N_2O precursor gases at 400 and 900 sccm, respectively, are flowed into the chamber at a pressure of 900 mTorr. The platform is held at a temperature of 350^oC for 8 minutes with a plasma power of 25W. Oxide thickness is measured using a Woollam (Lincoln, NE) variable angle spectroscopic Ellipsometer.

Upon deposition of the oxide layer, photolithography is carried out as described in §3.1. The photoresist is used as an etch mask. The developed portions of the photolithography mask are etched down to the p-Si substrate with an Advanced Vacuum (Lomma, Sweden) Vision RIE system. The etch is carried out at a pressure of 40 Torr with a flow rate of 45 sccm CHF_3 and 5 sccm O_2. The RF power is held constant at 250W. The etch is monitored by profilometry. The etch rate for this process is approximately 33nm/min.

After etching, the catalyst is deposited via thermal evaporation and VACNTs are grown via CVD. CdTe and CdS are deposited via MBE and ITO is deposited via IAD as described in Chapter 3. Table 9 shows the figures of merit for the cells fabricated using this process flow.

The I_{sc} of MBEOx cells are comparable to the previously created 3DCNTPV cells. The I_{sc} values range from 0.866 to 47.1μA/cm^2, which is slightly lower than the 3DCNTPV cells.

The V_{oc} values for the MBEOx cells vary from 2.95 to 73.00mV. These values do not show an increase with the introduction of a passivation layer, compared to the 3DCNTPV MBE cells. This indicates that the shunting is not occurring between VACNTs in the 3DCNTPV cells. Shunting may be occurring inside the VACNT towers or he deposition of ITO may be occurring around the periphery of the cell. Since the shunting is apparent in cells without CNTs, this indicates that the ITO deposition may be depositing ITO around the edges of the cell, leading to a shunt. Figure 91 shows the MBE and MBEOx cells on a graph with the I_{sc} density on the

Table 9: Figures of merit for MBEOx cells created with a passivating SiO_2 layer between VACNTs. The I_{sc} values are similar to the 3DCNTPV cells previously created. The V_{oc} values are similar to the 3DCNTPV cells without a passivating oxide, indicating that the shunting may not be occurring between the VACNT towers. The FF values are still close to 25%, indicating that the shunting present in the 3DCNTPV is not abated by the passivation layer.

Sample Name	I_{sc} μA/cm^2	V_{oc} mV	FF %	P_{mp} nW/cm^2	R_{sh} Ω	R_s Ω
MBEOx 04	25.1	25.86	24.43	158.3	423.19	189.21
MBEOx 05	11.5	14.30	22.98	37.8	685.59	183.46
MBEOx 06	18.6	4.95	25.05	23.0	102.45	84.96
MBEOx 09	16.6	9.88	10.13	16.6	106.64	77.69
MBEOx 21	12.2	13.21	24.57	39.4	1,358.97	1,168.50
MBEOx 32	0.866	12.33	30.06	3.21	11,611.16	7,342.14
MBEOx 36	47.1	73.00	25.68	882.4	2,066.29	1,739.89
MBEOx 37	1.52	2.95	24.74	1.11	890.71	724.38

abscissa and the V_{oc} on the ordinate. The MBE cells are shown by diamonds while the MBEOx cells are represented as circles.

The FF values of the MBEOx cells are also consistent with the MBE cells and are very nearly equal to 25%, indicating that these cells also suffer from a shunt. Figure 92 shows a typical dark IV curve from an MBEOx cell. The curve in Figure 92 is from MBEOx 036. This curve is very similar to the curves taken from the planar cells and has curvature in the reverse voltage, though the effect is not as large is in the planar cells. The IV curve then becomes flat in the positive voltage direction due to the shunt. The semilog plot of the dark IV curve shows that the shunt current still dominates.

The light curve of MBEOx 036 is similar to those from other 3DCNTPV cells. It is a straight line offset from the dark curve into the fourth quadrant.

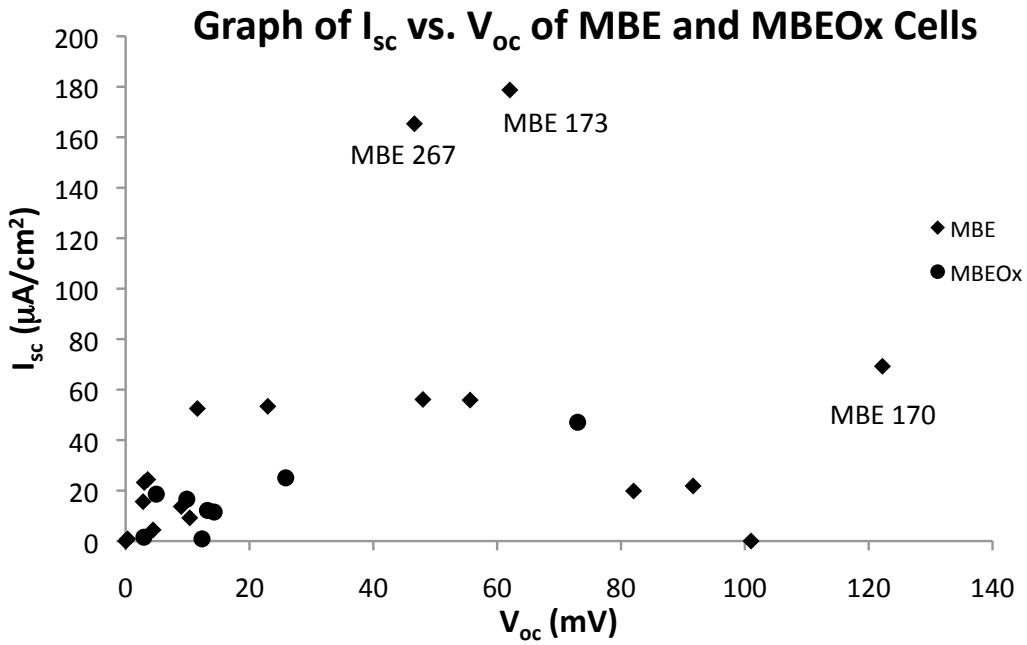

Figure 91: Graph of I_{sc} vs. V_{oc} for MBE cells with patterned VACNTs (diamonds) and MBEOx cells with a passivating oxide layer between VACNTs (circles). The V_{oc} values for both cells are fairly consistent. The MBEOx cells do not show an increased V_{oc} over the unpassivated MBE cells. This indicates that passivating between the VACNTs does not disrupt the shunting problem observed in all previously manufactured cells and is either occurring in the interior of VACNTs or around the edges of cells. Since shunting occurs for cell with no CNTs, ITO deposition around the edge of cells is the most likely cause.

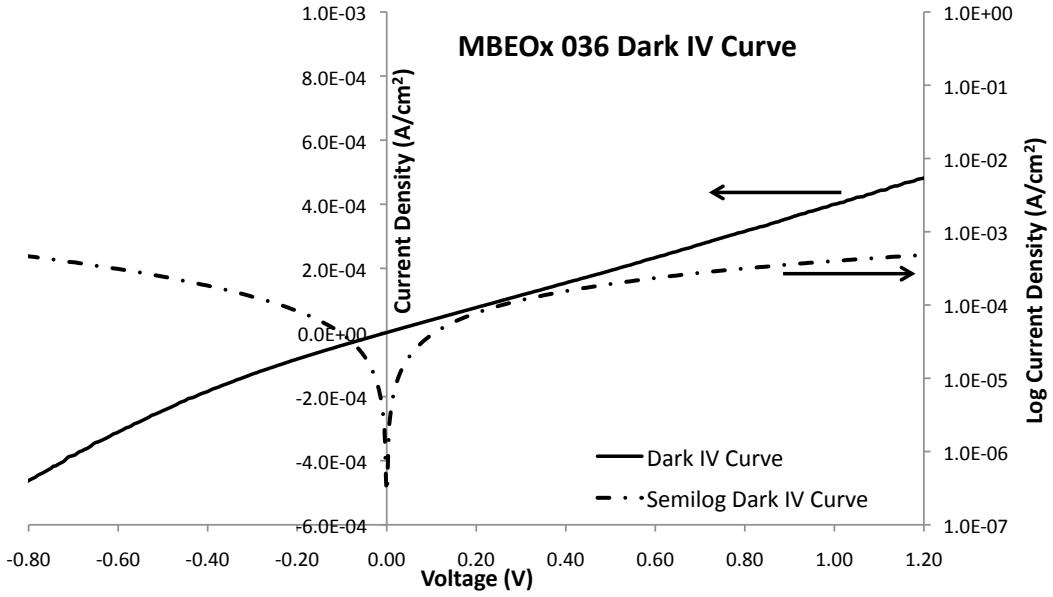

Figure 92: Dark curve of MBEOx 036 under an applied voltage -1 to 1.5V on a linear (solid line) and semilog (dashed line) scale. The IV curve is typical of all the cells created using this process flow. There is curvature in the negative voltage regime, similar to the IV curves from the planar cells, though the curvature is slighter. In the positive voltage direction, the IV curve has very little curvature, much like the MBE cells. The shunt current dominates the behavior of the dark IV curve. This indicates that the cell shunting is not occurring between VACNTs but may be occurring along the edges of the cells.

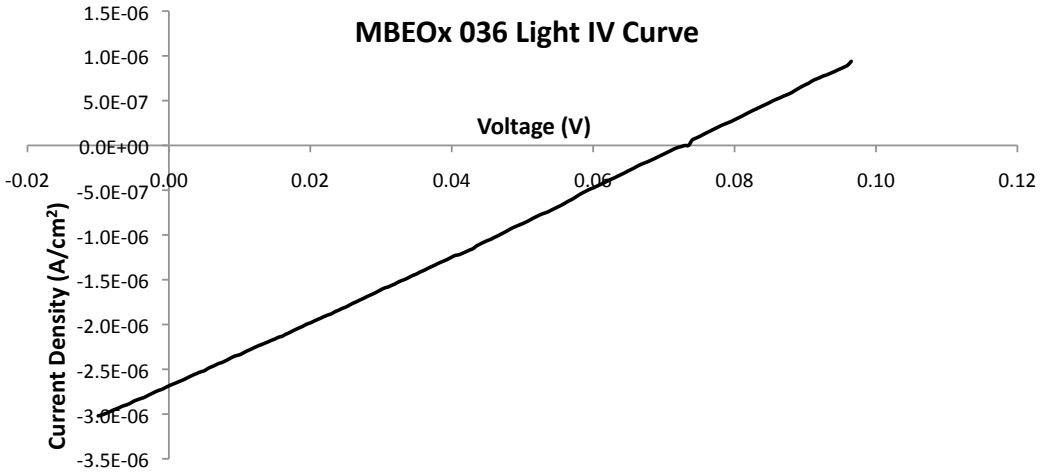

Figure 93: Light curve of MBEOx 036 showing an I_{sc} of 47.1μA/cm^2 and a V_{oc} of 73.00mV for a P_{mp} of 256.8nW/cm^2. The light curve shows no curvature, but is offset from the dark curve into the fourth quadrant, indicating power production.

5.5 Area Fraction Cells

In order to progress towards eliminating the shunt present in the 3DCNTPV cells, another set of cells were created. This set of 14 cells has two differences compared to previously manufactured MBE cells. The first difference is that where MBE cells were composed of only the block and the waffle pattern, this set of samples was made with a different photolithography mask. In this mask every sample has a different repeating geometrical shape to pattern the VACNTs. Each sample differs in both shape and size of the pattern with a constant pitch between tower centers of 150μm. This mask is composed of patterns for making VACNT samples of:

100, 50, and 20μm circles

50, 25, and 12μm lines

75, 50, and 60μm rings

50 and 10μm squares

50, 25, and 10μm triangles, stars, and diamonds

Since the density of VACNTs differs whith each sample, these samples were labeled Area Fraction. Figure 94 shows a sample with VACNTs grown in the shape of a 50μm diameter circle with a pitch between circles of 150μm.

The second difference in the production of these cells involves a change in process parameters. During MBE deposition, it is necessary to fix the sample onto the sample holding using molybdenum clips. The area around these clips are shadowed from some of the CdTe and CdS beam flux and therefore, have a different thickness than most of the sample. It is possible that these regions with less semiconductor could be leading to the shunting observed in previously manufactured cells. During the IAD of ITO, the Area Fraction cells have the semiconductor portions around these clips masked with Al foil. If the shunt exists in these areas, then preventing the deposition of ITO

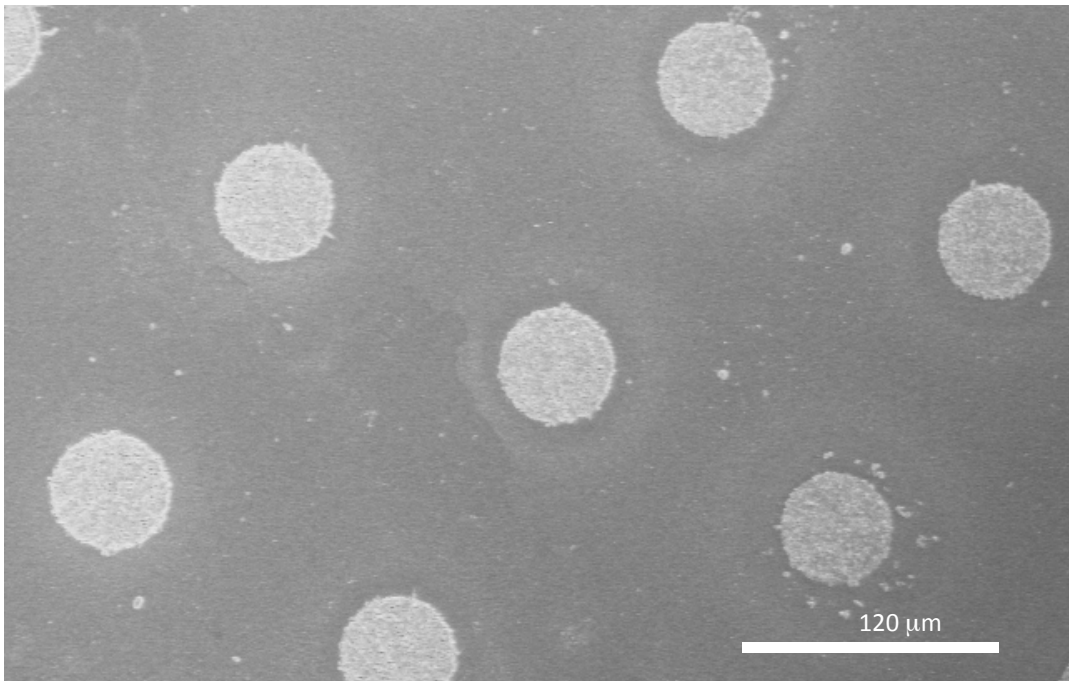

Figure 94: Sample grown from a photolithography mask which can be used to grow VACNTs in many different shapes. The SEM micrograph is of a sample which has VACNTs grown in circles 50μm in diameter.

should eliminate the shunting. Table 10 shows the figures of merit for cells created in this manner.

The I_{sc} of Area Fraction cells are slightly lower than the previously created MBE cells. The I_{sc} values range from 0.87 to 44.4μA/cm^2.

The V_{oc} values for the Area Fraction cells vary from 11.00 to 303.56mV. Area Fraction cells 01.04, 01.07, 01.22, 02.01, 02.10, 02.20, and 02.22 have V_{oc} values larger than the largest value for the MBE series cells. This indicates that the shunting may be slightly abated by masking regions of low MBE deposition during IAD of ITO. Figure 91 shows the MBE and Area Fraction cells on a graph with the I_{sc} density on the abscissa and the V_{oc} on the ordinate. The MBE cells are shown by diamonds while the Area Fraction cells are represented as stars.

Of the Area Fraction cells with a larger V_{oc} than the MBE cells, Area Fraction 01.07, 01.22, 02.01, 02.20, and 02.22 have FF values significantly lower than 25%. As

Table 10: Figures of merit for Area Fraction cells created with VACNTs of different shapes and partially masked during ITO depostion. The I_{sc} values are similar to the 3DCNTPV cells previously created. The V_{oc} values are similar to the 3DCNTPV cells, however, there are some cells which have larger values than were previously measured. The FF values are still close to 25% for most of the cells. The cells which larger V_{oc} have FF values less than 25%. This indicates an IV curve which has an inverse curvature in the fourth quadrant.

Sample Name	I_{sc} μA/cm^2	V_{oc} mV	FF %	P_{mp} nW/cm^2	R_{sh} Ω	R_s Ω
01.04	4.22	209.24	22.42	197.8	10,523.77	6,969.13
01.05	14.4	109.21	23.32	367.7	23,960.70	23,589.36
01.07	44.4	253.35	12.37	1,382.5	16,107.73	9,779.95
01.11	1.42	11.00	24.92	3.90	1,994.53	1,903.93
01.14	0.87	45.19	24.54	9.61	27,027.03	5,291.00
01.15	5.05	60.88	24.78	76.1	5,319.15	4,016.06
01.22	6.71	147.97	18.70	187.0	18,181.82	6,451.61
01.24	0.86	20.00	25.43	4.39	6,275.89	2,951.68
02.01	3.04	129.27	13.88	54.5	4,739.34	2,770.08
02.05	3.09	24.67	23.88	18.2	5,193.19	3,467.89
02.10	8.61	134.21	21.29	246.1	61,496.83	27,328.38
02.11	1.27	25.21	24.57	7.84	15,352.49	7,644.09
02.20	3.81	303.56	10.57	122.8	91,190.95	68,601.22
02.22	33.3	253.82	12.51	1,057.0	84,054.80	93,240.09

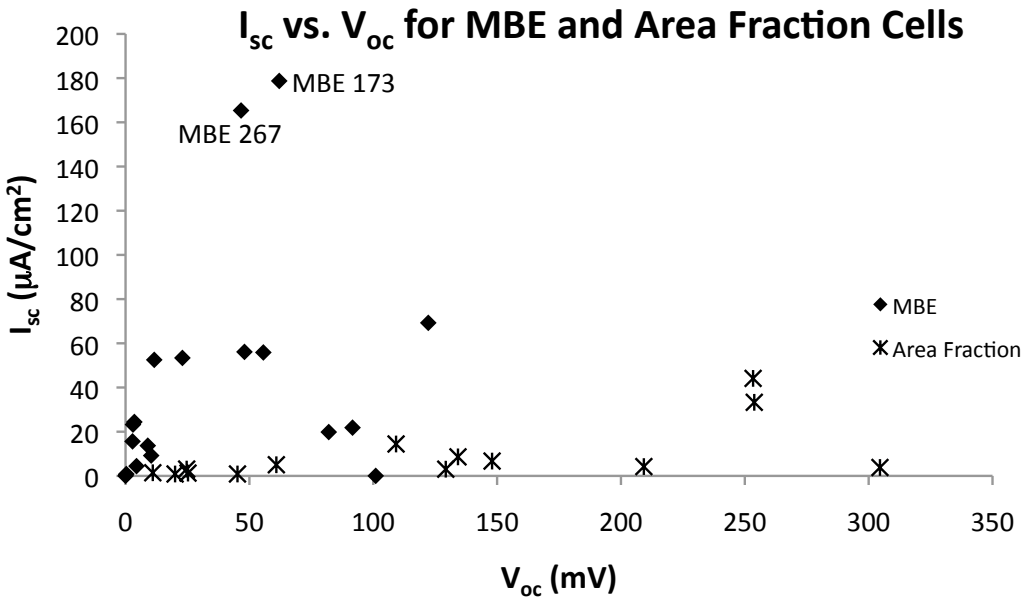

Figure 95: Graph of I_{sc} vs. V_{oc} for MBE cells with patterned VACNTs (diamonds) and Area Fraction cells (stars). The I_{sc} values for Area Fraction cells are lower than the MBE cells, however, some of the cell show an increased V_{oc}. The cells with those increased V_{oc} values also have FF values below 25%.

demonstrated in equations 15 through 22, the only way this can occur is for the cell to demonstrate an IV curve with inverted curvature compared to a normal solar cell IV curve. Figure 96 shows the dark and light IV curves for Area Fraction 01.07, which is typical of these cells with an increased V_{oc}. While the dark IV curve looks similar to the curves taken of other cells, the light IV curve has a very large curvature. This difference in curvature indicates that the photocurrent gain is not constant across the entire voltage range. The shadowing during IAD eliminated enough of the shunt that is was possible to see this effect in the light curve.

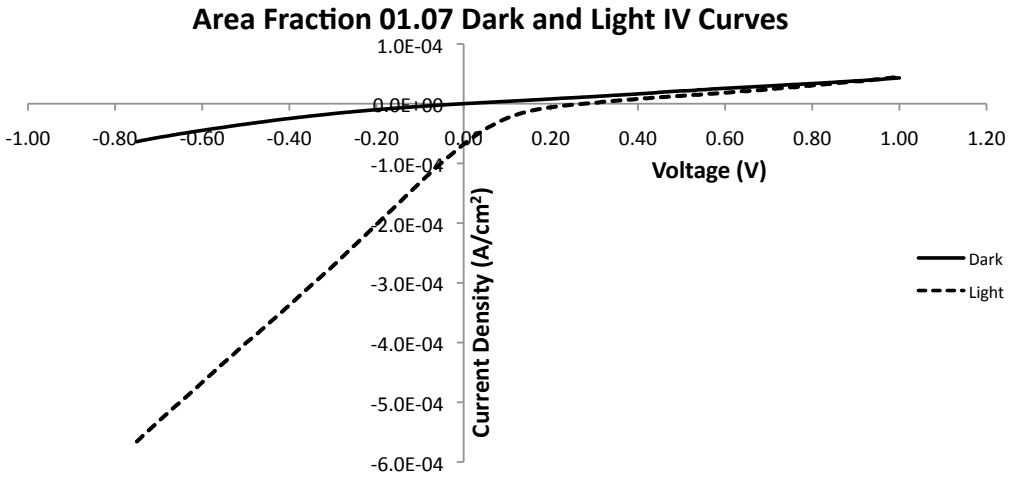

Figure 96: Dark and light IV curves for Area Fraction 01.07. The light curve is not simply offset from the dark curve, but has a much greater curvature in both the third and fourth quadrants. This effect was being masked in previously made cells by the amount of shunting.

This change in photocurrent gain has the effect of inversion of the IV curvature in the fourth quadrant, as Figure 97 shows. This change in curvature can be attributed to RO of the IV curve as discussed in §2.1.3.8. It is very unusual in CdTe cells for RO to occur in the fourth quadrant instead of the first and indicates a very large rectifying back contact barrier. In the case of 3DCNTPV, this barrier is caused by the contact between the CdTe and p-Si layer.

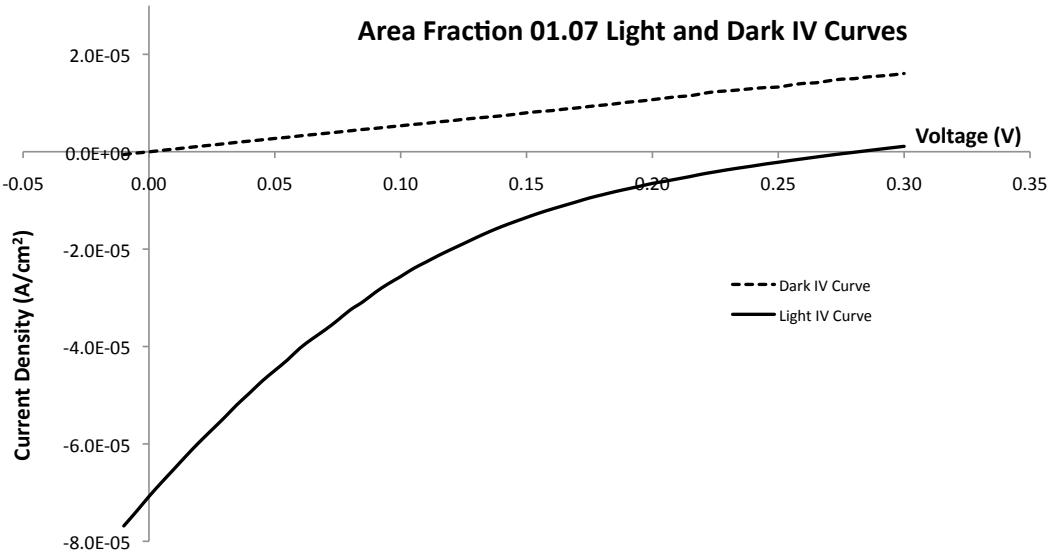

Figure 97: Closeup of the dark and light IV curves of Area Fraction 01.07 in the fourth quadrant. A nonconstant photocurrent offset between the dark and light curves is present. While the dark curve is a straight line, the light curve actually has an inverted curvature. This inverted curvature is RO occurring in the fourth quadrant due to a very large rectifying barrier between the CdTe and p-Si back contact.

5.6 Metallized Cells

In order to eliminate the CdTe/p-Si interface to prevent the formation of a rectifying barrier, the 3DCNTPV structure was changed to the schematic shown Figure 98. In this schematic, the p-Si wafer is replaced with an undoped Si wafer. This wafer is passivated by the deposition of SiO_2 via PECVD. Metal is then deposited via electron beam evaporation to act as a back contact. Photolithography is then used to pattern this metal/SiO_2/Si structure and Fe catalyst is deposited via thermal evaporation. VACNTs are grown followed by deposition of CdTe and CdS via MBE. ITO is deposited via IAD to form a top contact.

The metals of choice for CdTe back contacts, as shown in Figure 16, are Pt, Au, Ni, Co, Ag, Fe, and Cu. Ni, Co, and Fe are unusable for this application, since they are catalysts for CNT growth and cannot be used as a substrate for patterned VACNT growth. Pt is a difficult metal to evaporate and tends to incorporate impurities easily.

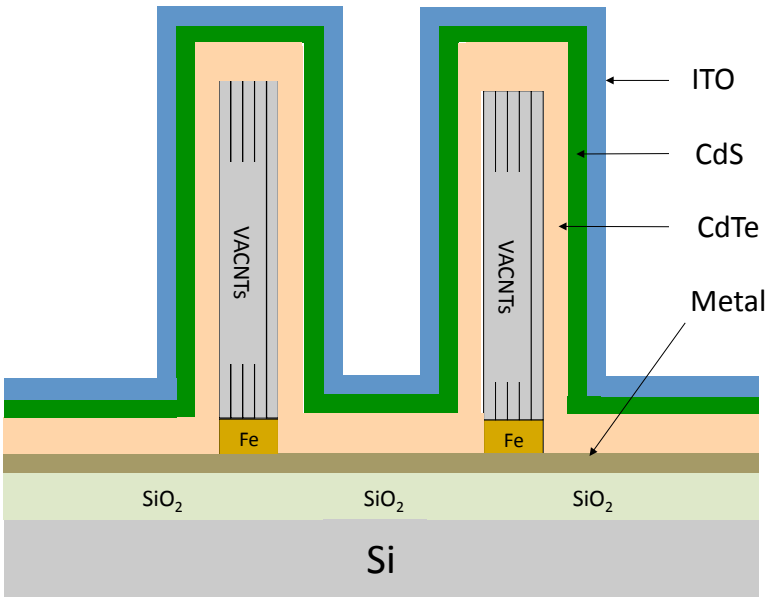

Figure 98: In order to eliminate the CdTe/p-Si interface which causes RO in the fourth quadrant of sample IV curves, the above schematic for 3DCNTPV cells is proposed. The Si wafer is passivated by an SiO_2 layer deposited via PECVD. A metal layer is deposited via electron beam evaporation to form the back contact. The sample preparation then follows the rest of the procedure outlined in §3.1. In this setup, the growth of VACNTs directly on a metal film while still allowing for conductivity between the metal and CNTs is quite challenging.

This leaves the available metals for a back contact in 3DCNTPV cells as Au, Ag, and Cu, which are the typical back contact materials used in planar CdTe solar cells.

Growing VACNTs directly onto metal films while still maintaining conductivity between the CNTs and metal underlayer is quite challenging. In order to grow tall, aligned CNTs, diffusion barriers such as TiO_2, Al_2O_3, and TiN are typically used. These layers prevent metal atoms from the catalyst nanoparticles diffusing into metal underlayers at the high temperatures required for growth [243]. Without these diffusion layers, CNTs on metal underlayers tend to be short, unaligned, and defect ridden. However, the diffusion layers are electrically insulating and negatively affect the conductivity between the CNTs and metal layer, so they are undesireable for this application.

In addition, the FirstNano furnace is incompatible for the growth of VACNTs on metal underlayers. The furnace runs at atmospheric pressures and even with H_2 flow before, during, and after the soak period, enough oxygen subsists in the system that the metal underlayers are oxidized and no CNTs are grown. Since thermal CVD does not work, growing CNTs on metal layers was tried using an Aixtron Black Magic PECVD system (Figure 99).

This system has a four inch substrate platform capable of reaching a maximum wafer temperature of 800^oC measured by thermocouple and infrared sensor. The substrate can be heated at ramp rates from 1-300^oC/min. Plasma power is provided by a 1kW dc pulse plasma supply and gas concentration is regulated by MFCs. Usable gases for the system include Ar or N_2 for the carrier gas, H_2 or NH_3 as a reducing agent, and C_2H_2 or CH_4 as carbon feedstock.

Experience has shown that the growth of VACNTs via PECVD is better suited to the Ni catalyst system. This choice of Ni dictates which metal underlayer to use. Figure 100 shows the binary phase diagrams for the four possible metal underlayers. The Cu-Ni phase diagram Figure 100(a) shows a miscibility gap at low temperatures.

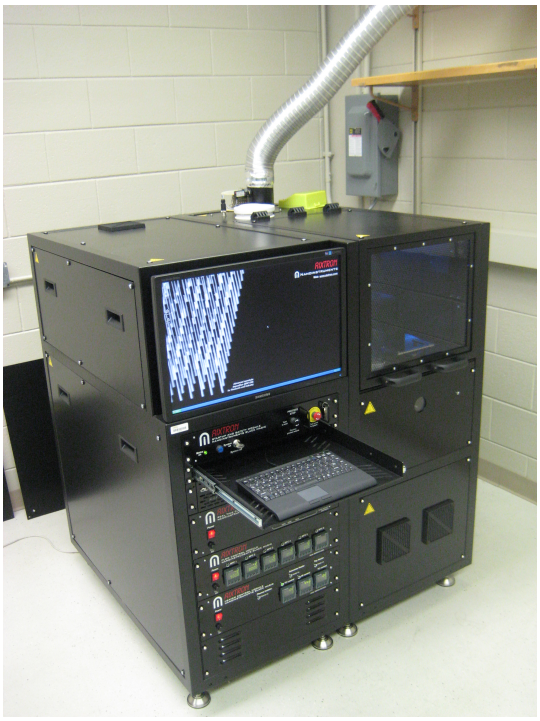

Figure 99: Aixtron Black Magic PECVD system used to grow VACNTs on metal underlayers

However, Cu and Ni have complete solid solubility at temperatures close to those required for CNT growth, so Cu is not a suitable underlayer for CNT growth without additional barrier layers. Au and Ni have a miscibility gap which exists at higher temperatures Figure 100(b), but is very small at the temperature of growth, around 800^oC, and interdiffusion of the two metals would most likely be large during growth. Pt is not suitable because Pt and Ni are completely soluble at all concentrations up to temperatures of 1455^oC (Figure 100(c)). Ag and Ni are completely immiscible at temperatures lower than 959^oC Figure 100(d) and is the best metal/catalyst combination for PECVD growth of CNTs directly on a metal for a 3DCNTPV cell.

To grow VACNTs directly onto an Ag underlayer, samples are made by taking an Si wafer and depositing SiO_2 via PECVD for 5 minutes as described in §5.4. A 25nm Ti adhesion layer, followed by a 125nm Ag metal is then deposited using a CVC electron beam evaporator at a rate of $1.5\mathring{A}$/sec. Film thickness is monitored

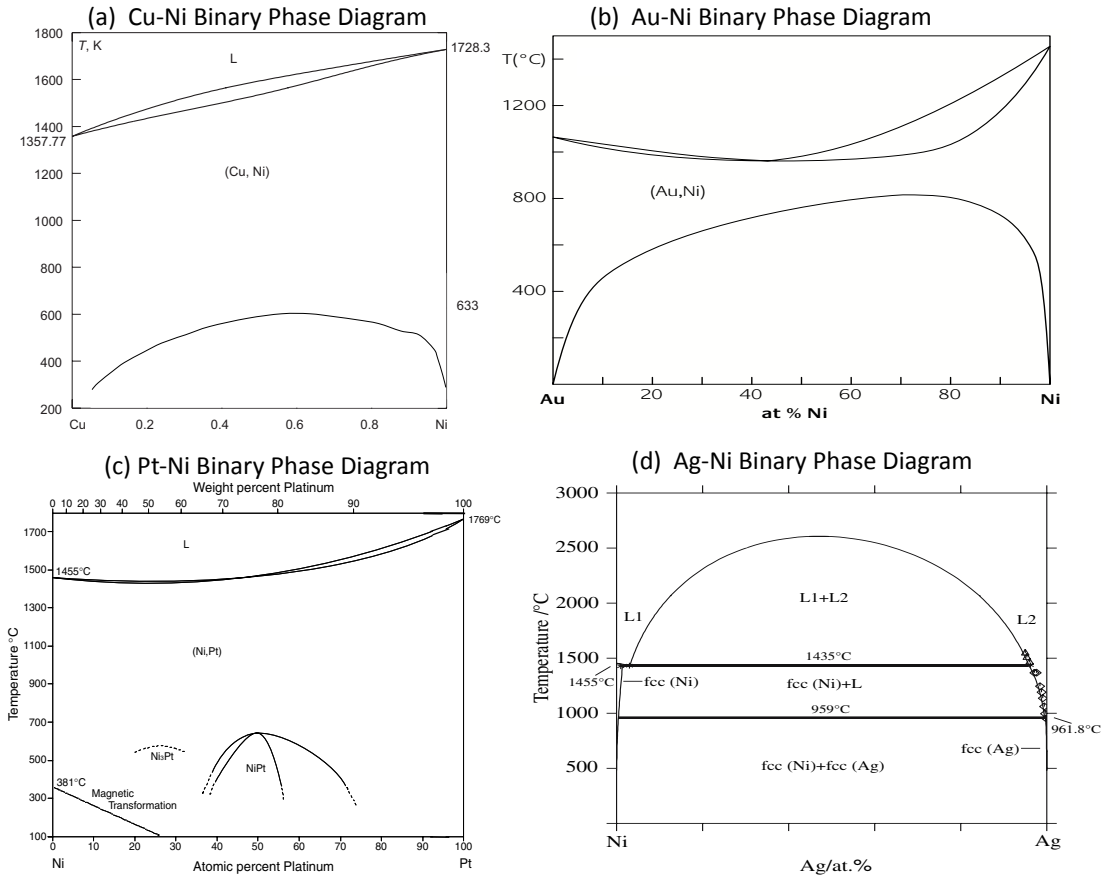

Figure 100: (a)The Cu-Ni binary phase diagram shows complete solubility at temperatures used to grow CNTs [244]. (b) The Au-Ni binary phase diagram shows a miscibility gap, but this gap is very small at CNT growth temperatures and it is likely significant interdiffusion of the metals would occur [245]. (c) The Pt-Ni binary phase diagram shows complete solubility at all concentrations for temperatures up to 1455^{o}C [246]. (d) The Ag-Ni binary phase diagram shows complete insolubility up to temperatures of 955^{o}C [247] and is the most likely candidate for CNT growth.

using a quartz crystal sensor. After metal deposition, photolithography is carried out as described in §3.1. 10nm Ni is deposited via CVC electron beam evaporator at a rate of 0.5$\mathring{A}$/sec. Liftoff of the excess photoresist is accomplished via sonication in acetone. The samples are then diced.

The most successful PECVD growth recipe found to grow VACNTs on an Ag underlayer utilizes a 300^{o}C/min heating rate to raise the wafer temperature (monitored by an IR sensor) from ambient to 630^{o}C under 700sccm H_2 and 200sccm N_2 to prevent oxidation. The temperature is then held at 630^{o}C at a pressure of 60 Torr for 5 minutes to anneal the Ni catalyst layer. After the annealing stage, the temperature is raised to 770^{o}C at a heating rate of 300^{o}C/min. 50sccm C_2H_2 as a carbon feedstock is flowed into the chamber in addition to the H_2 and N_2 gases. An 8W DC plasma is ignited for 15 minutes to facilitate the breakdown and deposition of the hydrocarbon feedstock. After the soak period, the gas flows and plasma power are turned off, and the system is quenched with 4,000 sccm N_2 until the wafer temperature is down to 400^{o}C. The system is vented and the wafer is then cooled to ambient before it is retrieved.

Figure 101 shows the results of this recipe. The CNTs produced using this recipe are densely packed, have a larger median diameter than the AcUHYCNT recipe, and are shorter. Although the CNTs are aligned, the largest vertical length that was achieved with this recipe was only 10μm. The larger diameter and short CNTs are due to the low plasma power used in this recipe. Where many recipes have plasma powers around 100W, this recipe uses only 7.31$\pm$2.30 W of DC plasma at a higher pressure in order to abate the deleterious effects of the plasma on the Ag underlayer.

The low power density is necessary because larger power densities tend to destroy the Ag underlayer. Figure 102 shows the results of a PECVD deposition using the Black Magic system with a plasma power of 40W. The Ag layer under the Ni catalyst

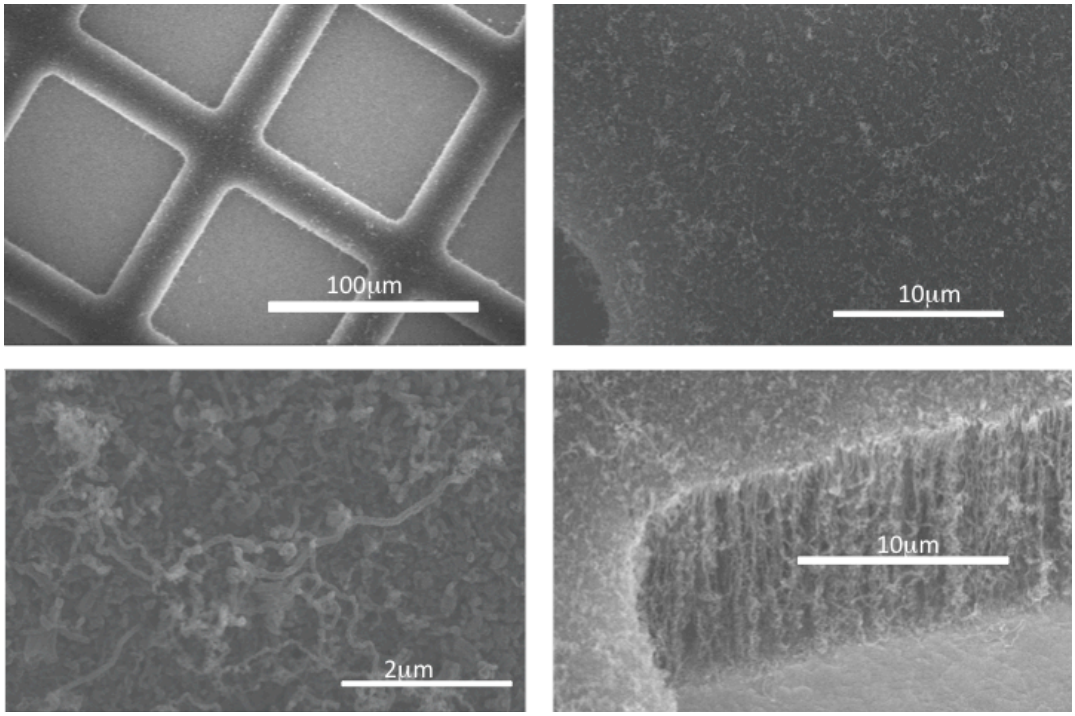

Figure 101: SEM micrographs of an Ni/Ag/SiO_2/Si sample which has undergone PECVD CNT growth with a plasma power of 7.31±2.30W. The CNTs in this sample are very densely packed, especially at the tops of the towers. They are aligned, but have a small vertical length, around 10μm. This is due to the low plasma power. Even with the low plasma power, it is still possible to see damage to the Ag underlayer. In the bottom right micrograph, the Ag underlayer exhibits buckling due to a mismatch in the coefficient of thermal expansion with the layers underneath.

has undergone cracking and rearrangement, almost as if the plasma power has melted the Ag metal during the run.

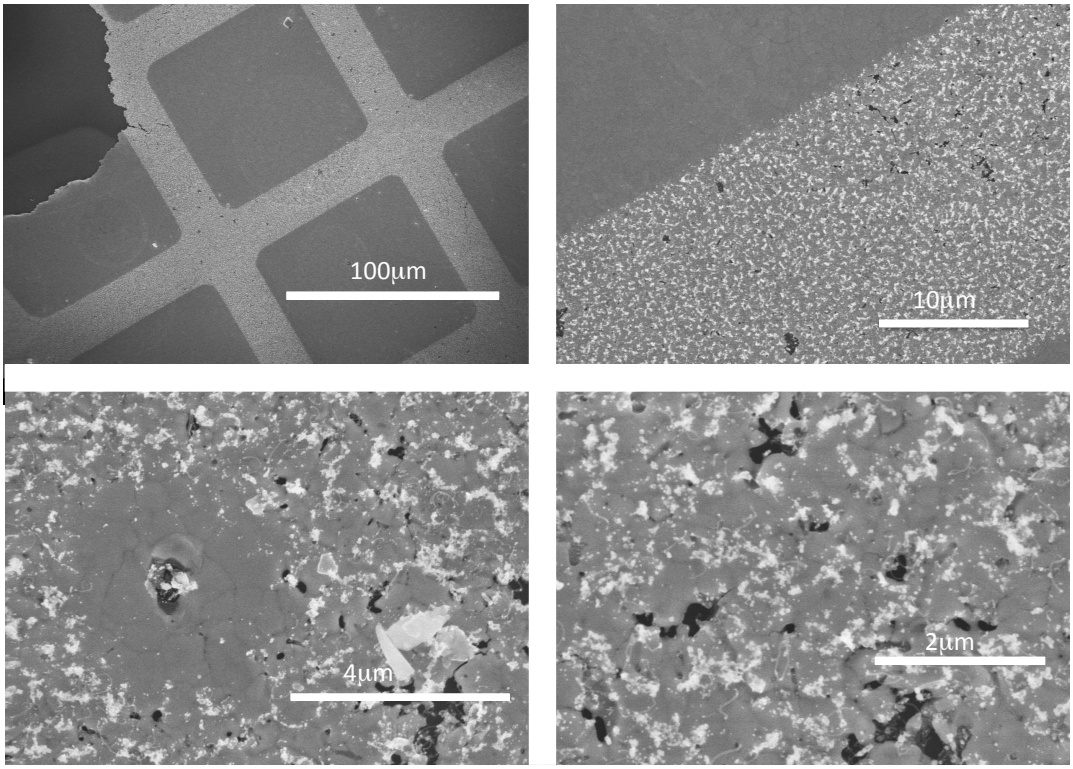

Figure 102: SEM micrographs of a Ni/Ag/SiO_2/Si sample which has gone through a PECVD recipe with a 40W DC plasma. No growth has taken place and voids have opened up in the Ag layer. This damage would be catastrophic for a 3DCNTPV device made using this recipe. Therefore, the 3DCNTPV cells can only be grown at low plasma powers, which inhibits the alignment and vertical height of the grown CNTs.

As stated previously, the tallest VACNTs grown using this recipe were only 10μm, which is too small to have a noticeable effect on the power output of the 3DCNTPV CdTe cells created here. The difficulty in producing the regular growth of tall, straight VACNTs without deleterious effects on the metal underlayer necessitated the alteration of the proposed 3DCNTPV cells from Figure 98 to Figure 103. In Figure 103, the VACNTs are grown on the SiO_2 passivation layer using thermal CVD. The VACNTs are then covered by the metal back contact layer via ebeam evaporation. CdTe, CdS, and ITO deposition are then carried out as in Chapter 3.

This change eliminates the use of VACNTs as the back contact in exchange for ease of processing. VACNTs are only being used to provide the 3D topography of the 3DCNTPV cell. However, the use of a metal coating on the CNTs has an added advantage in providing a back contact reflection layer. CNTs are one of the most absorptive materials in existence [248]. In a 3DCNTPV cell, this means that if a photon passes through the CdS and CdTe layer without absorption, the photon will most likely be parasitically absorbed by the VACNTs. Coating the VACNTs with metal decreases the amount of light absorbed. A photon which passes completely through the CdTe layer may reflect back and be absorbed. The back contact reflector becomes much more important as the thickness of the semiconductor layer is decreased. This is important in later optimizing manufacturing costs, due to the reduced cost associated with cells containing less semiconductor material.

Three sets of these metallized cells were made with Cu, Au, and Ag back contacts. In addition to the metallized back contact, these cells were manufactured so that both contacts were on the top side of the cell. Each cell manufactured in this manner has the entire periphery shadowed during both CdTe/CdS and ITO deposition. The cell is shaded during MBE by Ta foil and during IAD by Al foil around the edges. By making the back connection directly to the metal instead of through a Si wafer and Cu tape as described in §3.6, the series resistance of the cells should be lower. The masking around the entire periphery during IAD also eliminates possible shunting around the edges of the cell. The masking during MBE deposition prevents semiconductor deposition on the metal back contact. The masking during IAD prevents ITO deposition on both the metal outside and a small portion of the semiconductor layer so that each cell has three distinct regions (Figure 104), an outer ring with only the metal back contact, a ring with CdS/CdTe on the metal contact, and an inner portion with the completed ITO top contact.

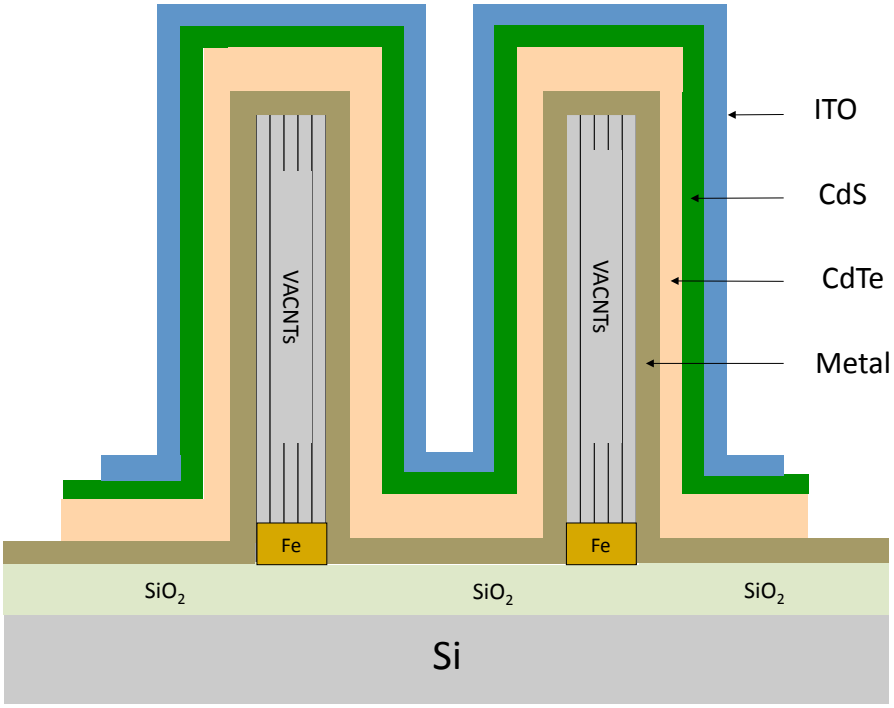

Figure 103: Schematic for a metallized 3DCNTPV cell. Since the growth of VACNTs directly onto a metal underlayer presents many processing problems, the VACNTs in this cell are grown on SiO_2 and then coated with a metal layer. In this case, the VACNTs are providing the structural support for the third dimensionality, but have no part in the electrical conduction. Coating the VACNTs with a metal increases their reflectance, turning the VACNTs into a back contact reflector.

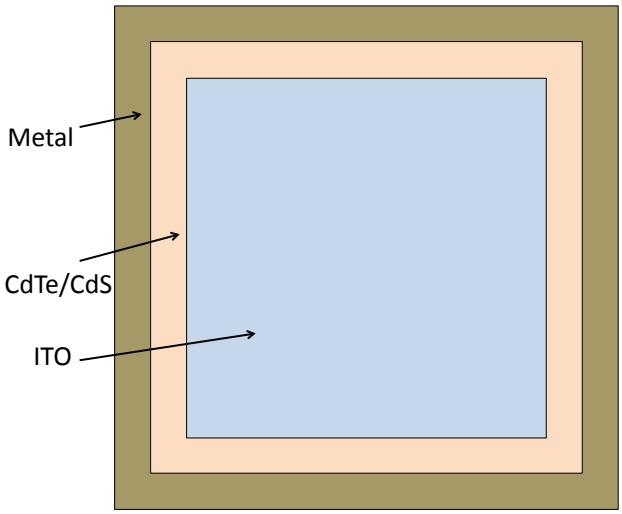

Figure 104: Plan view of a solar cell with a dual top contact. The outer portion is metal and is shadowed during both MBE and IAD. The middle portion is CdTe/CdS on metal and is shadowed only during IAD. The center portion is ITO on CdTe/CdS on metal and is not shadowed. The area for the cell in determining current density is considered to be the portion covered by CdTe/CdS.

The Cu back contact had two cells made in the form of Figure 103 and three cells in a planar format. Table 11 shows the figures of merit for the Cu backed cells. Of these five cells, only one type of each were operational. The working 3DCNTPV cell has an I_{sc} value over twice as large as any 3DCNTPV cell previously made. For both of the working cells, however, the FF values are still close to 25%, indicative of a shunt. This is further realized by the R_{sh} values, which have decreased down to the single to hundreds of ohms.

The Ag back contact cells had two cells manufactured in the 3DCNTPV form and three in the planar format. All the cells were in working order when manufactured. Of these cells, there is a wide spread in the I_{sc} values ranging from 301.7 to 5.20 μA/cm^2, which is more comparable to the 3DCNTPV cells manufactured on an Si wafer. The FF values are also close to 25% and the R_{sh} values, which are in the tens to hundreds of ohms, are too low to show good curvature due to shunting. The

Table 11: Figures of merit for cells metallized with Cu. Only two of the cells were functional, one planar, and one 3DCNTPV cell. The I_{sc} value for the 3DCNTPV cell is twice any previously created cell. The V_{oc} values are similar to other 3DCNTPV cells. The FF values are still close to 25%. The R_{sh} values are much smaller than previously created cells, on the order of one to tens of ohms.

Sample Name	I_{sc} μA/cm^2	V_{oc} mV	FF %	P_{mp} nW/cm^2	R_{sh} Ω	R_s Ω
PlanarCu 01	-	-	-	-	14.68	14.59
PlanarCu 05	0.517	1.49	25.78	0.012	181.36	165.13
PlanarCu 06	-	-	-	-	156.27	156.81
MBECu 429	-	-	-	-	4.64	3.54
MBECu 433	434.7	93.81	25.05	10,217.6	53.4	23.54

addition of a metal layer seems to have exacerbated the shunting problem instead of mitigating it.

Table 12: Figures of merit for cells metallized with Ag. The I_{sc} values are similar to other 3DCNTPV cells previously created. The V_{oc} values are similar to the 3DCNTPV cells. The FF values are still close to 25%. The shunting is increased in these cells, as the decreased R_{sh} values show. These values are much smaller than previously created cells, on the order of ten to hundreds of ohms.

Sample Name	I_{sc} μA/cm^2	V_{oc} mV	FF %	P_{mp} nW/cm^2	R_{sh} Ω	R_s Ω
PlanarAg 01	301.7	141.26	24.70	10,523.6	153.85	121.60
PlanarAg 03	15.7	67.55	24.83	262.9	239.36	135.18
PlanarAg 101	5.20	1.76	22.99	2.10	24.27	23.17
MBEOxAg 03	21.0	2.25	25.02	11.8	41.39	37.12
MBEOxAg 04	16.1	1.88	25.02	7.58	50.35	46.66

The Au back contact cells had two cells manufactured in the 3DCNTPV form and three in the planar format. One of the 3DCNTPV cells was nonfunctional. Of these cells, the I_{sc} values are small with less spread, ranging from 0.84 to 19.1 μA/cm^2, which is more comparable to the 3DCNTPV cells manufactured directly on a p-Si wafer. The FF values are also close to 25% and the R_{sh} values, which are in the single to tens of ohms, are too low to show good curvature due to shunting. As with Ag, the addition of an Au metal layer seems to have exacerbated the shunting problem instead of mitigating it.

Table 13: Figures of merit for cells metallized with Au. The I_{sc} values are similar to the 3DCNTPV cells previously created and smaller than the other metallized cells. The V_{oc} values are similar to previously manufactured 3DCNTPV cells. The FF values are still close to 25%. The shunting is increased in these cells, which is shown by the decreased R_{sh} values. These values are much smaller than previously created cells, on the order of tens of ohms.

Sample Name	I_{sc} μA/cm^2	V_{oc} mV	FF %	P_{mp} nW/cm^2	R_{sh} Ω	R_s Ω
PlanarAu 01	15.7	6.92	26.16	28.4	9.17	8.48
PlanarAu 02	62.7	10.25	26.15	160.5	25.00	24.93
PlanarAu 03	37.8	3.93	25.45	37.8	11.00	9.67
MBEAu 430	0.84	1.91	25.33	327.0	13.93	11.71
MBEAu 427	-	-	-	-	70.57	40.43

Figure 105 shows dark and light IV curves for MBEOxAg 03. The IV curve for this cell is typical of all the cells produced with a metallized layer. The cell is totally shunted with an R_{sh} value of 41.39Ω, lower than similar 3DCNTPV cells on Si substrates, though the metallized layer did stop the curvature in the third quadrant which resulted from the CdTe/p-Si barrier. The shunt current dominates the dark IV curve for these metallized cells.

The light curve of MBEOxAg 03 is similar to those from other metallized cells. It is a straight line offset from the dark curve into the fourth quadrant. The inverse curvature in the fourth quadrant has disappeared due to the deposition of the metallized back contact layer.

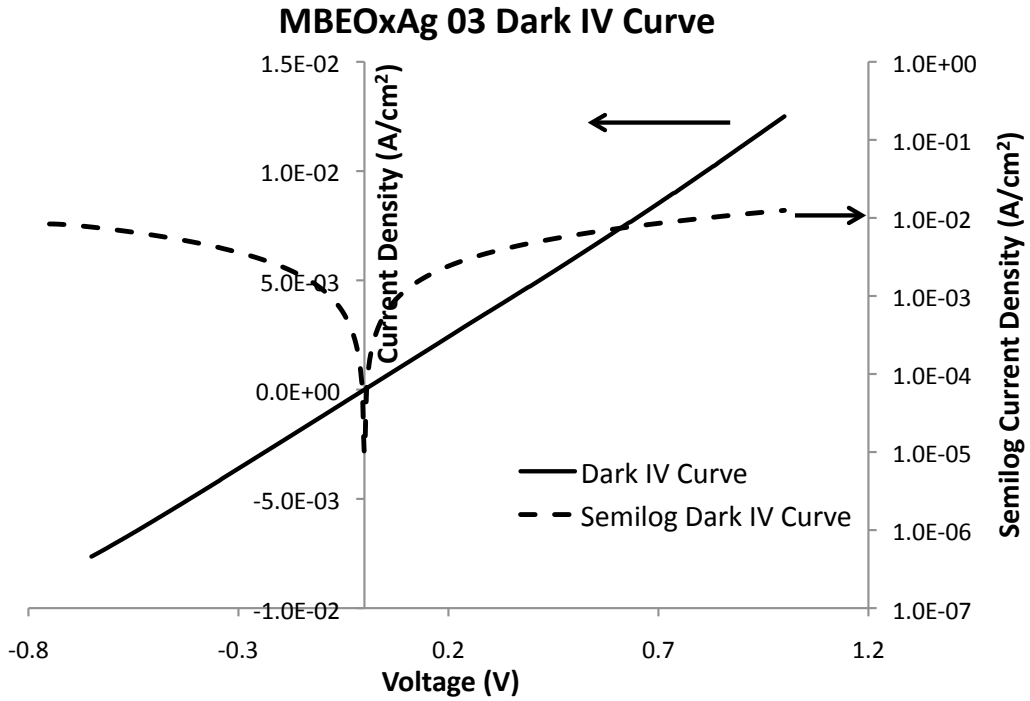

Figure 105: Dark curve for MBEOxAg 03 under an applied voltage from -0.75 to 1.0V. The solid line is the dark IV curve on a linear scale. The dashed line is the dark IV curve on a semilog scale. The dark curve is shunted with a resistance value of 41.39 Ω along the entire length. The curvature in the third quadrant is gone, indicating less of a rectifying barrier between the CdTe and metal back contact.

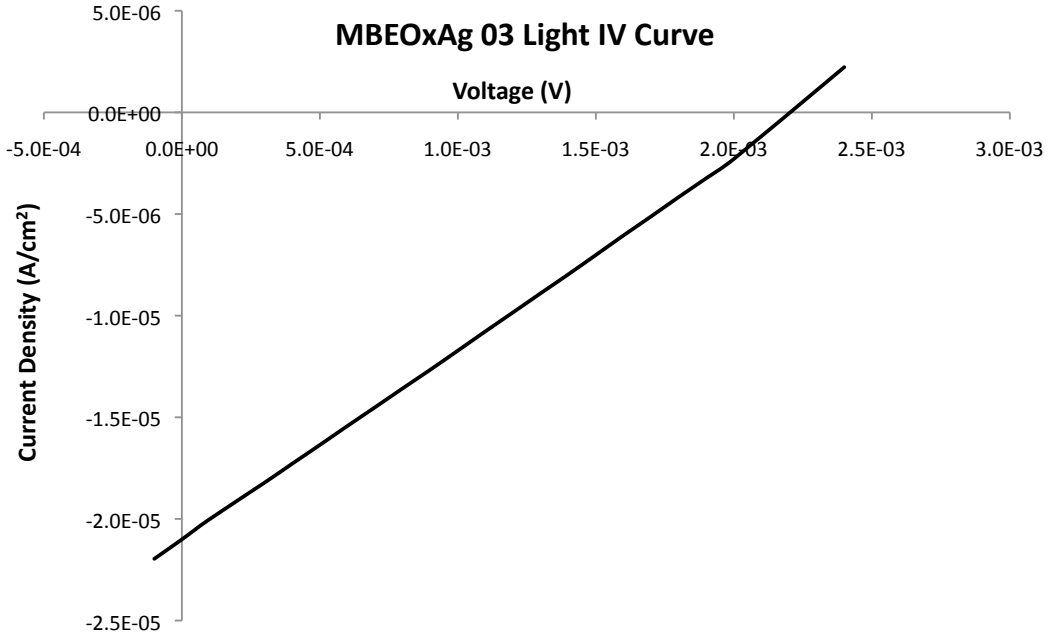

Figure 106: Light curve of MBEOxAg 03 showing an I_{sc} of 21.0μA/cm^2 and a V_{oc} of 2.25mV for a P_{mp} of 11.8nW/cm^2. The light curve shows no curvature and is offset from the dark curve into the fourth quadrant, indicating power production. The inverse curvature resulting from a large rectifying barrier between the CdTe and p-Si has disappeared, indicating that the metal back layer makes a more ohmic back contact to the CdTe.

5.7 Increased Growth Time

If the shunting is due to pinholes and inhomogeneities in the CdTe and CdS layers, then it should be possible to abate the shunt simply by increasing the MBE deposition time. A series of three planar cells metallized with Ag and three 3DCNTPV cells metallized with Ag and Cu were created. The CdTe and CdS deposition times were increased by 150 and 200% for this series of cells. CdTe deposition was increased from 45 minutes to 70 and 90 minutes. CdS deposition time was increased from 75 minutes to 120 and 150 minutes. Table 14 shows the sample names and the MBE deposition times for this series of cells.

Table 14: A series of cells was created with increased MBE deposition times for CdTe and CdS by 150 and 200%. CdTe deposition was increased from 45 minutes to 70 and 90 minutes. CdS deposition was increased from 75 minutes to 120 and 150 minutes.

Sample Name	CdTe deposition time (min)	CdS deposition time (min)
PlanarAg 102 PlanarAg 103 PlanarAg 104 MBEOxAg 07	70	120
MBEOxAg 02 MBEOxCu 07	90	150

Table 15 shows the figures of merit for cells with increased MBE deposition times. Two of the 3DCNTPV cells with increased deposition time, show increased I_{sc} values. One of the 3DCNTPV cells with 70 minutes CdTe deposition and 120 minutes CdS deposition has an I_{sc} very close to 1mA/cm^2, which is on the order of magnitude for other substrate configuration cells before $CdCl_2$ treatment. The V_{oc} values of these cells are also increased compared to previously manufactured 3DCNTPV cells.

Figure 91 shows the MBE and the cells metallized with Ag, Cu, and Au on a graph with the I_{sc} density on the abscissa and the V_{oc} on the ordinate. The MBE cells are shown by diamonds, planar metallized cells as x's, and 3DCNTPV metallized cells as squares. Four of the metallized 3DCNTPV cells (MBEOxAg 06, MBEOxAg

Table 15: Figures of merit for cells metallized with increased MBE deposition time. The I_{sc} values are similar to the 3DCNTPV cells previously created, though two of the 3DCNTPV cells have I_{sc} values larger than any of the MBE cells created. The V_{oc} values are similar to previously manufactured 3DCNTPV cells. The FF values are still close to 25%. The shunting is not abated in most of these cells. However, in cell MBEOxCu 07, the ratio of R_{sh} to R_s is ≈ 100, which indicates the presence of curvature.

Sample Name	I_{sc} μA/cm^2	V_{oc} mV	FF %	P_{mp} nW/cm^2	R_{sh} Ω	R_s Ω
PlanarAg 102	25.2	11.66	25.10	73.8	37.29	34.85
PlanarAg 103	93.9	18.71	24.72	434.2	27.31	23.36
PlanarAg 204	0.232	0.135	26.78	2,116.6	238.78	81.78
MBEOxAg 07	998.1	111.06	25.21	27,944.0	62.43	32.18
MBEOxAg 02	412.6	85.80	24.94	8,829.7	64.69	58.50
MBEOxCu 07	5.14	9.34	27.92	13.4	940.73	7.48

02, MBECu 433, and MBEOxAg 01) are better than the MBE cells in I_{sc} and on par with the best V_{oc} values.

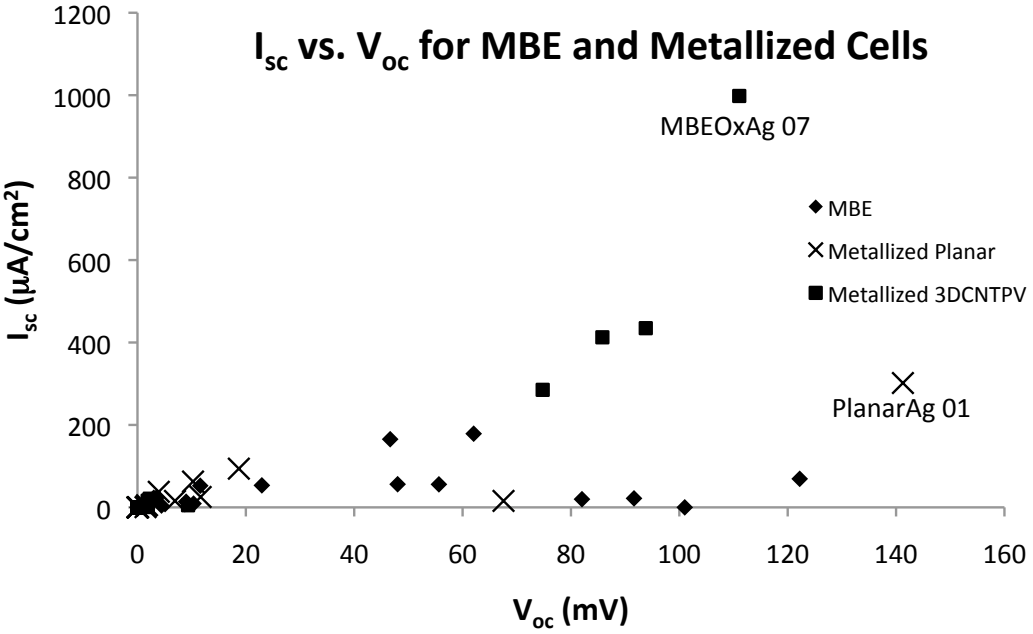

Figure 107: Graph of I_{sc} vs. V_{oc} for MBE cells with patterned VACNTs (diamonds), metallized planar cells (x's), and metallized 3DCNTPV cells (squares). The I_{sc} values for the working metallized cells are greater than the MBE cells with about the same V_{oc} values.

None of the increased deposition time cells showed any curvature except for MBEOxCu 07. Although the I_{sc} and V_{oc} values were low, the cell did demonstrate good curvature over the entire voltage range. Even though the R_{sh} value is low at 940Ω, it is still over a hundred times the R_s, which is enough to demonstrate curvature. This curvature was not in the fourth quadrant, however, due to the low figures of merit for this cell.

Figure 108 shows the dark IV curve MBEOxCu 07. This IV curve shows excellent curvature, with a knee at around 630mV. The dashed curve is the semilog plot of the dark IV curve. For voltages from zero to around 600mV the shunt current is clearly dominant. The dark current then increases rapidly as recombination current dominates for voltages from 600 to 750mV. After 750mV the dark IV curve flattens due to series resistance effects dominating the device behavior.

MBEOxCu 07 is the first significant evidence of curvature in any of the cells, 3DCNTPV or planar, yet manufactured. The existence of a cell with curvature demonstrates that the substrate process flow detailed here can make a PV device without shunting. It also demonstrates that a 3DCNTPV device with VACNTs can be used to manufacture solar cells without a shunt. Since the increased deposition time seemed to increase the power output and curvature of the manufactured cells, all cells in the following section have increased CdTe and CdS deposition times. CdTe deposition time is increased to 70 minutes while CdS deposition time is increased to 120 minutes.

Making one cell with curvature is still a far cry from mass manufacturability of these types of cells. Many different cells, both 3DCNTPV and planar, have been created which are shunted. Figure 109 shows a graph with R_s on the absisca and R_{sh} on the ordinate axis. On this graph, a cell which is a perfect shunt would have a value of $R_{sh} = R_s$ and thus would lie on the hashed straight line. In comparison, an 'x' demonstrates where the small scale laboratory CdTe cell produced by NREL

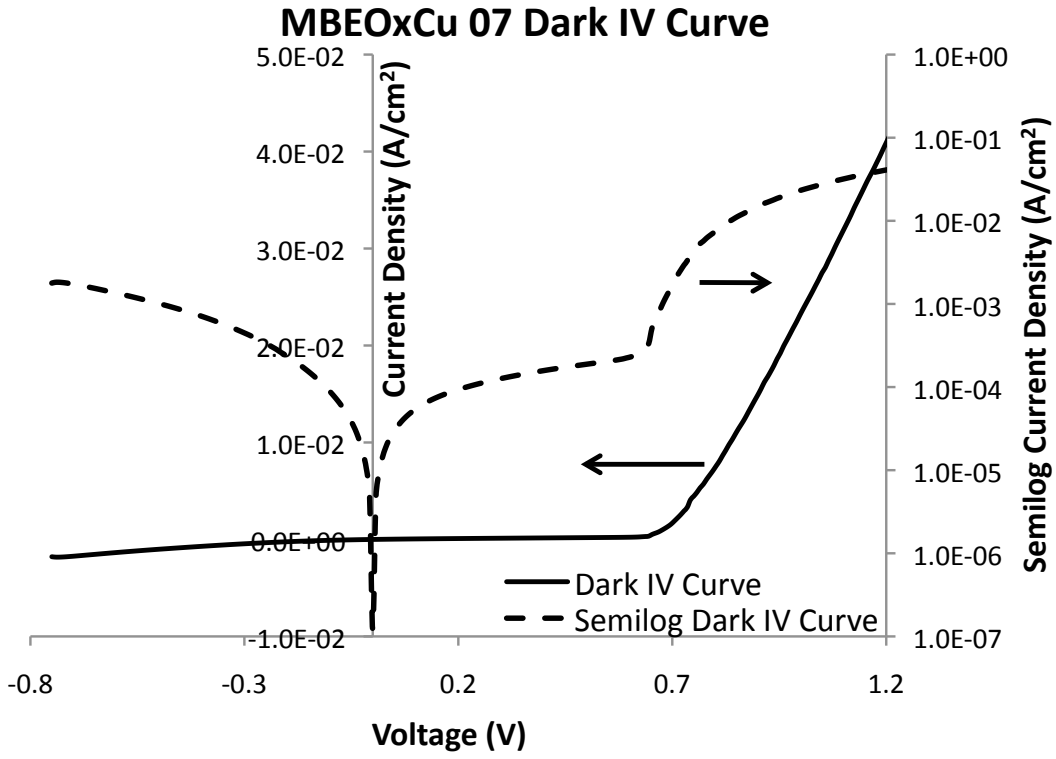

Figure 108: Dark curve for MBEOxCu 07 under an applied voltage from -0.1 to 1.0V. The solid line is the dark IV curve on a linear scale while the dashed line is the same curve on a semilog plot. The dark curve has a low shunt resistance of 940.73 ohms, but this resistance is over a hundred times larger than R_s so the cell demonstrates good curvature. The knee of this curve is located at around 615mV. This is easily seen in the semilog plot of the dark IV curve. The flat shunt current dominates for voltages from zero to around 600mV. At this point, the current increases dramatically as the dark curve is dominated by the recombination current. At a voltage of around 750mV the IV curve flattens as series resistance in the cell dominates. Though this cell has curvature in the dark, the I_{sc} of this cell in the light is not nearly large enough to catch any curvature in the fourth quadrant.

and described in §3.6 would reside on the graph. The R_s and R_{sh} values of every cell manufactured is plotted. Except for one point, that corresponding to MBEOxCu 07, every cell is very close to being a perfect shunt. The natural question to ask is why is very nearly every cell manufactured shunted. Is this shunt due to the top contact or due to an incomplete diode formation in the semiconductor layers?

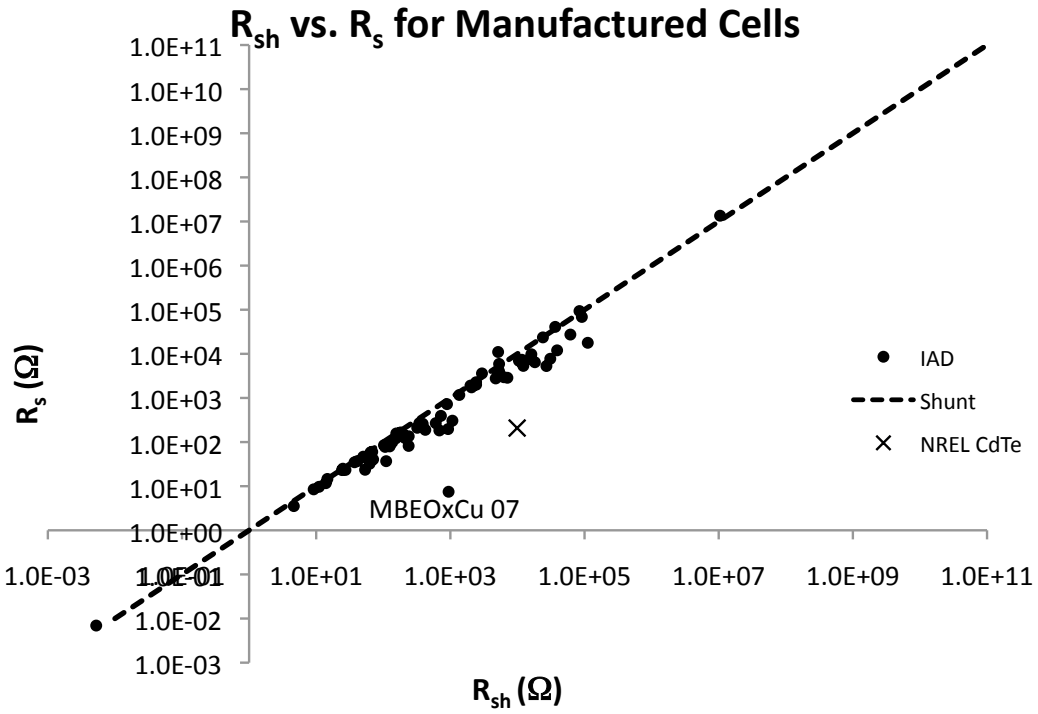

Figure 109: The R_s and R_{sh} values for every cell, both 3DCNTPV and planar, produced. Every point except for one, corresponding to MBEOxCu 07, lies on or near the line of $R_s = R_{sh}$, which indicates a complete shunt. In comparison, the 'x' marks the R_s and R_{sh} values for the research CdTe cell from NREL as described in §3.6.

Since these cells with dual top contacts have a region with CdTe/CdS which was shadowed during IAD, it is possible to measure IV curves on the semiconductor layers only and compare that to the inner portion with ITO deposited. Figure 110 shows the results of these two IV curves from PlanarAg 102. While the ITO curve (black) demonstrates a straight line shunt, the IV curve run on the semiconductor

portion (hashed line) shows good curvature. The right side of Figure 110 shows the semilog plot of the dark IV curves. For the ITO contact (solid line), shunt current is dominant for the entire voltage range. The curve with the contact on the MBE deposited semiconductor layer (dashed line) shows an inflection at around 200mV where the recombination current starts to have an effect. For voltages larger than 500mV, the curve flattens due to series resistance effects.

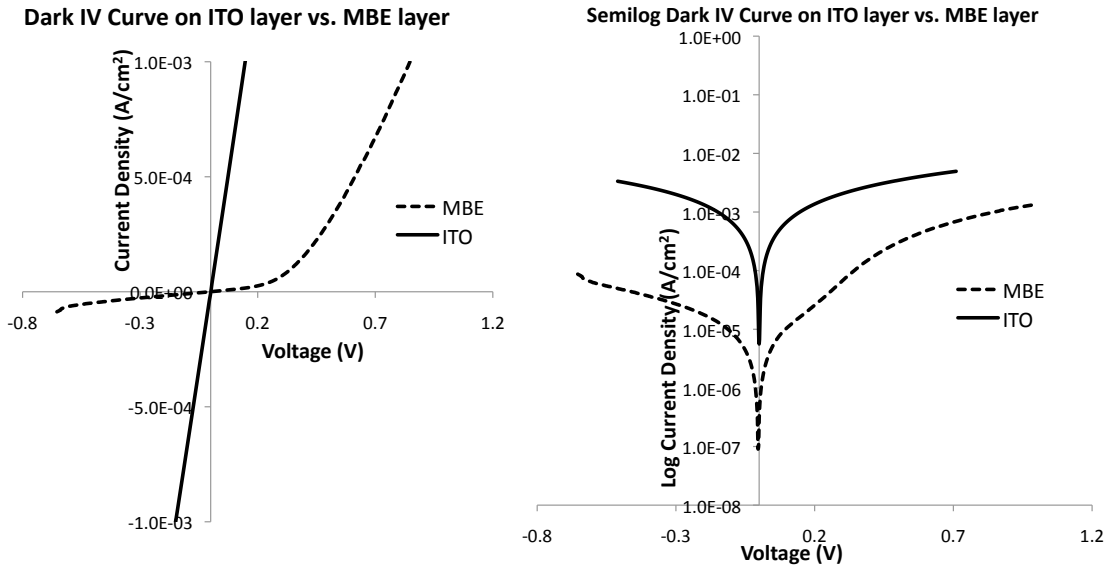

Figure 110: (Left)IV curves with electrical connection on the ITO top contact layer (black line) and directly on the MBE deposited semiconductor layer (dotted line) which was shadowed during ITO deposition. The IV curve on the ITO top electrode indicates a shunt, while the IV curve directly on the MBE deposited layer shows a knee. This indicates that the ITO deposition is the cause of the shunting and is not inherent to the semiconductor layers. (Right) Semilog plot of the dark IV curve for contact on the ITO (solid line) and MBE deposited semiconductor layer (dashed line). While the ITO contact is dominated by shunt current for the entire voltage range, the MBE contact has an inflection point around 200mV where the recombination current begins to have an effect. For voltages larger than 500mV series resistance effects flatten the dark IV curve.

By determining the R_{sh} and R_s values from the dark IV curves of the semiconductor layer for all the metallized cells and comparing those values to the ones obtained from the dark IV curves on the ITO layer, it is possible to determine if the as-deposited semiconductor layer reliably forms a diode. Figure 111 shows the

difference in the values of R_s and R_{sh} between the semiconductor layer and the ITO layer. The semiconductor layer IV curves have much higher R_{sh} values. The R_s values are also much larger, but this is to be expected since R_s is largely determined by the intrinsic resistance of the top layer, which is much smaller for ITO than for CdS. However, regardless of the particular value of R_{sh} and R_s, each of the IV curves taken from the semiconductor layer showed excellent curvature similar the curves in Figure 110. This indicates that the IAD, and not the MBE deposition, is the cause of the lack of curvature in the manufactured cells.

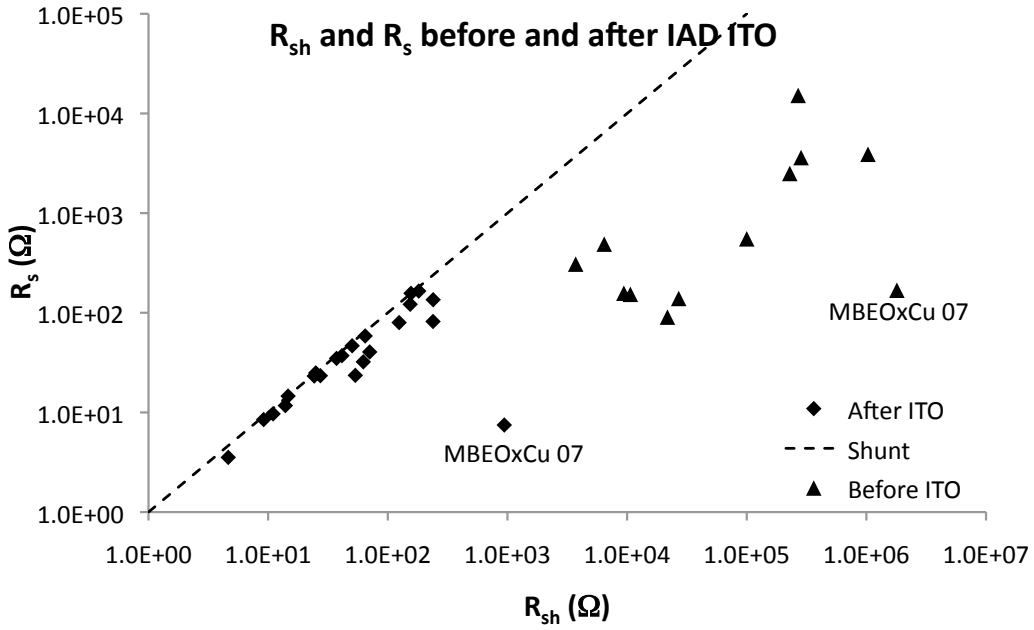

Figure 111: R_s and R_{sh} values calculated from IV curves from the ITO top contact and the MBE semiconductor layer. The semiconductor layer IV curves have much greater values of R_{sh} and exhibit curvature similar to the curves in Figure 110. This indicates that the MBE deposition of CdTe and CdS forms a working diode and shunting only occurs with the deposition of ITO. The R_s values are significantly larger in the IV curves from the semiconductor layer, but this is mainly due to the differences in the intrinsic resistance of the contact layer. ITO has a much lower resistance, so R_s values will be lower than for IV curves taken from CdS, which has a much higher comparative resistance. For a perfect top contact deposition, the R_{sh} from an IV curve on the semiconductor layer should be unchanged while the R_s becomes nearly zero.

If ITO deposition via IAD is the cause of the shunting, then it may be occurring due to two processes. ITO could be coating the sidewalls of pinholes and inhomogeneities in the semiconductor layer to form complete pathways between ITO and the metal back contact layer. If this is the cause of the shunting, then ITO deposition must be carried out in a process which is nearly line of sight. Though this would stop the shunting due to the complete coating of sidewalls, it has the disadvantage of no longer forming a complete coating over the VACNTs and the I_{sc} of cells would suffer since there would not longer be efficient collection of carriers around the entire face of a given VACNT.

The other process which may be causing the shunt is that the plasma in the IAD may be etching away semiconductor material. One of the reasons that IAD creates good quality ITO layers is that the argon plasma constantly partially etches the newly deposited ITO layer, so that the surface is pristine and free of impurities. It is possible, that at the very beginning of ITO deposition, the plasma begins to etch the semiconductor layer of the 3DCNTPV cell. This etching may only occur at the beginning of the deposition before enough ITO has been deposited to protect the face of the cell. However, since the CdS layer is so small, even this small time period may induce pinholes and inhomogeneities which would lead to shunts when ITO is deposited.

In order to determine if the plasma in the IAD was of high enough energy to etch the CdS layer, an Ag metallized planar cell was manufactured and placed in the IAD. The outside portion of the cell was masked with Al foil, while the inside portion was left bare. An IAD run was carried out with a closed shutter on the electron beam, so that no ITO would be deposited on the face of the cell. After removal from the IAD, the inner portion of the cell was clearly a different color than the protected outer portion of the cell (Figure 112 Bottom Left). This is an indication that etching of the semiconductor layer did take place. SEM imaging further showed that the surface of

the cell had been etched away (Figure 112). Where the protected portion has smooth, faceted grains of the CdS covered CdTe, the unprotected portion was much rougher, especially along GBs.

This indicates that the plasma in the IAD is capable of etching the semiconductor layer. Depending on the rate of this etch and how long it occurs, this may be the cause of the shunting in the 3DCNTPV cells.

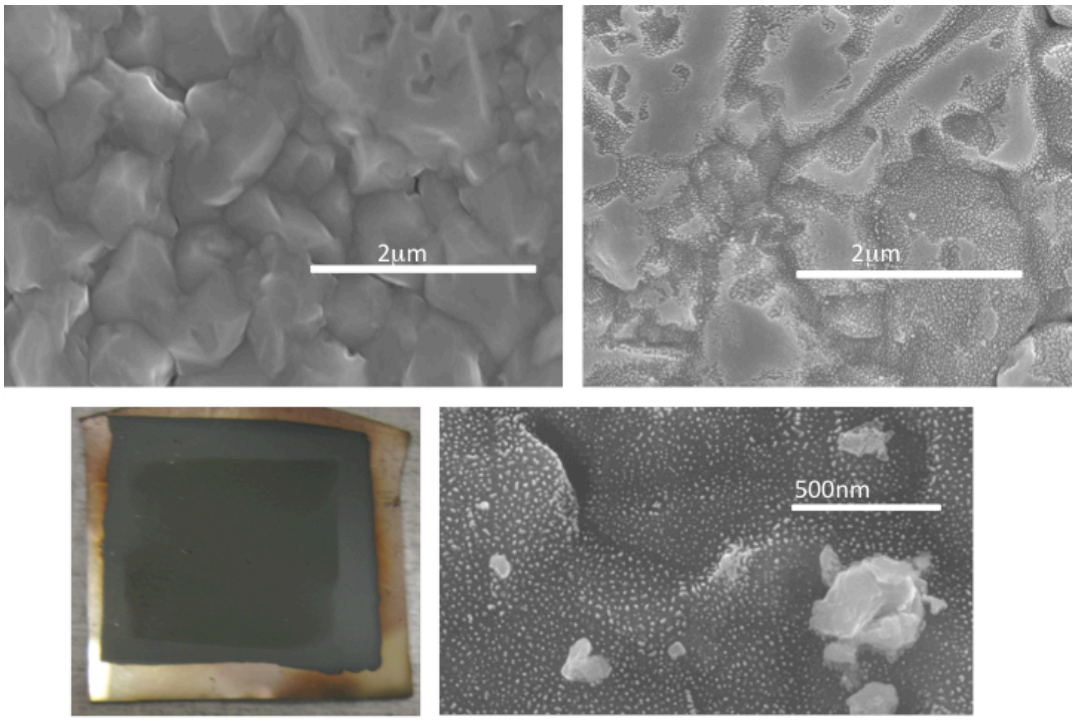

Figure 112: A planar cell which was exposed to the IAD plasma without ITO deposition shows clear evidence of etching by the plasma. (Bottom Left) A photograph of the cell. The portions of the cell which were masked during the IAD run are clearly a different color than the portion which was exposed to plasma. (Top Left) SEM micrograph of the protected outer portion of the cell. The CdS/CdTe layer shows smooth faceting of grains. (Top Right) SEM micrograph of the unprotected inner portion of the cell. The normally smooth semiconductor layer appears to have been etched by the IAD plasma. (Bottom Right) SEM micrograph closeup of the unprotected portion showing the etching away of the semiconductor layer.

Whether the cause of the shunting is through the coating of pinholes, etching away of the semiconductors, or a combination of the two, changes must be made to the

ITO deposition in order to create cells without debilitating shunts. There are three possible changes that can be made to ITO deposition:

1. Use IAD, but protect the semiconductor layer during deposition, discussed in §5.7.1

2. Change to a line of sight method without plasma such as electron beam evaporation, discussed in §5.7.2

3. Change to a method with a less intense plasma which will not etch the semiconductor layer, discussed in §5.7.3

5.7.1 Altered ITO Deposition

The first of these solutions tried was protecting the semiconductor layers during IAD deposition. There are two possible methods to do this. The first is to deposit onto the semicoductor layer a very thin barrier which is either less susceptible to plasma etching, or is thick enough that it will be etched away before ITO deposition instead of the semiconductor layer. The second method is to delay the use of plasma until a protective layer of ITO has already been deposited on the semiconductor face. In this case the deposition of ITO will occur in two stages, the first stage will be electron beam evaporation of ITO followed by regular IAD of ITO.

Three cells, one planar and two 3DCNTPV, were created with a barrier layer between the CdS and ITO layers. One 3DCNTPV cell was metallized with Cu, the other with Ag. The planar cell was metallized with Ag. In all three of the cells, after CdTe/CdS deposition 4 nm Ni was deposited via electron beam evaporation at a rate of 0.25$\mathring{A}$/s. Ni was chosen as a barrier metal because, for a metal, it is relatively transparent and holds up well to plasma. After Ni deposition, 50nm ITO was deposited via the regular IAD recipe. A thinner ITO layer was used to account for the parasitic absorption of the Ni layer, so that the I_{sc} would not be too low. The figures of merit for these cells are shown in Table 16.

The PlanarAg 202 and the MBEOxAg 62 cell were functional, albeit with very low I_{sc} and V_{oc} values. The barrier layer did little to alleviate the shunting problem in these cells. The values of R_{sh} in the cells are only in the hundreds of ohms. The third cell, MBEOxCu 02, demonstrated good curvature with R_{sh} of 741Ω and R_s of 12Ω. However, this cell demonstrated no photocurrent.

In order to account for a rectifying barrier between the CdS and Ni layers, this process was repeated for cells with 4nm In. All of the cells showed similar shunting and none of them were functional. This is probably due to the increased parasitic absorption of In compared to Ni.

Table 16: Figures of merit for cells with 4nm Ni deposited prior to IAD of ITO. The Ni metal was meant as a barrier to prevent any unintended etching of the semiconductor layers. For the cells created using this method, the I_{sc} values are low due to parasitic absorption of the Ni layer and the R_{sh} values were not improved. The barrier layer did nothing to alleviate the shunt in the two working cells. The nonworking cell, MBEOxCu 02, did show good curvature, but no photocurrent.

Sample Name	I_{sc} μA/cm^2	V_{oc} mV	FF %	P_{mp} nW/cm^2	R_{sh} Ω	R_s Ω
MBEOxCu 02	-	-	-	-	741.02	12.14
MBEOxAg 62	8.0	1.43	25.46	2.90	165.42	52.13
PlanarAg 202	1.25	0.191	52.42	0.12	110.15	47.73

Two planar cells were created using a two stage deposition method. In the IAD chamber, 10nm of ITO was deposited at 1.5$\mathring{A}$/s in the IAD chamber with plasma power off. After the first 10nm were deposited, the plasma was ignited and 40nm ITO was deposited via the normal IAD recipe. A thinner layer of ITO was used in this method because the ITO which is deposited without plasma absorbs far more light and would decrease the I_{sc} values of the cells. Table 17 shows the figures of merit for these cells.

PlanarAu 106 was functional with good I_{sc} and V_{oc} values at 100.1μA/cm^2 and 167.83mV, respectively. However, it still showed shunting. PlanarAg 205 was not functional, though with R_{sh} of 870Ω and R_s of 51Ω it did show acceptable curvature.

This nonfunctional cell was the only cell which exhibited curvature using the 2-stage ITO recipe. Figure 113 shows the difference in IV curves between the two cells created using the 2-stage ITO deposition. One IV curve has curvature, but displays no photocurrent, while the other IV curve has no curve, but has good photocurrent.

Table 17: Figures of merit for cells with a 2-stage deposition of of ITO. 10nm ITO was evaporated in the IAD chamber with no plasma power. The remaining 40nm ITO was deposited with plasma assistance. For the cells created using this method, the I_{sc} value of one cell was non-zero, however it was totally shunted. The other cell had good curvature, but showed no photocurrent. This deposition was abandoned due to the inability to reliably make functional cells.

Sample Name	I_{sc} μA/cm^2	V_{oc} mV	FF %	P_{mp} nW/cm^2	R_{sh} Ω	R_s Ω
PlanarAu 206	100.1	167.87	24.33	4,088.1	870.17	848.03
PlanarAg 205	-	-	-	-	853.96	51.24

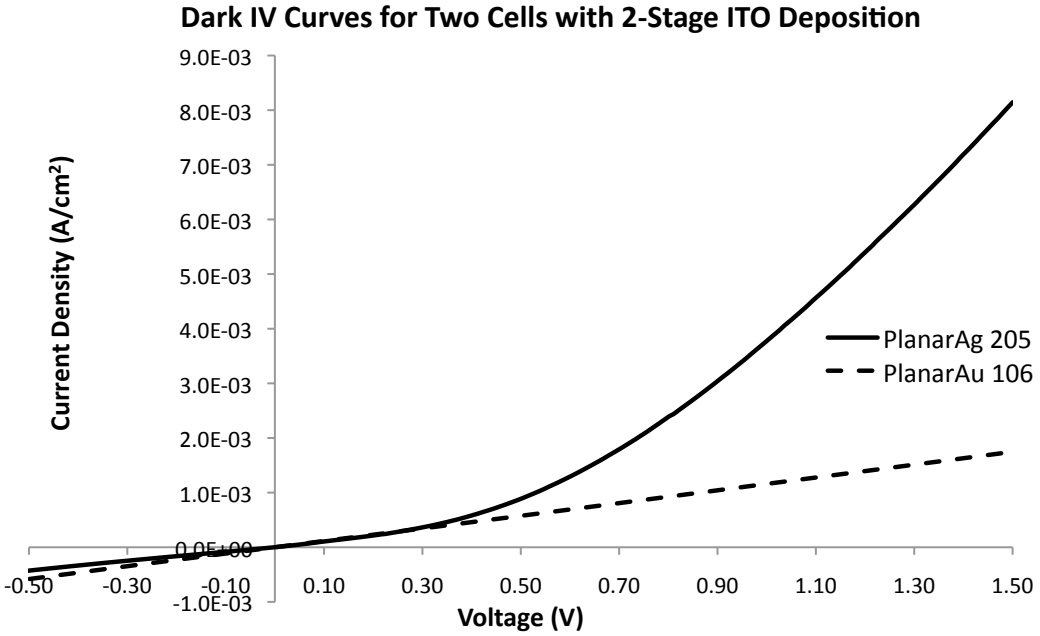

Figure 113: Dark IV curves of cells with a 2-stage ITO deposition. PlanarAu 206 has no curvature, indicating it is shunted, but demonstrates good photocurrent with a I_{sc} of 100.1μA/cm^2 and a V_{oc} of 167.87mV. On the other hand, PlanarAg 205 demonstrates good curvature, but has no photocurrent. For both types of altered IAD process, it was not possible to create a cell with both good curvature and good photocurrent properties. This line of ITO deposition was ultimately abandoned for other types of ITO deposition.

Altering the IAD of ITO was ultimately abandoned due to the inability to reliably create cells which demonstrated both photocurrent and curvature. A new line of sight method of ITO deposition was tried, electron beam evaporation of ITO.

5.7.2 Electron beam Depostion

Electron beam evaporation is a non reactive, line of sight method of depositing ITO. Since the deposition is non reactive, the oxygen content of the film is the same as the source material. This oxygen content is lower than the film produced in IAD, so it is expected to have a lower bandgap and be less transparent. Normally, this transparency due to lack of oxygen would be offset by the increase in conductivity, however, the lack of plasma etching during deposition increases impurities and dangling bonds which increase the resistance of the ITO.

Figure 114 shows the transmission spectra of 150nm ITO deposited via IAD and electron beam evaporation. The electron beam deposited ITO has less than half (41%) of the transmission of the IAD deposited ITO at 700nm. The decreased crystallinity of the electron beam deposited film can be observed by the wide absorption band around 600nm. While the IAD ITO has a near constant high transmission value (>90%) for wavelengths from 600 to 933nm, the electron beam deposited ITO does not show this plateau. It is instead a hump centered at 700nm with a transmission of 38.1%. The transmission then falls off on either side of that maximum.

The IAD ITO is also more conductive. The R_{sheet} of both samples was measured as in §3.5.1. The IAD sample was found to have a R_{sheet} value equal to $23.13 \pm 4.64\Omega/\square$, while the electron beam deposited ITO was over three times more resistive at $83.03 \pm 12.59\Omega/\square$.

Twenty-one solar cells were created with a 50nm ITO top contact deposited via electron beam evaporation in a CVC electron beam evaporator at a rate of $1.0\mathring{A}$/s. 50nm ITO was deposited because it is a good compromise between having enough

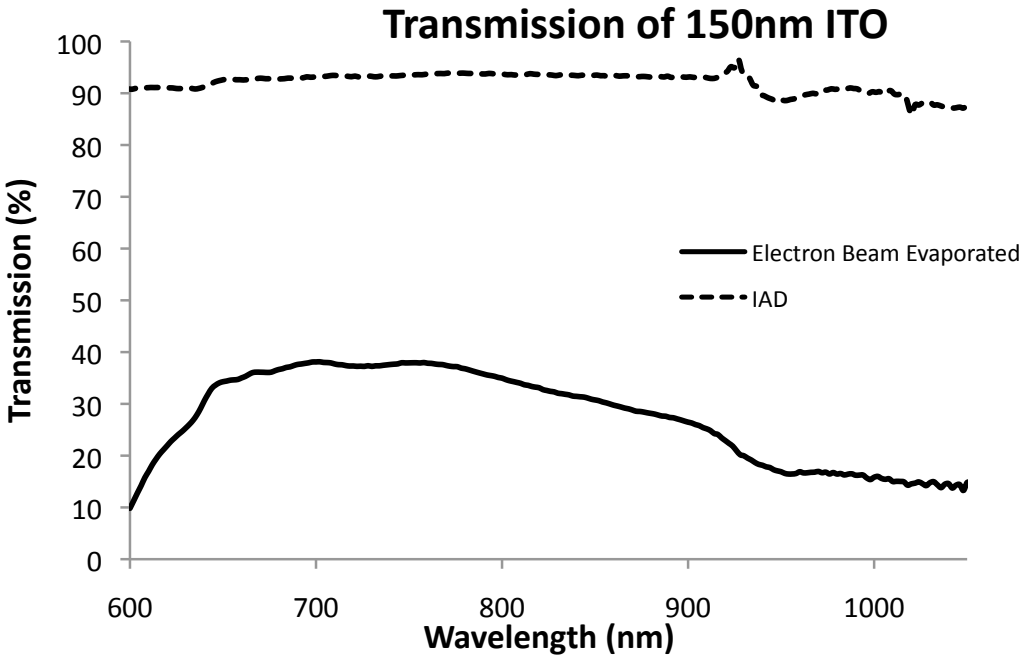

Figure 114: Transmission of IAD ITO and electron beam deposited ITO was measured as in §3.5.1. The IAD deposited ITO has a much broader transmission plateau between 600 and 933nm with higher transmission (>90%) than the electron beam deposited ITO. The electron beam deposited ITO also has a much greater absorption of incident light around 600nm.

ITO to form a complete, conductive top contact while still being thin enough to compensate for the increased parasitic absorption of the ITO layer. Six of these cells were 3DCNTPV type cells, while the rest were planar cells with coatings of Cu, Ag, Au, and Ti. Of the cells created, 12 were operational. The I_{sc} values for these cells were lower than the metallized cells coated with IAD ITO, most likely due to the lack of transmission of the electron beam deposited ITO. Table 18 shows the figures of merit for cells produced with an ITO top contact deposited via electron beam evaporation.

.

Table 18: Figures of merit for cells with a 50nm ITO top contact layer deposited via electron beam evaporation. The I_{sc} values are, in general, lower than the previous metallized 3DCNTPV cells with a 150nm IAD ITO top contact. The V_{oc} values, in general, are larger, with several cells having values above 100mV. The average value of R_{sh} has been increased and the ratio of R_{sh} to R_s is one to three orders of magnitude. This indicates that the electron beam evaporation of ITO has decreased the amount of shunting. However, the shunt is not decreased enough to show curvature in the fourth quadrant, so FF values are still close to 25%.

Sample Name	I_{sc} μA/cm^2	V_{oc} mV	FF %	P_{mp} nW/cm^2	R_{sh} Ω	R_s Ω
MBEOxCu 01	-	-	-	-	437.56	58.84
MBEOxCu 05	0.52	2.95	26.98	0.42	6,826.87	15.56
MBEOxAg 64	-	-	-	-	123.65	24.43
MBEOxAu 54	0.21	1.91	24.60	0.10	12,481.28	10,181.54
MBEOxAu 57	1.018	41.65	25.56	10.8	4,372.35	1,460.49
PlanarCu 02	0.083	82.67	25.46	1.74	221,896.77	123.70
PlanarCu 04	0.006	67.34	25.81	0.11	153,843.79	64.99
PlanarCu 07	1.96	138.04	22.35	60.5	7,346.46	30.22
PlanarCu 08	11.5	173.17	23.29	462.4	2,031.57	35.23
PlanarAg 105	-	-	-	-	6,813.38	2,562.66
PlanarAg 113	-	-	-	-	7,431.08	2,261.27
PlanarAg 108	-	-	-	-	279,728.10	10,195.55
PlanarAg 114	-	-	-	-	5,464,182.29	222,261.74
PlanarAg 116	0.67	137.18	25.04	22.9	674,354.31	880,979.65
PlanarAg 201	-	-	-	-	730.78	65.65
PlanarAg 205	-	-	-	-	853.96	51.24
PlanarAg 207	-	-	-	-	2,509.54	94.64
PlanarAu 201	56.3	55.98	25.00	786.0	573.49	563.89
PlanarTi 02A	19.4	265.45	25.38	1,309.5	133,525.61	19,216.73
PlanarTi 02B	34.5	265.30	25.54	2,334.2	3,039,790.86	403,763.07

In these cells, the I_{sc} values, which range from 0.006 to 56.3μA/cm^2 are generally lower. The V_{oc} values range from 1.91 to 265.45mV have been increased (Figure 115). Many cells have V_{oc} values in excess of 100mV. Coupled with the higher R_{sh} values of the cell, there is good evidence that the shunting has been partially abated for a number of the produced cells.

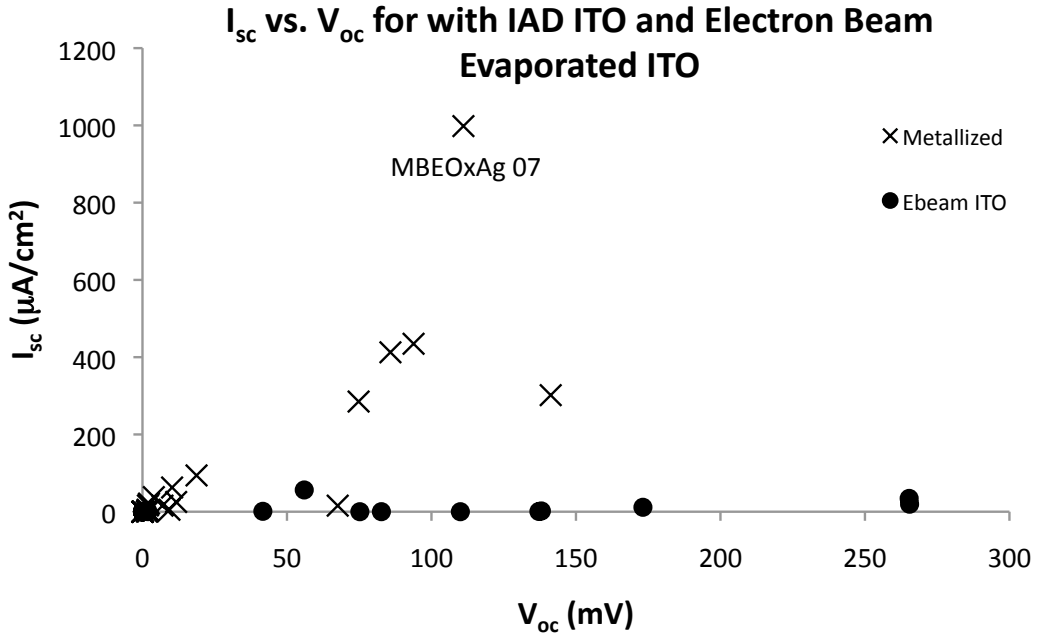

Figure 115: Graph of I_{sc} vs. V_{oc} for metallized cells with 150nm IAD ITO (x's), and metallized cells with 50nm ITO deposited via electron beam evaporation (circles). The I_{sc} values for the cells with electron beam evaporated ITO are much smaller than the cells with IAD ITO. This is due to the smaller light transmission through the electron beam evaporated ITO. While the I_{sc} values are smaller, in general, the V_{oc} values are larger for the electron beam evaporated ITO. These cells also show much larger R_{sh} values, indicating that electron beam evaporation of ITO does not exacerbate the shunting problem in these cells.

Only one cell out of many (MBEOx Cu 07) showed curvature for ITO deposited via IAD. Most of the cells created with electron beam evaporated ITO have at least a factor of 10 difference between the fabricated R_{sh} and R_s values. Only 7 of the cells have an R_{sh} value less than fives times the R_s. This is shown in Figure 116. Whereas all the IAD ITO cells were shunted except for one, the electron beam evaporation cells show a wide range of final R_{sh} and R_s values.

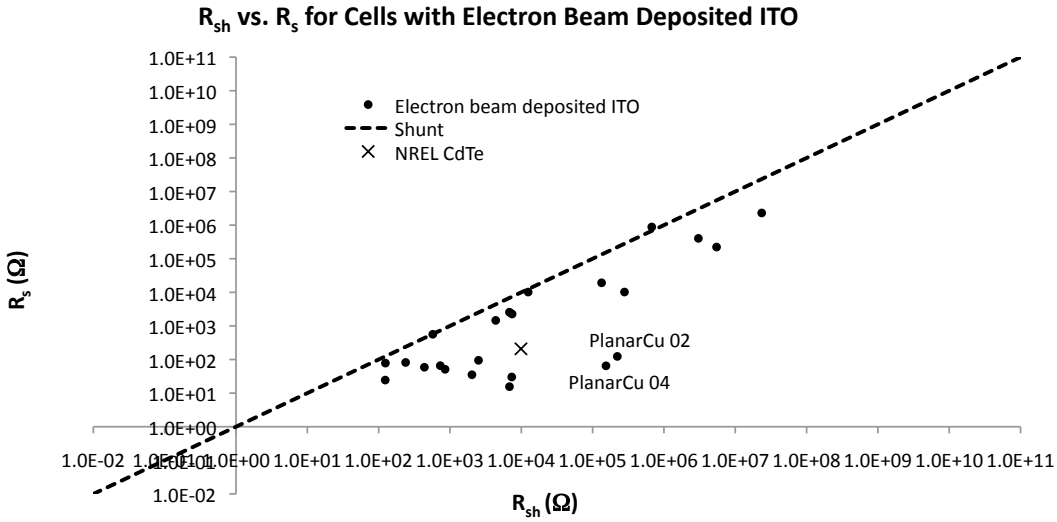

Figure 116: The R_s and R_{sh} values for cells produced with a top contact consisting of 50nm electron beam deposited ITO. As opposed to the cells with an ITO top contact deposited by IAD, the points representing the cells with electron beam deposited ITO do not lie on the line $R_s = R_{sh}$. There is a large range of R_{sh} and R_s values in completed cells, but in most cases, R_{sh} is a least five times larger than R_s. Though not a perfect top contact deposition method, this indicates the electron beam evaporated ITO can produced cells without a shunt. The 'x' marks the R_s and R_{sh} values for the research CdTe cell from NREL (§3.6). Some of the cells with electron beam evaporated ITO have R_{sh} larger than the NREL CdTe cell and some have R_s values lower than the cell.

Figure 117 shows the dark IV curve of a 3DCNTPV cell (MBEOxCu 05) with a top contact of 50nm electron beam evaporated ITO on a linear scale (solid line) and semlog scale (dashed line). The semilog plot of the dark IV curve for this cell is similar to the curve for MBEOxCu 07 shown in Figure 108. For voltages from zero to 600mV, the shunt current is dominant. For voltages from 600 to 700mV, the recombination current of the cell has a greater effect. For voltages larger than 700mV, the IV curve flattens as parasitic series resistance becomes more important. Overall, this cell demonstrates excellent curvature with an R_{sh} value over 400× the R_s. However, the I_{sc} for this cell is only $0.52\mu A/cm^2$, which is not large enough to offset the IV curve into the fourth quadrant so that the knee appears there. This is why the FF of the cells with electron beam evaporated ITO still have values close to 25%. The low value of I_{sc} for the cells is likely due to the lack of transparency in the electron beam evaporated ITO and it may be necessary to investigate ways to increase light transmission in the ITO, such as by a post deposition anneal.

5.7.2.1 Post Deposition anneal

Although electron beam deposited ITO reduces the shunting found in some of the cells with IAD top contacts, it is too resistive and opaque to be used for the production of solar cells. One of the most common ways to increase the conductivity and transparency of ITO is through annealing [249]. With annealing, the ITO films becomes more conductive and transparent [75]. The increase in conductivity and transparence is due to diffusion of Sn atoms which decrease lattice disorder and increase both mobility in the films and scattering off GBs [250]. An increase in conductivity may also occur in nonoxygenated environments due to the expulsion of interstitial oxygen [251]. In oxygen rich environments, this increase in conductivity from a decrease in lattice disorder is offset by the incorporation of oxygen into the film and the film will become much more transparent and less conductive.

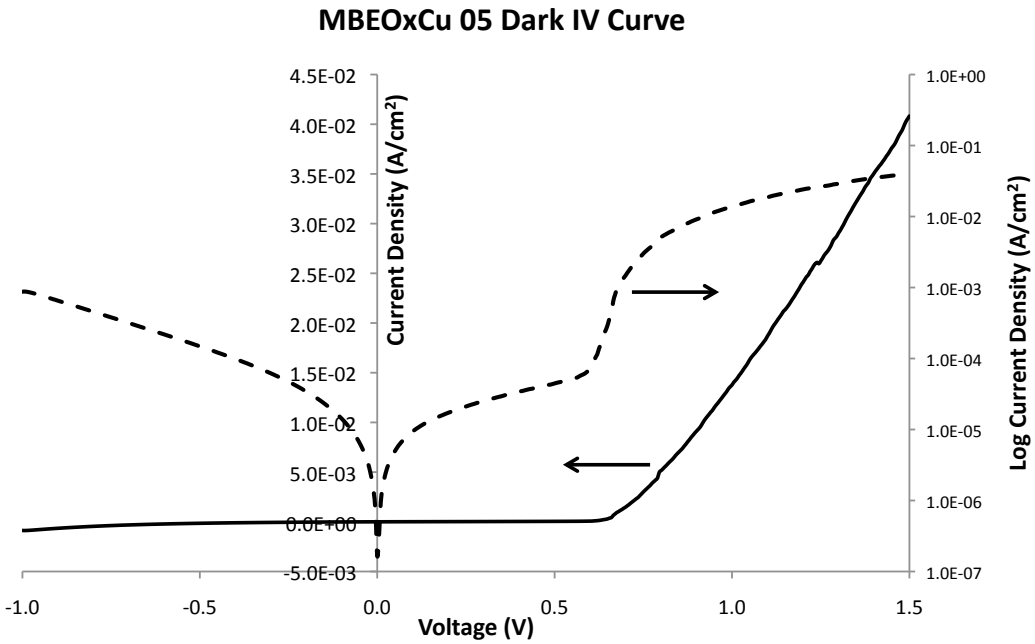

Figure 117: Dark curve for MBEOxCu 05 under an applied voltage from -1.0 to 1.5V. The solid line shows the dark IV curve on a linear scale. The dashed line shows the dark IV on a semilog scale. The dark curve has a high shunt resistance of 6,826.87 ohms, and a low R_s of 15.56 ohms, so the cell demonstrates good curvature. The knee of this curve is located at around 635mV. Though this cell has curvature in the dark, the I_{sc} of this cell is not nearly large enough at $0.52\mu\text{A/cm}^2$ to catch any curvature in the fourth quadrant. The semilog plot of the dark IV curve for this cell looks similar to the curve for MBEOxCu 07. The shunt current is dominant for voltages from zero to 600mV. From 600 to 700mV, the recombination current is dominant. For voltages larger than 700mV, the curve flattens as parasitic series resistance becomes dominant.

While annealing ITO on ceramic substrates may be straightforward, extra care must be taken in the case of substrate solar cell. For the 3DCNTPV cells the metal underlayer on SiO_2/Si has the potential to oxidize if annealed in an oxygen rich environment, or to delaminate due to a mismatch of coefficients of thermal expansion.

A layer of 150nm thick ITO was deposited onto glass slides using a CVC electron beam evaporator at a rate of 1.0$\mathring{A}$/s. Samples were then annealed in H_2, N_2, vacuum, and air environments. For the H_2 and N_2 anneals, samples were heated to 400^{o}C at a rate of 100^{o}C/min under 200sccm H_2 or N_2 gas flow. The pressure was reduced to 7.5 Torr and the samples were kept at 400^{o}C for 1 hour. For the vacuum anneal, the samples were heated to 400^{o}C at 100^{o}C/minute without gas flow. The pressure was reduced to 0.15 Torr and the temperature was held at 400^{o}C for 1 hour. For the air annealing, the samples were heated to 400^{o}C at a rate of ^{o}C/minute at atmospheric pressure.

The sheet resistance and transmission of ITO annealed in various environments was measured using the setups described in §3.5.1. The results of the 4-point probe measurement are shown in Table 5.7.2.1. The R_{sheet} of the as-deposited ITO was found to be 83.03±12.59Ω/□. This value was decreased to 52.85±1.90Ω/□ by annealing in H_2, to 58.46±2.32Ω/□ by annealing in N_2, and to 71.66±3.74Ω/□by annealing in vacuum. Annealing the samples in air raised the resistance of the sample to 97.89±7.33Ω/□ due to oxygen incorporation.

Table 19: Change in R_{sheet} of electron beam evaporated ITO after anneal in various environments. The anneal was carried out at a tempearture of 400^{o}C for one hour. The R_{sheet} value of the as-deposited ITO decreased after annealing in H_2, N_2, and vacuum environments and increased after annealing in air.

Deposited R_{sheet} Ω/□	Annealing Environment	Temperature ^{o}C	Time *minutes*	Pressure *Torr*	R_{sheet} Ω/□	Percent Change
83.03±12.59	H_2	400	60	7.5	52.85±1.90	-36.34
	N_2			7.5	58.46±2.32	-29.59
	Vacuum			0.15	71.66±3.74	-13.69
	Air			750	97.89±7.33	17.90

The transmission results for ITO annealed in each environment are shown in Figure 118 for wavelengths from 600 to 1100nm. The as-deposited ITO, denoted by the solid black line has the lowest transmission throughout the entire spectrum. Annealing in a Hydrogen environment increases the transmission only slightly for wavelengths greater than 900nm. For larger wavelengths, there is not change in the transmission. Annealing in a nitrogen environment increases the transmission to a maximum transmission of 47.4% at 698nm. Annealing in vacuum increased the transmission to nearly 60% at its largest point. By far the highest transmission was from annealing in air. Though, not as large as the transmission from IAD ITO, annealing in air increased the transmission to nearly 90% for a wavelength range of 650 to 900nm.

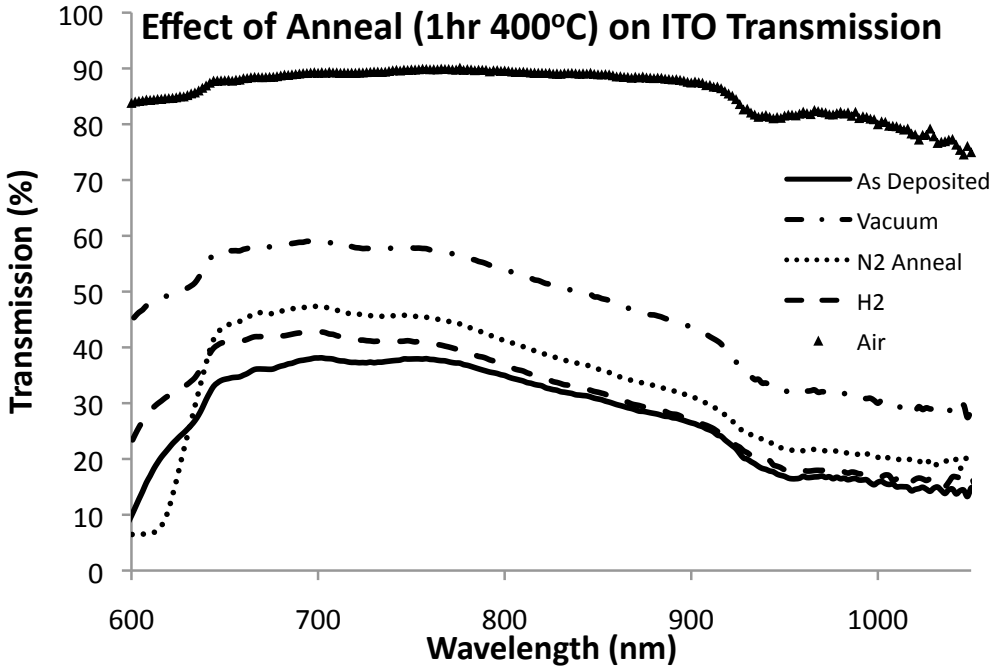

Figure 118: Transmission results from electron beam deposited ITO after annealing in various environments at 400^{o}C for 1 hour. A slight increase in transmission was found for samples annealed in H_2 and N_2. Moderate transmission increases were realized for annealing in vacuum. By far the largest transmission increase was for sample annealed in air. Due to the incorporation of oxygen into the sample, the transmission was increased to nearly 90% for a wavelength range of 650 to 900nm. However, this transmission is still lower than that for IAD ITO.

In order to anneal a sample without oxidation, PlanarCu 08 was annealed for 5 minutes in an H_2 environment using the procedure followed for the electron beam evaporated ITO onto glass slides. Figure 119 shows the dark IV curves for this cell before and after the 5 minute anneal. While the dark IV curve shows good curvature, the cell is completely shunted after only 5 minutes at 400^{o}C. The I_{sc} for this cell went from 11.5 to 0μA/cm^2. The shunting may occur due to migration of metal ions at high temperatures or the formation of a rectifying barrier between the CdS and ITO layers as mentioned in Chapter 2.

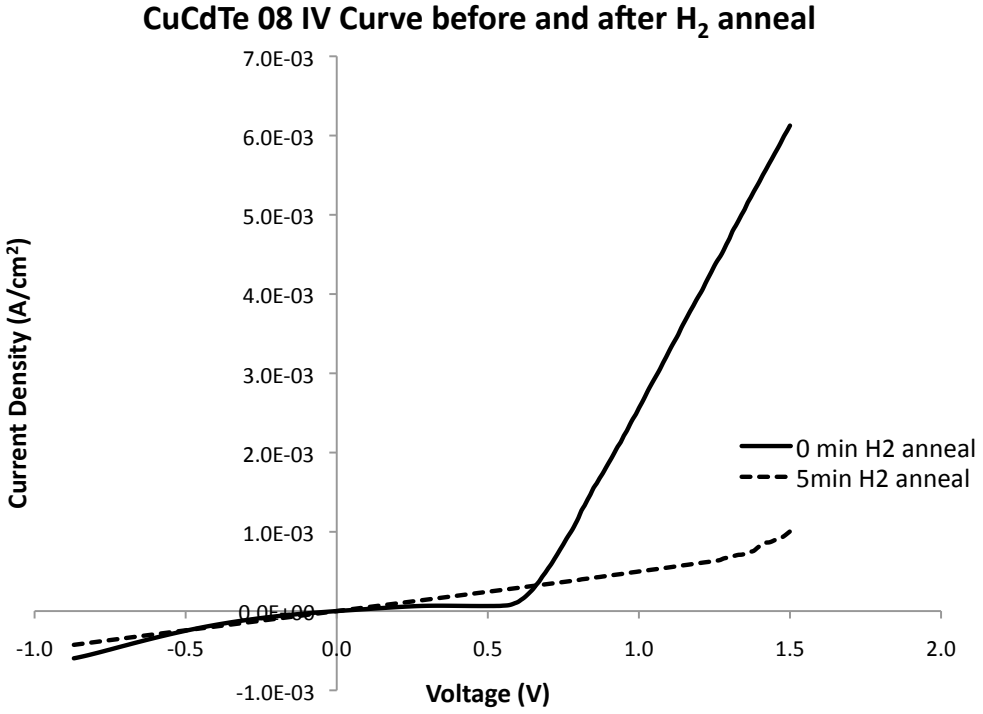

Figure 119: Dark IV curve for PlanarCu 08 before annealing and after a single 5 minute anneal in H_2. The curvature in the IV curve of the cell before anneal is totally gone after annealing, indicating that the cell is a shunted. Under light conditions, the cell went from an I_{sc} and V_{oc} of 11.5 μA/cm^2 and 173.17mV, respectively, to having no detectible photocurrent.

A post deposition anneal in air was also carried out on PlanarAu 201. The anneal was carried out in 1 minute increments and IV curves were used to monitor the state of the cell.

Similar to the IV curves shown in Figure 119, PlanarAu 201 was fully shunted by the first 1 minute annealing period. Figure 120 shows the results of the air anneal on the R_{sh} and V_{oc} values of the cell. Both of R_{sh} and V_{oc} values begin to rapidly decrease with annealing due to shunting of the cell. This indicates that although annealing electron beam evaporated ITO after deposition on a PV device increases transmission and decreases R_{sheet}, the annealing is deleterious to the photocurrent produced by the cell. The cause of this in PlanarAu 201 may be exacerbated by stress induced thermal shock from multiple annealing attempts. However, the results are the same as in PlanarCu 08, which only underwent one anneal with a much longer cool down period.

Although electron beam deposited ITO does a much better job of reducing shunting in the solar cells produced here, it is too resistive and absorptive. Using only a 50nm thin film parasitically absorbs enough light to have a noticeable effect on the output current on the cells. Therefore it is necessary to increase the conductivity and transmission of the ITO after deposition. This was tried by annealing the cells at 400^oC in H_2 and air environments. However, annealing for as short a time as 1 to 5 minutes shunted the cells and decreased the V_{oc} of the cells.

Since post deposition annealing of electron beam evaporated ITO was unsuccessful, a third deposition method was tried, RF sputter of ITO. RF sputtering of ITO is a deposition method which utilizes relatively low plasma power while still depositing relatively transparent and conductive ITO.

5.7.3 RF sputter Deposition

A Kurt J. Lesker PVD75 RF Sputterer was used to deposit an ITO top contact using a 3-inch diameter indium bonded, copper plated ITO sputter target (Kurt J. Lesker #EJTITOX403A4). To deposit ITO, a sample is placed in the chamber and sample rotation is turned on. The chamber is pumped down to a pressure of 5mTorr.

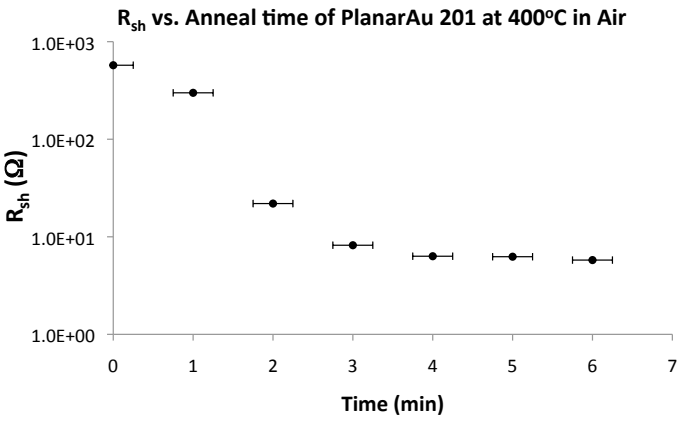

Time (min)	R_{sh} (Ω)	Error
0	573.49	1.15
1	299.11	0.14
2	21.91	0.04
3	8.19	0.002
4	6.32	0.002
5	6.25	0.002
6	5.77	0.002

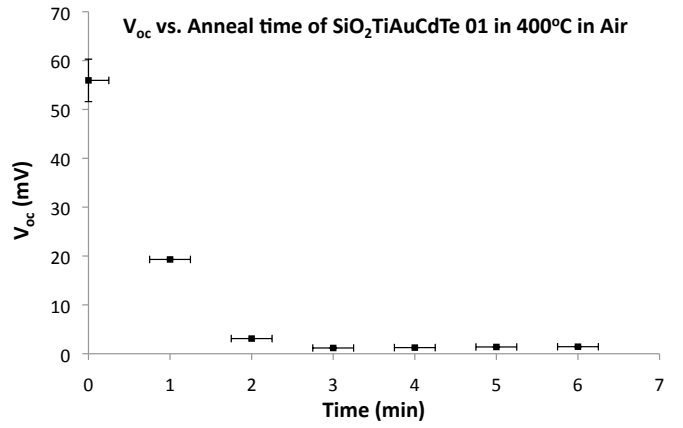

Time (min)	V_{oc}(mV)	Error
0	55.95	4.35
1	19.30	0.03
2	3.10	0.01
3	1.18	0.03
4	1.26	0.05
5	1.39	0.07
6	1.44	0.08

Figure 120: R_{sh} and V_{oc} values from the IV curves of PlanarAu 201 during a 400^{o}C anneal in air. Both R_{sh} and V_{oc} begin to immediately decrease. After only a 1 minute anneal in air at 400^{o}C, PlanarAu 201 was fully shunted. While increasing transmission and conductivity, annealing as-deposited ITO is deleterious to the solar cell and cannot be used to improve the ITO properties.

Argon gas (50 sccm) is flowed into the chamber and a gate valve is used to stabilize the pressure at 5 mTorr. After pressure stabilization, the plasma power is ramped to 100W at a rate of 120W/min. The plasma power is held at 100W during ITO deposition. After deposition, the plasma power is ramped down to 0W at a rate of 60W/min and the system is allowed to cool for 5 minutes before venting and sample removal.

Figure 121 shows the results of ITO thickness versus deposition time for ITO deposition using the PVD75. Samples were created by masking portions of glass slides with kapton tape during ITO deposition of various times. After deposition, the thickness of the ITO was measured via optical profilometry using the same process as described in §3.2.1. ITO deposition was found to vary linearly with deposition time at a rate of approximately 9.09±0.34 nm/min.

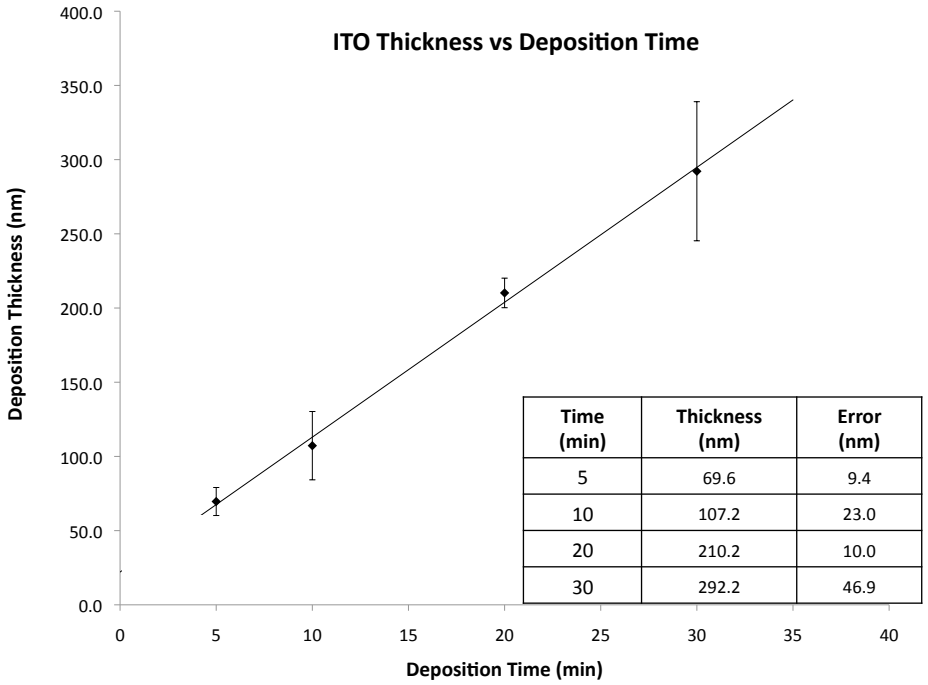

Figure 121: Optical profilometery results of ITO deposited via RF sputterer. ITO film thickness is roughly linear with time with a deposition rate of 9.09±0.34 nm/min

Figure 122 shows transmission results for the RF sputtered, electron beam evaporated, and IAD ITO film using the setup discussed in §3.5.1. The transmission of ITO deposited via RF sputter is much more comparable to IAD ITO than electron beam evaporated ITO. The RF sputtered ITO has a wide range of wavelengths (600 to 900nm) with a near constant transmission of 88%.

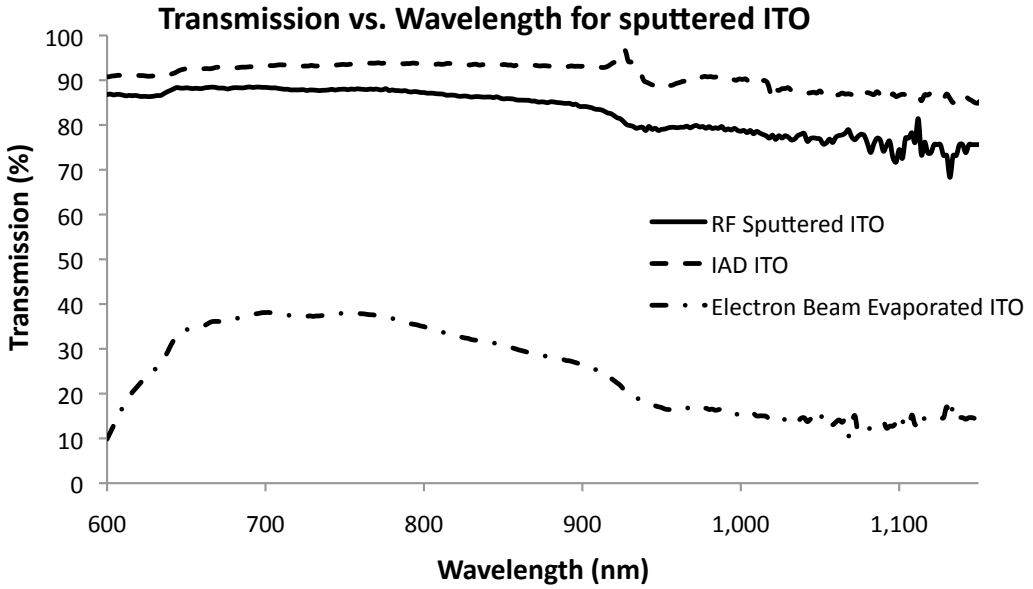

Figure 122: Transmission results for RF sputtered, electron beam evaporated, and IAD ITO film. The sputtered and IAD films are much more transparent across all wavelengths than the electron beam evaporated ITO. The RF sputter ITO is still slightly less transparent than the IAD ITO. The sputtered ITO has a more constant transparency (≈88%) for wavelength ranges between 600 and 900nm compared to electron beam evaporated ITO.

A series of 6 cells were created using RF sputter deposited ITO. Table 20 shows the figures of merit for these cells. Two of these cells were functional. These cells exhibit much the same behavior as cells created using the altered IAD ITO. There are cells, such as MBEOxCu 06 and PlanarCu 106 which have a large enough difference between the values of R_{sh} and R_s to demonstrate curvature in the IV curves. However, these cells demonstrate no photocurrent. The other cells exhibit photocurrent, but are shunted and have no curvature in the IV curves. One cell in particular, PlanarAu 105, demonstrated good photocurrent with an I_{sc} of 863.4μA/cm^2 and a V_{oc} of 136.90mV,

but is also totally shunted. Figure 112 shows typical dark IV curve from both of these types of cells, PlanarAu 105 and MBEOxCu 06.

Table 20: Figures of merit for cells with an ITO top contact layer deposited via RF sputter. There are generally two types of cells produced by this method. Cells which exhibit no photocurrent have enough difference between R_{sh} and R_s to show curvature. Cells which exhibit photocurrent are shunted. The R_{sh} values of both types of cells are very low, less than 200Ω. These values are similar to the cells created using altered IAD processes.

Sample Name	I_{sc} μA/cm^2	V_{oc} mV	FF %	P_{mp} nW/cm^2	R_{sh} Ω	R_s Ω
MBEOxCu 06	-	-	-	-	87.75	0.15
PlanarAg 110	-	-	-	-	0.12	0.12
PlanarAg 203	4.83	0.485	25.29	0.59	33.58	24.33
PlanarCu 106	-	-	-	-	109.59	12.12
PlanarAu 105	863.4	136.90	25.10	29,672.0	116.52	107.09
PlanarTi 01	56.2	35.65	25.56	515.6	193.57	89.43

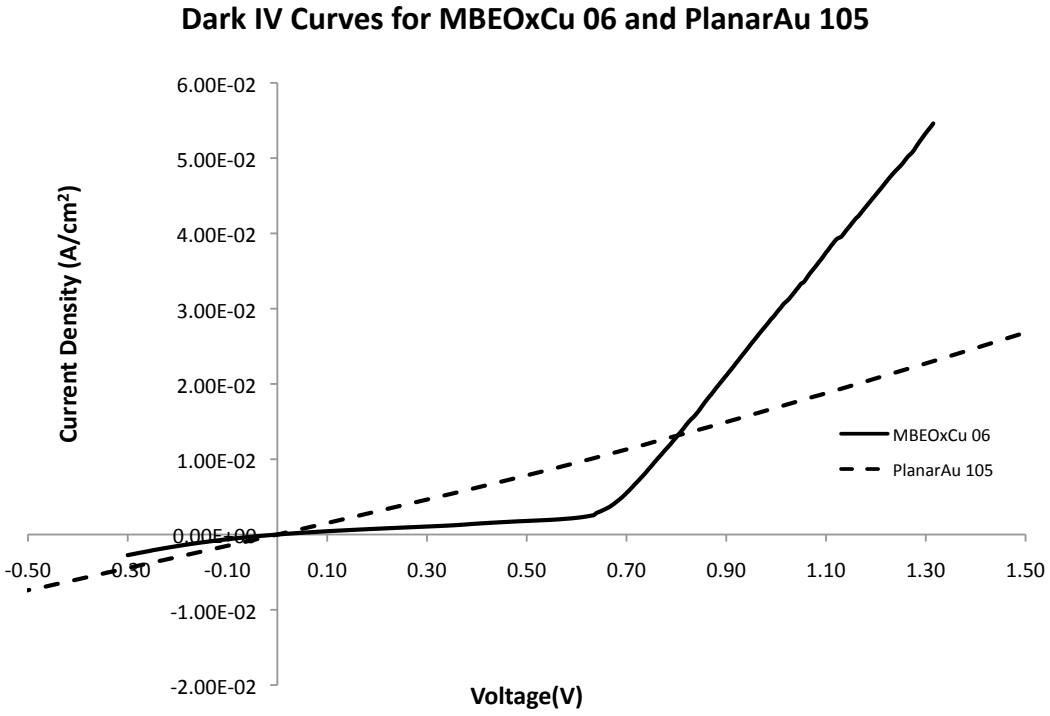

Figure 123: Dark IV curves of two types of cells created with an ITO top contact deposited via RF sputter. MBEOxCu 06 demonstrates curvature, but no photocurrent. PlanarAu 105 demonstrates photocurrent, with an I_{sc} of 863.4μA/cm^2, but is totally shunted.

RF sputtering of ITO has been demonstrated to deposit a relatively transparent, conductive layer of ITO as a top contact. However, the cells constructed with an RF sputtered top contact either exhibit photocurrent and straight line shunted dark IV curves, or exhibit good dark IV curvature with no appreciable photocurrent. In order to develop a cell which demonstrates both photocurrent and IV curvature, a new RF sputter deposition step was added.

In this step, an HRT layer of ZnO is deposited via RF sputter immediately prior to the ITO sputter deposition. The HRT should increase the shunt resistance of cells which exhibit photocurrent by passivating any inhomogeneities or pinholes which are present either from incomplete MBE deposition or plasma etching during top contact deposition.

5.8 High Resistance and Transparent Layer

To deposit the ZnO HRT layer, a Kurt J. Lesker PVD75 RF Sputterer was used with a 3-inch diameter indium bonded, copper plated ZnO sputter target (Kurt J. Lesker #EJTZNOX303A2). To deposit ZnO, a sample is placed in the chamber and sample rotation is turned on. The chamber is pumped down to a pressure of 6 mTorr. A 50% mixture of O_2 and Argon gas (20 sccm of each) is flowed into the chamber and a gate valve is used to stabilize the pressure at 6 mTorr. After pressure stabilization, the plasma power is ramped to 125W at a rate of 120W/min. The plasma power is held at 125W during the time of ZnO deposition. After deposition, the plasma power is ramped down to 0W at a rate of 60W/min and the system is allowed to cool for 5 minutes before ITO deposition is carried out.

Figure 121 shows the results of ZnO thickness versus deposition time for ZnO deposition using the PVD75. Samples were created by masking portions of glass slides with kapton tape during ZnO deposition of various times. After deposition, the thickness of the ZnO was measured via optical profilometry using the same process as

described in §3.2.1. ZnO deposition was found to vary logarithmically with deposition time.

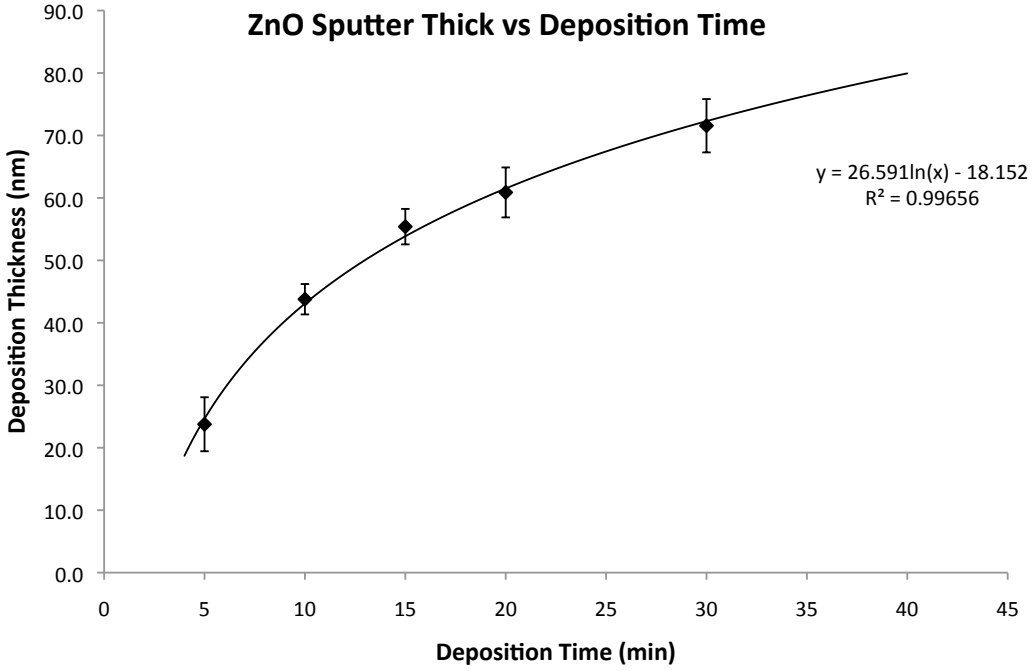

Figure 124: Optical profilometry results for RF sputtered ZnO at a plasma power of 125W. The graph shows thickness of the ZnO layer deposited via RF sputter vs. time. The thickness follows a logrithmic relation with the deposition time

Unfortunately, the 4-point probe technique used in §3.5.1 is only able to measure the sheet resistance of conductive samples (R_{sheet} <1MΩ/□). This setup is unable to measure the ZnO R_{sheet} for any undoped ZnO layers. Since the 4 point probe technique cannot be used, this gives an R_{sheet} for the ZnO layer of at least 1MΩ/□. Such a large sheet resistance means any pinholes and inhomogeneities in the semiconductor layers can be passivated by relatively small thicknesses of ZnO.

While the ZnO HRT layer transmits most light, it can still parasitically absorb light. In order to minimize this effect on the I_{sc} of the produced cells, the effect of changing the chamber O_2 concentration during ITO deposition was investigated. Increasing the oxygen content during ITO deposition should decrease the oxygen vacancies in the ITO film, increasing both transmission and R_{sheet}. ITO deposition

was carried out with O_2 concentrations of 0, 0.60, 1.19, and 1.96%. Figure 125 shows the transmission and conductivity results of the depositions.

For O_2 concentrations of 0 and 0.60%, the R_{sheet} of the film is relatively equal. Increasing the O_2 concentration to higher values results in an exponential increase in the value of R_{sheet}. This condition is inverted for transmission of the ITO film. Figure 125 also shows the transmission percentage of the ITO films at 650nm. For O_2 concentrations of 0 and 0.60%, the transmission at 650nm increases exponentially. As the O_2 concentration is increased to 1.19 and 1.96%, the transmission levels off.

A series of 12 cells were created with a ZnO HRT layer deposited via RF sputter immediately before the deposition of ITO. The ZnO deposition occurred in a 50/50 Ar/O_2 environment with a plasma power of 125W for 30 minutes to give a nominal ZnO thickness of 71.6±4.3 nm. ITO was deposited in the same chamber with a gas mixture of 50 sccm Ar and 0.3 sccm O_2 (0.6% O_2) at a power of 100W for 10 minutes to give a nominal ITO layer thickness of 107.2±23.0nm. Table 21 lists the figures of merit for cells created with a ZnO HRT layer.

The I_{sc} values for these cells range from 7.44 to 476.5μA/cm^2. The spread in the I_{sc} values for these cells is much smaller than previous cells, with only three cells having an I_{sc} lower than 140μA/cm^2. The majority of values are in the range of 200-400μA/cm^2. The V_{oc} values range from 0.358 to 341.36mV with the majority of cells being between 50 and 150mV. MBEOxAu 58 also has the largest V_{oc} of any cell at 341.36mV. The increase in the V_{oc} and relative consistency of I_{sc} can be attributed to the HRT layer passivating defects which are deleterious to cell performance.

The R_{sh} of the cells has been increased for most of the cells into the 1,000 to 10,000Ω range without a large increase in the R_s values. The difference in the R_{sh} and R_s values leads to good curvature for almost all of the cells. However, the FF values of all the cells still remains around 25%. This is due to the fact that the I_{sc}

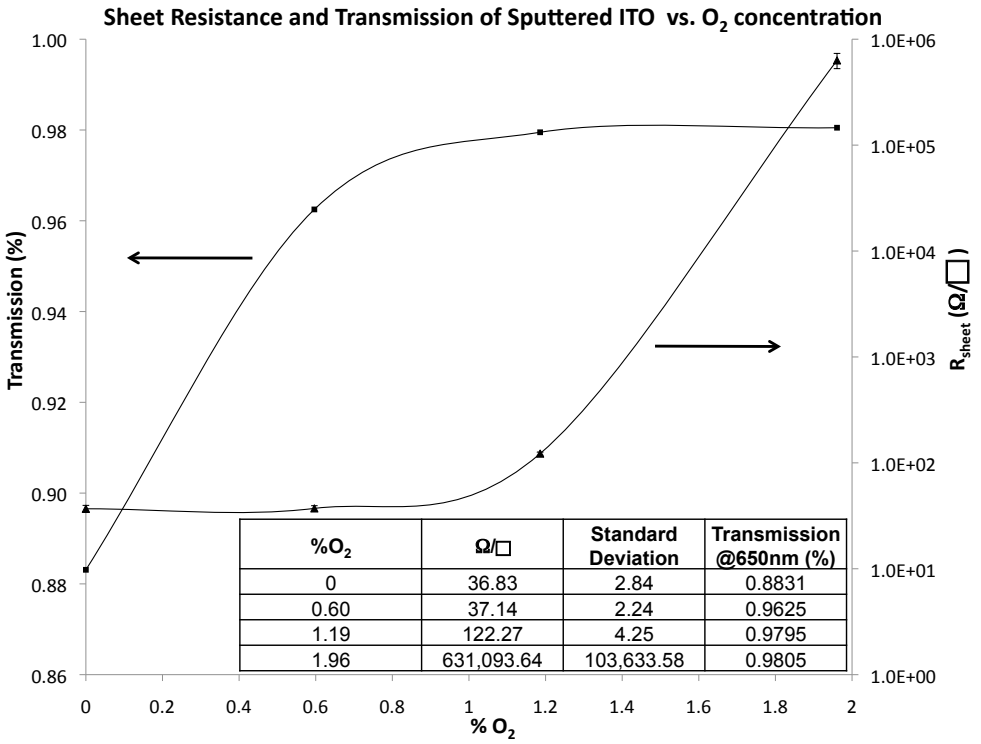

%O_2	Ω/□	Standard Deviation	Transmission @650nm (%)
0	36.83	2.84	0.8831
0.60	37.14	2.24	0.9625
1.19	122.27	4.25	0.9795
1.96	631,093.64	103,633.58	0.9805

Figure 125: Changes in the conductivity and transmission of RF sputtered ITO with different amounts of oxygen present during deposition. Sheet resistance (triangles, right axis) increases with increased oxygen during deposition. The increased oxygen present decreases oxygen vacancies, so conductivity increases exponentially. For small concentrations (<1% O_2) there is little change in the conductivity with oxygen concentration. Transmission of the oxygen film at 650nm (squares, left axis) increases with increased oxygen concentration during deposition. Increased oxygen content in the film increases the bandgap, so less light is absorbed. For small concentrations (<1% O_2) there is a large dependence of transmission on oxygen content. However, for contents above 1%, the transmission is nearly constant. It is possible to tune the ITO deposition oxygen concentration so that the resultant ITO film can be both highly transparent and conductive.

Table 21: Figures of merit for cells created with an HRT layer deposited via RF sputtering. The I_{sc} values of the cells are much more consistant, with the majority being in the range of 200-400μA/cm^2. These values are comparable to the best cells with an IAD ITO top contact. The V_{oc} values for these cells are, on average, much larger than those produced with IAD ITO. The V_{oc} values are comparable to the cells with ITO deposited via electron beam evaporation, with much higher values of I_{sc}. The FF values of these cells are still close to 25%. This is not due to a lack of curvature, but due to the I_{sc} not being large enough to catch any of the cell curvature. The R_{sh} values have been increased in these cells to the thousands of ohms, while R_s has been decreased to less than a hundred ohms in many cases. The HRT layer has increased V_{oc} and R_{sh} without drastically affecting R_s.

Sample Name	I_{sc} μA/cm^2	V_{oc} mV	FF %	P_{mp} nW/cm^2	R_{sh} Ω	R_s Ω
MBEOxCu 03	15.4	18.43	24.10	68.5	678.06	14.16
MBEOxAg 59	199.5	100.31	25.06	5,015.0	2,228.91	112.49
MBEOxAg 60	17.6	1.98	24.74	8,630.1	135.83	32.77
MBEOxAg 61	7.44	0.358	20.65	551.2	53.85	41.65
MBEOxAg 63	206.7	51.24	25.38	2,688.4	470.70	82.97
MBEOxAu 53	240.3	168.25	23.76	9,607.0	1,694.51	638.77
MBEOxAu 58	444.5	341.36	24.65	37,407.0	10,945.59	186.78
MBEOxAu 66	344.2	258.49	26.98	23,998.0	10,318.96	348.07
MBEOxAu 68	266.8	139.34	26.02	9,673.8	2,261.93	24.18
MBEOxAu 77	142.8	81.51	24.66	2,870.4	1,083.15	58.23
MBEOxAu 80	476.5	70.18	24.74	8,272.4	205.43	129.47
PlanarAg 117	9.17	1.22	25.06	2,814.2	111.57	43.76

values for the cell is not large enough to offset the light IV curve and bring the knee of the IV curve into the fourth quadrant.

Figure 126 shows the light IV curve for MBEOxAu 68. The large curve shows good curvature and offset of the curve into the fourth quadrant. The inset picture shows a closeup of the IV curve in the fourth quadrant. This part of the curve has no curvature, so the FF value is approximately 25%. This photocurrent offset is not large enough to incorporate the curvature into the fourth quadrant, but it is apparent that by adding an HRT layer, cells which have both curvature and photocurrent have been developed.

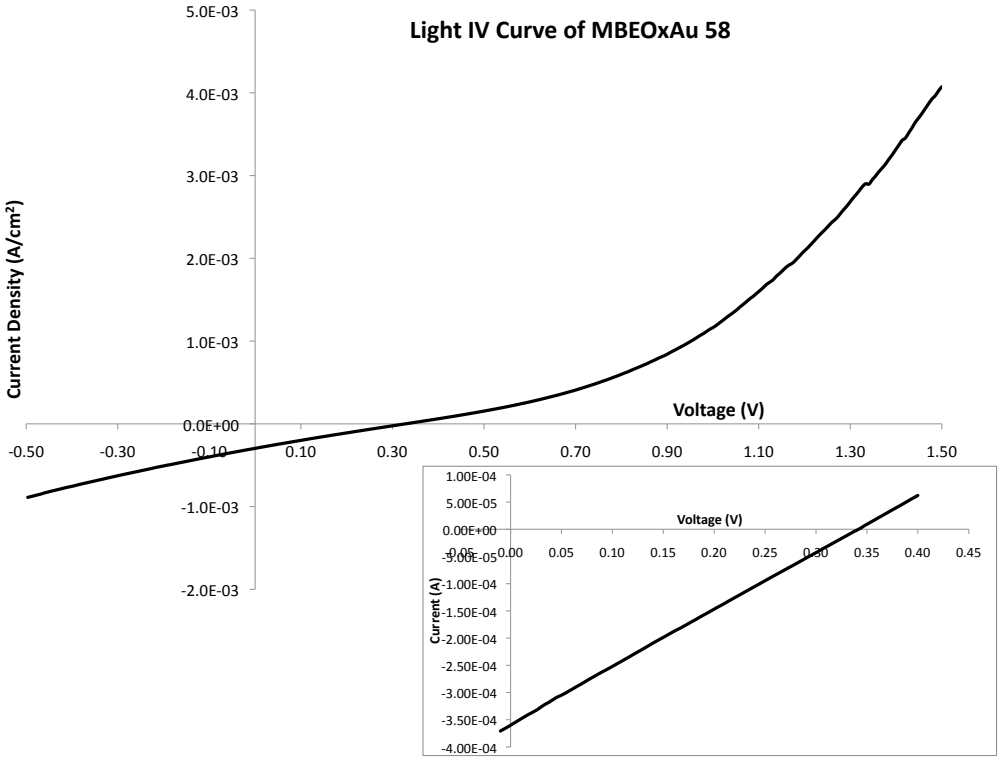

Figure 126: Light IV curve of MBEOxAu 68. The large curve demonstrates good curvature in the IV curve, though the portion of the curve in the fourth quadrant is straight. The inset graph is a closeup of the light curve in this power production quadrant. The photocurrent offset is not large enough to show curvature in the fourth quadrant.

One way to easily increase I_{sc} is to increase the transmission of the top contact layers. Much like ITO, an increase in the oxygen content of the ZnO film should increase the film bandgap, R_{sheet}, and transmission. Figure 122 shows transmission results for ZnO films deposited with different O_2 concentrations in the deposition chamber. Transmission measurements were made using the setup discussed in §3.5.1. ZnO deposited via RF sputter has good transmission properties, even for films deposited with no oxygen present during deposition. The transmission of ZnO increases greatly (from 88.3 to 93.6% at 650nm) for an increase in O_2 concentration of 0 to 50%. There is only a slight increase in transmission (93.6 to 94.9% at 650nm) if the O_2 concentration during deposition is increased from 50 to 100%. To create cells with a ZnO layer which is as resistive and transparent as possible, the ZnO deposition was changed from a 50/50 mixture of Ar and O_2 to a 100% O_2 atmosphere during RF sputter deposition.

A series of 9 cells were created with the ZnO deposition occurring in a 100% O_2 environment. Table 22 shows the figures of merit for these cells. There is very little difference in the figures of merit for the cells with a ZnO layer deposited under 100% O_2 atmosphere compared to cells with ZnO deposited in a 50/50 Ar/O_2 environment.

Table 22: Figures of merit for cells created with a 100% O_2 concentration during ZnO deposition. The I_{sc}, V_{oc}, P_{mp}, and FF values of the cells is roughly equivalent to the cells with ZnO deposited with a 50/50 Ar/O_2 mixture.

Sample Name	I_{sc} $\mu A/cm^2$	V_{oc} mV	FF %	P_{mp} nW/cm^2	R_{sh} Ω	R_s Ω
MBEOxAu 55	551.4	104.86	26.55	15,352.0	301.61	72.12
MBEOxAu 56	839.5	198.48	25.17	41,935.0	604.56	124.62
MBEOxAu 67	446.9	30.69	24.98	3,425.6	170.00	24.64
MBEOxAu 78	189.6	173.50	24.32	8,003.6	3,147.92	100.55
MBEOxAu 79	272.26	136.73	25.74	9,581.6	1873.36	103.75
MBEOxAu 81	447.1	151.61	25.47	17,264.2	507.64	188.78
MBEOxAu 84	155.61	55.14	25.10	2,153.6	583.81	188.88
MBEOxAg 74	136.59	54.26	27.46	2,035.3	662.21	141.77
MBEOxAg 89	181.76	13.90	24.80	626.50	152.34	22.23

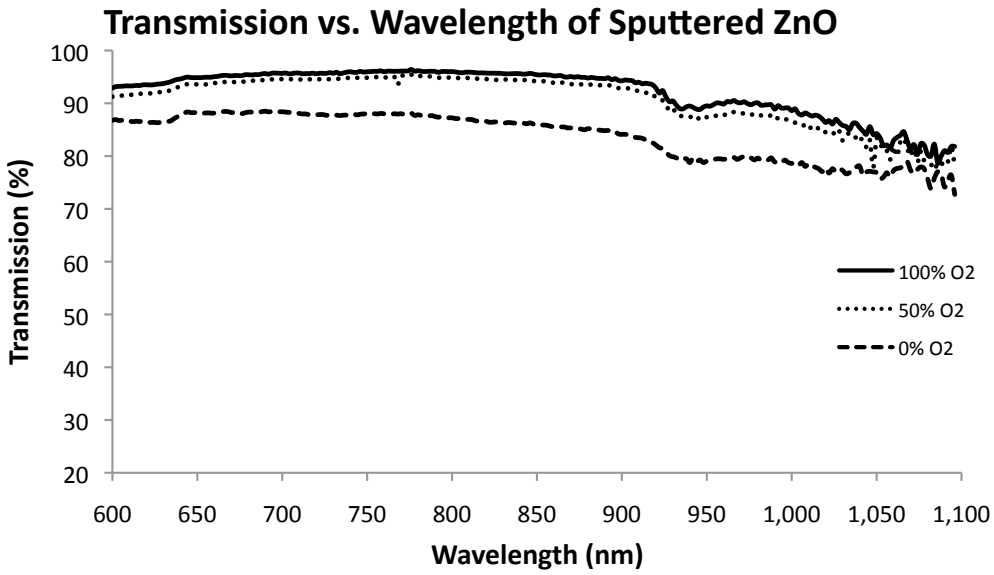

Figure 127: Transmission of ZnO films with different O_2 concentrations during deposition. ZnO films with no oxygen during deposition are relatively transparent with a transmission of 88.3% at 650nm. There is a large increase in transmission, from 88.3 to 93.6%, as the O_2 concentration during deposition is increased from 0 to 50%. If the O_2 concentration is increased to 100%, there is only a slight corresponding increase in the transmission of the film, from 93.6 to 94.9% at 650nm. At 100% O_2 concentration, the film transmits about 95% of incident light for all wavelengths between 600 and 925nm.

For both the ZnO recipes, the inclusion of an HRT layer increased R_{sh} while leaving R_s relatively unchanged. Figure 128 shows a graph of R_{sh} vs. R_s for the cells created with an HRT layer. Almost all of the cells are not shunted and some are well off the R_{sh}=R_s line. Two of the cells (MBEOxAu 66 and MBEOxAu 58) even come very close to matching the R_{sh} and R_s values for the CdTe cell created by NREL (§3.6).

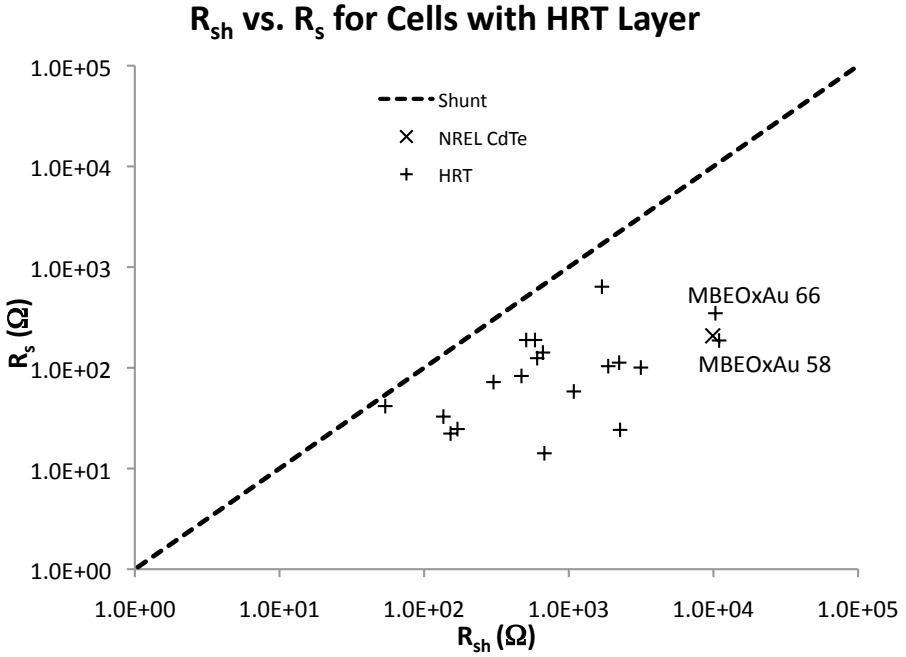

Figure 128: The R_s and R_{sh} values for cells produced with an HRT layer. Most of the cells have R_{sh} and R_s values which lie far from the line $R_s = R_{sh}$. The 'x' marks the R_s and R_{sh} values for the research CdTe cell from NREL from §3.6. While none of the cells had an R_{sh} value larger than the NREL cell, two of the cells have R_{sh} and R_s values about equal to the NREL cells. Some of the cells have R_s values lower than the NREL cell.

While changing the HRT deposition conditions from a 50/50 Ar/O_2 atmosphere to a 100% O_2 atmosphere during deposition did not have a profound effect on the figures of merit of the cell, the presence of an HRT layer did have a advantageous effect on the cells. Figure 129 shows the I_{sc} and V_{oc} values of the HRT cells compared to metallized cells with IAD ITO and metallized cells with electron beam evaporated ITO. The HRT cells, denoted by squares, have I_{sc} values roughly equivalent to the

best IAD ITO cells (x's). The HRT cells also have far fewer cells which perform poorly or not at all. The V_{oc} values of the HRT cells have roughly the same distribution as the electron beam evaporated ITO cells, denoted by circles.

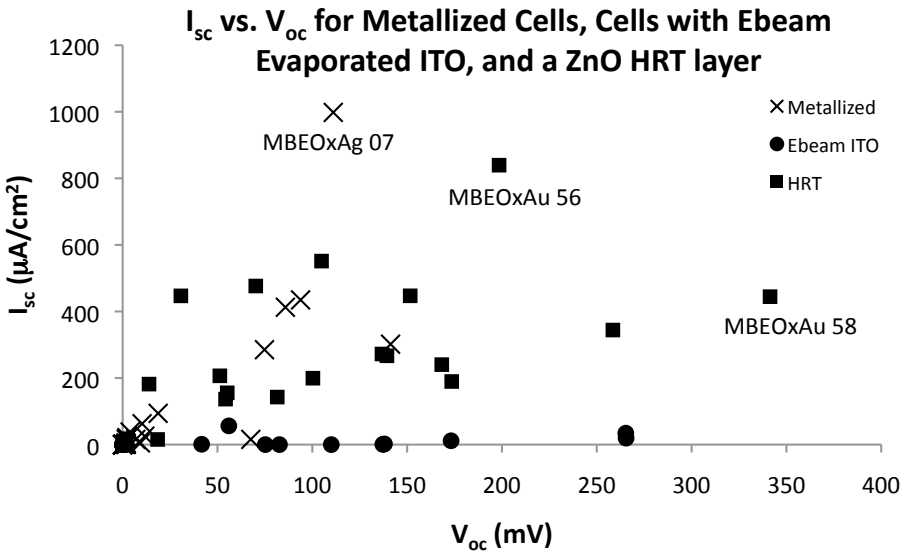

Figure 129: I_{sc} vs. V_{oc} values of HRT samples (squares), compared to metallized cells with IAD ITO (x's) and metallized cells with electron beam evaporated ITO (circles). The HRT cells have I_{sc} values comparable to the IAD ITO cells, with V_{oc} values comparable to the cells with electron beam evaporated ITO. The HRT layer has also caused a tightening in the distribution of both I_{sc} and V_{oc}, eliminating many of the nonfunctional or poorly functioning cells.

The addition of the HRT layer to the 3DCNTPV architecture has increased the V_{oc} values of cells to those accomplished using line of sight deposition methods without adverse effects to the I_{sc} of the cells. In fact, the HRT layer has caused a tighter distribution in the I_{sc} and V_{oc} values and eliminated many of the poorly performing cells which regularly plagued production. The cells also demonstrate high values of R_{sh} and good curvature in the IV curves. However, the I_{sc} values are not high enough to catch any of this curvature in the fourth quadrant, so the FF of these cells remains around 25%. In order to increase the I_{sc} of the cells, other production processes must be investigated. One of the most common methods of increasing power output for

CdTe cells, and a process which is used by virtually all production and research cells, is $CdCl_2$ annealing.

5.9 $CdCl_2$ Processing

5.9.1 Post-CdTe Deposition

5.9.1.1 Wet $CdCl_2$ Anneal

In order to increase the I_{sc} values for manufactured cells, a wet $CdCl_2$ anneal step was carried out. $CdCl_2$ annealing should result in an increase of I_{sc} and V_{oc}. Cells with CdTe and CdS deposited via MBE are placed in a ceramic boat and completely submerged in a saturated $CdCl_2/CH_3OH$ solution (20.8g/L). The cells are then placed in a 3-zone Lindbergh tube furnace (Riverside, MI #59722-A) set at 400^oC. After 20 minutes at 400^oC, the boats are slowly removed and set aside to cool. The cell is finished by ITO deposited via IAD.

Five planar cells were created using p-Si as a back contact. These cells were dual top contact, so the total periphery of the cell was shaded during both CdTe/CdS and ITO depositions. Three cells were of the planar metallized variety with Al metal as the back contact.

Table 23 shows the figures of merit for the cells created using this method. The I_{sc} values of these cells are in the same range as those created without $CdCl_2$ annealing with values ranging between 3.01 and 303.3μA/cm^2. The V_{oc} of the p-Si back contact cells are among the highest among all created cells. Planar 101 has the highest V_{oc} of any cell yet created at 423.91mV. The rest of the p-Si cell also have very high V_{oc} values above 100mV. However, these cells exhibited RO prior to the first quadrant due to the rectifying barrier with CdTe, which may explain the large values of V_{oc} and FF values less than 25%.

The addition of an Al metal layer decreased both the I_{sc} and V_{oc} of the cells produced. The values of I_{sc} ranged from 2.34 to 55.7μA/cm^2 and the V_{oc} values

Table 23: Figures of merit for cells created with a wet $CdCl_2$ anneal. Planar cells with a p-Si back contact show no increase in I_{sc}. They do show an increase in V_{oc}. These high V_{oc} values were similar to other cells with the p-Si/CdTe interface which exhibited RO. With the addition of a Al back contact, the I_{sc} and V_{oc} values are both decreased to similar values as cells without $CdCl_2$ annealing. The R_{sh} and R_s values are very large for these cells. While the R_{sh} increase may be due to grain coarsening in the CdTe layer, the R_s increase is most likely due to residual $CdCl_2$ on the cell surface and the formation of a CdO layer from the high temperature anneal in air.

Sample Name	I_{sc} μA/cm^2	V_{oc} mV	FF %	P_{mp} nW/cm^2	R_{sh} Ω	R_s Ω
Planar 101	303.3	423.91	12.64	16,254.0	184,084.09	8,256.27
Planar 102	12.1	348.22	13.93	588.4	643,359.24	2,297.21
Planar 103	14.7	196.17	19.51	563.5	14,419.40	2,297.21
Planar 104	55.1	158.64	23.64	2,066.5	8,003.84	3,199.18
Planar 105	16.5	161.58	21.00	559.8	10,615.15	9,510.28
PlanarAl 01	2.34	149.63	24.92	78.1	2,873.48	12,780.37
PlanarAl 02	3.01	1.03	25.51	791.5	246.03	290.39
PlanarAl 04	55.7	16.03	24.92	222.5	27.11	26.87

were between 1.03 and 149.63mV. These cells had figures of merit commensurate with 3DCNTPV cells created without an anneal step. All of the cells, both with p-Si and Al back contacts have very high R_{sh} and R_s values well into the kΩ range. The anneal may have increased R_{sh} by coarsening grains and closing any pinholes and inhomogeneities. However, R_s is also drastically increased after the anneal, most likely due to residual $CdCl_2$ and the formation of a cadmium oxide layer from the high temperature oxygen anneal.

While the $CdCl_2$ anneal may have increased the V_{oc}, it had deleterious effects on the structure of the cell. The anneal caused delamination of the CdTe from the p-Si and Al back contacts. Figure 130 shows a series of SEM micrographs demonstrating delamination of the semiconductor layers from the substrate. It is thought that this delamination is caused by the penetration of the liquid $CdCl_2/CH_3OH$ solution into the area between the CdTe and back contact. This liquid then evaporates and the increased volume of the vapor causes semiconductor delamination.

This delamination could also be due a mismatch in the coefficient of thermal expansion of CdTe compared to the back contact material. However, this delamination

occurred no matter how slowly the sample was removed from the furnace and was also observed when the $CdCl_2/CH_3OH$ solution was applied to the cell and evaporated using a 100^oC hotplate.

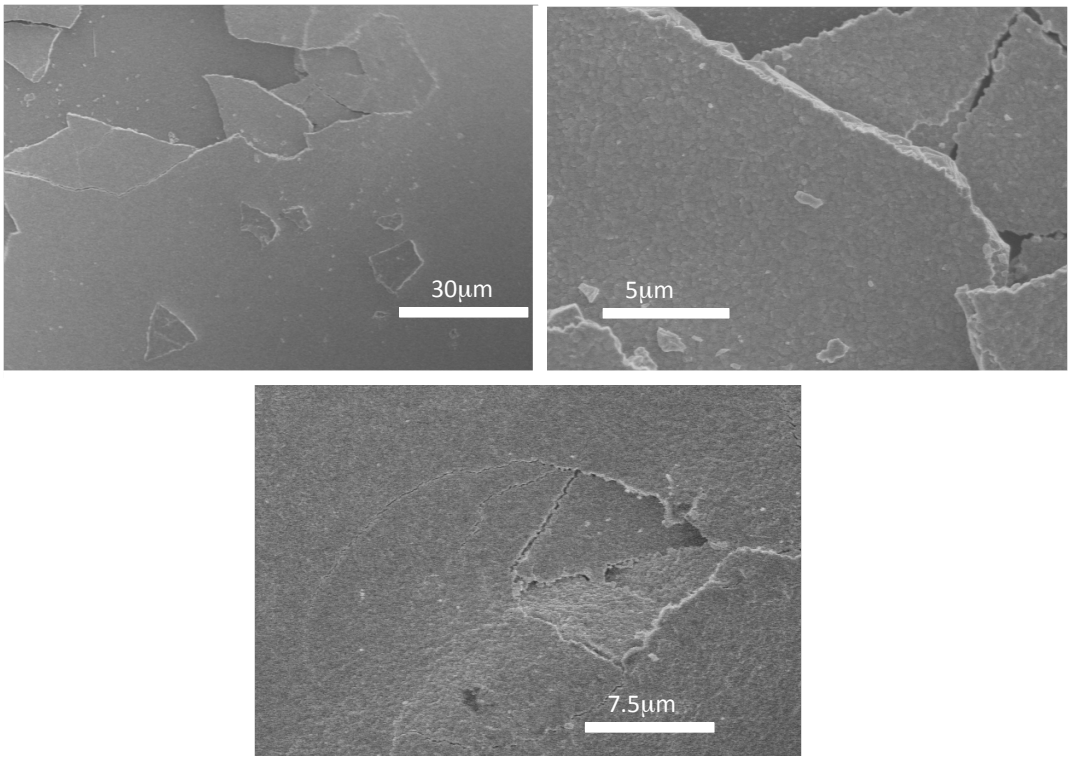

Figure 130: SEM micrographs showing CdTe/CdS delamination from the solar cell substrate. The top row shows two magnifications of delamination on a p-Si back contact. The bottom micrograph is from an Al backed cell.

5.9.1.2 Dry $CdCl_2$ Anneal

Since the delamination of CdTe from the back contact was thought to be due to the liquid penetration of the $CdCl_2/CH_3OH$ solution, a dry $CdCl_2$ anneal was attempted. In this process, after CdTe/CdS deposition, a cell is placed in a beaker and submerged in a $CdCl_2/CH_3OH$ saturated solution and allowed to sit for at least 3 hours. The cell is removed from the solution and rinsed with methanol to remove any excess $CdCl_2$. The cell is then air dried before being put in the Lindbergh furnace at

400^{o}C for 20 minutes. After annealing, these cells have ZnO and ITO layers deposited via RF sputter.

These cell did not exhibit any of the delamination of the CdS/CdTe layers so prevalent in the cells which underwent wet $CdCl_2$ treatment. Table 24 shows the figures of merit for cells with a dry $CdCl_2$ processing step. The figures of merit for these cells are similar to the cells fabricated with an HRT layer but without the $CdCl_2$ anneal. The I_{sc} values vary between 10.44 and 512.55μA/cm^2 with V_{oc} values between 4.16 and 126.32mV. The FF values are not improved over other 3DCNTPV cells. The R_{sh} and R_s values are in the hundreds of ohms. The dry $CdCl_2$ anneal did not have any effect on the cells over the advantages gained from the presence of an HRT layer without a $CdCl_2$ anneal step.

Table 24: Figures of merit for cells with a dry $CdCl_2$ anneal step. Unlike, the cells which underwent a wet $CdCl_2$ anneal, these cells exhibit no delamination of the CdS/CdTe layer. In general, the figures of merit for these cells are similar to the cells with an HRT layer, but no $CdCl_2$ anneal step. The cells which underwent a dry $CdCl_2$ anneal have I_{sc} values which vary from 10.44 to 512.55μA/cm^2 and V_{oc} values between 4.16 and 126.31mV.

Sample Name	I_{sc} μA/cm^2	V_{oc} mV	FF %	P_{mp} nW/cm^2	R_{sh} Ω	R_s Ω
MBEOxAg 93	512.55	63.55	24.84	8091.34	393.56	53.30
MBEOxAg 96	183.98	12.97	24.76	590.7	115.10	69.89
MBEOxAg 107	26.61	5.97	25.09	39.83	376.73	296.09
MBEOxAg 114	10.44	4.16	23.09	10.04	671.37	597.59
MBEOxAg 119	91.78	10.42	25.17	240.71	204.86	160.34
MBEOxAu 11	126.00	68.58	25.23	2,180.2	710.63	215.27
MBEOxAu 70	38.04	126.31	21.95	1,054.6	8,615.49	601.14

5.9.1.3 CdTe Only $CdCl_2$ Anneal

It has been reported that a CdS layer which is too thick may inhibit diffusion of $CdCl_2$ into the junction [43] and negate any advantageous effects of the anneal. In order to determine if the thickness of the CdS hindered $CdCl_2$ duffusion during the wet and dry anneal steps, a series of three planar cells were created. One of these cells had a Ag back contact while the remaining two had Au back contact.

To create these cells, a metal coated substrate is placed in the MBE chamber and CdTe is deposited as normal. Instead of directly depositing CdS onto the CdTe layer, the sample is removed and soaked in a saturated $CdCl_2/CH_3OH$ solution for at least 3 hours. After soaking, the substrate is removed, washed with excess CH_3OH, and allowed to air dry. Once dry, the cell is placed in the Lindbergh furnace at 400^oC for 20 minutes to anneal the CdTe layer. The sample is placed back into the MBE chamber and CdS is deposited as normal followed by ITO.

Table 25 shows the figures of merit for cells created using this CdTe only $CdCl_2$ anneal. Two of the cells, PlanarAg 105 and PlanarAu 103, did not function. The third cell, PlanarAu 103, was functional, but did not have the gains in I_{sc} and V_{oc} which would be expected from a $CdCl_2$ anneal. PlanarAu 103 has a I_{sc} of $8.82\mu A/cm^2$ with a V_{oc} of 222.36mV.

Table 25: Figures of merit for cells which had only a CdTe layer present during the dry $CdCl_2$ anneal. After the anneal, CdS and ITO were deposited as normal. Two of the cells created using this method were nonfunctioning. The third cell, PlanarAu 103, did not show any gains from the $CdCl_2$ anneal. PlanarAu 103 had a I_{sc} of $8.82\mu A/cm^2$ with a V_{oc} of 222.36mV.

Sample Name	I_{sc} $\mu A/cm^2$	V_{oc} mV	FF %	P_{mp} nW/cm^2	R_{sh} Ω	R_s Ω
PlanarAg 105	-	-	-	-	-	-
PlanarAu 102	-	-	-	-	-	-
PlanarAu 103	8.82	222.36	24.89	488.5	85,135.37	48,813.82

5.9.1.4 Two-Stage CdS Deposition $CdCl_2$ Anneal

One of the major consequences of $CdCl_2$ annealing is the intermixing between the CdTe and CdS layers. If too much of this intermixing occurs, the rectifying properties of the CdTe/CdS junction may be affected. To restore the rectifying properties of the pristine junction, it may be necessary to develop a two-stage CdS deposition as described by Singh et. al [86].

Two cells, MBEOxAu 69 and MBEOxAu 72, were created with a two-stage CdS deposition process. To create these cells, Au coated substrates are placed in the MBE chamber and a 70 minute CdTe deposition is carried out. A shortened CdS deposition is run for 20 minutes. The sample is removed from the chamber and soaked in a saturated $CdCl_2/CH_3OH$ solution for 3 hours. The sample is then removed from the solution, air dried, washed with excess CH_3OH, and annealed at 400^oC in the Lindbergh furnace for 20 minutes. After the annealing step, the sample is placed back into the MBE chamber and another CdS deposition is run for 90 minutes. The sample is removed and ZnO and ITO are deposited via RF sputter.

Table 26 shows the figures of merit for the cells created with a two-stage CdS deposition. One cell, MBEOxAu 69 has a I_{sc} of $440.0\mu A/cm^2$ with a V_{oc} of 24.24mV. The other cell, MBEOxAu 72, has a I_{sc} of $144.0\mu A/cm^2$ with a V_{oc} of 226.59mV. Neither of these cells outperform the cells that have an HRT layer, but no $CdCl_2$ anneal step.

Table 26: Figures of merit for cells created with a two-stage CdS deposition before and after the $CdCl_2$ anneal. One cell, MBEOxAu 69 has a I_{sc} of $440.0\mu A/cm^2$ and a V_{oc} of 24.24mV. Another cell, MBEOxAu 72 has a I_{sc} of $144.0\mu A/cm^2$ and a V_{oc} of 226.59mV. Neither of these cells outperforms cells with an HRT layer, but not $CdCl_2$ anneal step.

Sample Name	I_{sc} $\mu A/cm^2$	V_{oc} mV	FF %	P_{mp} nW/cm^2	R_{sh} Ω	R_s Ω
MBEOxAu 69	440.0	24.24	24.18	2,579.0	66.02	44.91
MBEOxAu 72	144.0	226.59	23.86	7,785.1	10,187.66	120.39

5.9.2 Pre-MBE Deposition

One reason that the $CdCl_2$ anneal has had very little effect on the I_{sc} and V_{oc} values for fabricated cells may be because the $CdCl_2$ molecules have difficulty diffusing into the CdTe bulk through the CdS layer on the front surface. It would be ideal to apply the $CdCl_2$ solution directly to the back of the CdTe layer. Unfortunately, the substrate configuration does not allow for this after CdTe/CdS deposition.

To accomplish $CdCl_2$ diffusion into the back surface of the CdTe layer, a solar cell substrate is submerged in a saturated $CdCl_2/CH_3OH$ solution prior to CdTe/CdS deposition and allowed to soak for at least 3 hours. The substrate is then removed, rinsed with excess CH_3OH and blown dry. The $CdCl_2$-coated substrate is loaded into the MBE chamber for CdTe and CdS deposition. The growth of CdTe in the MBE system occurs at a temperature of 280^oC for 70 minutes. At this elevated temperature, $CdCl_2$ should be able to diffuse through the CdTe film as it is being deposited, doping the entirety of the deposited film. After CdTe deposition, CdS deposition is carried out and the sample is removed from the MBE chamber. At this point, the cell is either annealed in the Lindbergh furnace at 400^oC for 20 minutes before ITO is deposited, or ITO is deposited without the anneal.

A series of 13 cells were created with $CdCl_2$ deposited on the substrate prior to CdTe/CdS deposition. These cells include 3 cells with a p-Si back contact, 4 with a Ag back contact, 3 with a Cu back contact, and 3 with a Au back contact. Three cells (PlanarAg 107, PlanarAg 109, and Planar Ag 112) were annealed after CdTe/CdS deposition.

Table 27 shows the figures of merit for these cells. Two cells, PlanarAg 107 and PlanarAg 112 were nonfunctional. Among the functioning cells, the I_{sc} values range from 0.070 to 699.2μA/cm^2 and the V_{oc} values ranged from 0.896 to 308.67mV. Annealing after MBE deposition was deleterious to device performance, with only one of the three annealed cells being functional. None of the cells showed any benefit from the presence of $CdCl_2$, with figures of merit for these cells similar to the cells with an HRT layer.

In order to improve the values of I_{sc} and V_{oc} of manufactured cells, various methods of $CdCl_2$ annealing have been attempted. A wet $CdCl_2$ anneal was first attempted, but suffered from delamination between the CdTe and back contact. This delamination was abated by moving to a dry $CdCl_2$ anneal, but no improvement in

Table 27: For the 11 functional cells, the values of I_{sc} range from 0.07 to 699.2μA/cm^2 and values of V_{oc} range from 0.896 to 308.67mV. None of the cells show any benefits from the presence of $CdCl_2$ prior to the semiconductor deposition. The cells with the best values of I_{sc} and V_{oc} are similar to cell with an HRT layer, but no $CdCl_2$ anneal step.

Sample Name	I_{sc} μA/cm^2	V_{oc} mV	FF %	P_{mp} nW/cm^2	R_{sh} Ω	R_s Ω
Planar 108	21.8	126.68	23.53	650.7	9,615.38	2,020.20
Planar 116	70.4	308.67	19.02	4,129.3	250,000.45	27027.03
Planar 117	57.9	111.39	24.58	1,584.9	1,288.66	1,386.96
PlanarAg 107	-	-	-	-	407,381.76	486.03
PlanarAg 109	0.82	1.03	25.12	0.21	602.88	510.39
PlanarAg 111	0.070	1.13	32.12	0.026	2,936.00	1,418.12
PlanarAg 112	-	-	-	-	202,195,846.90	154,815.54
PlanarCu 101	1.15	131.01	24.99	37.7	637.43	7.92
PlanarCu 102	1.59	10.62	24.74	4.17	2,263.88	14.19
PlanarAu 104	699.2	67.63	25.01	11,826.4	52.70	52.03
MBEOxCu 04	0.53	0.896	25.63	0.121	879.28	14.39
MBEOxAu 51	19.07	34.87	25.00	166.2	2,200.46	1,469.81
MBEOxAu 52	5.50	1.32	26.54	1.93	238.37	211.18

device performance was evident. To determine if CdS was preventing the diffusion of $CdCl_2$ to the junction, a series of cells were created with only CdTe present during the $CdCl_2$ anneal. A two-stage CdS deposition was attempted in case intermixing of CdTe/CdS was degrading junction characteristic. The deposition of $CdCl_2$ onto the cell substrate before semiconductor deposition was also tried. However, none of these $CdCl_2$ anneal methods yielded cells with better electrical characteristics than cells without the anneal step.

Figure 131 shows a graph of the I_{sc} vs. V_{oc} values for all cells created with various $CdCl_2$ anneal strategies. Most of the cells created have very poor values of I_{sc} and perform more poorly than cells with an HRT layer, but no $CdCl_2$ annealing step (asterisks). Only a few cells using the two-stage CdS technique, dry $CdCl_2$ anneal, and $CdCl_2$ pre-treatment can approach the I_{sc} values of the cells with only an HRT layer. On average, cells with an HRT layer, but no $CdCl_2$ annealing step have better device characteristics than those cells with a $CdCl_2$ anneal step.

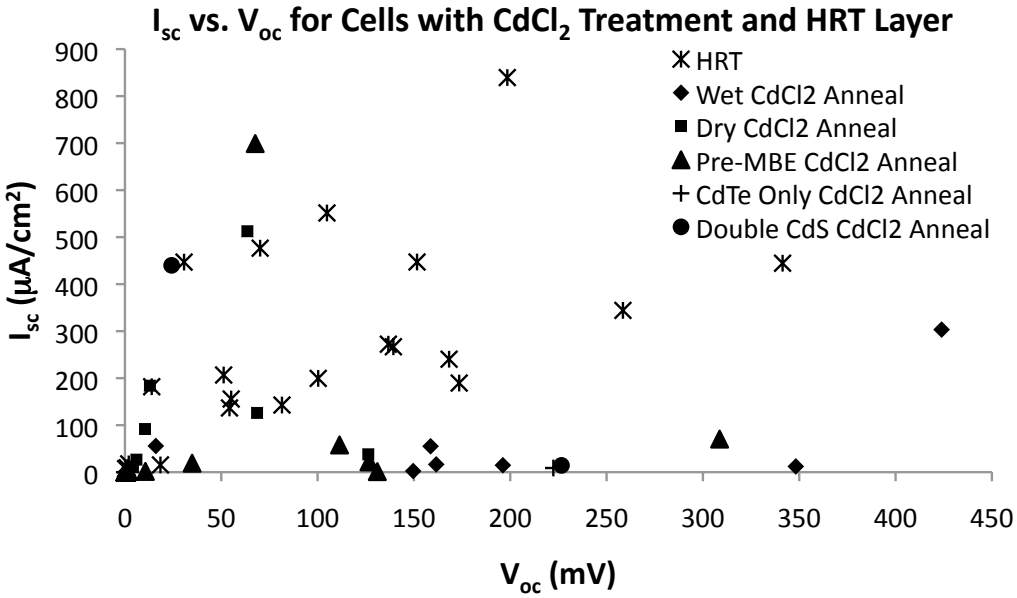

Figure 131: I_{sc} vs. V_{oc} for cells with various $CdCl_2$ annealing strategies compared to cells without a $CdCl_2$ anneal (asterisks). Cells represented by a diamond utilize a wet $CdCl_2$ anneal. Cells represented by a square utilize a dry $CdCl_2$ anneal. Cells represented by a triangle have a pre-treatment of $CdCl_2$ applied to the substrate prior to CdTe/CdS deposition. Cells represented by a cross have the $CdCl_2$ anneal step carried out when only CdTe is present. Cells represented by a circle have a two-stage CdS deposition to account for CdS intermixing with CdTe. The best cell from each category may have a I_{sc} value on the order of those regularly achieved by cells with an HRT layer. On average, the cells with an HRT layer and no $CdCl_2$ anneal step have better electrical characteristics than cells with a $CdCl_2$ anneal step.

5.10 Summary of Device Production

The production of 3DCNTPV cells has been demonstrated to create working solar cells using both MBE and a combination of MBE and CDB deposition methods. However, these cells are plagued by low I_{sc} and V_{oc} values. They also suffer from a massive shunt which causes a straight line IV curve. By transferring the production processes both to planar and unpatterned CNT cells, it was determined that the shunting and low power output of the cells was caused by production methods and was not inherent to the 3D architecture of the 3DCNTPV cells.

A major cause of the shunting in the produced cells was determined to be caused by ITO deposition around the edges of the cell and semiconductor shadowing during MBE deposition. By eliminating these shunts, the light IV curve was shown to have inverted curvature in the fourth quadrant. It was determined that this inverted curvature was due to a rectifying diode from the CdTe/p-Si back contact. This necessitated the removal of the p-Si as a back contact and substituting in a Cu, Ag, or Au metal layer.

VACNTs were successfully grown directly on Ag metal layers, but the resultant CNTs were not tall enough and the results of growth were extremely inconsistent. The 3DCNTPV architecture was then altered so that the VACNTs were grown on an SiO_2/Si layer. These VACNTs were then metallized to act as the back contact. Removing the CNTs as a back contact means that they are only present to provide a 3D structure to the cell. However, it is advantageous to have the metal layer on the CNTs to act as a back contact reflector.

The cells with the metallized layer showed much higher I_{sc} values, but were still plagued by a massive shunt. It was eventually determined that the IAD ITO process was the cause of this shunting, either from coating pinholes in the semiconductor layers or etching away semiconductor material before ITO deposition. Altering the IAD process by adding a Ni or In etch barrier and completing the ITO deposition in

a 2-stage manner were unsuccessful in consistently creating cells with curvature. The cells created possessed either IV curvature or photocurrent, but not both.

Other ITO deposition methods were examined. Electron beam evaporated ITO produced cells with curvature and good V_{oc} values, but very bad I_{sc} values. This is due to the high R_{sheet} and absorption of the ITO. In order to make the ITO more transparent and conductive, a post deposition anneal step was examined. Annealing the cells in either a vacuum or air environment at 400^{o}C caused the cells to shunt in as little as 5 minutes. Depositing ITO via RF sputter was determined to deposit a transparent, conductive ITO layer, but all the cells produced were shunted.

This shunt was eventually reduced by the addition of intrinsic ZnO as an HRT layer. This layer passivated any defects or pinholes in the semiconductor film to decrease the amount of shunting. 3DCNTPV cells were created with good curvature, I_{sc} values regularly five times larger than the original production series, and V_{oc} values up to 350mV. Though these cells showed curvature in the IV curve, the current offset into the fourth quadrant was not enough to raise the FF values above 25%.

In order to further increase the I_{sc} values, a $CdCl_2$ anneal step was introduced. A wet $CdCl_2$ anneal at 400^{o}C was tried after deposition of CdTe and CdS, but resulted in delamination of the semiconductor layers from the back contact. This delamination was eliminated by moving to a dry $CdCl_2$ step, but the anneal did not increase the figures of merit of the cells more than adding the HRT layer. In order to determine if the presence of CdS was inhibiting diffusion of $CdCl_2$ into the junction, a series of cells were attempted in which CdTe was the only layer present during the $CdCl_2$ anneal. These cells did not perform any better than the HRT cells. A final $CdCl_2$ process was attempted where a thin, sacrificial layer of CdS was deposited onto the CdTe layer. After annealing a thicker layer of CdS was deposited in order to restore diode functionality lost by diffusion of CdS into CdTe. These cells were functional, but showed no increase in either the I_{sc} or V_{oc} values.

In the event that the CdS layer was too thick in previous anneals for the $CdCl_2$ to penetrate via diffusion, a process was developed were $CdCl_2$ was deposited on the back contact layer before CdTe/CdS deposition. After the semiconductor layers were deposited, the cell was annealed. By depositing the $CdCl_2$ first, it was hoped that there would be more of an effect on the CdTe layer. However, the figures of merit for these cells remained consistent with the cells produced with an HRT layer.

Even though the $CdCl_2$ layer was ultimately unsuccessful, the 3DCNTPV cells were clearly improved from the initial production series through the addition of a metal back contact and an HRT layer. The I_{sc} values were increased by at least an order of magnitude and the amount of nonfunctional or poorly functional cells was decreased. The V_{oc} values of the cells were increased to the hundreds of millivolt range. The sources of shunting were identified and eliminated, resulting in IV curves which demonstrated curvature, with R_{sh} and R_s values similar to research cells provided by NREL (§3.6).

5.11 Power versus solar incident angle

Having produced a number of cells which demonstrate that the 3DCNTPV type structure can be used to successfully create functional solar cells, it is necessary to evaluate the theoretical claims of the 3DCNTPV structure made in Chapter 4. The theory put forth previously in this work predicts an inverted C-type curve for the behavior of P_{mp} as ψ of incident light is varied. In this chapter, the P_{mp} of a 3DCNTPV cell is taken at ψ varying from 0 to 90^o. The behavior of the P_{mp} vs ψ curve for a 3DCNTPV cell is compared to a similarly measured planar cell and the theory proposed in Chapter 4.

5.11.1 Testing Setup

Figure 132 shows a schematic of the test setup. The device under test remains stationary and the basic setup is the same as described in §3.6. The device rests on a

water chilled stage. Data is taken by a Keithley 4200SCS system with contact to the device made by two Alessi industries micromanipulators. The micromanipulator tip used for the top contact is tipped with In solder to provide an ohmic contact to the ITO. A GE 300W ELH lamp, which has a color rating of 3350K, is used to provide light with the intensity varied through the use of a variac. The lamp is air cooled by a fan capable of 15 cubic feet of air flow per minute.

The lamp is able to rotate due to two rings. The inside ring remains stationary and is attached to the base of the setup. This ring is graduated with markings every 5^o. The outside ring is able to freely rotate through the presence of ball bearings through an angle range of -90^o to 90^o.

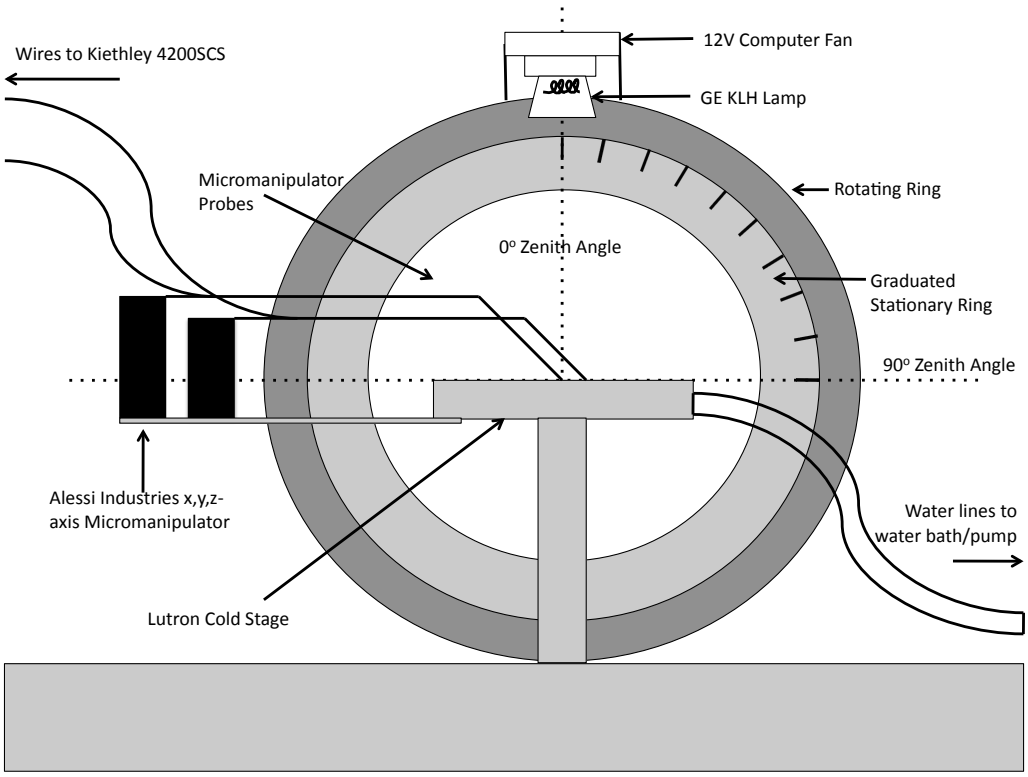

Figure 132: The equipment used to test the P_{mp} vs. ψ curve of a 3DCNTPV cell consists of a chilled stage, pair of three axis micromanipulator probes, Kiethley SCS system, GE ELH lamp, and graduated rotating ring. The ring can be rotated to provide incident ψ angles from -90 to 90^o.

5.11.2 Error Source Discussion

The experimental setup which is used to measure the electrical characteristics of the 3DCNTPV cells has several error sources which must be accounted for and eliminated in order to accept measured data as accurate. It is necessary to understand the extent of measurement errors in the system. Only after that can a sensible procedure be developed to minimize inherent inaccuracy. The sources of error considered here are from (1) a light source is which cannot be approximated as a point source (2) a lamp which does not provide standard AM1.5 illumination, (3) a lamp which heats the device under test during measurement, and (4) a discretized measurement of a continuous function.

5.11.2.1 Non-point Light Source Error

The theory proposed in Chapter 4 assumes that the sun is a point source of photons, so every photon originating from it has the same values of ψ and ω. This is a valid approximation since the solar disc only has an apparent size of 0.5^o.

With an aperture of 4.5cm and a distance from the solar cell of 21cm, the GE ELH lamp has an apparent size of 12.09^o. This relatively large apparent size means photon trajectories no longer form a line to the solar cell surface, but a cone in spherical coordinates. Incoming photons will have a range of ψ and ω values which will shift the average value of Γ.

For example, if the center of the lamp is located at a position corresponding to $\psi = \omega = 0^o$, the nominal average value of Γ would be unity. However, the solar cell surface will actually sample photons with $-6.045^o \leq \psi \leq 6.045^o$ and $-6.045^o \leq \omega \leq 6.045^o$. Since $\psi = \omega = 0^o$ represents a minimum in the value of Γ, the average value of Γ for a non-point source will be larger than what would be expected from a point source.

As the nominal value of ψ increases, so too will the difference between the nominal value of Γ and the actual value of Γ due to the exponential nature of the Γ vs. ψ curve. However, since relatively few photons are able to enter the space between the towers(or gridlines) at high values of ψ, this difference contributes relatively little difference to the power output.

The values of Γ for a non-point source were calculated for all nominal ψ values from 0 to 85^o and a nominal ω value of 0^o. The 3D cell for which Γ was calculated is an ideal cell composed of square towers 100μm tall, 40μm in diameter with a 20μm pitch. In order to consider a circular volume element in spherical space and not a rectangular element, the only points calculated are those which satisfy the equation

$$(dist \times tan(\psi_\delta - \psi))^2 + (dist \times tan(\omega_\delta - \omega))^2 \leq \varrho^2 \tag{89}$$

Where ψ and ω are the nominal values, dist is the distance of the lamp from the solar cell (21cm), ϱ is aperture of the lamp (4.5 cm), and ψ_δ and ω_δ vary from the nominal value $\pm$ 6.045^o.

These values of Γ are then used to calculate P_{mp} assuming a η_{2D} value of 0.6. Table 28 shows the results of these calculations. The error in the value of Γ due to the non-point light source is less than 10% for all nominal ψ values less than 75^o. Above 75^o the percent error reaches much higher values. At 85^o the error is over 250%. However, this error does not necessarily propagate to the output power of the solar cell. Although the value of Γ might be very large at large ψ values, the actual change in P_{mp} is small due to the relatively small number of photons entering the spaces between vertical towers. The percent error in P_{mp} from a non-point source of light is less than 1% for all angles from 5 to 85^o.

Table 28: Values of Γ and P_{mp} calculated for a theoretical point source of light and simulated for a non-point light source. The simulated non-point light source has an angular aperture of 12.09^o with a distance of 21cm from the cell. To calculate P_{mp}, the model cell has a 2D array of square towers 40μm in diameter with a 20μm pitch. The cell also has an η_{2D} of 0.6 and a tower height of 100μm. The value of Γ for a non-point source of light differs from a point source by a few percent for most of the range of ψ. This difference is decreased drastically to less than 1% when P_{mp} is calculated from the respective values of Γ.

Nominal ψ	Point Γ	Non-point Γ	Error (%)	Point P_{mp} (AU)	Non-point P_{mp}	Error (%)
0^o	1	1.059	5.890	0.600	0.619	3.113
5^o	1.109	1.115	0.526	0.631	0.636	0.271
10^o	1.220	1.231	0.835	0.655	0.658	0.406
15^o	1.335	1.350	1.166	0.670	0.674	0.534
20^o	1.455	1.476	1.467	0.678	0.682	0.629
25^o	1.583	1.610	1.738	0.677	0.682	0.695
30^o	1.722	1.756	1.993	0.669	0.674	0.736
35^o	1.875	1.917	2.242	0.652	0.657	0.757
40^o	2.049	2.100	2.495	0.628	0.633	0.759
45^o	2.250	2.312	2.756	0.596	0.600	0.741
50^o	2.490	2.566	3.045	0.556	0.560	0.705
55^o	2.785	2.879	3.379	0.508	0.512	0.646
60^o	3.165	3.286	3.805	0.453	0.456	0.564
65^o	3.681	3.843	4.409	0.391	0.393	0.455
70^o	4.434	4.674	5.409	0.322	0.323	0.321
75^o	5.665	6.090	7.510	0.246	0.246	0.168
80^o	8.089	9.251	14.364	0.166	0.166	0.037
85^o	15.288	54.682	257.69	0.083	0.083	0.0000767

Figures 133 and 134 show graphical representations of Γ and P_{mp} vs. ψ, respectively, for both a point source and a non-point source with an aperture of 12.09^o. The error bars indicate the maximum and minimum values obtained for the calculations at each value of ψ.

The two calculations for Γ are close for low values of ψ. The calculations for a point source of light begin to differ at higher values of ψ. Also, the spread between the maximum and minimum value of Γ increases with increasing value of ψ.

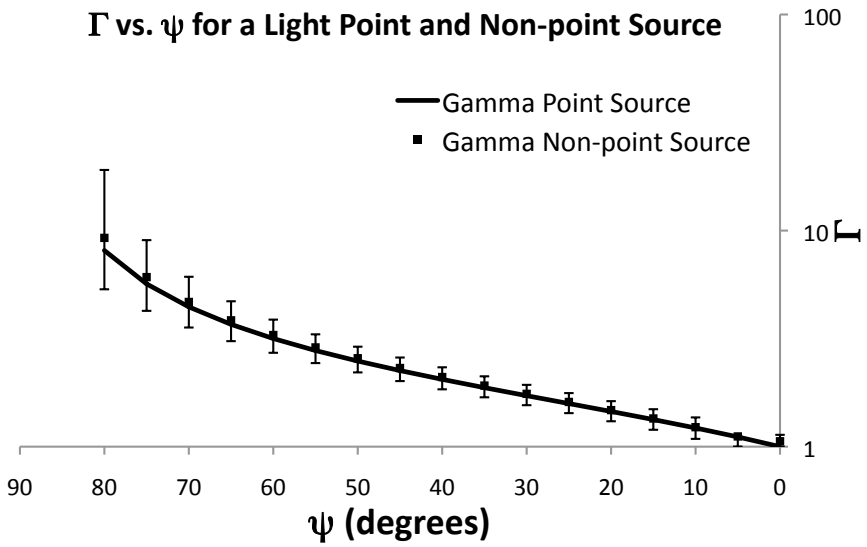

Figure 133: Graph of Γ vs. ψ for values of Γ calculated for a point source of photons (solid line) and simulated for an non-point source of photons (squares) with a circular aperture of 12.09^o. The square dots represent the average value of Γ assuming the non-point source is isotropic over the entire aperture. The error bars represent the minimum and maximum values of Γ found by simulating photons from each point of the light source.

However, this deviation in Γ does not propagate to a deviation in P_{mp} between a point source and non-point source of light. The deviation between the two calculations is very small with the only noticeable separation between the two curves occurring at $\psi = 0^o$. While the spread in Γ may increase with increasing ψ, the spread in P_{mp} actually decreases with increasing ψ. This is due to the fact that the value of Γ has less impact on the value of P_{mp} as the ψ increases.

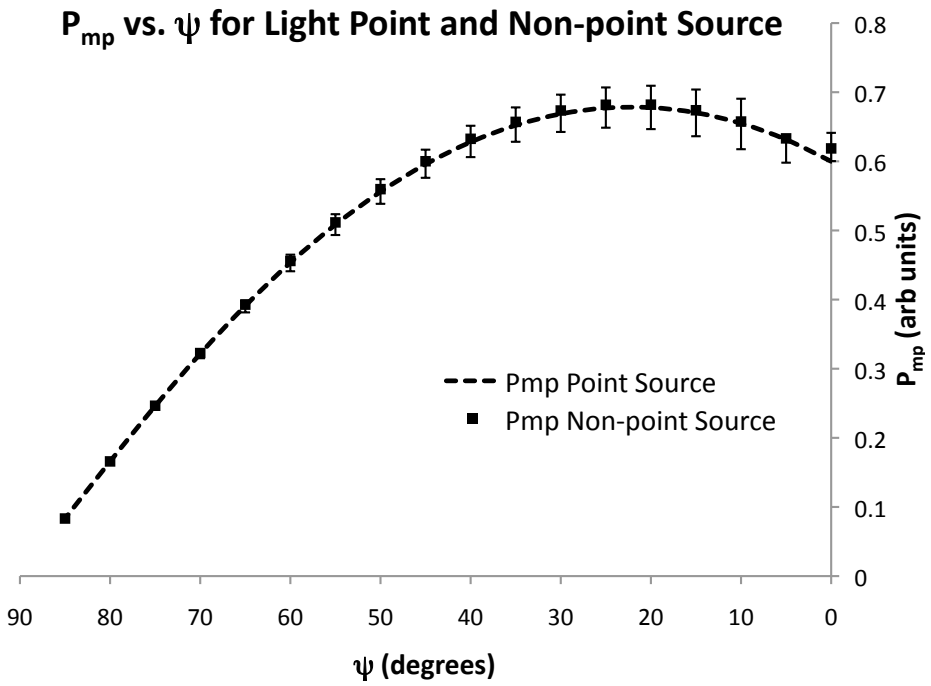

Figure 134: Graph of P_{mp} vs. ψ calculated for a cell illuminated with a point source (dashed line) and a non point source (squares). The square dots represent the calculation of P_{mp} using the average value of Γ for a non-point source of light. The error bars represent the P_{mp} values calculated from the minimum and maximum values of Γ found during the simulation. The values of P_{mp} were calculated for a model cell composed of a 2D array of towers 100μm in height with a diameter of 40μm and a 20μm pitch. The value of η_{2D} for the cell is 0.6.

5.11.2.2 Non-AM1.5 light source

The GE ELH bulb used in the setup described in §3.6 is not an AM1.5 light source. It is listed by the manufacturing company, General Electric, as having an output spectrum which can be approximated by a blackbody at 3350K. The intensity at a given wavelength for a blackbody can be calculated by the blackbody equation made famous by Planck [252].

$$I(\lambda) = \frac{2\pi hc}{\lambda^5} \frac{1}{e^{\frac{hc}{\lambda k_B T}} - 1} \tag{90}$$

where I is intensity of the output radiation at a certain wavelength, h is Planck's constant, c is the velocity of light, lambda is the output wavelength, k_B is Boltzmann's constant, and T is the blackbody temperature.

For the GE ELH bulb used in this work, the output spectrum would resemble that shown in Figure 135 as the solid black line. The vertical hashed line indicates the wavelength at the bandgap of CdTe (λ_g). The dotted line is the standard AM1.5 spectrum. Only wavelengths smaller than λ_g should be energetic enough to add to the photocurrent. For the ELH bulb, the intensity range from approximately 300 to 855nm contain that majority of photons which can add to the photocurrent of the cell.

There are two main difference between the output spectrum of an AM1.5 light source and the GE ELH bulb. The first is that the maximum output intensity of the ELH bulb spectrum occur at a longer wavelength (835nm for ELH vs. 531nm for AM1.5). The second is that the ELH spectrum has a much longer tail into the higher wavelengths region with a larger percentage of the total output spectrum existing below λ_g. The higher intensity at longer wavelengths is energy which is thermalized

by the solar cell. This means that a solar cell under the ELH spectrum should heat much more readily than under an AM1.5 spectrum.

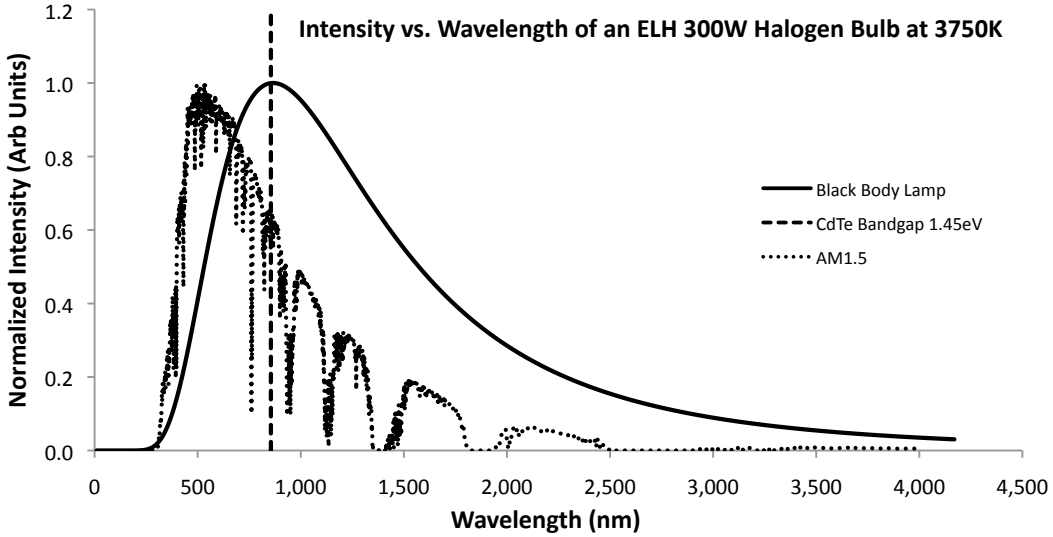

Figure 135: Normalized Intensity vs. wavelength for the standard AM1.5 spectrum (dotted line) and the ELH lamp used in this work (solid line). The E_g of CdTe is denoted by the vertical hashed line. The spectrum of the ELH lamp can be approximated as a blackbody at 3350K. This blackbody temperature is less than the approximate blackbody temperature of sunlight (5800K), so the maximum intensity of the ELH lamp is at a longer wavelength than sunlight. A greater percentage of the intensity of the ELH lamp is at an energy below the E_g of CdTe. This indicates that a greater percentage of the lamp's intensity will be thermalized by the cell and cell heating should be more drastic for the ELH lamp than for the AM1.5 spectrum.

5.11.2.3 Temperature Error

Heating of a solar cell has deleterious consequences on cell performance. Therefore, it is necessary to understand how much and how quickly heating of a solar cell under test is occurring. Procedures can be adjusted to minimize temperature effects on the electrical performance of the cell.

Both CdS and CdTe have bandgaps which decrease in size as temperature increases. CdS has a $\frac{dE_g}{dT}$=-3.33×10^{-4} eV/K, while for CdTe that value is -3×10^{-4} eV/K [229]. Decrease in the bandgap of CdS leads to parasitic absorption of photons with wavelength lower than the RT λ_g of CdS. This decreases the photocurrent

produced by the cell from the blue region of the incident light spectrum. However, the overall photocurrent is increased due a similar decrease in the bandgap of CdTe. Absorption of the cell increases at longer wavelengths and extends the PV response to wavelengths in the red region of the incident light spectrum.

Since the light intensity is generally larger in the region of the CdTe bandgap than the CdS bandgap, the increased absorption of both layers tends to increase the output photocurrent which, in turn, increases the value of I_{sc}. However, this effect is slight and only accounts for an I_{sc} increase on the order of 0.01mA/^{o}C [253].

The increase in the value of I_{sc} with temperature is offset by a decrease in the value of V_{oc}. V_{oc} decreases with increasing temperature due to exponentially increased recombination at higher temperature and lower bandgap. For CdTe cells, $\frac{dV_{oc}}{dT}$=-2.1mV/^{o}C [254].

Heating of a solar cell increases I_{sc} while decreasing V_{oc}. Overall the decrease in V_{oc} is larger, so the power output of the cell decreases as cell temperature increases. If a cell is heated during an IV curve sweep, then the cell would be at different temperatures when data is taken at the I_{sc} and V_{oc} points. The I_{sc} value would be relatively unaffected, since the data is taken at the beginning of an IV curve when relatively little heating of the solar cell has occurred. The V_{oc}, measured at the end of the IV curve, would be lowered. This would lead to an increased and artificial curvature in the fourth quadrant of the IV curve.

In order to test the amount of heating to a solar cell caused by the ELH lamp in this work, a K-type thermocouple is attached to the top of a 1×1" square p-Si substrate with Cermabond 865 high thermal conductivity epoxy from Aremco (Valley Cottage, NY) . This thermocouple/Si wafer combination is used because measuring the top of an Si wafer should give a more accurate picture of the true temperature of the CdTe cell. The temperature of the thermocouple is measured with a Keithley 2700 DAQ unit controlled by Labview 8.6.

Room temperature water is flowed through the cold stage at a rate of 3.4 gallons/minute. The lamp is turned on for a time period of 8, 18, 30, 44, and 60 seconds. After a given period of time the lamp power is turned off and the substrate is allowed to cool. The results of the heating and cooling are shown in Table 29.

Table 29: Temperature change of a Si wafer heated by the illumination of a ELH lamp for various times while being continuously cooled by a Lutron cold stage. The temperature of the cell rises quickly as the lamp is left on. For longer period of time, the temperature reaches a maximum value of approximately 10^oC above RT. Once the lamp is turned off, the cell begins to quickly cool due to the chilled stage.

Lamp on (s)	Maximum ΔT (^oC)	Time to 1^oC above RT (s)	Time to 0.5^oC above RT (s)
8.0	6.95	19.52	25.49
18.0	8.84	31.30	37.86
30.0	9.44	45.06	53.34
44.3	9.66	61.69	73.54
59.5	9.69	76.92	94.71

Figure 136 shows the results of substrate heating by the ELH lamp shown in Table 29. The zero point of the x-axis indicates the time the lamp is turned on while the y-axis shows the change in temperature with respect to ambient. The temperature of the Si wafer increases rapidly initially before reaching a maximum temperature change of $\approx 10^oC$ above ambient. After the lamp is turned off, the temperature of the wafer rapidly decreases.

From the data in Figure 136, it is apparent that the lamp being on heats the Si wafer. This heating approaches a maximum value of around 10^oC for long time lengths. In order to cool the substrate again, it is necessary to minimize the duty cycle of the lamp. Figure 137 is a graph showing the cooling time necessary for a given time of lamp heating for the substrate temperature to return to 2, 1, 0.5, and 0.25^oC above RT.

Since a submersible pump is used to flow water through the chilled stage, the only choices for fluid temperature are RT water or ice water. As is apparent from Figures 136 and 137, the cooing time necessary for RT water may be long depending on the

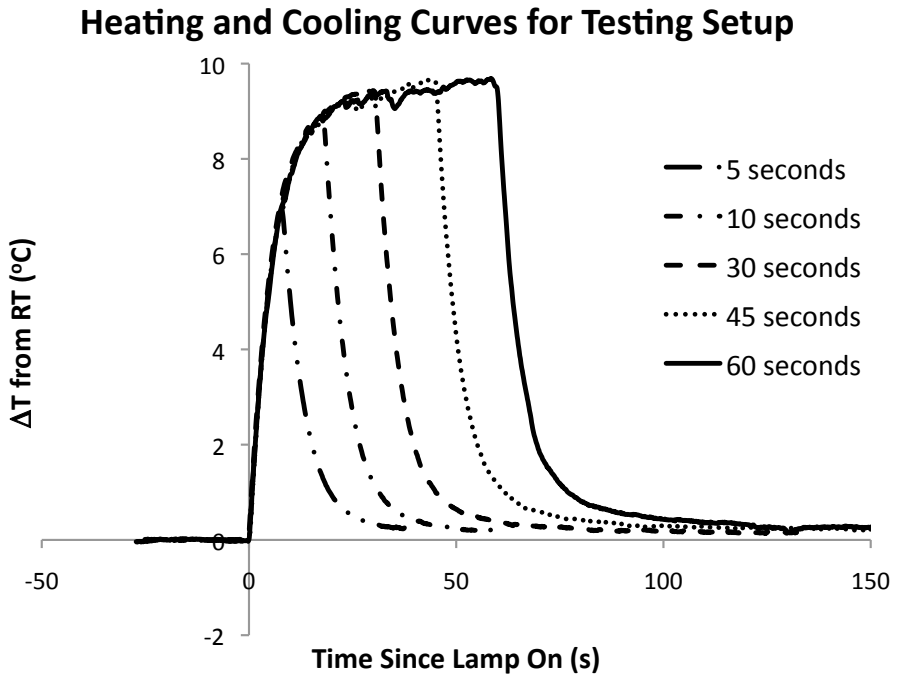

Figure 136: Change in temperature of an Si wafer vs. time as the ELH lamp is turned on for various times and then turned off. The temperature of the wafer increases rapidly for the first 10 seconds after the lamp is turned on before reaching a maximum temperature of 10^oC above RT. Once the lamp is turned off, the temperature rapidly decreases

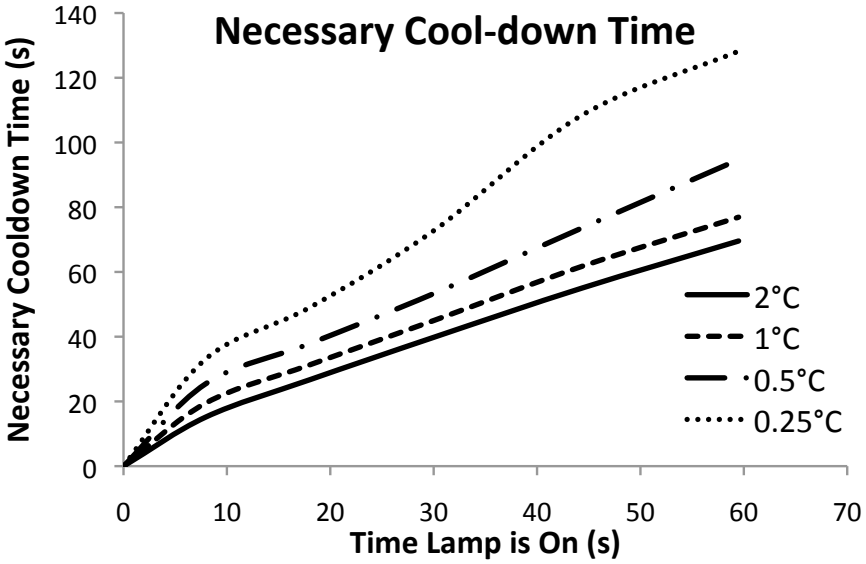

Figure 137: Graph of necessary cool-down time vs. amount of time the lamp is left on to bring the temperature of the wafer down to 0.25, 0.5, 1, and 2^oC above ambient. The longer the lamp is left on, the longer the time necessary to wait for the wafer to reach a temperature suitable for testing. This indicates that to cool the device back to 0.25^oC above ambient, the lamp should have a duty cycle of around 25%. To cool the device to 0.5^oC above ambient, the duty cycle of the lamp should be around 35%. To cool the device to 1^oC and 2^oC above ambient, lamp duty cycles of 40 and 45% are necessary.

amount of time the lamp is on. By using ice water, the cooling rate could be increased, limiting the amount of heating from the lamp. Flowing ice water through the cold stage was attempted. However, after running for long periods of time, atmospheric moisture condensed on the testing stage, damaging any device on the stage.

It is important to remember that the temperatures measured in this section were on a Si wafer. Since this wafer does not produce a current, all of the lamp's output energy is thermalized, unlike a solar cell where much of the lamp's output energy is translated into electrical power with a smaller portion of the lamp energy thermalized. Therefore, the temperature change of the Si wafer gives a maximum for the temperature change of a solar cell under test.

Since the heating of a solar cell during IV curve tracing induces curvature in the fourth quadrant, and the IV curves in Chapter 5 show almost no curvature, it is reasonable to conclude that although the GE ELH lamp does heat the sample, this heating does not ruin the electrical characteristics of the devices under test. However, it is still judicious when testing cells over long periods of time to limit the duty cycle of the lamp.

5.11.2.4 Discretization Error

The value of P_{mp} for a PV device is a continuous function. In order to measure the power output of a cell, the measuring apparatus only samples a finite number of points as the device sweeps the applied voltage from 0 to V_{oc}. Depending on the step size, the finite sampling of a continuous function could lead to a large error, since it is unlikely that the maximum of a continuous function occurs at the exact same point as the maximum of a discretized function. For simple IV curves, such as the ones shown in the previous chapter, the power function is symmetric and the value of this discretization error can be derived exactly.

For the majority of 3DCNTPV cells in this work, the FF values are around 25%. This means that the power as a function of voltage for those cells may be described by Equation 16 in §2.1.3.1.

$$P(V) = I_{sc}\left(V - \frac{V^2}{V_{oc}}\right) \tag{91}$$

The value of P_{mp} occurs at a voltage of $\frac{V_{oc}}{2}$. The difference between the measured and actual P_{mp} is the discretization error.

Figure 138 demonstrates this discretization error between a continuous function and a discrete set of measured points. The fourth quadrant of an IV curve of a solar cell similar to those seen in Chapter 5 (I_{sc}=1mA, V_{oc}=400mV, FF=25%) is shown by a hashed line. The power vs voltage curve for this cell is shown by the black solid line with the P_{mp} point denoted with a black circle. A voltage sweep starting at V=0 with a step size, ΔV, of 40mV is denoted by black squares. Since the voltage sweep has a large step size, the actual P_{mp} and the maximum power found during the sweep are different. For a symmetric function, this error has a maximum value at V=$\frac{V_{oc}}{2} \pm \frac{\Delta V}{2}$.

$$P_{mp}^{maxerror} = P\left(\frac{V_{oc}}{2} \pm \frac{\Delta V}{2}\right) \tag{92}$$

ΔV is equal to the distance covered by the voltage sweep in the fourth quadrant divided by the number of sampled points.

$$\Delta V = \frac{V_{oc}}{N-1} \tag{93}$$

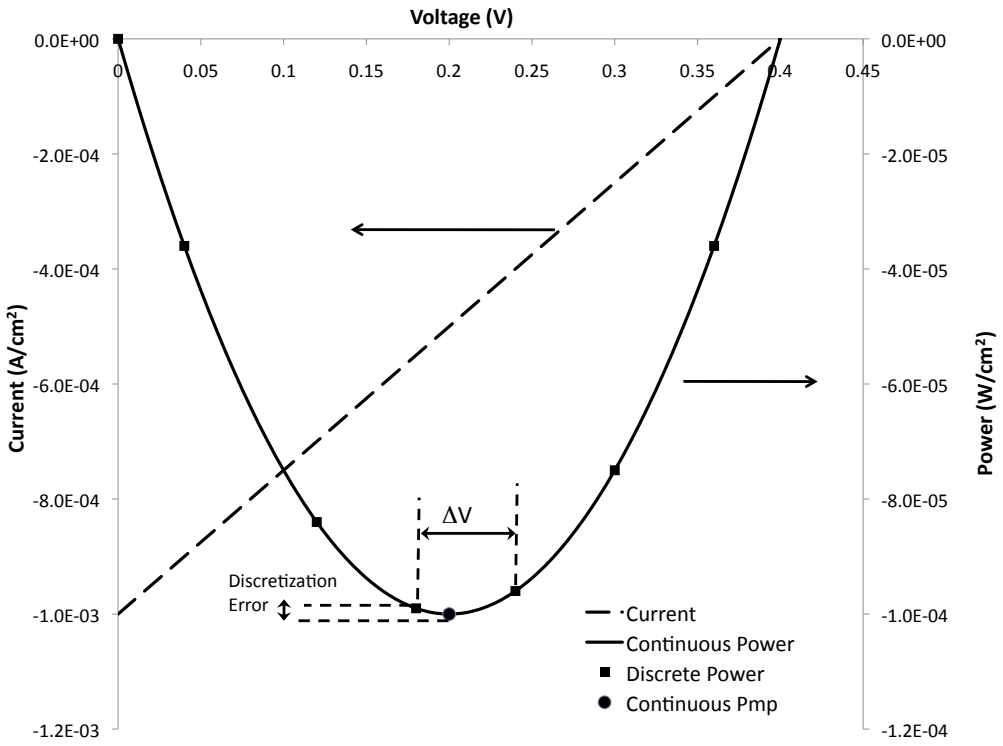

Figure 138: For a straight line IV curve in the fourth quadrant (dashed line) with an I_{sc} of 1mA/cm^2 and a V_{oc} of 400mV, the resultant power vs. voltage curve is the solid line with the P_{mp} denoted by the circle. For an IV curve sweep, only certain power values are sampled and power is calculated from those points (squares). If a sampled point is not equal to the real value of P_{mp}, then there exists an error due to the discretization of the IV curve. The maximum value of this discretization error is dependent on the voltage step size, ΔV.

where N is the number of sampled points in the fourth quadrant.

Substituting equation 92 into equation 91 and simplifying gives

$$\begin{aligned} P_{mp}^{maxerror} &= I_{sc}\left(\frac{V_{oc}}{2}+\frac{\Delta V}{2}-\frac{(\frac{V_{oc}}{2}+\frac{\Delta V}{2})^2}{V_{oc}}\right) \\ &= I_{sc}\left(\frac{V_{oc}}{2}+\frac{\Delta V}{2}-\frac{\frac{V_{oc}^2}{4}+\frac{2V_{oc}\Delta V}{4}+\frac{\Delta V^2}{4}}{V_{oc}}\right) \\ &= I_{sc}\left(\frac{V_{oc}}{4}-\frac{\Delta V^2}{4V_{oc}}\right) \\ &= \frac{I_{sc}V_{oc}}{4}\left(1-\frac{1}{(N-1)^2}\right) \end{aligned} \tag{94}$$

The maximum difference in power between the true P_{mp} and the measured P_{mp} is

$$\begin{aligned} \Delta P^{max} &= P_{mp}-P_{mp}^{maxerror} \\ &= \frac{I_{sc}V_{oc}}{4}\left(1-\frac{1}{(N-1)^2}\right)-\frac{I_{sc}V_{oc}}{4} \\ &= \frac{I_{sc}V_{oc}}{4}\left[-\frac{1}{(N-1)^2}\right] \end{aligned} \tag{95}$$

which leads to a percentage error of

$$\begin{aligned} \%Error &= \frac{\left|\frac{I_{sc}V_{oc}}{4}\left(-\frac{1}{(N-1)^2}\right)\right|}{\frac{I_{sc}V_{oc}}{4}}\times 100 \\ &= \frac{1}{(N-1)^2}\times 100 \\ &\approx \frac{1}{N^2}\times 100 \end{aligned} \tag{96}$$

The discretization error inherent in the P_{mp} measurement falls as the inverse of the square of the number of data points in the fourth quadrant. For an IV curve with

a sweep comprised of 10 points, the percent error in the value of P_{mp} derived from the measurement is only 1%.

5.11.3 Testing Procedure

In order to reliably test the power output of different incident angles of light, a cell is placed on the stage and RT water is flowed. The lamp is positioned at a ψ=0^o and turned on. An IV curve is taken taken from -5mV to 100mV with a voltage step of 1mV. This voltage sweep lasts 12 seconds and takes 101 data points in the fourth quadrant. After the sweep is completed, the lamp is then shut off as quickly as possible and the substrate is allowed to cool for at least 45 seconds. A total of five IV curves are taken at a given value of ψ with at least 45 seconds between each IV curve. The lamp is then moved to another value of ψ and another 5 IV curves are taken. Sets of 5 IV curves are taken in ψ steps of 10^o from 0 to 90^o.

The P_{mp} of each IV curve is calculated and an average and standard deviation is found for each ψ. With 101 measurements in the fourth quadrant, the discretization error (§5.11.2.4) should be decreased to less than 0.01%. The duty cycle of the lamp is held at or below 21%, insuring that the solar cell substrate will cool to at least 0.25^oC above the baseline temperature (§5.11.2.3). Waiting a long period of time does not decrease the temperature much less than 0.25^oC above baseline because the lamp heats the air in the testing room, increasing the ambient temperature.

5.11.4 Results

Table 30 shows the results of the P_{mp} vs ψ measurements for MBEOxAu 80. The third column is the normalized P_{mp} corrected for indirect background light. The background light is assumed to be isotropic and, at ψ=90^o, only the background component of light adds to the power output of the cell. To correct for this background light component, the P_{mp} at ψ=90^o is subtracted from the P_{mp} value at each ψ. The

normalized value of P_{mp} is calculated by dividing the background subtracted P_{mp} values by the background corrected P_{mp} value at ψ=0^o.

$$P_{mp}^{\text{Norm}}(\psi) = \frac{P_{mp}(\psi) - P_{mp}(\psi = 90^o)}{P_{mp}(\psi = 0^o) - P_{mp}(\psi = 90^o)} \tag{97}$$

For this cell, the value of the P_{mp} at a ψ=0^o is equal to 10,726.5±380.5 nW/cm^2. This value increases to 12,338.3±134.9 nW/cm^2 at a ψ=20^o. This is a 15% increase in the P_{mp} value from $\psi = 0^o$.

Table 30: Average measured P_{mp} at different values of ψ for 3DCNTPV cell MBEOxAu 80. The P_{mp} increases from a value of 10,726.5±380.5 nW/cm^2 at ψ=0^o to a maximum P_{mp} of 12,338.3±134.9 nW/cm^2 at ψ=20^o. After the maximum, the values of P_{mp} decrease steadily to ψ=90^o.

ψ	P_{mp} (nW/cm^2)	Normalized P_{mp}
0^o	10,726.5±380.5	1.000±0.035
10^o	11,982.1±408.4	1.119±0.038
20^o	12,338.3±134.9	1.153±0.013
30^o	11,867.0±103.3	1.11±0.009
40^o	10,737.5±105.0	1.00±0.010
50^o	9,310.5±97.9	0.865±0.009
60^o	7,194.2±71.3	0.664±0.007
70^o	4,770.2±32.6	0.434±0.003
80^o	2,152.0±9.6	0.185±0.001
90^o	207.5±1.2	0.000±0.001

In order to ensure that the P_{mp} increase at off-normal ψ values seen in MBEOx Au 80 is due to the 3D nature of the cell structure and not substrate heating, ambient light, or some other effect, the same measurement was carried out with Planar Cell 07. The results of this measurement are shown in Table 31. The second column shows the measured P_{mp} while the third column is the normalized P_{mp} corrected for background light.

The maximum value of P_{mp} for Planar Cell 07 is 167.1±1.7nW/cm^2 at ψ=0^o. This value monatomically decreases as ψ moves to greater values. This behavior is what

would be expected of a planar cell and in no way shows the increase in power output at off-normal angles that was both theoretically predicted and experimentally shown in the 3DCNTPV cell.

Table 31: Average measured P_{mp} at different values of ψ for Planar cell 07. The P_{mp} decreases steadily from a maximum value of 167.1±1.7nW/cm^2 at ψ=0^o to a minimum at ψ=90^o.

Angle	P_{mp} (nW/cm^2)	Normalized P_{mp}
0^o	167.1±1.7	1.000±0.027
10^o	166.6±1.7	0.995±0.010
20^o	160.5±1.4	0.955±0.0089
30^o	151.4±8.3	0.895±0.005
40^o	139.9±7.9	0.817±0.005
50^o	125.6±1.3	0.722±0.008
60^o	104.8±8.7	0.583±0.005
70^o	74.8±1.1	0.382±0.006
80^o	44.3±7.8	0.178±0.005
90^o	17.8±3.2	0.000±0.002

Figure 139 shows a graph of normalized P_{mp}, corrected for background illumination vs ψ for a 3DCNTPV cell and a planar cell. There is a clear, discernible difference between the two curves. The planar cell has the maximum power output for ψ=0^o. This curve falls to zero as ψ goes to 90^o. In stark contrast is the 3DCNTPV cell. This cell shows a C-type curve with a maximum in the power output at an off-normal ψ that is qualitatively similar to the type of curve proposed by theory (Figure 61 in §4.1).

5.11.5 Experimental Comparison to Theory

In order to quantitatively compare the experimental P_{mp} vs. ψ curve for MBEOx Au 80 against what is expected by the theory proposed in Chapter 4, more information is needed about the morphology of the cell. SEM analysis is used to quantify the geometric aspects. Reflectometry is used to gather data about η_{2D} of the cell.

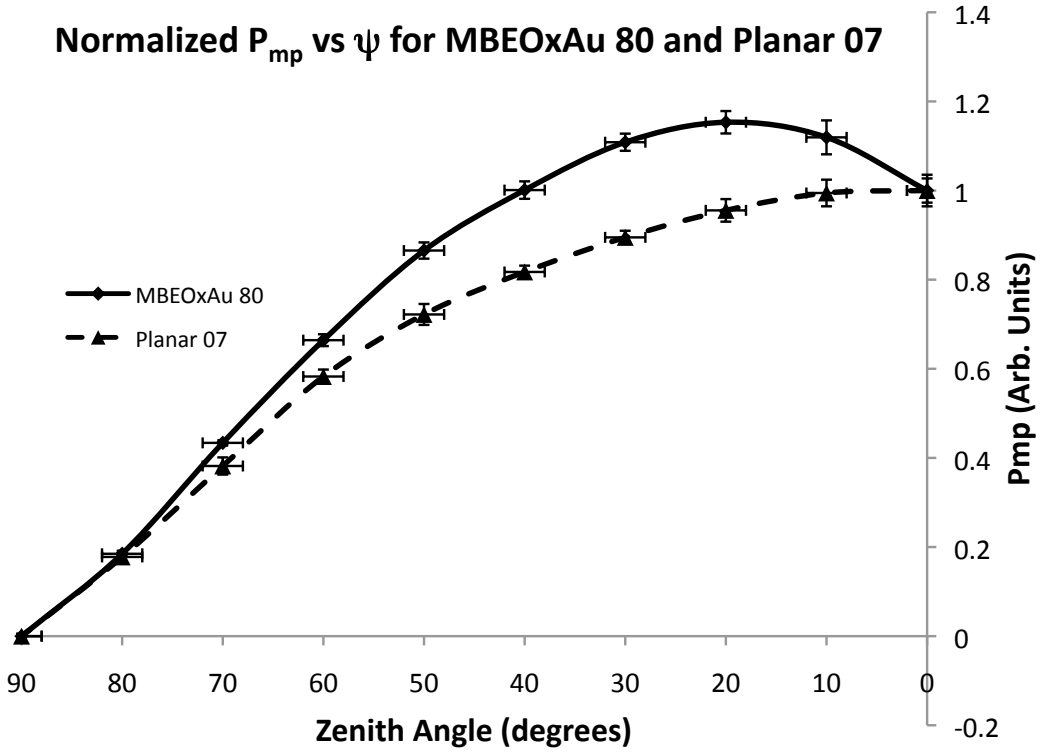

Figure 139: Normalized P_{mp} vs. ψ for 3DCNTPV cell MBEOxAu 80 and Planar cell 07. The 3DCNTPV cell shows an inverted C-type curve as the value of P_{mp} increases for angles larger than 0^o before reaching a maximum value at ψ=20^o. After the maximum, the value of P_{mp} decreases steadily until ψ=90^o. The planar cell has a maximum P_{mp} value at ψ=0^o, which decreases steadily as the value of ψ increases.

5.11.6 Geometry of MBEOxAu 80

Figure 140 shows two SEM micrographs of MBEOxAu 80. The top micrograph is a plan view of the cell. The bottom micrograph is taken with the cell tilted at 30^o. The pattern for this cell is a waffle type pattern discussed in §3.1. The crossbars of the grid, w, nominally measure 25μm. The interior pores of the grid are a square with the sides, d, having a nominal value of 75μm. The height of these towers are found via SEM analysis to be 54.59±3.63 μm.

The open area fraction is needed to calculate η_{3D}. For a grid pattern, the open area fraction is equal to

$$F_o = \frac{d^2}{(w+d)^2} \tag{98}$$

For MBEOxAu 80, the value of F_o is calculated to be 0.5625.

5.11.6.1 Reflectance Measurement

To determine the value of η_{2D} for a 3DCNTPV sample, the reflectance of a planar cell with a Au back contact (PlanarAu 105) was measured via reflectometry. A Hamamatsu (Hamamatsu, Japan) Photonics L7893 Series halogen and deuterium lamp connected to a Filmetrics (San Diego, CA) F20 series Thin Film Analyzer was used to find the reflection spectrum from 220 to 845nm. Background illumination is compensated for in the spectrum. Assuming no transmission through the cell is taking place, the absorption is the reflectance subtracted from unity. Figure 141 shows the absorbance spectrum for this 2D cell. At small wavelengths, the absorption is relatively constant at nearly 90%. The absorbance drops as the incident wavelength approaches λ_g of CdTe with a sharp drop in absorbance occurring for wavelengths near 830nm.

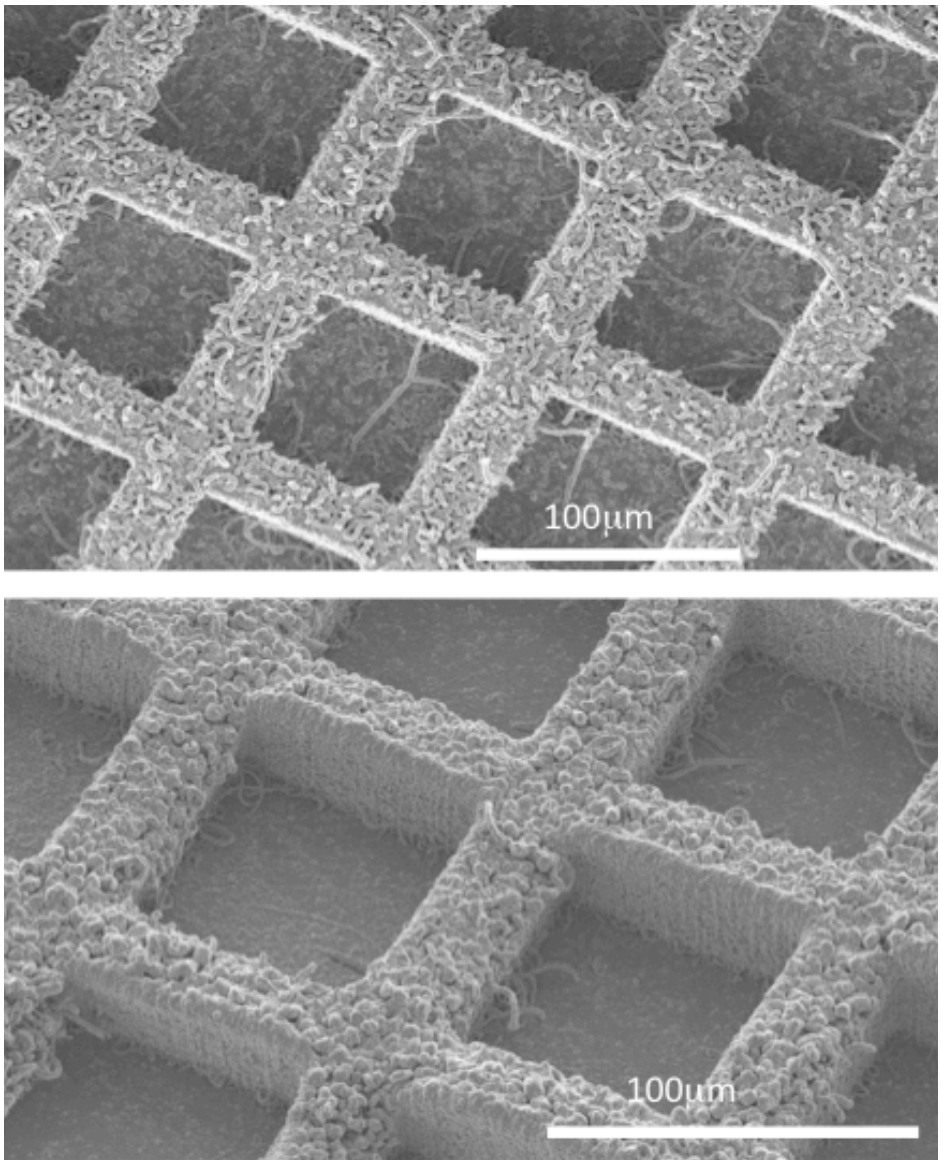

Figure 140: SEM micrographs of MBEOxAu 80 (top) untilted and (bottom) tilted at an angle of 30^o. The VACNTs are grown in a grid pattern with crossbars measuring 25μm and interior pores of 75μm. The tilt corrected height of the towers was found by SEM analysis to be 54.59 ± 3.63 μm.

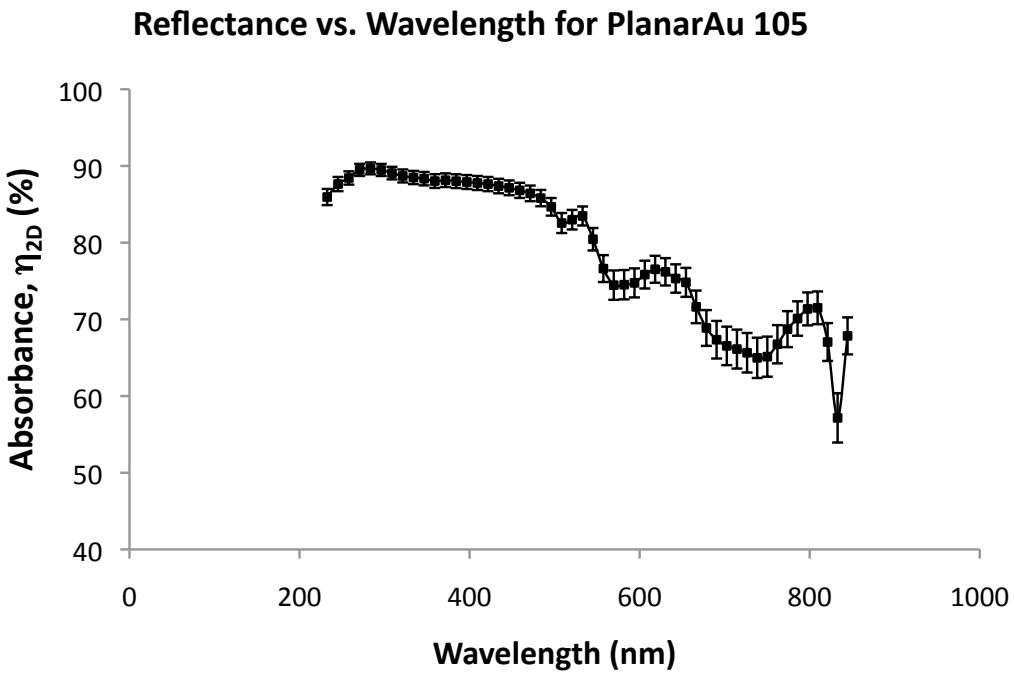

Figure 141: Reflectance vs. wavelength of PlanarAu 105 as measured by a Filmetrics Thin Film Analyzer. Only every 10^{th} point is shown for clarity. At small wavelengths, the absorption of the cell is relatively high at nearly 90%. As the wavelength approaches λ_g of CdTe, the absorbance of the cell drops. A sharp decrease in absorbance is present for wavelengths around 830nm.

As is obvious from Figure 141, the value of η_{2D} is wavelength dependent. Each of these values of η_{2D} contribute to the overall value of η_{2D} weighted by the intensity output of the ELH lamp. Wavelengths longer than λ_g do not possess enough energy to add to the cell photocurrent. The maximum in the output intensity of the lamp occurs very close to λ_g of CdTe with the majority of the lamp intensity in the region between 650 to 850nm. The calculation for the overall η_{2D} over all wavelengths from 650 to 850nm can be described by

$$\eta_{2D} = \frac{\sum_{\lambda=650nm}^{\lambda=850nm} \left[I(\lambda) \times \eta_{2D}(\lambda) \right]}{\sum_{\lambda=650nm}^{\lambda=850nm} I(\lambda)} \tag{99}$$

Where I(λ) is the wavelength dependent intensity output of the ELH lamp at 3350K found in Equation 90 and $\eta_{2D}(\lambda)$ is measured via reflectometry. Using this equation, the overall η_{2D} can be calculated to be 67.6%.

Table 32 summarizes the parameters used to calculate Γ, η_{3D}, and P_{mp} for a 3DCNTPV cell with the same geometry as MBEOxAu 80.

Table 32: Parameters used to calculate theoretical Γ, η_{3D}, and P_{mp} for a model 3DCNTPV cell with the same morphology as MBEOxAu 80.

Parameter	Value
Tower height, h (μm)	54.58
Tower separation, w (μm)	25
Tower diameter, d (μm)	75
Azimuthal angle, ω (^{o})	0
2D absorption efficiency, η_{2D}	0.626
Open area fraction, F_o	0.5625

The equations used to calculate Γ, η_{3D}, and P_{mp} for the theoretical cell modeled after MBEOxAu 80 can be found in Chapter 4. The values of Γ are calculated using

Equation 66, η_{3D} with Equation 42, and P_{mp} with Equation 36. The results of these calculations are shown in Table 33.

Table 33: Theoretical Γ, η_{3D}, and P_{mp} for a 3DCNTPV cell with the same morphology as MBEOxAu 80 using theory found in Chapter 4. Parameters used in the calculation are found in Table 32.

Angle	Γ	η_{3D}	Normalized P_{mp}
0^o	1	0.626	1
10^o	1.257	0.673	1.059
20^o	1.530	0.711	1.068
30^o	1.840	0.744	1.030
40^o	2.222	0.773	0.946
50^o	2.735	0.798	0.820
60^o	3.521	0.819	0.654
70^o	4.999	0.832	0.455
80^o	9.254	0.836	0.232
90^o	2.38×10^{16}	0.836	8.18×10^{-17}

Qualitatively, the P_{mp} vs. ψ curves for both MBEOxAu 80 and Planar 07 agree well with theory. Planar 07 decreases monotonically from a maximum normalized P_{mp} of 1 at ψ=0^o. The values of P_{mp} are larger than expected in the range of ψ from 30 to 70^o. There may be a number of explanations for this. It is possible that a non-isotropic background illumination is present. When background is subtracted from the experimental results, it is assumed that the background is constant for all values of ψ. If this background is larger in the range of ψ from 30 to 70^o, a larger P_{mp} value for these values of ψ would be expected. Another possible explanation is that even when controlling the duty cycle of the ELH lamp, heating of the solar cell is occurring. This heating would be worse at low values of ψ and would decrease the value of P_{mp}. This, in turn, would alter the normalized values of P_{mp} over the entire range of angles. The end result would be an increased normalized P_{mp} at lower ψ values.

MBEOxAu 80 shows the characteristic C-type curve which theory predicts for the 3DCNTPV type of cell. However, the experimental P_{mp} vs. ψ curve differs slightly from the theoretically calculated curve. At $\psi \leq 40^o$ the experimental P_{mp} is larger

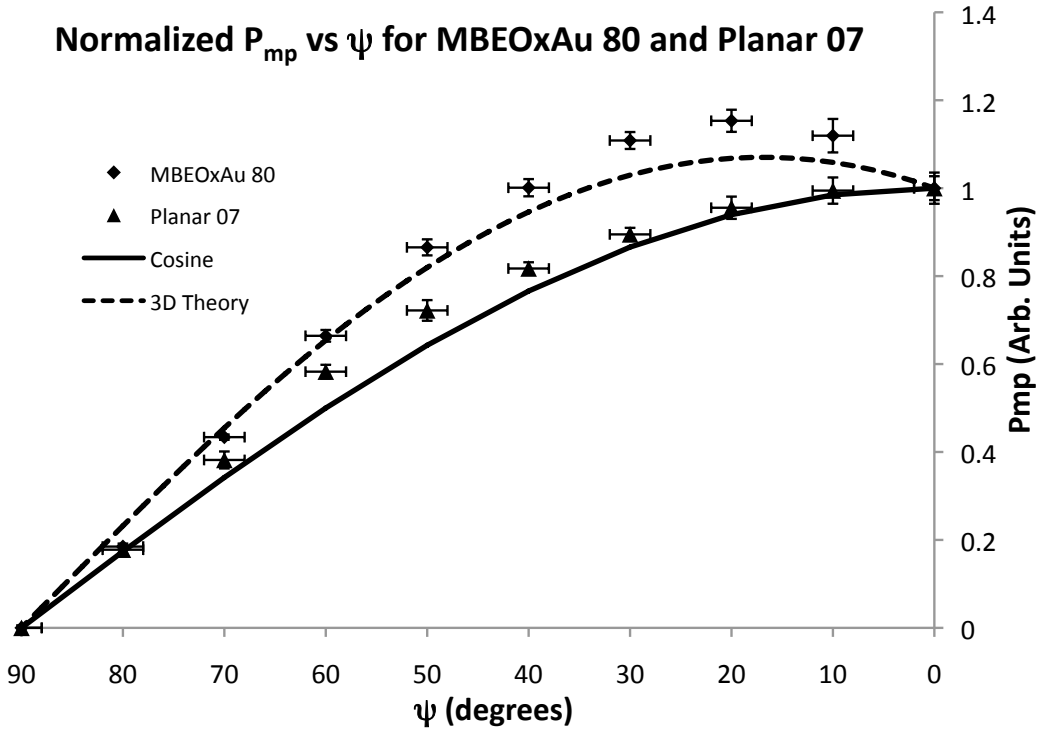

Figure 142: P_{mp} vs. ψ for Planar Cell 07 and MBEOxAu 80. Qualitatively, both experimental curves follow the trends of what is expected theoretically. Planar Cell 07 has a maximum P_{mp} at ψ=0^o and decreases continuously for larger angles of ψ. The experimental values for Planar Cell 07 are larger for values of ψ between 30 and 70^o. This may be caused by cell heating or the presence of a non-isotropic background. MBEOxAu 80 shows a greater increase of P_{mp} at small values of ψ than is predicted by theory, especially for angles between 10 and 50^o. In addition to cell heating and non-isotropic background, MBEOxAu 80 may have this increased power due to a overestimation of η_{2D} due to nonspecular reflection, misalignment of the cell causing a nonzero value of ω, or porosity in the VACNT towers.

than what would be expected by theory. As explained earlier, this increase P_{mp} may be caused by cell heating or the presence of a non-isotropic background. With the 3DCNTPV cell, the P_{mp} difference between experiment and theory may be affected by other factors, namely an overestimation of η_{2D} by reflectometry, a nonzero ω angle during testing due to misalignment of the cell, or a deviation from theory due to VACNT tower porosity.

One of the major flaws of reflectometry is that the angle between the lamp output and the photodiode is constant. This means that a reflectometer can only measure light which is specularly reflected from the sample. Any light which is diffusely reflected will not be measured by the photodiode and result in an artificially decreased measurement of the reflection. This decreased reflection measurement means that the absorbance of a sample tends to be overestimated. The overestimation of absorption by reflectometry is especially apparent for samples with surface texture.

The CdTe/CdS layer on PlanarAu 105 may not be perfectly smooth and at least a portion of the incident light from the reflectometer should be reflected nonspecularly. Figure 73 in Chapter 4 shows that a small change in the value of η_{2D} may result in a large change in the ratio between the maximum value of P_{mp} and the P_{mp} at ψ=0^o.

The nominal value of ω for the 3DCNTPV cell during testing is 0^o, however, there is no procedure for determining the exact value of ω during testing. Any twist in the position of the cell during measurement will result in a value of ω which is no longer 0^o. At ω=0^o, the value of Γ is at a minimum. The value of Γ then increases to a maximum at ω=45^o. This change in Γ will be reflected in the measured values of P_{mp} for the cell. Depending on the shape of the cell and the exact placement of the metal and ITO contacts, it is nearly impossible to position the cell at ω=0^o.

In addition to a nonzero value of ω resulting from the cell being physically twisted during IV measurement setup, the actual pattern of the VACNTs on the wafer may be misoriented. This misorientation can result from errors during the photolithography

and/or dicing fabrication steps. The twisting of the cell during either measurement or fabrication may result in an increased maximum P_{mp} over what is theoretically predicted.

One of the primary assumptions for the theory presented in Chapter 4 is that the VACNT towers may be approximated by Euclidean figures with straight, non-rough sidewalls. As can be seen from the SEM micrographs in Figure 140, this assumption breaks down for real devices. The tops of the VACNTs are quite rough while the CdTe/CdS conformally coats portions of the VACNT sidewalls. The porosity of the VACNT structures may increase the absorption of light at off-normal ψ angles above what would be expected for smooth, straight walled towers. This porosity may be the reason the experimental P_{mp} vs. ψ for MBEOxAu 80 is slightly larger than would be expected theoretically at low values of ψ.

These three effects can drastically change the values of P_{mp} at different values of ψ as calculated by theory and may explain the deviation in Figure 142 between the theoretical and experimental P_{mp} vs. ψ curves. As mentioned previously, PlanarAu 105 would be expected to have a certain percentage of diffuse reflection which would not be accounted for in the reflectometry measurement. If this diffuse reflection component is only 7.5% for all wavelengths between 650 and 850nm, then the final η_{2D} calculated by Equation 99 would be 0.6. A twist in the cell during testing or production can alter the value of ω. The combination of both these effects is nearly enough to match the experimental and theoretical P_{mp} vs. ψ curves for MBEOxAu 80.

Figure 143 shows how a change in η_{2D} and ω can affect the theoretical P_{mp} vs. ψ curve. The diamonds represent the experimental data points of P_{mp} vs. ψ from MBEOxAu 80. The dashed line is the theoretical P_{mp} vs. ψ curve calculated in Table 33. The solid line is a theoretical calculation if the value of η_{2D} is 0.6 due to nonspecular reflection effects and the value ω is 45^o due to misorientation during

measurement. Considering these two sources of error, the fit to the measured data is much closer, especially for small values of ψ. The remaining small difference between experimental and theoretical curves can be accounted for by heating effects or surface roughness of the VACNT towers.

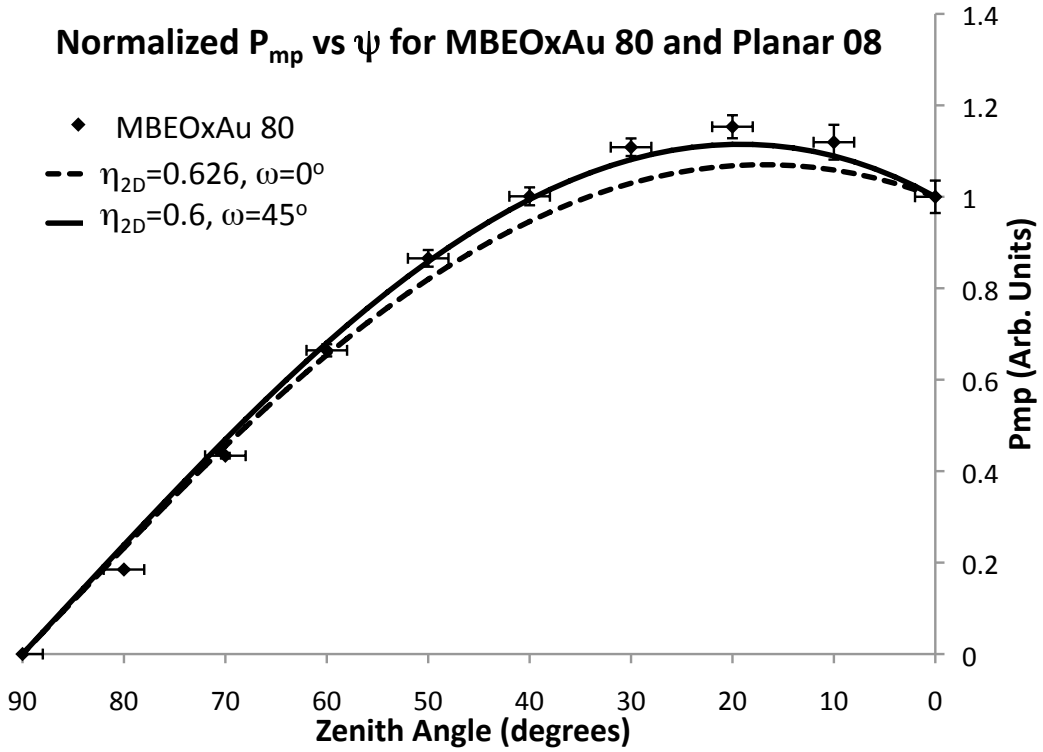

Figure 143: P_{mp} vs. ψ curves for MBEOxAu 80. The diamonds represent the experimental data points measured from the IV curves of MBEOxAu 80. The dashed line is the theoretical calculation of P_{mp} vs. ψ from Table 33 with η_{2D}=0.626 and ω=0^o. The solid line is a theoretical calculation assuming an overestimation of η_{2D} by 7.5% due to diffuse reflection and a misorientation of ω to 45^o. Considering these possible sources of error, the theoretical fit to the measured data is much closer, especially at low values of ψ. The remaining difference could be accounted for by heating effects or porosity and surface roughness of the VACNT towers.

The experimental measurement of P_{mp} vs. ψ for a 3DCNTPV cell has been shown to follow the inverted C-type curve predicted by theory. This experimental P_{mp} was larger than predicted for small values of ψ. However, by investigating some of the sources of experimental error, including overestimation of η_{2D} by reflectometry and the misorientation of ω, a new theoretical curve could be calculated. This new

theoretical curve matches the experimental curve quite closely, even for small values of ψ. The small difference between the two curves can be accounted for by heating effects or porosity and surface roughness of the VACNT towers.

CHAPTER VI

SUMMARY AND FUTURE WORK

6.1 Summary of Contributions

In order to summarize the value of this work regarding 3DCNTPV devices, it is necessary to understand their historical context. Generation III inorganic PV devices utilizing 3D geometries via 1D structures are a relatively recent research focus. This is as opposed to Generation I and II type cells, which have been well studied for over 50 and 35 years, respectively.

The use of one-dimensional structures for PV devices was first proposed independently by two groups in 2005. Kayes et. al. [138] proposed a radial junction silicon nanowire device while Mehta and Kruis [255] proposed a thin film nanowire embedded junction device. The first functional devices utilizing 1D Si NWs was developed by Peng et. al. (I_{sc}=1.36 mA/cm^2, V_{oc}=0.73V) [256] in 2005 and followed in 2007 by Si NW devices synthesized by Tian et. al. (I_{sc}=0.503 nA, V_{oc}=0.26V) [145] and Tsakalakos et. al. (I_{sc}=1.6mA/cm^2, V_{oc}=0.13V) [257].

The same year as the publications by Tian et. al. and Tsakalakos et. al., the first publication showing a proof of concept 3DCNTPV device was published [148]. The 3DCNTPV device structure is unique because it is the first Generation III device to utilize a CdTe/CdS heterojunction and is one of the first devices to create a 3D geometry from a "bottom up" type approach. In this type of cell construction, the 3D structure is formed via deposition to create a functional PV device. Patents for the 3DCNTPV idea have been awarded in China [258], South Korea [259], and Australia [260] (pending in the Europe Union [261] and United States [262]).

This work also shows the development of the first Generation III inorganic PV device to use CNTs as the 1D charge collector. Since the first paper on the 3DCNTPV device was published, the use of CNTs in PV devices has since been used by several other groups to great effect. In 2009, Zhou et al. [60] used the same 3DCNTPV structure, referencing this work, but utilized a-Si as the photoactive material. These cells possess an I_{sc} of 7mA/cm^2 and V_{oc} of 0.287V with the 3DCNTPV cells showing higher power output over similar planar cells, even at ψ=0^o. In 2010, Schriver et. al. [263] used a textured mat of CNTs as a back contact for a-Si cells. The cells exhibited many of the parasitic effects found in this work, namely RO and shunting, and exhibited low power outputs (I_{sc}=0.22mA/cm^2, V_{oc}=0.38V). Also in 2010, Mohseni et. al. [264] developed a device with a SWNT back contact and GaAs nanowire active materials with an I_{sc} of 45μA and V_{oc} of 0.325V.

In addition to providing one of the first demonstrable inorganic solar cells utilizing 1D nanostructures, this work has developed a complete theoretical model of the 3DCNTPV cell. This model quantifies the increase in average photon interactions with the solar cell surface, Γ, and proposes a new efficiency for these types of 3D cells, η_{3D}. The values of these parameters are completely described in the model through device tower height, diameter, spacing, shape and solar disc position. The model also indicates that the 3DCNTPV type cells should show an increase in P_{mp} over similar planar cells when the solar flux is off-normal. As the sun subtends all zenith angles, more energy will be produced throughout the day by a 3DCNTPV cell than a cell without the 3D structure .

This work has further shown working proof of concept devices based on the 3DCNTPV structure. By altering processing conditions, the figures of merit of produced cells have been increased. The first 3DCNTPV cells created posses I_{sc} values of 0.085 to 17.872mA/cm^2 and V_{oc} values in the range of 2 to 122mV. By altering process flows, subsequent 3DCNTPV cells have been made more efficient. I_{sc}

for these cells has been increased to $\sim$1mA/cm^2 even without $CdCl_2$ post processing. V_{oc} values have been increased to 350mV.

This work has also shown progress in increasing R_{sh} of the cells from values around 300Ω to values of 3,000 Ω and increasing the IV curvature from a straight line to one resembling a working diode.

Finally, this work matched theoretical P_{mp} vs. ψ results with both monte carlo computational simulations and experimentally produced cells. 3DCNTPV cells showed an increase in power output with an off-normal solar flux compared to a flux which is normal to the substrate. This increase matched well with the theoretical models and simulations presenting in this work.

6.2 Future Work

This work only represents the first step in research towards a 3DCNTPV type cell architecture which could eventually be used for commercial solar cells. Future research must focus on increasing the efficiencies of produced cells and further exploring their increased power output with an off-normal solar flux.

A working $CdCl_2$ processing step for 3DCNTPV cells must be developed. A successful post processing step should increase I_{sc} and V_{oc} so that completed cells have efficiencies more in line with commercially produced CdTe devices (8-15% efficient).

The power gain at off-normal angles should be further studied. While monte carlo simulations were run in order to determine how Γ varied with tower layout to find P_{mp} vs. ψ, this reliance should be determined experimentally. Cells should be made with varying tower shapes, spacing, diameter, and heights. P_{mp} vs. ψ can be determined for all these cells and compared to theoretical models. It could then be determined how well the theory matches experimental power output and if any changes must be made to the theory.

The 3DCNTPV cells in this work were metallized in order to avoid a rectifying barrier at the CdTe/p-Si interface. Future work should be done to grow tall, vertically aligned CNTs directly onto a suitable back contact metal layer without impacting the conductivity of the metal/CNT interface. Much work has been done in the literature to successfully grow vertically aligned CNTs on metal utilizing various diffusion layers, but growth directly on metal underlayers is a difficult processing step and more research into this area is needed.

Finally, the 3DCNTPV structure is very versatile and can be used for any semiconductor system which can be deposited. Work should be done to pair other semiconductor systems with the 3DCNTPV structure including a-Si, GaAs, CIGS, CZTS, GaTe, semiconducting polymers, and QDs. However, the most interesting semiconductor system for use in the 3DCNTPV system may be a semiconductor which is deemed ill-suited to planar morphologies. Since the absorbance of a material is the most important variable in determining the ratio of power output of the 3D cell versus a planar cell, the 3DCNTPV structure has the greatest advantage when used with a semiconductor with a relatively low absorbance. While such a material would have low power output when in a planar morphology, using a 3D structure could increase the energy output to levels more comparable to more traditional PV systems. So, an ideal PV material for a 3DCNTPV cell would have a low absorbance, low cost, and low surface recombination velocity. Further research should be done to identify any qualified photoactive materials, if any, that exist.

REFERENCES

[1] A. Vasko. *Issues in the Development of All-Sputtered ZnO/CdS/CdTe Flexible Solar Cells*. PhD thesis, University of Toledo, 2009.

[2] P. Kamat. Meeting the clean energy demand: Nanostructure architectures for solar energy conversion. *Journal of Physical Chemistry C*, 111:2834–2860, 2007.

[3] M. I. Hoffert, K. Caldeira, A. K. Jain, E. F. Haites, L. D. Danny Harvey, S. D. Potter, M. E. Schlesinger, S. H. Schneider, R. G. Watts, T. M. L. Widley, and D. J. Wuebbles. Energy implications of future stabilization of atmospheric CO_2 content. *Nature*, 195:881–884, 1998.

[4] N.S. Lewis. Powering the planet. *MRS bulletin*, 32:808–820, 2007.

[5] R. Socolow and A. Glaser. Balancing risks: nuclear energy & climate change. *Daedalus*, 138(4):31–44, 2009.

[6] C.L. Archer and M.Z. Jacobson. Evaluation of global wind power. *Journal of Geophysical Research*, 110:1–20, 2005.

[7] M. Grätzel. Solar energy conversion by dye-sensitized photovoltaic cells. *Inorganic Chemistry*, 44:6841–6851, 2005.

[8] M. Prince. Silicon solar energy converters. *Journal of Applied Physics*, 26(5):534–540, 1955.

[9] E. Kymakis. The impact of carbon nanotubes on solar energy conversion. *Nanotechnology Law and Business*, 3(4):405–410, 2006.

[10] X. Matthew, J. Enriquez, A. Romeo, and A. Tiwari. CdTe/CdS solar cells on flexible substrates. *Solar Energy*, 77:831–838, 2004.

[11] C.D. Mickey. Solar photovoltaic cells. *Journal of Chemical Education*, 58(5):418–423, 1981.

[12] A. Einstein. Über einen die erzeugung und verwandlung des lichtes betreffenden heuristischen gesichtspunkt. *Annalen der Physik*, 322(6):132–148, 1905.

[13] W. Schottky. Halbleitertheorie der sperrschicht. *Naturwissenschaften*, 26:843–843, 1938.

[14] R.S. Ohl. Light-sensitive electric device including silicon. *US Patent 2,402,662*, 1948.

[15] G. Conibeer. Third-generation photovoltaics. *Materials Today*, 10(11):42–50, 2007.

[16] J. Zhao, A. Wang, M. Green, and F. Ferrazza. 19.8% efficient "honeycomb" textured multicrystalline and 24.4% monocrystalline silicon solar cells. *Applied Physics Letters*, 73(14):1991–1993, 1998.

[17] R. Swanson. Approaching the 29% limit efficiency of silicon solar cells. In *Conference Record of the Thirty-first IEEE Photvoltaic Specialist Conference*, pages 889–894, 2005.

[18] M.M. Tessema. Shunt passivation process for cdte solar cell-new post deposition technique. Master's thesis, The University of Toledo, 2009.

[19] I. Repins, M. Contreras, B. Egaas, C. DeHart, J. Scharf, C. Perkins, B. To, and R. Noufi. Short communication: Accelerated publication 19.9%-efficient ZnO/CdS/$CuInGaSe_2$ solar cell with 81.2% fill factor. *Progress in Photovoltaics: Research and Applications*, 16:235–239, 2008.

[20] G. Beaucarne, F. Duerinckx, I. Kuzma, K. Van Nieuwenhuysen, H. Kim, and J. Poortmans. Epitaxial thin-film Si solar cells. *Thin Solid Films*, 511-512:533–542, 2006.

[21] D.L. Staebler and C.R. Wronski. Optically induced conductivity changes in dischargeproduced hydrogenated amorphous silicon. *Journal of Applied Physics*, 51(6):3262–3268, 2009.

[22] D. Bonnet and H. Rabenhorst. New results on the development of a thin-film p-CdTe-n-CdS heterojunction solar cell. In *IEEE Photovoltaic Spec Conf, 9th, May 2-4 1972*, pages 129–131, 1972.

[23] B. Basol. Electrodeposited CdTe and HgCdTe solar cells. *Solar Cells*, 23:69–88, 1988.

[24] T. Chu. Thin film cadmium telluride solar cells by two chemical vapor deposition techniques. *Solar Cells*, 23:31–48, 1988.

[25] K. Mitchell, C. Eberspacher, F. Cohen, J. Avery, G. Duran, and W. Bottenberg. Progress towards high efficiency thin film CdTe solar cells. *Solar Cells*, 23:49–57, 1988.

[26] J. J. Loferski. Theoretical considerations governing choice of optimum semiconductor for photovoltaic solar energy conversion. *Journal of Applied Physics*, 27(7):777–784, 1956.

[27] A. Tiwari, G. Khrypunov, F. Kurdzesau, D. Batzner, A. Romeo, and H. Zogg. CdTe solar cell in a novel configuration. *Progress in Photovoltaics: Research and Applications*, 12:33–38, 2004.

[28] X. Wu, J. Keane, R. Dhere, C. DeHart, A. Duda, T. Gessert, S. Asher, and D. Levi. 16.5% efficiency CdS/CdTe polycrystalline thin-film solar cell. In *Proceedings of the 17th European Photovoltaic Solar Energy Conference*, pages 996–1000, 2001.

[29] B. McCandless and K. Dobson. Processing options for CdTe thin film solar cells. *Solar Energy*, 77:839–856, 2004.

[30] T. Surek. Crystal growth and materials research in photovoltaics: progress and challenges. *Journal of Crystal Growth*, 275:292–304, 2005.

[31] A. Luque and S. Hegedus. *Handbook of Photovoltaic Science and Engineering*. Wiley, West Sussex, 2003.

[32] H. Hoppe and N. S. Sariciftci. Organic solar cell: An overview. *Journal of Materials Research*, 19(7):1924–1945, 2004.

[33] U. Balasubramanian. *Indium Oxide as a High Resistivity Buffer Layer for CdTe/CdS Thin Film Solar Cells*. PhD thesis, University of South Florida, 2004.

[34] J. S. Yuan and J. J. Liou. *Semiconductor device physics and simulation*. Plenum Press, 1998.

[35] H. Chou. *Efficiency limiting defects and mechanisms in CdTe/CdS heterojunction solar cells*. PhD thesis, Georgia Institute of Technology, 1995.

[36] Martin A. Green. *Solar cells: operating principles, technology and system applications*. University of New South Wales, 1998.

[37] R. Miles, K. Hynes, and I. Forbes. Photovoltaic solar cells: An overview of state-of-the-art cell development and environmental issues. *Progress in Crystal Growth and Characterization of Materials*, 51:1–42, 2005.

[38] I. Martil and G. Diaz. Determination of the dark and illuminated characteristic parameters of a solar cell from IV characteristics. *European Journal of Physics*, 13:193–197, 1992.

[39] A. Bosio, N. Romeo, S. Mazzamuto, and V. Canevari. Polycrystalline CdTe thin films for photovoltaic applications. *Progress in Crystal Growth and Characterization of Materials*, 52:247–279, 2006.

[40] X. Wu, R.G. Dhere, Y. Yan, I.J. Romero, Y. Zhang, J. Zhou, C. DeHart, A. Duda, C. Perkins, and B. To. High-efficiency polycrystalline CdTe thin-film solar cells with an oxygenated amorphous CdS (a-CdS:O) window layer. In *Photovoltaic Specialists Conference, 2002. Conference Record of the Twenty-Ninth IEEE*, pages 531–534, 2003.

[41] W. Shockley and H.J. Queisser. Detailed balance limit of efficiency of pn junction solar cells. *Journal of Applied Physics*, 32(3):510–519, 1961.

[42] A.D. Compaan. The fabrication and physics of high-efficiency CdTe thin-film solar cells. Technical report, National Renewable Energy Laboratory, 2002.

[43] A. Compaan, R. Collins, V. Karpov, and D. Giolando. Fabrication and physics of CdTe devices by sputtering. Technical report, National Renewable Energy Laboratory, 2007.

[44] X. Mathew, J. Enriquez, C. Segura, A. Sanchez-Juarez, U. Pal, G. Contreras, D. Acosta, and C. Magana. Development of a substrate configuration CdTe/CdS solar cell on flexible molybdenum substrate. In *Thirty-first IEEE Photovoltaic Specialists Conference, 2005*, pages 434–436, 2005.

[45] J. Perrenoud and S. Buecheler. Flexible CdTe solar cells with high photovoltaic conversion efficiency. In *IEEE Photovoltaic Spec Conference*, pages 695–699, 2010.

[46] A Romeo, G Khrypunov, F Kurdesau, M Arnold, D Batzner, H Zogg, and A Tiwari. High-efficiency flexible CdTe solar cells on polymer substrates. *Solar Energy Materials & Solar Cells*, 90:3407–3415, 2006.

[47] X. Wu, R.G. Dhere, Y. Yan, M.J. Romero, Y. Zhang, J. Zhou, C. DeHart, A. Duda, C. Perkins, and B. To. High-efficiency polycrystalline CdTe thin-film solar cells with an oxygenated amorphous CdS (a-CdS:O) window layer with an oxygenated amorphous CdS (aCdS:O) window layer. In *29th IEEE Photovoltaic Specialists Conference, May 19, 2002 - May 24, 2002*, pages 531–534, 2002.

[48] R. Mamazza, S. Yu, D.L. Morel, and C.S. Ferekides. Co-sputtered Cd_2SnO_4 films as front contacts for CdTe solar cells. In *IEEE photovoltaic specialists conference*, pages 612–615, 2002.

[49] R. Mamazza, U. Balasubramanian, D.L. Morel, and C.S. Ferekides. Thin films of $CdIn_2O_4$ as transparent conducting oxides. In *IEEE photovoltaic specialists conference*, pages 616–619, 2002.

[50] M. S. Dresselhaus, G. Dresselhaus, and P. Avouris. *Carbon Nanotubes Synthesis, Structure, Properties, and Applications*, volume 80 of *Topics in Applied Physics*. Springer, Berlin, 2001.

[51] K. Durose, P. R. Edwards, and D.P. Halliday. Materials aspects of CdTe/CdS solar cells. *Journal of Crystal Growth*, 197:733–742, 1999.

[52] S. Alamri. Effect of transparent conductive oxide stability on CdS/CdTe solar cell performance. *Japanese Journal of Applied Physics*, 41:L1052–1054, 2002.

[53] S. A. Bashar. *Study of Indium Tin Oxide (ITO) for Novel Optoelectonic Devices*. PhD thesis, King's College of London, 1997.

[54] K. Chopra, S. Major, and D. Pandya. Transparent conductors–a status review. *Thin Solid Films*, 102:1–46, 1983.

[55] H.U. Habermeier. Properties of indium tin oxide thin films prepared by reactive evaporation. *Thin Solid Films*, 80(1-3):157–160, 1981.

[56] A.K. Kulkarni, K.H. Schulz, T.S. Lim, and M. Khan. Electrical, optical and structural characteristics of indium-tin-oxide thin films deposited on glass and polymer substrates. *Thin Solid Films*, 308:1–7, 1997.

[57] M. Mizuhashi. Electrical properties of vacuum-deposited indium oxide and indium tin oxide films. *Thin Solid Films*, 70(1):91–100, 1980.

[58] A.J. Steckl and G. Mohammed. The effect of ambient atmosphere in the annealing of indium tin oxide films. *Journal of Applied Physics*, 51(7):3890–3895, 1980.

[59] I. Elfallal, R. Pilkington, and A. Hill. Formulation of a statistical thermodynamic model for the electron concentration in heavily doped metal oxide semiconductors applied to the tin-doped indium oxide system. *Thin Solid Films*, 223:303–310, 1993.

[60] J. Zhou. Indium tin oxide (ITO) deposition, patterning and Schottky contact fabrication. Master's thesis, Rochester Institute of Technology, 2006.

[61] F. Bachner and G. Foley. Effect of O pressure during deposition on properties of RF-Sputtered Sn-doped InO films. *Applied Physics Letters*, 31(11):773–775, 1977.

[62] N. Balasubramanian and A. Subrahmanyam. Effect of substrate temperature on the electrical and optical properties of reactively evaporated indium tin oxide films. *Materials Science and Engineering*, 81:279–281, 1988.

[63] J. Bregman, Y. Shapira, and H. Aharoni. Effects of oxygen partial pressure during deposition on the properties of ion-beam-sputtered indium-tin oxide thin films. *Journal of Applied Physics*, 67(8):3750–3753, 1990.

[64] M. Buchanan, J. Webb, and D. Williams. The influence of target oxidation and growth-related effects on the electrical properties of reactively sputtered films of tin-doped indium oxide. *Thin Solid Films*, 80:373–382, 1981.

[65] H. Haitjema and J. Elich. Physical properties of pyrolytically sprayed tin-doped indium oxide coatings. *Thin Solid Films*, 205:93–100, 1991.

[66] M. Higuchi, S. Uekusa, R. Nakano, and K. Yokogawa. Postdeposition annealing influence on sputtered indium tin oxide film characteristics. *Japanese Journal of Applied Physics*, 33:302–306, 1994.

[67] H. Kim, J. Horwitz, W. Kim, Z. Kafafi, and D. Chrisey. High quality Sn-doped In_2O_3 films grown by pulsed laser deposition for organic light-emitting diodes. In *Materials Research Society Proceedings*, volume 780, pages Y1.6.1–Y1.1.12, 2003.

[68] K. Sreenivas, S. Rao, A. Mansingh, and S. Chandra. Preparation and characterization of RF-Sputtered indium tin oxide films. *Journal of Applied Physics*, 57(2):384–392, 1985.

[69] Nisha M, S. Anusha, A. Antony, R. Manoj, and M. Jayaraj. Effect of substrate temperature on the growth of ITO thin films. *Applied Surface Science*, 252:1430–1435, 2005.

[70] F. Kurdesau, G. Khripunov, A. Da Cunha, M. Kaelin, and A. Tiwari. Comparative study of ITO layers deposited by DC and RF-Magnetron sputtering at room temperature. *Journal of Non-Crystalline Solids*, 352:1466–1470, 2006.

[71] D Kim, M Park, and G Lee. Preparation of high quality ITO films on a plastic substrate using RF-Magnetron sputtering. *Surface and Coatings Technology*, 201:927–931, 2006.

[72] K. Ellmer, R. Mientus, and H. Rossner. In situ investigation by energy dispersive x-ray diffraction (EDXRD) of the growth of magnetron sputtered ITO films. *Surface and Coatings Technology*, 142-144:1094–1099, 2001.

[73] A. Mansingh and P. Srivastava. Band gap narrowing and the band structure of tin-doped indium oxide films. *Thin Solid Films*, 176:33–44, 1989.

[74] T. Gorjanc, D. Leong, C. Py, and D. Roth. Room temperature deposition of ITO using RF-Magnetron sputtering. *Thin Solid Films*, 413:181–185, 2002.

[75] R. Tahar, T. Ban, Y. Ohya, and Y. Takahashi. Tin doped indium oxide thin films: Electrical properties. *Journal of Applied Physics*, 83(5):2631–2645, 1998.

[76] Y. Wu, C. Maree, R. Haglund, D. Hamilton, and M. Paliza. Resistivity and oxygen content of indium tin oxide films deposited at room temperature by pulsed-laser ablation. *Journal of Applied Physics*, 86(2):991–994, 2009.

[77] T. Ishida, H. Kobayashi, and Y. Nakato. Structures and properties of electron-beam-evaporated indium tin oxide films as studied by Xray photoelectron spectroscopy and workfunction measurements. *Journal of Applied Physics*, 73(9):4344–4350, 1993.

[78] M.G. Mason, L.S. Hung, C.W. Tang, S.T. Lee, K.W. Wong, and M. Wang. Characterization of treated indium–tin–oxide surfaces used in electroluminescent devices. *Journal of Applied Physics*, 86(3):1688–1692, 1999.

[79] D. Albin, D. Rose, R. Dhere, D. Niles, A. Swartzlander, A. Mason, D. Levi, H. Moutinho, and P. Sheldon. Tin oxide stability effects—their identification, dependence on processing and impacts on CdTe/CdS solar cell performance. In *AIP Conference Proceedings*, volume 394, pages 665–681, 1997.

[80] Y. Roussillon, D. Giolando, D. Shvydka, A. Compaan, and V. Karpov. Blocking thin-film nonuniformities: Photovoltaic self-healing. *Applied Physics Letters*, 84(4):616–618, 2004.

[81] K. Chopra, P. Paulson, and V. Dutta. Thin-film solar cells: an overview. *Progress in Photovoltaics: Research and Applications*, 12:69–92, 2004.

[82] U. Rau and M. Schmidt. Electronic properties of ZnO/CdS/Cu(InGa)Se_2 solar cells–aspects of heterojunction formation. *Thin Solid Films*, 387:141–146, 2001.

[83] J. Britt and C. Ferekides. Thin-film CdS/CdTe solar cell with 15.8% efficiency. *Applied Physics Letters*, 62(22):2851–2852, 1993.

[84] A. Compaan. The status of and challenges in CdTe thin-film solar-cell technology. In *Spring 2004 Materials Research Society Symposium*, volume 808, page A.7.6, 2004.

[85] K.B. Sundaram and A. Khan. Work function determination of zinc oxide films. *Journal of Vacuum Science & Technology A: Vacuum, Surfaces, and Films*, 15(2):428–430, 1997.

[86] V. Singh and J. McClure. Design issues in the fabrication of CdS-CdTe solar cells on molybdenum foil substrates. *Solar Energy Materials & Solar Cells*, 76:369–385, 2003.

[87] A. Brinkman and S.N. Alamri. The effect of the transparent conductive oxide on the performance of thin film CdS/CdTe solar cells. *Journal of Physics D: Applied Physics*, 33:L1–L4, 2000.

[88] A. Oliva, R. Castro-Rodriguez, O. Solis-Canto, V. Sosa, P. Quintana, and J. Pena. Comparison of properties of CdS thin films grown by two techniques. *Applied Surface Science*, 205:56–64, 2003.

[89] J. Lee. Comparison of CdS films deposited by different techniques: Effects on CdTe solar cell. *Applied Surface Science*, 252:1398–1403, 2005.

[90] K. Omura, A. Hanahusa, H. Higuchi T. Arita, T. Aramoto, T. Nishio, S. Sibutani, S. Kumazawa, M. Murozono, Y. Yabuuchi, and H. Takakura. Recent technical advances in thin-film CdS/CdTe solar cells. *Renewable Energy*, 8(1-4):405–409, 1996.

[91] M. Kobayashi, S. Nakamura, K. Kitamura, H. Umeya, A. Jia, A. Yoshikawa, M. Shimotomai, and Y. Kato. Luminescence properties of CdS quantum dots on ZnSe. *Journal of Vacuum Science & Technology B*, 15(5):2005–2008, 1999.

[92] N. Dhere and R. Dhere. Thin-film photovoltaics. *Journal of Vacuum Science & Technology A: Vacuum, Surfaces, and Films*, 24(4):1208–1214, 2005.

[93] T. L. Chu and S. S. Chu. Thin film II-VI photovoltaics. *Solid-State Electronics*, 38(3):533–549, 1995.

[94] A. D. Compaan, J. R. Sites, R. W. Birkmire, C. S. Ferekides, and A. L. Fahrenbruch. Critical issues and research needs for CdTe solar cells. In *Electrochemical Society Proceedings*, volume 99-11, 1999.

[95] S. Hegedus and B. McCandless. CdTe contacts for CdTe/CdS solar cells: effect of Cu thickness, surface preparation and recontacting on device performance and stability. *Solar Energy Materials & Solar Cells*, 88:75–95, 2005.

[96] S. Feldman, L. Mansfield, T. Ohno, V. Kaydanov, J.D. Beach, and T. Nagle. Non-uniformity mitigation in CdTe solar cells: the effects of high-resistance transparent conducting oxide buffer layers. In *Conference Record of the Thirty-first IEEE Photvoltaic Specialist Conference*, pages 271–274, 2005.

[97] J. H. Lee, H. Y. Lee, Y. K. Park, S. H. Shin, and K. J. Park. Effects of the annealing temperature and $CdCl_2$ treatment on the photovoltaic properties of the CdS/CdTe solar cell. *Japanese Journal of Applied Physics*, 37(6A):3357–3362, 1998.

[98] M. H. C. Jin and L. Dai. *Vertically Aligned Carbon Nanotubes for Organic Photovoltaic Devices*. Optical engineering. Taylor & Francis, Boca Raton, 2005.

[99] E. Kymakis, I. Alexandou, and G. A. J. Amaratunga. Single-walled carbon nanotube-polymer composites: electrical, optical and structural investigation. *Synthetic Materials*, 127:59–62, 2002.

[100] R. W. Birkmire and E. Eser. Polycrystalline thin film solar cells: Present status and future potential. *Annual Review of Materials Science*, 27:625–653, 1997.

[101] A. Marales-Acevedo. Thin film CdS/CdTe solar cells: Research perspectives. *Solar Energy*, 80:675–681, 2006.

[102] K. Durose, M. A. Cousins, D. S. Boyle, J. Beier, and D. Bonnet. Grain boundaries and impurities in CdTe/CdS solar cells. *Thin Solid Films*, 403-404:396–404, 2002.

[103] A. R. Davies and J. R. Sites. Effects of non-uniformity on rollover phenomena in CdS/CdTe solar cells. In *33rd IEEE Photovoltaic Specialists Conference, 2008*, 2008.

[104] K. Dobson, I. Visoly-Fisher, G. Hodes, and D. Cahen. Stability of CdTe/CdS thin-film solar cells. *Solar Energy Materials & Solar Cells*, 62:295–325, 2000.

[105] J. Sites and P. Mauk. Diode quality factor determination for thin-film solar cells. *Solar Cells*, 27:411–417, 1989.

[106] J. Sites. Quantification of losses in thin-film polycrystalline solar cells. *Solar Energy Materials & Solar Cells*, 75:243–251, 2003.

[107] S. Demtsu, D. Albin, J. Pankow, and A. Davies. Stability study of CdS/CdTe solar cells made with Ag and Ni back-contacts. *Solar Energy Materials & Solar Cells*, 90:2934–2943, 2006.

[108] S. Asher, F. Hasoon, T.A. Gessert, M.R. Young, P. Sheldon, J. Hiltner, and J. Sites. Determination of Cu in CdTe/CdS devices before and after accelerated stress testing. In *Conference Record of the Twenty-Eighth IEEE Photovoltaic Specialists Conference, 2000*, pages 479–482, 2000.

[109] Richard H. Bube. *Photovoltaic materials*. Imperial College Press, 1998.

[110] A. Pudov, M. Gloeckler, S.H. Demtsu, J.R. Sites, K.L. Barth, R.A. Enzenroth, and W.S. Sampath. Effect of back-contact copper concentration on CdTe cell operation. In *Conference Record of the Twenty-Ninth IEEE Photovoltaic Specialists Conference, 2002*, pages 760–763, 2002.

[111] D. Grecu and A.D. Compaan. Photoluminescence study of Cu diffusion and electromigration in CdTe. *Applied Physics Letters*, 75(3):361–363, 1999.

[112] D. Rose, R. Powell, U. Jayamaha, and M. Maltby. Advances in performance and high-throughput manufacturing of thin-film CdS/CdTe modules. In *Conference Record of the Twenty-Ninth IEEE Photovoltaic Specialists Conference, 2002.*, pages 555–558, 2002.

[113] B.O. Wartlick, C. Blanchard, and J. Barbot. Study of silver and copper diffusion in p-type $Hg_{0.3}Cd_{0.7}Te$ and CdTe by capacitance measurements. *Materials Science and Engineering B*, 71:254–257, 2000.

[114] S. Krumbein. Tutorial: Electrolytic models for metallic electromigration failure mechanisms. *IEEE Transactions on Reliability*, 44(4):539–549, 2002.

[115] Y. Roussillon, V. Karpov, D. Shvydka, J. Drayton, and A. Compaan. Back contact and reach-through diode effects in thin-film photovoltaics. *Journal of Applied Physics*, 96(12):7283–7288, 2004.

[116] A. Niemegeers and M. Burgelman. Effects of the Au/CdTe back contact on IV and CV characteristics of Au/CdTe/CdS/TCO solar cells. *Journal of Applied Physics*, 81:2881–2886, 1997.

[117] A. D. Pasquier, H. E. Unalan, A. Kanwal, S. Miller, and M. Chhowalla. Conducting and transparent single-wall carbon nanotube electrodes for polymer-fullerene solar cells. *Applied Physics Letters*, 87(20):203511, 2005.

[118] B. E. McCandless, L. V. Moulton, and R. W. Birkmire. Recrystallization and sulfur diffusion in $CdCl_2$-treated CdTe/CdS thin films. *Progress in Photovoltaics: Research Applications*, 5:249–260, 1997.

[119] A.D. Compaan. The fabrication and physics of high-efficiency CdTe thin-film solar cells. Technical report, National Renewable Energy Laboratory, 2002.

[120] I. Visoly-Fisher, S. R. Cohen, A. Ruzin, and D. Cahen. How polycrystalline devices can outperform single-crystal ones: Thin film CdTe/CdS solar cells. *Advanced Materials*, 16(11):879–883, 2004.

[121] A. Smith and A. Rohatgi. Ray tracing analysis of the inverted pyramid texturing geometry for high efficiency silicon solar cells. *Solar Energy Materials & Solar Cells*, 29:37–49, 1993.

[122] M. Tao, W. Zhou, H. Yang, and L. Chen. Surface texturing by solution deposition for omnidirectional antireflection. *Applied Physics Letters*, 91:81118, 2007.

[123] A. Parretta, A. Sarno, P. Tortora, H. Yakubu, P. Maddalena, J. Zhao, and A. Wang. Angle-dependent reflectance measurements on photovoltaic materials and solar cells. *Optics Communications*, 172:139–151, 1999.

[124] B. Dale and H. Rudenberg. Photovoltaic conversion-high efficiency silicon solar cells. In *Proceedings of the 14th Annual Power Sources Conference, US Army Signal Research and Development Lab*, page 22, 1960.

[125] W. Bailey, M. Coleman, C. Harris, and I. Lesk. Texture etching of silicon: Method. *US Patent 4,137,123*, 1979.

[126] G. Willeke, H. Nussbaumer, H. Bender, and E. Bucher. A simple and effective light trapping technique for polycrystalline silicon solar cells. *Solar Energy Materials & Solar Cells*, 26:345–356, 1992.

[127] T. Nunoi, S. Okamoto, K. Nakajima, S. Tanaka, N. Shibuya, K. Okamoto, T. Nammori, and H. Itoh. Cast polycrystalline silicon solar cell with grooved surface. In *Conference Record of the Photovoltaic Specialists Converence*, pages 664–665, 1990.

[128] S. Narayanan, J. Zolper, F. Yun, S. Wenham, A. Sproul, C. Chong, and M. Green. 18% efficient polycrystalline silicon solar cells. In *Conference Record of the Photovoltaic Specialists Conference*, pages 678–680, 1990.

[129] U. Kaiser, M. Kaiser, and R. Schindler. Texture etching of multicrystalline silicon. In *Conference Record of the European PVSEC*, pages 293–294, Lisbon, Port, 1991.

[130] S. Winderbaum, O. Reinhold, and F. Yun. Reactive ion etching (RIE) as a method for texturing polycrystalline silicon solar cells. *Solar Energy Materials & Solar Cells*, 46:239–248, 1997.

[131] Q. Chen, G. Hubbard, P. Shields, C. Liu, D. Allsopp, W. Wang, and S. Abbott. Broadband moth-eye antireflection coatings fabricated by low-cost nanoimprinting. *Applied Physics Letters*, 94:263118, 2009.

[132] L. Zeng, P. Bermel, Y. Yi, B. Alamariu, K. Broderick, J. Liu, C. Hong, X. Duan, J. Joannopoulos, and L. Kimerling. Demonstration of enhanced absorption in thin film Si solar cells with textured photonic crystal back reflector. *Applied Physics Letters*, 93:221105, 2008.

[133] K. Yu and J. Chen. Enhancing solar cell efficiencies through 1-D nanostructures. *Nanoscale Research Letters*, 4(1):1–10, 2009.

[134] J. Czaban, D. Thompson, and R. LaPierre. GaAs core shell nanowires for photovoltaic applications. *Nano Letters*, 9(1):148–154, 2009.

[135] E. Garnett and P. Yang. Silicon nanowire radial p n junction solar cells. *Journal of the American Chemical Society*, 130:9224–9225, 2008.

[136] Z. Fan, D. Ruebusch, A. Rathore, R. Kapadia, O. Ergen, P. Leu, and A. Javey. Challenges and prospects of nanopillar-based solar cells. *Nano Research*, 2:829–843, 2009.

[137] Z. Fan, H. Razavi, J. Do, A. Moriwaki, O.Ergen, Y. Chueh, P. W. Leu, J. C. Ho, T. Takahashi, L. A. Reichertz, S. Neale, K. Yu, M. Wu, J. W. Ager, and A. Javey. Three-dimensional nanopillar-array photovoltaics on low-cost and flexible substrates. *Nature Materials*, 8(8):648–653, 2009.

[138] B.M. Kayes, H.A. Atwater, and N.S. Lewis. Comparison of the device physics principles of planar and radial pn junction nanorod solar cells. *Journal of applied physics*, 97:114302, 2005.

[139] L. Kosyachenko, A. Savchuk, and E. Grushko. Dependence of efficiency of thin-film CdS/CdTe solar cell on parameters of absorber layer and barrier structure. *Thin Solid Films*, 517:2386–2391, 2009.

[140] C. Bridge, P. Dawson, P.D. Buckle, and M.E. Orzsan. Photoluminescence spectroscopy and decay time measurements of polycrystalline thin film CdTe/CdS solar cells. *Journal of Applied Physics*, 88(11):6451–6456, 2000.

[141] S. Marsillac, V.Y. Parikh, and A. Compaan. Ultra-thin bifacial CdTe solar cell. *Solar Energy Materials & Solar Cells*, 91:1398–1402, 2007.

[142] K. Van Nieuwenhuysen, F. Duerinckx, I. Kuzma, M. Payo, G. Beaucarne, and J. Poortmans. Epitaxially grown emitters for thin film crystalline silicon solar cells. *Thin Solid Films*, 517:383–384, 2008.

[143] A. Romeo, G. Khrypunov, S. Galassini, H. Zogg, and A. Tiwari. Bifacial configurations for CdTe solar cells. *Solar Energy Materials & Solar Cells*, 91:1388–1391, 2007.

[144] J. Schermer, P. Mulder, G.J. Bauhuis, P. Larsen, G. Oomen, and E. Bongers. Thin-film GaAs epitaxial lift-off solar cells for space applications. *Progress in Photovoltaics: Research and Applications*, 13:587–596, 2005.

[145] B.Z. Tian, X.L. Zheng, T.J. Kempa, Y. Fang, N.F. Yu, G.H. Yu, J.L. Huang, and C.M. Lieber. Coaxial silicon nanowires as solar cells and nanoelectronic power sources. *Nature*, 91:885–889, 2007.

[146] C. Colombo, M. Heiss, M. Gratzel, and A. FI. Morral. Gallium arsenide p-i-n radial structures for photovoltaic applications. *Applied Physics Letters*, 94:173108, 2009.

[147] M.D. Kelzenberg, D.B. Turner-Evans, B.M. Kayes, M.A. Filler, M.C. Punam, N.S. Lewis, and H.A. Atwater. Photovoltaic measurements in single-nanowire silicon solar cells. *Nano Letters*, 8:710–714, 2008.

[148] R. E. Camacho, A. R. Morgan, M. C. Flores, T. A. McLeod, V. S. Kumsomboone, B. J. Mordecai, R. Bhattacharjea, W. Tong, B. K. Wagner, J. D. Flicker, S.P. Turano, and W.J. Ready. Carbon nanotube arrays for photovoltaic applications. *Journal of Materials*, 59(3):39–42, 2007.

[149] A. Colli, T. Butler, N. Rupesinghe, A. Mumtaz, G. Amaratunga, and J. Wilson. Carbon nanotube arrays for optical design of amorphous silicon solar cells. *International Journal of Materials*, 1:113–116, 2008.

[150] X. Guo, H. Li, B. Y. Ahn, E. Duoss, K. Hsia, J. Lewis, and R. Nuzzo. Two-and three-dimensional folding of thin film single-crystalline silicon for photovoltaic power applications. In *Proceedins of the National Academy of Sciences*, volume 106, pages 20149–20154, 2009.

[151] T. Lin, F. Huang, J. Liang, and Y. Wang. A facile preparation route for boron-doped graphene, and its CdTe solar cell application. *Energy & Environmental Science*, 4:862–865, 2011.

[152] M. Contreras, T. Barnes, J. Lagemaat, G. Rumbles, T. Coutts, C. Weeks, P. Glatkowski, I. Levitsky, J. Peltola, and D. Britz. Replacement of transparent conductive oxides by single-wall carbon nanotubes in Cu(InGa)Se_2-based solar cells. *Journal of Physical Chemistry C: Letters*, 111:14045–14048, 2007.

[153] J. van de Lagemaat, T.M. Barnes, G. Rumbles, S.E. Shaheen, T.J. Coutts, C. Weeks, I. Levitsky, J. Peltola, and P. Glatkowski. Organic solar cells with carbon nanotubes replacing InO:Sn as the transparent electrode. *Applied Physics Letters*, 88:233503, 2006.

[154] T. Barnes, X. Wu, J. Zhou, A. Duda, J. van de Lagemaat, T. Coutts, C. Weeks, D. Briz, and P. Glatkowski. Single-wall carbon nanotube networks as a transparent back contact in CdTe solar cells. *Applied Physics Letters*, 90:234503, 2007.

[155] T. Kawano, D. Christensen, S. Chen, C. Cho, and L. Lin. Formation and characterization of silicon/carbon nanotube/silicon heterojunctions by local synthesis and assembly. *Applied Physics Letters*, 89:163510, 2006.

[156] M. Tzolov, B. Chang, A. Yin, D. Straus, and J. Xu. Electronic transport in a controllably grown carbon nanotube-silicon heterojunction array. *Physical Review Letters*, 92(7):75505, 2004.

[157] S. Datta. The non-equilibrium green's function (NEGF) formalism: An elementary introduction. In *2002 International Electronic Devices Meeting*, pages 703–706, 2002.

[158] J. Guo, S. Datta, M. Lundstrom, and M. Anantam. Towards multi-scale modeling of carbon nanotube transistors. *Arxiv preprint*, 2003.

[159] A.G. Milnes and D.L. Feucht. *Heterojunctions and metal-semiconductor junctions*. Academic Press, 1972.

[160] P. Liu, Q. Sun, F. Zhu, K. Liu, K. Jiang, L. Liu, Q. Li, and S. Fan. Measuring the work function of carbon nanotubes with thermionic method. *Nano Letters*, 8(2):647–651, 2008.

[161] H. W. Kroto, S. C. Heath, J. R. O'Brien, R. F. Curl, and R. E. Smalley. C_{60}: Buckmisterfullerene. *Nature*, 318:162–163, 1985.

[162] A. A. Lucas, F. Moreau, and Ph. Lambin. Optical simulations of electron diffractions by carbon nanotubes. *Reviews of Modern Physics*, 74(1):1–10, 2002.

[163] Y. X. Liang, Q. H. Li, and T. H. Wang. Current saturation in multiwalled carbon nanotubes by large bias. *Applied Physics Letters*, 84(17):3379–3381, 2004.

[164] S. Iijima. Helical microtubules of graphitic carbon. *Nature*, 354:56–58, 1991.

[165] M. Monthioux and V. L. Kuznetsov. Who should be given credit for the discovery of carbon nanotubes? *Carbon*, 44:1621–1623, 2006.

[166] L. V. Radushkevich and V. M. Lukyanovich. O strukture ugleroda, obrazujucegosja pri termiceskom razloznii okisi ugleroda na zeleznom kontakte. *Zhurnal Fizicheskoi Khimii*, 26:88–95, 1952.

[167] R. T. K. Baker. Catalytic growth of carbon filaments. *Carbon*, 27:315–323, 1989.

[168] A. Oberlin, M. Endo, and T. Koyama. Filamentous growth of carbon through benzene decomposition. *Journal of Crystal Growth*, 32:335–349, 1976.

[169] H. G. Tennent. Carbon fibrils, method for producing same and compositions containing same. *US Patent 4,663,230*, 1984.

[170] S. Iijima and T. Ichihashi. Single-shell carbon nanotubes of 1-nm diameter. *Nature*, 363:603–605, 1993.

[171] D. S. Bethune, C. H. Kiang, M. S. de Vries, G. Gorman, R. Savoy, J. Vazquez, and R. Beyers. Cobalt-catalysed growth of carbon nanotubes with single-atomic-layer walls. *Nature*, 363:605–607, 1993.

[172] P. M. Ajayan and T. W. Ebbesen. Nanometer-size tubes of carbon. *Reports on Progress of Physics*, 60:1025–1062, 1997.

[173] M. S. Dresselhaus, G. Dresselhaus, and R. Saito. Physics of carbon nanotubes. *Carbon*, 33(7):883–891, 1995.

[174] Y. Yi. *Ballistic conduction in multiwalled carbon nanotubes*. PhD thesis, Georgia Institute of Technology, 2004.

[175] Ph. Avouris. Carbon nanotube electronics. *Chemical Physics*, 281:429–445, 2002.

[176] H. Dai. Carbon nanotubes: opportunities and challenges. *Surface Science*, 500:218–241, 2002.

[177] R. Saito, G. Dresselhaus, and M. S. Dresselhaus. Electronic structure of double-layer graphene tubules. *Journal of Applied Physics*, 73(2):494–500, 1993.

[178] J. W. Mintmire and C. T. White. Electronic and structural properties of carbon nanotubes. *Carbon*, 33(7):893–902, 1995.

[179] D. H. Robertson, D. W. Brenner, and J. W. Mintmire. Energetics of nanoscale graphitic tubules. *Physical Review B: Condensed Matter and Materials Physics*, 45(21):12592–12595, 1992.

[180] S. B. Sinnott, R. Andrews, D. Qian, A. M. Rao, Z. Mao, E. C. Dickey, and F. Derbyshire. Model of carbon nanotube growth through chemical vapor deposition. *Chemical Physics Letters*, 315:25–30, 1999.

[181] S. Agrawal, M. J. Frederick, F. Lupo, P. Victor, O. Nalamasu, and G. Ramanath. Directed growth and electrical-transport properties of carbon nanotube architectures on indium tin oxide films on silicon-based substrates. *Advanced Functional Materials*, 15(12):1922–1926, 2005.

[182] N. Hamada, S. Sawada, and A. Oshiyama. New one-dimensional conductors: Graphitic microtubules. *Physical Review Letters*, 68(10):1579–1581, 1992.

[183] S. Frank, P. Poncharal, Z. L. Wang, and W. A. deHeer. Carbon nanotube quantum resistors. *Science*, 280:1744–1746, 1998.

[184] S. Datta. *Electronic Transport Properties in Mesoscopic Systems*. Cambridge University Press, Cambridge, 1995.

[185] M.Z. Kauser and P.P. Ruden. Effects of chirality and diameter on the transport properties of semiconducting carbon nanotubes. *Journal of Applied Physics*, 102:33712, 2007.

[186] S. Roche, F. Triozon, D. Mayou, and A. Rubio. Conduction mechanism in multiwall carbon nanotubes. In *American Institute of Physics Conference*, AIP Conf. Proc. (USA), pages 145–148, Kamakura, Japan, 2001. AIP.

[187] J. Robertson. Growth of nanotubes for electronics. *Materials Today*, 10(1-2):36–43, 2007.

[188] P. L. McEuen, M. S. Fuhrer, and H. Park. Single-walled carbon nanotube electronics. *IEEE Transactions on Nanotechnology*, 1(1):78–84, 2002.

[189] A. Naeemi and J. D. Meindl. Carbon nanotube interconnects. *Annual Review of Materials Research*, 39:255–275, 2009.

[190] R. Landauer. Conductance determined by transmission: probes and quantised constriction resistance. *Journal of Physics: Condensed Matter*, 43(1):8099–8110, 1989.

[191] A. Bachtold, C. Strunk, J. P. Salvetat, J. M. Bonard, L. Forro, T. Nussbaumer, and C. Schonenberger. Aharonov-Bohm oscillations in carbon nanotubes. *Nature*, 397:673–675, 1999.

[192] C. Schonenberger, A. Bachtold, C. Strunk, J. P. Salvetat, and L. Forro. Interference and interaction in multi-wall carbon nanotubes. *Applied Physics A: Materials Science and Processing*, 69(3):283–295, 1999.

[193] J. Cumings, P. G. Collins, and A. Zettl. Materials: Peeling and sharpening multiwall nanotubes. *Nature*, 406:586–586, 2000.

[194] P. G. Collins, M. Hersam, M. Arnold, R. Martel, and Ph. Avouris. Current saturation and electrical breakdown in multiwalled carbon nanotubes. *Physical Review Letters*, 86(14):3128–3131, 2001.

[195] P. G. Collins and Ph Avouris. Multishell conduction in multiwalled carbon nanotubes. *Applied Physics A: Materials Science and Processing*, 74(3):329–332, 2002.

[196] Y. Hayashi, T. Tokunaga, K. Kaneko, and Z. Horita. Characterization of transport properties of multiwalled carbon nanotube networks by microwave plasma chemical vapor deposition. *Diamond & Related Materials*, 15(4-8):1138–1142, 2006.

[197] B. Wei, R. Spolenak, P. Kohler-Redlich, M. Ruehle, and E. Arzt. Electrical transport in pure and boron-doped carbon nanotubes. *Applied Physics Letters*, 74(21):3149–3151, 1999.

[198] F. Kreupl, A. Graham, G. Duesberg, W. Steinhogl, M. Liebau, E. Unger, and W. Honlein. Carbon nanotubes in interconnect applications. *Microelectronic Engineering*, 64:399–408, 2002.

[199] A. Naeemi and J.D. Meindl. Compact physical models for multiwall carbon-nanotube interconnects. *IEEE Electron Device Letters*, 27(5):338–340, 2006.

[200] S. Haruehanroengra and W. Wang. Analyzing conductance of mixed carbon-nanotube bundles for interconnect applications. *IEEE Electron Device Letters*, 28(8):756–759, 2007.

[201] K. Liu, Ph. Avouris, R. Martel, and H. K. Hsu. Electrical transport in doped multiwalled carbon nanotubes. *Physical Review B: Condensed Matter and Materials Physics*, 63(16):161404, 2001.

[202] J. B. Park, G. S. Choi, Y. S. Cho, S. Y. Hong, D. Kim, S. Y. Choid, J. H. Lee, and K. I. Cho. Characterization of Fe-catalyzed carbon nanotubes grown by thermal chemical vapor deposition. *Journal of Crystal Growth*, 244:211–217, 2002.

[203] S. Turano. *Carbon Nanotubes: Chemical Vapor Deposition, Synthesis and Applications in Electrochemical Double Layer Supercapacitors*. PhD thesis, Georgia Institute of Technology, 2005.

[204] M. Meyyappan, L. Delzeit, A. Cassell, and D. Hash. Carbon nanotube growth by PECVD: a review. *Plasma Sources Science and Technology*, 12(2):205–216, 2003.

[205] S. Hofmann, C. Ducati, B. Kleinsorge, and J. Robertson. Direct growth of aligned carbon nanotube field emitter arrays onto plastic substrates. *Applied Physics Letters*, 83(22):4661–4663, 2003.

[206] Y. C. Choi, D. W. Kim, T. J. Lee, C. J. Lee, and Y. H. Lee. Growth mechanism of vertically aligned carbon nanotubes on silicon substrates. *Synthetic Materials*, 117:81–86, 2001.

[207] S. Musso, G. Fanchini, and A. Tagliaferro. Growth of vertically aligned carbon nanotubes by CVD by evaporation of carbon precursors. *Diamond & Related Materials*, 14:784–789, 2005.

[208] Z.F. Ren, Z. P Huang, J. W. Xu, J. H. Wang, P. Bush, M. P. Seigal, and P. N. Provencio. Synthesis of large arrays of well-aligned carbon nanotubes on glass. *Science*, 282:1105–1107, 1998.

[209] C. J. Lee and J. Park. Growth and structure of carbon nanotubes produced by thermal chemical vapor deposition. *Carbon*, 39:1891–1896, 2001.

[210] M. Endo, K. Takeuchi, S. Igarashi, K. Kabori, M. Shiraishi, and H. W. Kroto. The production and structure of pyrolytic carbon nanotubes. *Journal of Physics and Chemistry of Solids*, 54(12):1841–1848, 1993.

[211] C. J. Lee, S. C. Lyu, Y. R. Cho, J. H. Lee, and K. I. Cho. Diameter-controlled growth of carbon nanotubes using thermal chemical vapor deposition. *Chemical Physics Letters*, 341:245–249, 2001.

[212] Y. C. Choi, Y. M. Shin, Y. H. Lee, B. S. Lee, G. S. Park, W. B. Choi, N. S. Lee, and J. M. Kim. Controlling diameter, growth rate, and density of vertically aligned carbon nanotubes synthesized by plasma enhanced carbon vapor deposition. *Applied Physics Letters*, 76(17):2367–2369, 2000.

[213] C. J. Lee, D. W. Kim, T. J. Lee, Y. C. Choi, Y. S. Park, W. S. Kim, Y. H. Lee, W. B. Choi, N. S. Lee, J. M. Kim, Y. G. Choi, and S. C. Yu. Synthesis of uniformly distributed carbon nanotubes on a large area of Si substrates by thermal chemical vapor deposition. *Applied Physics Letters*, 75(12):1721–1723, 1999.

[214] D. Macdonald, A. Cuevas, M. Kerr, C. Samundsett, D. Ruby, S. Winderbaum, and A. Leo. Texturing industrial multicrystalline silicon solar cells. *Solar Energy*, 76:277–283, 2004.

[215] W. Tong. *Chemical beam epitaxial growth of ZnS: growth kinetics and novel electroluminescent strutures*. PhD thesis, Georgia Institute of Technology, 1996.

[216] X.J. Wang, J.D. Flicker, B.J. Lee, W.J. Ready, and Z.M. Zhang. Visible and near-infrared radiative properties of vertically aligned multi-walled carbon nanotubes. *Nanotechnology*, 20:215704, 2009.

[217] P. Nednoor, N. Chopra, V. Gavalas, L. G. Bachas, and B. J. Hinds. Reversible biochemical switching of ionic transport through aligned carbon nanotube membranes. *Chemistry of Materials*, 17(14):3595–3599, 2005.

[218] G. D. Nessim, A. J. Hart, J. S. Kim, D. Acquaviva, J. Oh, C. D. Morgan, M. Seita, J. S. Leib, and C. V. Thompson. Tuning of vertically-aligned carbon nanotube diameter and areal density through catalyst pre-treatment. *Nano Letters*, 8(11):3587–3593, 2008.

[219] P. Vinten, J. Lefebvre, and P. Finnie. Kinetic critical temperature and optimized chemical vapor deposition growth of carbon nanotubes. *Chemical Physics Letters*, 469(4-6):293–297, 2009.

[220] Y. Y. Wang, S. Gupta, R. J. Nemanich, Z. J. Liu, and L. C. Qin. Hollow to bamboolike internal structure transition observed in carbon nanotube films. *Journal of Applied Physics*, 98(1):14312, 2005.

[221] R.F.C Farrow, editor. *Molecular Beam Epitaxy - Applications to Key Materials*. Noyes Publications, 1995.

[222] M. A. Herman and H. Sitter. *Molecular beam epitaxy: fundamentals and current status*. Springer, 1996.

[223] J. Jeans. *Introduction to kinetic theory of gases*. Cambridge University Press, 1940.

[224] K.Y. Cheng, A.Y. Cho, and W.R. Wagner. Molecular-beam epitaxial growth of uniform $Ga_{0.47}In_{0.53}As$ with a rotating sample holder. *Applied Physics Letters*, 39:607–609, 1981.

[225] Airco inc. *Physical Vapor Deposition*. Airco Incorporated, 1976.

[226] C. Foxon and B.A. Joyce. Interaction kinetics of As_2 and Ga on {100} GaAs surfaces. *Surface Science*, 64:293–304, 1977.

[227] C.E.C. Wood and B.A. Joyce. Tin-doping effects in GaAs films grown by molecular beam epitaxy. *Journal of Applied Physics*, 49(9):4854–4861, 1978.

[228] R. Fitch. Total pressure gauges. *Vacuum*, 37(8-9):637–641, 1987.

[229] M. Schulz, O. Madelung, H. Weiss, H. Landolt, and R. Börnstein, editors. *Zahlenwerte und Funktionen aus Naturwissenschaften und Technik-Halbleiter*, volume 16. Springer, 1982.

[230] C.C Kuo, C.C Liu, C.C Lin, Y.Y Liou, J.L He, and F.S Chen. Effects of oxygen gas flow rate and ion beam plasma conditions on the opto-electronic properties of indium molybdenum oxide films fabricated by ion beam-assisted evaporation. *Thin Solid Films*, 516(16):5612–5617, 2008.

[231] J. Cuomo, S. Rossnagel, and H. Kaufman. *Handbook of Ion Beam Processing Technology - Principles, Deposition, Film Modification and Synthesis*. Noyes Publications, 1989.

[232] S.P. Turano, J.D. Flicker, and W.J. Ready. Nanoscale coaxial cables produced from vertically aligned carbon nanotube arrays grown via chemical vapor deposition and coated with indium tin oxide via ion assisted deposition. *Carbon*, 46(5):723–728, 2008.

[233] R. Perez and R. Stewart. Solar irradiance conversion models. *Solar Cells*, 18(3):213–222, 1986.

[234] K.K. Govil. Maximum-power points of solar cells with simultaneous series and shunt losses. *International Journal of Electronics*, 56(2):223–227, 1984.

[235] A. Ambroziak. *Semiconductor Photolectric Devices: an Introduction to Design*. University of California, 1968.

[236] J. Flicker and J. Ready. Simulations of absorbance efficiency and power production of three dimensional tower arrays for use in photovoltaics. *Journal of Applied Physics*, 103(11):113110, 2008.

[237] R Burnham. *Burnham's celestial handbook: an observer's guide to the Universe beyond the solar system*. General Publishing Company, Ltd., 1978.

[238] R. Snieder. *A guided tour of mathematical methods for the physical sciences*. Cambridge University Press, 2004.

[239] C.D. Cantrell. *Modern mathematical methods for physicists and engineers*. Cambridge University Press, 2000.

[240] S. Demtsu, D. Albin, J. Sites, W. Metzger, and A. Duda. Cu-related recombination in CdS/CdTe solar cells. *Thin Solid Films*, 516:2251–2254, 2008.

[241] D. Rose, F. Hasoon, R. Dhere, D. Albin, R. Ribelin, X. Li, Y. Mahathongdy, T. Gessert, and P. Sheldon. Fabrication procedures and process sensitivities for CdS/CdTe solar cells. *Progress in Photovoltaics: Research and Applications*, 7:331–340, 1999.

[242] M. Ozsan, D. Johnson, M. Sadeghi, and D. Sivapathasundaram. Optical and electrical characterization of chemically deposited cadmium sulfide thin films. In *Conference Record of the twenty fourth IEEE Photovoltaic Specialists Conference*, pages 327–330, 1994.

[243] J. García-Céspedes, J. Álvarez-García, X. Zhang, J. Hampshire, and E. Bertran. Optimal deposition conditions of TiN barrier layers for the growth of vertically aligned carbon nanotubes onto metallic substrates. *Journal of Physics D: Applied Physics*, 42:104002, 2009.

[244] M. Turchanin, P. Agraval, and A.R. Abdulov. Phase equilibria and thermodynamics of binary copper systems with 3 d-metals. VI. Copper-nickel system. *Powder Metallurgy and Metal Ceramics*, 46(9-10):467–477, 2007.

[245] R. Ferro, A. Saccone, D. Maccio, and S. Delfino. A survey of gold intermetallic chemistry. *Gold Bulletin*, 36(2):39–50, 2003.

[246] X. Liu, F. Gao, C. Wang, and I. Kiyohito. Thermodynamic assessments of the Ag-Ni binary and Ag-Cu-Ni ternary systems. *Journal of Electronic Materials*, 37(2):210–217, 2008.

[247] H.S. Yoo, C.H. Park, S.J. Yun, S.K. Joo, and N.M. Hwang. Effect of base layers beneath Ni catalyst on the growth of carbon nanofibers using plasma enhanced chemical vapor deposition. *Japanese Journal of Applied Physics*, 47(4):2306–2312, 2008.

[248] Z.P. Yang, L. Ci, J.A. Bur, S.Y. Lin, and P.M. Ajayan. Experimental observation of an extremely dark material made by a low-density nanotube array. *Nano Letters*, 8(2):446–451, 2008.

[249] D. Kim. Improvement of structural and optoelectrical properties by post-deposition electron beam annealing of ITO thin films. *Renewable Energy*, 36:525–528, 2011.

[250] L. Ryabova, V. Salun, and I. Serbinov. Transparent conductive films of In_2O_3:Sn prepared by the pyrolysis method. *Thin Solid Films*, 92:327–332, 1982.

[251] L. Bardos and M. Libra. Effect of the oxygen absorption on properties of ITO layers. *Vacuum*, 39(1):33–36, 1989.

[252] Max Planck and Morton Masius. *The theory of heat radiation*. P. Blakiston's Son And Co., 1914.

[253] F. Treble. Solar cells. *Physical Science, Measurement and Instrumentation, Management and Education-Reviews, IEEE Proceedings A*, 127(8):505–527, 1980.

[254] J.E. Phillips, W.N. Shafarman, and E. Shan. Evidence for amorphous like behavior in small grain thin film polycrystalline solar cells. In *Photovoltaic Energy Conversion, 1994., Conference Record of the Twenty Fourth. IEEE Photovoltaic Specialists Conference-1994, 1994 IEEE First World Conference on*, volume 1, pages 303–306, 1994.

[255] B.R. Mehta and F.E. Kruis. A graded diameter and oriented nanorod-thin film structure for solar cell application: a device proposal. *Solar Energy Materials & Solar Cells*, 85:107–113, 2005.

[256] K. Peng, Y. Xu, Y. Wu, Y. Yan, S.T. Lee, and J. Zhu. Aligned single-crystalline Si nanowire arrays for photovoltaic applications. *Small*, 1(11):1062–1067, 2005.

[257] L. Tsakalakos, J. Balch, J. Fronheiser, and B. Korevaar. Silicon nanowire solar cells. *Applied Physics Letters*, 91:233117, 2007.

[258] Jud Ready. Three dimensional multi-junction photovoltaic device. *State Intellectual Property Office of the PRC #200680006941*, 2006.

[259] Jud Ready. Three dimensional multi-junction photovoltaic device. *Korean Intellectual Property Office #10-2007-7022061*, 2007.

[260] Jud Ready. Three dimensional multi-junction photovoltaic device. *IP Australia #2006297870*, 2006.

[261] Jud Ready. Three dimensional multi-junction photovoltaic device. *European Patent Office Application #WO 2007/040594 A2*, 2006.

[262] Jud Ready. Three dimensional multi-junction photovoltaic device. *US Patent App. #2008/0251122 A1*, 2006.

[263] M. Schriver, W. Regan, M. Loster, and A. Zettl. Carbon nanostructure a-Si:H photovoltaic cells with high open-circuit voltage fabricated without dopants. *Solid State Communications*, 150:561–563, 2010.

[264] P. Mohseni, G. Lawson, A. Adronov, and R. LaPierre. Hybrid GaAs-nanowire–carbon-nanotube flexible photovoltaics. *IEEE Journal of Selected Topics in Quantum Electronics*, PP(99):1–8, 2010.

VITA

Jack D. Flicker was born in Harrisburg, Pennsylvania. He received a B. S. in Physics and in Chemistry from the Pennsylvania State University in 2006 before coming to Georgia Tech to pursue a doctorate in Materials Science and Engineering. When he is not working on his research, Mr Flicker enjoys playing sports and spending time with his dogs.

THREE-DIMENSIONAL CARBON NANOTUBE BASED PHOTOVOLTAICS

Jack Flicker

308 Pages

Directed by Dr. W. Jud Ready

Photovoltaic (PV) cells with a three dimensional (3D) morphology are an exciting new research thrust with promise to create cheaper, more efficient solar cells. This work introduces a new type of 3D PV device based on carbon nanotube (CNT) arrays. These arrays are paired with the thin film heterojunction, CdTe/CdS, to form a complete 3D carbon nanotube PV device (3DCNTPV). Marriage of a complicated 3D structure with production methods traditionally used for planar CdTe solar cell is challenging. This work examines the problems associated with processing these types of cells and systematically alters production methods of the semiconductor layers and electrodes to increase the short circuit current (I_{sc}), eliminate parasitic shunts, and increase the open circuit voltage (V_{oc}).

The main benefit of 3D solar cell is the ability to utilize multiple photon interactions with the solar cell surface. The three dimensionality allows photons to interact multiple times with the photoactive material, which increases the absorption and the overall power output over what is possible with a two dimensional (2D) morphology. To quantify the increased power output arising from these multiple photon interactions, a new absorption efficiency term, η_{3D}, is introduced. The theoretical basis behind this new term and how it relates to the absorption efficiency of a planar cell, η_{2D}, is derived.

A unique model for the average number of multiple photon impingements, Γ, is proposed based on three categories of 3D morphology: an infinite trench, an enclosed box, and an array of towers. The derivation of η_{3D} and Γ for these 3D PV devices gives a complete picture of the enhanced power output over 2D cells based on CNT array

height, pitch, radius, and shape. This theory is validated by monte carlo simulations and experiment.

This new type of 3D PV devices has been shown to work experimentally. The first 3DCNTPV cells created posses I_{sc} values of 0.085 to 17.872mA/cm^2 and V_{oc} values in the range of 2 to 122mV. These figures of merit are low for CdTe cells, so planar cells without CNTs and planar cells with unpatterned CNTs were developed. The planar cells had figures of merit about the same as the 3DCNTPV cells, indicating that the low efficiency of the 3DCNTPV cell is due to processing and not inherent to the 3D structure.

The CdTe/p-Si interface used as a back contact was determined to provide a rectifying barrier opposite normal current flow. This had the effect of inverting the normal curvature of the IV curve in the fourth quadrant. This problem was eliminated by replacing the CdTe/p-Si interface with a CdTe/metal interface.

CNTs were successfully grown directly on an Ag underlayer, but the growth reproducibility and the CNT height was not sufficient for use in 3DCNTPV devices. Therefore, CNTs were grown on a SiO_2 passivated Si wafer and then metallized. This eliminated the CNTs as the back contact and used them only as a structure to provide the 3D morphology. These cells exhibited low shunt resistances on the order of 300Ω, causing a straight line IV curve.

This shunting was found to be caused by the ion assisted deposition of ITO. This plasma process etched away semiconducting layers and caused pinholes in the CdTe/CdS film. Many different strategies were utilized to try and eliminate this shunt and induce curvature in the IV curve, including adding sacrificial metal layers before the ITO deposition, using electron beam evaporated ITO, and using RF sputtered ITO. The addition of metal layers before ITO deposition did not result in cells which could reliably demonstrate both photocurrent and IV curvature. Electron beam

deposition of ITO resulted in cells with excellent IV curvature, but the ITO deposited in this manner was too resistive and absorptive to create well functioning cells.

RF sputter was found to be an acceptable method of ITO deposition if an intrinsic ZnO layer was deposited beforehand. This high resistance and transparent ZnO layer was deposited in order to passivate any pinholes or inhomogeneities present in the CdTe/CdS layer. Cells with this ZnO layer exhibited I_{sc} values slightly less than 1mA/cm^2 with V_{oc} values of up to 350mV. This represents an order of magnitude increase in the I_{sc} and a 300% increase in the V_{oc}.

The cells with this ZnO layer also exhibited good IV curvature. Unfortunately, the increase in I_{sc} was not enough to catch this curvature in the fourth quadrant. In order to further increase the I_{sc} of the cells so that IV curvature could be measured in the fourth quadrant, a $CdCl_2$ anneal was attempted. A $CdCl_2/CH_3OH$ solution-based anneal resulted in delamination of the CdTe layer due to penetration of the liquid beneath the semiconductor layers. Soaking the cells in a $CdCl_2/CH_3OH$ solution and air drying before anneal eliminated this delamination, but did not increase the I_{sc} values of the cells. To determine if the $CdCl_2$ could not penetrate through the CdS layer, annealing with only the CdTe layer present was attempted, but did not result in an I_{sc} increase. To investigate if intermixing of CdS into the CdTe layer during annealing was preventing an increase in cell I_{sc}, a two-stage (pre- and post-anneal) CdS deposition was attempted. This did not result in an increase in cell I_{sc}. Finally, soaking cell substrates in the $CdCl_2/CH_3OH$ solution before CdTe/CdS deposition was attempted, but also did not result in an increase in I_{sc} values of the cells.

The output power of the cells at varying incident angles of light was measured. The cells show an increase in the normalized power output compared to similar planar cells when the solar flux is at off-normal angles. The power output vs. incident angle curve takes an inverted C-type curve as predicted by the theory developed here. The complete theory of 3DCNTPV presented in this work describes the power output vs.

incident angle of a 3DCNTPV cell based only on cell morphology. The experimental power output vs. zenith angle was compared to the theoretically calculated power output with very good agreement between the two.

This work has made a number of contributions to the field of 3D PV device research, including:

1. Developing one of the first Generation III inorganic PV devices to use CNTs as a charge collector
2. Developing a simple-cost effective way to texture thin film solar cells using a "bottom up" substrate-configuration approach
3. Developing a complete theoretical model of the 3DCNTPV cell
4. Creating working proof-of-concept devices using the 3DCNTPV structure
5. Increasing I_{sc} by an order of magnitude and V_{oc} by 300%
6. Demonstrating viable techniques towards eliminating shunting resistances and inducing IV curvature
7. Confirming theoretical model with experimental data of power output vs. incident angle